Theoretical and Experimental Explorations of Charge Transfer in Small Molecules and Peptide Nucleic Acids

by

Xing Yin

B.S., Nanjing University, 2006

M.S., Nanjing University, 2008

Submitted to the Graduate Faculty of the

Kenneth P. Dietrich School of Arts and Sciences in partial fulfillment

of the requirements for the degree of

Doctor of Philosophy

University of Pittsburgh

2014

UNIVERSITY OF PITTSBURGH

KENNETH P. DIETRICH SCHOOL OF ARTS AND SCIENCES

This dissertation was presented

by

Xing Yin

It was defended on

November 21, 2014

and approved by

Dr. Kenneth D. Jordan, Professor, Department of Chemistry

Dr. Geoffrey R. Hutchison, Assistant Professor, Department of Chemistry

Dr. Catalina Achim, Professor, Department of Chemistry, Carnegie Mellon University

Dissertation Advisor: Dr. David H. Waldeck, Professor, Department of Chemistry

Theoretical and Experimental Explorations of Charge Transfer in Small Molecules and Peptide Nucleic Acids

Xing Yin, PhD

University of Pittsburgh, 2014

Non-adiabatic charge transfer (CT) is one of the simplest but very important chemical reactions. As a model system, alkanedithiols are among the most popular ones for short- or medium-range CT. Peptide nucleic acid (PNA), which consists of nucleobases and peptide backbones, is another promising model system for long-range CT. Various models and computational methods have been developed to describe three major experimental configurations: electrochemical measurement with self-assembled monolayer films (SAMs), single-molecule conductance measurement and photoinduced electron transfer (PET).

This dissertation have employed above methods to study the two model systems. The first work focuses on electrochemical models. Single-step models are widely used for analyzing CT through SAMs. However, long-range CT can occur in a "hopping" regime that involves multiple events. This study describes a three-step kinetic scheme to model CT in this regime. It is corroborated by the experimental results of a 10-mer PNA. The second study compares single molecule conductances of alkanedithiols and alkoxydithiols. Both molecular junction measurements and theoretical simulations by non-equilibrium Green's function (NEGF) method show that the conductance is lower for alkoxydithiols and the difference is length dependent. A pathway analysis of the electronic coupling is used to explain the results. The last two studies address the importance of conformational distributions on CT in PNAs: The third study compares the electrochemical charge transfer rates of normal aeg-PNA and γ-PNA which has a less flexible

backbone. Theoretical simulations show that the greater flexibility of the aeg-PNA gives rise to a more frequent appearance of high-CT rate conformations. In the last study a new PNA scaffold with a $[Ru(Bpy)_3]^{2+}$ donor and a bis(8-hydroxyquinolinate)$_2$ copper acceptor for PET is described. Experiments show that whether the $[Ru(Bpy)_3]^{2+}$ is terminally or centrally situated affects PET. Molecular dynamics simulations reveal that the difference in conformational distributions is a possible explanation. The above findings provide a deeper understanding of CT in molecules, and may facilitate the development of non-adiabatic dynamics in a bigger picture.

TABLE OF CONTENTS

LIST OF TABLES

LIST OF FIGURES

LIST OF EQUATIONS

PREFACE

I have received a lot of help during the years and I feel truly grateful to many people who made the work possible. First and foremost, I would like to thank my academic advisor, Prof. David H. Waldeck. He has been a wonderful scientist and educator. Although he served as the Department Chair through almost all these years and have been very busy, he was always patient when I needed help and he has always provided me with useful guidance and invaluable advice. I am also thankful to my labmates, including Dr. Prasun Mukherjee, Dr. Emil Wierzbinski, Dr. Kathy Davis, Dr. Lei Wang, Dr. Yang Wang, Dr. Matthew Kofke, Dr. Mingyan Wu, Brian Bloom, Madu Mendis, Brittney Graff, Miles Batson, Daniel Lamont and Edward Beall. They are not only co-workers, but also my best friends.

I am very grateful to Prof. Catalina Achim, an excellent collaborator and as well as one of the dissertation committee members, and her group, especially Dr. Silvia Bezer, Dr. Arnie de Leon, Dr. Jing Kong, Selma Ulku, Yookyung Bae and Dilhara Jayarathna. They synthesized most of the PNAs and Prof. Achim's crucial advice and critical analysis helped to shape as a better scientist. I cannot image how I could finish the study without them.

I am also thankful to my other committee members, Prof. Kenneth Jordan and Prof. Geoffrey Hutchison, who have guided me over the years as well. Prof. Jordan is also the mentor of my research proposal and I have learnt a lot from him through our discussion about the proposal and electron transfer calculations. Prof. Geoffrey Hutchison's Avogadro and OpenBabel have become my favorite computational chemistry "Swiss knives" and I feel so lucky that I could discuss science and coding with him face to face.

I was also lucky to work with a number of excellent theoretical chemists from other institutes. I would like to thank Prof. David Beratan (Duke) and his group, especially Dr. Alexander Balaef, Dr. Ravindra Venkatramani and Dr. Shahar Keinan, who taught me the computational methods for PNA charge transfer. Dr. Marcela Madrid (PSC) and Dr. Yongle Li (NYU) helped me set up force field parameters and I would be amiss if I didn't thank them a lot.

I also want to express my appreciation to all the staff in the Department, especially the glass blower Lori who made a lot of custom glassware for me, and Richard and Albert from the Center for Simulation and Modeling who solved many technical problems I encountered.

Last but not the least, I am eternally indebted to my family. My parents have done everything to support me. Even in every phone call they always told me not to worry about them and just go ahead to pursue my dream of science, but I can understand the feelings behind the words. I miss you very much and I wish I could repay you one day! I am especially grateful to my beloved wife, Dr. Dujuan Lu, who has been together with me since college. During the toughest time of my life, she has always been there for me and I just cannot thank her enough for the love and support through all these years. Nevertheless, you mean the world to me and thank you!

1.0 INTRODUCTION

1.1 THE IMPORTANCE OF ELECTRON TRANSFER

Electron transfer or charge transfer is commonly seen as the simplest but very important (if not the most important) chemical reaction.[1,2] First, electron transfer is the key step in a lot of biological processes in nature, such as photosynthesis and respiration[3–6] Second, it is a fundamental process in many artificial systems of great technological impact, such as batteries, solar cells, modern electronics, ...etc.[7–14] Finally but perhaps most importantly for chemists, the methods used in electron transfer studies and the conclusions obtained from electron transfer studies connect all branches of chemistry. It has been more than half a century since Marcus's groundbreaking work, but new experiments keep emerging from different aspects of electron transfer processes and electron transfer theory keeps evolving to explain more phenomena. There is no sign that this trend will stop soon.

In this dissertation, experimental and computational methods are combined to study some fundamental aspects of electron transfer in newly developed nanoscale systems. In this chapter, features of the basic theory and related experimental/computational methods are reviewed.

1.2 BASIC ELECTRON TRANSFER MECHANISMS

1.2.1 Marcus Theory for Molecular Electron Tunneling

1.2.1.1 Classical Marcus Theory

The classical Marcus theory is probably the most famous and concise description of electron transfer. It can be derived from the following kinetic scheme for an outer-sphere bimolecular electron transfer in solvent:[15–19]

$$\begin{aligned} D + A &\underset{k_{-1}}{\overset{k_1}{\rightleftharpoons}} (DA)^{\dagger} \\ (DA)^{\dagger} &\underset{k_{-2}}{\overset{k_2}{\rightleftharpoons}} \left(D^{+}A^{-}\right)^{\dagger} \\ \left(D^{+}A^{-}\right)^{\dagger} &\xrightarrow{k_3} D^{+} + A^{-} \end{aligned} \qquad \textbf{Equation 1.1}$$

where $(DA)^{\dagger}$ is the transition state and $(D^{+}A^{-})^{\dagger}$ is the resonant state of activated products. These two states have the same nuclear configuration but different electronic configurations (Franck-Condon principle).[15] The first step corresponds to the solvent reorganization, the second step corresponds to the actual electron transfer, and the last step corresponds to the formation of the products. By applying the transition state theory and standard techniques in chemical kinetics, such as the steady-state approximation and detailed balance, the overall reaction rate can be written as:

$$k_{ET} \propto \exp\left(-\frac{\Delta G^{\ddagger}}{k_B T}\right) \qquad \textbf{Equation 1.2}$$

where $\Delta G^{\ddagger}$ is the activation energy and k_B is the Boltzmann constant. Marcus further assumed two parabolas (see Figure 1.1) as the potential energy surfaces, and the final expression of k_{ET} was obtained:

$$\begin{aligned} \Delta G^{\ddagger} &= -\frac{(\lambda + \Delta_r G\,)^2}{4\lambda} \\ \Longrightarrow k_{ET} &= A \exp\left(-\frac{(\lambda + \Delta_r G\,)^2}{4\lambda k_B T}\right) \end{aligned} \qquad \textbf{Equation 1.3}$$

where λ is the reorganization energy and $\Delta_r G$ is the reaction free energy. The relationship between $\Delta G^{\ddagger}$ and thermodynamic parameters λ and $\Delta_r G$ can be easily derived from Figure 1.1B. It will be revealed in the next section that the pre-exponential factor A is related to the electronic coupling H_{DA} in the non-adiabatic (or diabatic) limit. It is amazing that there are only three parameters in Equation 1.3 while it can describe a very wide range of experiments. One of the most striking predictions of the equation is the Marcus "inverted region". According to Equation 1.3, k_{ET} reaches its maximum at $\lambda = |\Delta_r G|$ and its value decreases if the driving force keeps increasing! It was not until about 25 years after Marcus' prediction that the first experimental evidence for the existence of the inverted region was reported by Miller *et al.*[20,21]

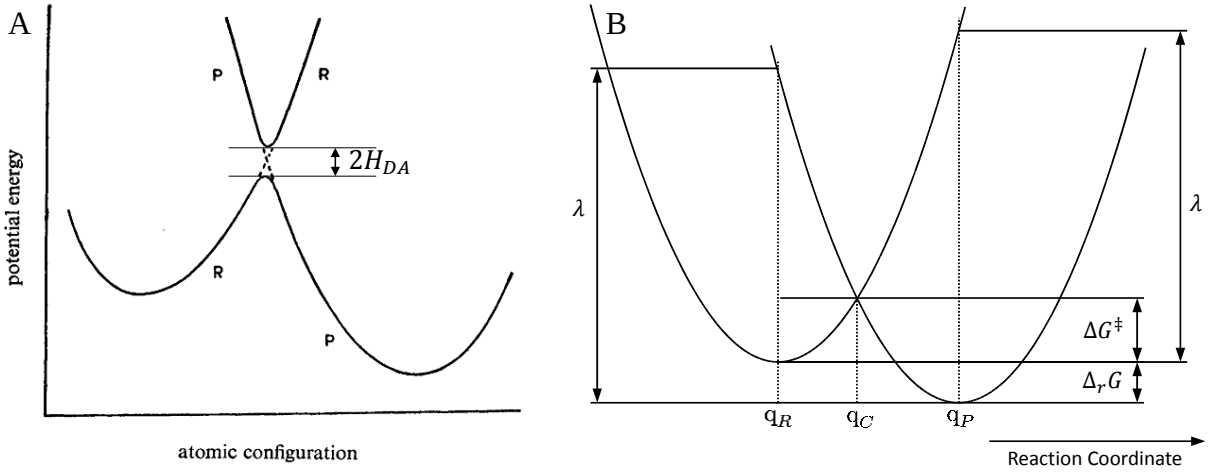

Figure 1.1. Panel A: Profile of an effective one-dimensional potential energy surface proposed by Marcus in 1960.[22] Adapted from Ref. 22 with permission of The Royal Society of Chemistry. The "inverted region" was predicted by Marcus in the same paper. The solid lines show the corresponding adiabatic potential energy surface and the dashed lines are the diabatic potential energy curves (See section 1.2.1.2) Panel B.: The definition of $\boldsymbol{\lambda}$, $\boldsymbol{\Delta G^{\ddagger}}$, and $\boldsymbol{\Delta_r G}$ in classical Marcus theory.

1.2.1.2 Diabatic States and the Semi-classical Marcus Theory

Before the discussion of semi-classical theory, it is useful to expand the pre-exponential factor in Equation 1.3 as:[23,24]

$$A = v_n \kappa_{el} \Rightarrow k_{ET} = v_n \kappa_{el} \exp\left(-\frac{(\lambda + \Delta_r G)^2}{4\lambda k_B T}\right) \qquad \textbf{Equation 1.4}$$

where v_n is the frequency of passage (nuclear motion) through the transition state corresponding to the reaction coordinate value q_C, and κ_{el} is the electronic transmission coefficient. Two limits of electron transfer (ET) reactions can be defined by κ_{el}: 1) an adiabatic limit if $\kappa_{el} \approx 1$, which means that almost every passage through q_C leads to electron transfer, and 2) a nonadiabatic limit if $\kappa_{el} \ll 1$, which means that only a very small fraction of passages through the transition state along the nuclear coordinate results in electron transfer. Note that 'bridge-mediated electron transfer' usually occurs in the nonadiabatic limit, hence the adiabatic limit will not be discussed.

The term "nonadiabatic" in the electron transfer literature is often viewed as a synonym for "weak-coupling". However, the usage of nonadiabatic (as well as adiabatic) has its root in chemical reaction dynamics. Within the Born-Oppenheimer approximation, adiabatic potential energy surfaces (or curves) are the eigenstates of the Born-Oppenheimer Hamiltonian **H**, as plotted in the solid line in Figure 1.1A. When the adiabatic potential curves are well separated (e.g. when the nuclear configuration **R** is close to the bottom of the reactant curve "R"), the change of nuclear configuration will not cause an electric transition and the Born-Oppenheimer approximation works very well. In contrast, the adiabatic potential curves might be very close to each other at some region(s) (e.g., when **R** is near the transition state in Figure 1.1) and the separation of nuclear motion and electronic motion are not reliable. In the representation of adiabatic potential curves, a change of nuclear configuration from **R** to $\mathbf{R} + \mathbf{\Delta R}$ results in an electronic transition from the ground state (lower potential curve) to an excited state (upper potential curve). The breakdown of

the Born-Oppenheimer approximation at this nuclear configuration is caused by the *nonadiabatic coupling* (also called as *vibronic coupling* or *derivative coupling*), which comes from the momentum operator of the full molecular Hamiltonian and has a form like:

$$\tau_{ij}(\mathbf{R}) \equiv \left\langle \Psi_{\mathrm{i}} \middle| \frac{\partial}{\partial \mathbf{R}} \Psi_j \right\rangle \qquad \textbf{Equation 1.5}$$

Direct calculation of the nonadiabatic coupling is usually not easy, especially when multiple adiabatic curves are close to each other and the main reason is that explicit derivatives of the wavefunctions are needed. To avoid such trouble, one can expand the wavefunctions on a complete orthonormal basis set that meets the following requirement:[18,25,26]

$$\mathbf{d}_{ij}(\mathbf{R}) \equiv \left\langle \Phi_{\mathrm{i}} \middle| \frac{\partial}{\partial \mathbf{R}} \Phi_j \right\rangle = 0, \quad \forall i, j, \mathbf{R} \qquad \textbf{Equation 1.6}$$

That is, the derivative coupling vanishes in this representation and $\{\Phi_{\mathrm{i}}\}$ is a strictly *diabatic* basis set. Of course $\{\Phi_{\mathrm{i}}\}$ are not the eigenstates of the Born-Oppenheimer electronic Hamiltonian **H** anymore, but we can still calculate a set of potential energy surfaces by using $\langle \Phi_i | \hat{H} | \Phi_i \rangle$, and the results are called diabatic potential energy surfaces (PES), as shown in the dashed line in Figure 1.1A. The adiabatic and nonadiabatic PES almost overlap everywhere expect for the small region near the transition state. More importantly, it has been shown that a dynamic process can be identically described in either the adiabatic picture with vibronic couplings (Equation 1.5) or in the diabatic picture with the *electronic couplings* $\langle \Phi_i | \hat{H} | \Phi_j \rangle$ —but the diabatic picture has the advantage of not requiring wavefunction derivatives and some important tools that deal with electronic couplings can be readily applied.

For electron transfer problems, a two-state model with two adiabatic potential curves as shown in Figure 1.1 is usually sufficient and one can relate the electronic couplings and adiabatic states analytically. **H** in a diabatic representation is a 2×2 matrix:

$$\mathbf{H} \equiv \begin{pmatrix} \mathbf{H}_D & \mathbf{H}_{DA} \\ \mathbf{H}_{AD} & \mathbf{H}_A \end{pmatrix} = \begin{pmatrix} E_D & \mathbf{H}_{DA} \\ \mathbf{H}_{DA} & E_A \end{pmatrix} \qquad \textbf{Equation 1.7}$$

It should be noted that in Equation 1.7, D denotes the reactant diabatic state $|D\rangle$ where charge is localized on the donor and A denotes the product diabatic state $|A\rangle$ where the charge is localized on the acceptor, unless Koopmans' theorem is assumed (see section 1.4.2.1).[7,27] E_D or E_A is not the "energy of the donor/acceptor" but the value of the reactant or product diabatic curve at nuclear configuration **R**. Diagonalize **H** and one obtains the eigenenergies of the adiabatic states:

$$E_{2(1)} = \frac{E_D + E_A}{2} \pm \sqrt{\left(\frac{E_D - E_A}{2}\right)^2 + H_{DA}^2} \qquad \textbf{Equation 1.8}$$

$$= \frac{E_D + E_A}{2} \pm |H_{DA}| \text{ if } E_D = E_A$$

$E_D = E_A$ is reached at $\mathbf{R} = \mathrm{q_C}$, see Figure 1.1B. Consequently, the energy gap between the two adiabatic curves at the transition state ($\mathbf{R} = \mathrm{q_C}$) is $2|H_{DA}|$. In the weak (diabatic electronic) coupling limit of electron transfer (i.e., $|H_{DA}|$ small), the two adiabatic curves are very close to each other, and the nonadiabatic coupling is indeed important. This limit can be considered as "nonadiabatic", even in the sense of chemical reaction dynamics. Actually, because of the assumption of the second step in Equation 1.1 (the nuclear configuration and energy of $(DA)^\dagger$ is the same as $(D^+A^-)^\dagger$ but their electronic states are different), Marcus theory is intrinsically a nonadiabatic theory in terms of reaction dynamics.

With this knowledge and these definitions in hand, one can derive the expression for the electron transfer rate constant, k_{ET}. From a quantum-mechanical perspective, electron transfer is a transition from state $|D\rangle$ to $|A\rangle$. In the weak coupling limit, Fermi's golden rule applies; and together with Franck-Condon principle, the following rate expression is obtained:[19]

$$k_{ET} = \frac{2\pi}{\hbar}|H_{DA}|^2|\langle D_{vib}|A_{vib}\rangle|^2\delta(E_D - E_A)$$
$$= \frac{2\pi}{\hbar}|H_{DA}|^2\mathrm{FCWD} \qquad \textbf{Equation 1.10}$$

where FCWD is short for "Franck-Condon weighted density-of-states". $|D_{vib}\rangle$ and $|A_{vib}\rangle$ are vibrational states of the reactant and product, respectively. The δ function ensures the conservation of energy in thermal electron transfer and distinguishes the FCWD from the common Franck-Condon factor in vertical excitation. To get an explicit analytical expression for the FCWD, harmonic oscillators are commonly assumed (corresponds to the parabolic shape of the potential curves in Figure 1.1). In the high-temperature limit, $k_BT \gg \hbar\omega$ (where ω is the angular frequency of the vibrational degree of freedom) and the vibrational mode can be treated classically. That is, the Boltzmann distribution can be used and the electron transfer occurs only at the crossing point. To find FCWD is equivalent to find the probability of the reactant at $\mathbf{R} = \mathrm{q_c}$ of an ensemble and the result is:[18]

$$f(\mathbf{R}) = \frac{1}{\mathcal{Z}}\exp\left(-\frac{E_D(\mathbf{R})}{k_BT}\right)$$
$$\Rightarrow \mathrm{FCWD} = \int \mathrm{d}\mathbf{R}\ f(\mathbf{R})\ \ \delta\big(E_D(\mathbf{R}) - E_A(\mathbf{R})\big) \qquad \textbf{Equation 1.9}$$

where $\mathcal{Z}$ is the partition function. After working out the expression for $\mathcal{Z}$ and $E_D(\mathbf{R}) - E_A(\mathbf{R})$ by using the parabolic shape assumption, the semi-classical expression of k_{ET} is obtained:[24]

$$k_{ET} = \frac{2\pi}{\hbar}|H_{DA}|^2\frac{1}{\sqrt{4\pi\lambda k_BT}}\exp\left(-\frac{(\lambda + \Delta G_r)^2}{4\lambda k_BT}\right) \qquad \textbf{Equation 1.11}$$

At room temperature Equation 1.11 usually applies for reactions that have low frequency modes linked to the electron transfer. However, at very low temperature this result predicts that the rate constant goes to zero, $\lim_{T\to 0} k_{ET} = 0$, which is in contradiction with experimental observations. The

expression for all temperature range has been derived by Jortner *et al.* and the details can be found in various reports.[19,28–30]

1.2.2 Long-Range Electron Transfer: the Switch from Tunneling to Hopping

Just as the meaning of "fast" changes in spectroscopy, the meaning of "long-range" seems to gradually changes with time. Before the discovery of "long-range" charge transfer in DNA, the electron tunneling in proteins or other donor-bridge-acceptor molecule over ~ 10 Å was already considered as long-range electron transfer.[27,31,32] They were considered "long" because the medium between the donor and acceptor is mostly saturated chains, which are usually considered insulating. The coupling should be much smaller than what is observed from a simple semi-classical direct tunneling model. The problem is solved by McConnell's superexchange model, which predicts an exponential decay with the distance at long enough distances:[33]

$$|H_{DA}|^2 \propto \exp(-\beta \cdot r_{DA}) \qquad \textbf{Equation 1.12}$$

where β is a parameter that characterizes the steepness of the coupling's decrease with distance. The superexchange model can be viewed as a variant of tunneling. Different from a semi-classical direct tunneling model, multiple pathways coexists and the molecular orbitals on the bridge participate, see Chapter 3 for a detailed discussion. Nevertheless, it is still a single-step and coherent model like direct tunneling. Marcus theory discussed in previous sections, applies.

Currently a charge transfer over ~ 10 Å is not often considered that "long", especially in nucleic acid studies. Charge transfer over a distance as long as 200 Å has been observed.[34] More importantly, the distance dependence of the charge transfer rate in such systems deviates drastically from a superexchange mechanism. Usually it is not an exponential decay in the "long-range" end but can be described by a power law:

$$k \propto r_{DA}^{-\gamma}$$ **Equation 1.13**

and the charge transfer still follows an exponential decay at the "short-range" end. The transition occurs at about ~ 10 to 20 Å depending on the sequence.[35,36] This behavior has attracted a lot of theoretical studies. By now, most groups believe that this long-range charge transfer proceeds through an incoherent multiple-step "hopping" mechanism, while the superexchange still dominates in the "short" range.[37,38] This does not mean that the Marcus theory cannot be used for long-range electron transfer, however. Actually, the fundamental steps in the various "hopping" mechanisms are often viewed as Marcus-like electron transfer events (usually multiple-step kinetic models do not impose much restraint on the elementary steps).[39–45] That is, the elementary steps could still be coherent tunneling or superexchange and thus the Marcus theory can be applied. For DNA, Ratner *et al.* has discussed the possibility of thermal activation for the elementary step in hopping,[46,47] and the conclusion is that the elementary step should occur by tunneling when there are three or fewer AT base pairs between two GC pairs (that is, the hopping sites for DNA). The prediction is consistent with our temperature dependence results of PNA, see Chapter 2.

1.3 EXPERIMENTAL METHODS

1.3.1 Electrochemical Measurement

1.3.1.1 Self-Assembled Monolayers

A SAM is a single ordered molecular layer formed spontaneously on a solid substrate through physical or chemical adsorption.[48] The formation of an alkanethiol SAM is a typical example; by immersing a clean gold substrate into a solution of alkanethiols with the alkyl chain of several -

CH_2- units for hours (12~48 hours usually), a compact monolayer forms spontaneously because of the chemical adsorption of the -SH group on the gold surface and the hydrophobic forces that drive the packing of the alkane chains together. A 'cartoon' of a SAM is shown in Figure 1.2. A well-ordered SAM has many potential applications. First, the SAM can be used as a protective coating by blocking access of undesired molecules to the metal surface.[49] Second, SAMs can be used to control the wetting of a surface by changing the end-group (hydrophilic or hydrophobic). The surface of OTS (Octadecyltrichlorosilane) coated cuvettes is very hydrophobic and this protocol is routinely applied in many photophysical labs. This property can also be used in friction or lubrication control.[50,51] In addition, the SAM motif offers the possibility to form a layer-by-layer structure and investigate more complex phenomena. For example, the direct electron transfer of proteins on SAMs is an extensive research field, with many potential applications.[52,53]

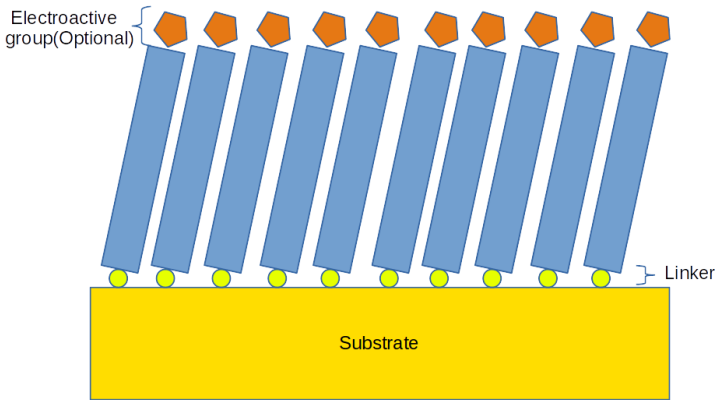

Figure 1.2. A cartoon of a self-assembled monolayer (SAM). Gold is the most typical substrate but SAMs can also form on other metals and semiconductors, or even glass or quartz.

In this work, a SAM provides a way to fix molecules on an electrode so that the charge transfer properties can be studied easily. The conductance of the SAM can be measured through a scanning probe microscopy (SPM), such as STM or C-AFM (Conductive-AFM). A more feasible way for many groups is to introduce an electroactive group (such as ferrocene), then the electron transfer process can be monitored by electrochemistry experiment, such as cyclic voltammetry. In

contrast to the more common solution electrochemistry, mass transport is fully eliminated for the case of immobilized redox molecules, and one can focus on the charge transfer process directly. For this reason, electroactive SAMs have become one of the more popular strategies for the study of charge transfer kinetics since the 1990s.[54–56]

1.3.1.2 k^0 Measurement

A kinetic scheme for a single electron transfer event in electrochemistry may be written as

$$O + e \underset{k_{ox}}{\overset{k_{red}}{\rightleftharpoons}} R \qquad \textbf{Equation 1.14}$$

where O and R denote the oxidized and reduced form of the redox species (or the electroactive group in the SAM), respectively.

A very important feature of electrochemistry is that the $\Delta_r G$ of the redox reaction in Equation 1.14 can be easily changed by the overpotential η, therefore the rate constants, k_{red} and k_{ox} are also subject to the overpotential η. To compare the intrinsic charge transfer properties of

$$k^0 = k_{red}(\eta = 0) = k_{ox}(\eta = 0) \qquad \textbf{Equation 1.15}$$

different systems, the standard heterogeneous rate constant k^0 is used:

Note that k^0 cannot be measured directly. For solution electrochemistry, an extrapolation of the Tafel plot can be used, but it is not feasible for SAM electrochemistry. An obvious reason is that the consumed redox species cannot be replenished to reach a steady-state current when η is kept as constant. Instead cyclic voltammetry is often used and the electric current can be expressed as:

$$i(t) = nFA\left[k_{red}\big(\eta(t)\big)C_O(t) - k_{ox}\big(\eta(t)\big)C_R(t)\right] \qquad \textbf{Equation 1.16}$$

where $C_O(t)$ and $C_R(t)$ are the concentration of O and R near the electrode at time t. As shown later, k^0 can be extracted by solving the above equation. The first step to solve Equation 1.16 is to eliminate $C_O(t)$ and $C_R(t)$ which are not direct observables in electrochemistry. This can be done formally by integrating the kinetic differential equation with proper boundary conditions:

$$\frac{dC_R(t)}{dt} = k_{red}C_O(t) - k_{ox}C_R(t) \qquad \textbf{Equation 1.17}$$

The special difficulty in cyclic voltammetry is that the rate constants k_{red} and k_{ox} also change with time because the overpotential is always changing. Therefore the crucial step left is to get the expression of k_{red} and k_{ox} in terms of η. Marcus theory is a natural solution to this problem. However, charge transfer through redox SAMs is a heterogeneous electron transfer process, and its description requires that the single level Marcus theory, derived in section 1.2.1, must be modified accordingly.

Consider an occupied electronic state $\hbar$ in the electrode with energy $\varepsilon_\hbar$. In a cathodic reaction, electrons will transfer to the redox molecule and the free energy for electrons at state k is:

$$\Delta G_r(\varepsilon_\hbar) = \varepsilon_f - \varepsilon_\hbar + e\eta \qquad \textbf{Equation 1.18}$$

where ε_f is the Fermi energy and η is the overpotential. In the non-adiabatic limit, Equation 1.11 applies and the rate constant for electronic state $\hbar$ is:

$$k_{red}(\varepsilon_\hbar) = \frac{2\pi}{\hbar}|H_{DA}|^2 \frac{1}{\sqrt{4\pi\lambda k_B T}} \exp\left(-\frac{\left(\lambda + \Delta G_r(\varepsilon_\hbar)\right)^2}{4\lambda k_B T}\right) \qquad \textbf{Equation 1.19}$$

Note that here the donor is actually the electrode. The overall reduction rate constant should be the sum over all occupied electronic states, that is,

$$k_{red} = \frac{2\pi}{\hbar}|H_{DA}|^2 \frac{1}{\sqrt{4\pi\lambda k_B T}} \int_{-\infty}^{\infty} \rho(\varepsilon)\, f(\varepsilon)\, \exp\left[-\frac{(\lambda + (\varepsilon_F - \varepsilon) + e\eta)^2}{4\lambda k_B T}\right] \mathrm{d}\varepsilon \qquad \textbf{Equation 1.20}$$

where $f(\varepsilon)$ is Fermi function, and $\rho(\varepsilon)$ is the density of states (DOS) of the electrode and is normalized with surface area. The subscript $\hbar$ is dropped for simplicity. Similar expression can be written for hole transfer or anodic reactions, see Chapter 2. This kind of approach was pioneered by Dogonadze *et al.*[57,58] On the other hand, if one assumes that the DOS of the oxidized form in solution is a normalized Gaussian distribution with $\sqrt{2\lambda k_B T}$ as the standard deviation, then

$$\rho_r(\varepsilon) = \frac{1}{\sqrt{4\pi\lambda k_B T}} \exp\left[-\frac{(\lambda + (\varepsilon_F - \varepsilon) + e\eta)^2}{4\lambda k_B T}\right] \qquad \textbf{Equation 1.21}$$

And Equation 1.20 can be obtained immediately by using Fermi's golden rule:

$$\begin{aligned} k_{red} &= \frac{2\pi}{\hbar}|H_{DA}|^2 \int_{-\infty}^{\infty} \rho(\varepsilon)\, f(\varepsilon) \cdot \rho_r\,(\varepsilon, \lambda)\mathrm{d}\varepsilon \\ &= \frac{2\pi}{\hbar}|H_{DA}|^2 \frac{1}{\sqrt{4\pi\lambda k_B T}} \int_{-\infty}^{\infty} \rho(\varepsilon)\, f(\varepsilon) \exp\left[-\frac{(\lambda + (\varepsilon_F - \varepsilon) + e\eta)^2}{4\lambda k_B T}\right] \mathrm{d}\varepsilon \end{aligned} \qquad \textbf{Equation 1.22}$$

A similar conclusion applies for k_{ox} and the energy diagram is shown in Figure 1.3A. The shape of $\rho_r(\varepsilon)$ can be rationalized by analyzing the charge transfer rate between the Fermi level of the electrode and the redox molecule using the single level Marcus theory.[23] This approach was first proposed by Gerischer[59] and is identical to Dogonadze's approach in the non-adiabatic limit, as shown here, although they will diverge in the adiabatic limit.[60–62]

Once Equation 1.20 or Equation 1.22 is obtained, Equation 1.16 can be solved numerically to simulate cyclic voltammetry. Figure 1.3B shows a set of cyclic voltammograms at different overpotential scan rate. One can find that the voltage of the faradaic current peak current shifts a lot. Actually, the shift depends on both the scan rate and k^0. By performing cyclic voltammetry at different scan rates and comparing the experimental voltammograms with simulated ones, the experimental k^0 can be determined,[55,56,63] see Chapter 2 for details.

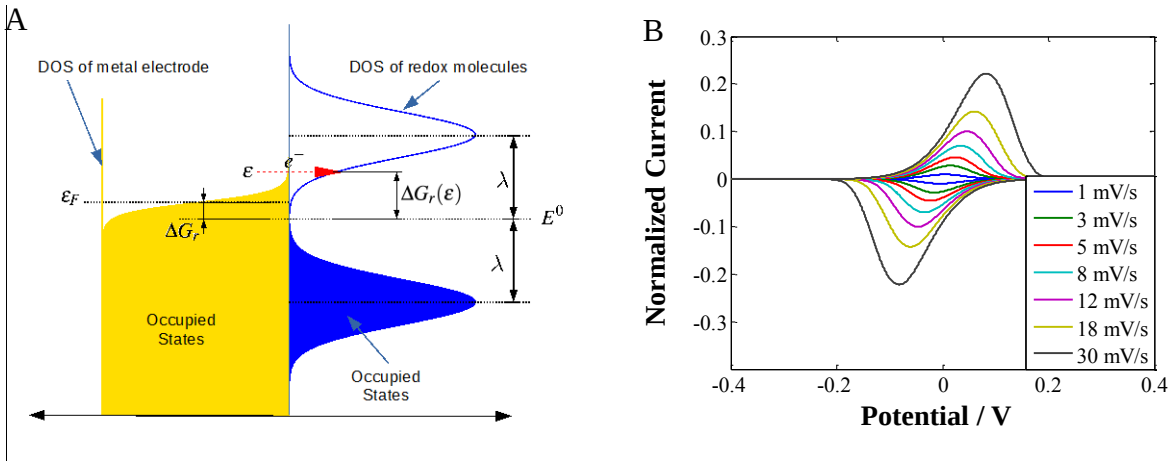

Figure 1.3. Panel A: Schematic presentation of the DOS (Density Of States) and occupancies of the electrode and the redox couple. Occupied states are shown as filled area. $\boldsymbol{\varepsilon_F(E)}$ is the Fermi level of the metal, whose value is equivalent to the applied potential $\boldsymbol{E}$. $\boldsymbol{E_0}$ is the formal potential of the redox couple. Panel B: Simulated cyclic voltammgrams for $\boldsymbol{k_0 = 0.125}$.

Equation 1.14 and Equation 1.20 only describe a single-step tunneling or superexchange process. They are adequate for systems such as a ferrocenated alkanethiol SAMs in which only superexchange is present. For more complicated systems such as peptide nucleic acid SAMs, the charge transfer mechanism is often in the incoherent multiple-step "hopping" regime. The validity of applying Equation 1.20 to such systems was never rigorously tested before. This is the main topic of Chapter 2, and a three-step model is developed to solve the problem. It turns out that the traditional single-step model can be used to fit the data, but the interpretation of the results requires some revision.

1.3.2 Single-Molecule Conductance Measurement by Molecular Junctions

1.3.2.1 Break Junction Experiments

Single-molecule conductance measurements are the newest methods to study charge transport through a molecule.[64] The earliest example is probably Reed's measurement of the single-molecule

conductance of benzene-1,4-dithiol in a mechanically controllable break junction (MCB).[65] Later, Tao *et al.*[66] developed the Scanning Tunneling Microscopy controlled Break Junction (STM-BJ), and this method is now widely used. In the experimental part of Chapter 2 this method is used to probe charge transport through saturated chains. In this method, a gold tip is alternately brought into contact with a gold surface that is pre-modified with the molecule to be studied and then withdrawn. The tunneling current-distance dependence is recorded while a constant bias is applied between the tip and the substrate. When one or more molecules are present in the junction, current plateaus are observed on the current-distance profile instead of a simple exponential decay. The procedure is repeated several thousand times to probe various geometries of the molecules in the junction.

The emergence of repeatable molecular junction technique might be the most important milestone in the development of molecular electronics which was initiated by H. Kuhn *et al.*[67,68] and Ratner *et al.*[69] in the early seventies. After several decades, workers finally have a reliable platform to test current flow through individual molecules and investigate its dependence on the molecular structure. This new ability has posed important challenges for theoretical chemists (and physicists) and spurred the development of non-equilibrium Green's function formalism[70] - because as an open system, the basic Marcus theory does not apply to the conductance experiment. An elementary quantum mechanics based introduction to NEGF will be presented in section 1.4.3.

1.3.2.2 The Relationship between Conductance g and Rate Constant k^0

The relationship between charge transfer and molecular conduction is a very fundamental question.[71] The former one has been studied for decades and the latter is an emerging area, people are eager to know if previously gained knowledge can be applied and whether or not the new experiments can help us to answer some old but hard questions. The two processes represent two

facets of electron transmission through a molecular environment, and as such should be related. Still this relationship is not trivial for several reasons.[72] First, as noted above, a molecular junction is an open system while intramolecular or intermolecular electron transfer is a closed system. Electrochemical systems with SAMs are also open systems, but for the studies with electroactive SAMs there is no steady-state current and therefore no "net" charge transport to a sink that is separate from the system. This means that the boundary conditions for those systems are totally different. Secondly, even though the core process in both situations is the same, the fact that in the conduction process one always puts a potential across the junction can change the electronic structure of the bridge. This problem can be eased in calculating g because one can also use the near-zero conductance and compare it with k^0. Finally, the rate constant and conductance are actually different physical observables of different dimensionalities.

Nitzan carefully studied this problem and he found that one is indeed proportional to other in the appropriate limit, and, surprisingly, this conclusion holds irrespective of whether they are in the superexchange or sequential hopping regime.[73,74] New developments on this topic have emerged recently,[75] however, within the scope of this dissertation, one can simply assume that the calculate near-zero conductance $g \propto k^0$. Therefore, theoretical calculations of the conductance can also provide insights into the charge transfer problems, as in Chapter 3 and 4.

1.3.3 Photoinduced Electron Transfer

Photoinduced electron transfer (PET) is probably one of the most common ways to study intramolecular charge transfer. Gray and Winkler's work on Ru-modified protein,[76,77] Barton, Lewis and Wasielewski's work on DNA charge transfer,[78–84] and many other studies on donor-bridge-acceptor molecules[85–89] have elaborated and deepened our understanding of electron

transfer and its dependence on electronic coupling and nuclear bath degrees of freedom. Photoinduced electron transfer is usually performed in solution and the $\Delta_r G$ is usually not zero. Importantly PET of unimolecular systems made it possible to explore clearly the Marcus inverted region.

PET studies can be distinguished by how the reaction progress is followed. It seems that most of the PET systems can be measured by transient absorption (TA) spectroscopy. TA is often operated in a pump-probe fashion. The PET process is initiated by a first short "pump" pulse and then concentration of the reaction and product as function of time are measured by following "probe" pulses (which is very different from electrochemistry and largely simplifies kinetics models, although $\Delta_r G$ cannot be controlled as easily as in electrochemistry). However, TA requires a high concentration of the sample to reach better S/N and might not be the best choice when the amount of sample is very limited or susceptible to aggregation.

In this dissertation, time-resolved fluorescence which monitors the loss of reactant population rather than the rise of product formation is used to follow the PET process. More specifically, the time-correlated single photon counting (TCSPC) technique is used.[90] In contrast to TA, TCSPC needs the sample to be fluorescent (or photoluminescent) and therefore not every system can be measured. However, if a system can be measured by TCSPC, it will have several advantages over TA. First, the concentration of the sample can be much lower, this is especially helpful when the amount of the sample is limited. TCSPC is based on photoluminescence and one can always increase the intensity of the light source (pulsed laser usually) as long as no photobleaching is observed. Even if the power of the laser cannot be increased, one can always increase the experimental time to collect enough counts. Second, photon counting is a Poisson process and the signal follows a Poisson distribution. Therefore a lot of statistical tools can be

applied and the maximum errors can be estimated pretty accurately. In Chapter 5 we implement a distributional fitting algorithm and show how new physics that cannot be found by traditional component fittings can be revealed. The details will be discussed there.

1.4 COMPUTATIONAL METHODS

1.4.1 $\Delta_r G$ and λ

In electrochemistry, k^0 is measured and $\Delta_r G$is set to be zero. $\Delta_r G$ is not zero in PET experiments but it can be calculated from Rehm-Weller equation based on the electrochemical data of the donor and acceptor.[91,92] In computational chemistry, the entropy change is hard to estimate but it is usually small and can be ignored. The energy difference between two ground states (with solvation models if necessary) or the energy levels of two molecular orbitals are among the most routine tasks and the calculated values can be used to corroborate the experimental values, or provide preliminary validation of a theoretical method for further calculations.

The accurate estimation of reorganization energy λ requires more effort and requires the calculation of the energy of one charge transfer state at the equilibrium geometry of the other state.[93] λ is divided into an inner-sphere, or intramolecular, reorganization energy λ_i and an outer-sphere, or solvent, reorganization energy λ_o. Experimentally, $\lambda\ (= \lambda_i + \lambda_o)$ can be determined by Equation 1.3 once the activation energy $\Delta G^{\ddagger}$ is obtained by a temperature dependence study and $\Delta_r G$ is estimated as above. In computational chemistry, however, λ_i and λ_o are usually estimated separately. Because the solvent is not involved, the estimation of λ_i is easier (comparing with λ_o).

For intermolecular charge transfer or an intramolecular charge transfer where the donor and acceptor can be isolated (the bridge contributes little to λ_i in the non-adiabatic limit), Nelson's four-point method is probably the easiest method and is widely used to compute λ_i.[94,95] Take the charge transfer in a cation donor-acceptor complex for example. The reactant consists of the neutral donor (denoted as Dn) and the acceptor cation (denoted as Acc^+). First one calculates the equilibrium energy of Dn and Acc^+, donated as $E_0(\mathrm{Dn})$ and $E_0(\mathrm{Acc}^+)$. Then the vertical ionization energy of Dn and the vertical electron affinity of Acc^+ are calculated, denoted as $IE(\mathrm{Dn})$ and $EA(\mathrm{Acc}^+)$ (*IE* and *EA* are all positive values). Finally, one relaxes the geometries of Dn^+ and Acc to get the equilibrium energy of the product, that is, $E_0(\mathrm{Dn}^+) + E_0(\mathrm{Acc})$. λ_i is then expressed as:

$$\begin{aligned}\lambda_i &= \lambda_i(\mathrm{Dn}) + \lambda_i(\mathrm{Acc}) \\ &= [E_0(\mathrm{Dn}) + IE(\mathrm{Dn}) - E_0(\mathrm{Dn}^+)] + [E_0(\mathrm{Acc}^+) - EA(\mathrm{Acc}^+) - E_0(\mathrm{Acc})]\end{aligned} \qquad \textbf{Equation 1.23}$$

Four geometries are optimized so it is called the "four-point" method.

For intramolecular charge transfers in which the donor and acceptor are strongly correlated and cannot be easily split, one can use the neutral molecule and its cation instead.[96] Besides, because $|DA^+\rangle$ is merely one excited state of $|D^+A\rangle$ ($|D^+A\rangle$ might be already an excited state, e.g. in PET), (further) excited state calculation can also be performed to get λ_i but one must be careful about picking up a clear charge transfer state and choosing the correct methods for excited state calculation. To avoid the trouble of excited state calculations, one may consider using constrained DFT (section 1.4.2.3) to get λ_i from a diabatic picture.[25,97,98] Alternatively, one can start from the vibrational frequency calculations.[96,99] In summary, several complementary methods are available for λ_i calculations and almost all donor/acceptor pairs are covered (unless for some large donors and acceptors that all computational methods are too expensive). In some cases, (e.g, when the

charge transfer emission is present), λ_i can also be extracted from spectroscopic data by sophisticated analysis to confirm the theoretical prediction.[30,89,100]

The outer-sphere part λ_o is much more challenging than λ_i in computational chemistry. λ_o arises from the polarization changes in the surrounding dielectric medium. In polar environments, λ_o is often the dominate contribution to λ. A proper description of solvent effects is crucial and commonly used implicit solvation models are usually not accurate enough. QM/MM method, which employs explicit solvent molecules, is probably the best method so far.[101,102] However, the best results of λ_o are still usually qualitatively correct.[103] The QM/MM calculation of λ_o is an interesting and active topic for theoretical chemists but it is not yet a routine prediction tool for experimental chemists, at least for now. The estimation of λ_o through classical or semi-classical models are more practical and popular. A standard estimation method for highly polar solvents from Marcus is:[104,105]

$$\lambda_o = (\Delta e)^2 \left(\frac{1}{2a_1} + \frac{1}{2a_2} - \frac{1}{R}\right)\left(\frac{1}{\epsilon_\infty} - \frac{1}{\epsilon_0}\right) \qquad \textbf{Equation 1.24}$$

where a_1, a_2, R, ϵ_∞ and ϵ_0 are the radii of the donor and acceptor, the distance between their centers, and the optical frequency and zero frequency dielectric constants of the solvent, respectively. In Equation 1.24, the donor and acceptor are treated as individual spheres immersed in a dielectric continuum medium and the dielectric image effects are neglected. The medium is assumed to be dielectrically unsaturated and only linear response is considered. The difference in the inverse dielectric constants relates to the fact that the electron configuration of the solvent molecules readjust nearly instantaneously and thus do not contribute. Although widely used, a lot of restrictions are assumed in Equation 1.24. The possibilities to relax some restrictions were discussed in the original paper but a fundamental improvement requires the consideration of individual molecules. Matyushov *et al.* developed a molecular solvation model and the discrete

nature of the solvent/solute and high-order interactions are incorporated.[106] The expression of λ_o in this model is

$$\lambda_o = \lambda_p + \lambda_{ind} + \lambda_{disp} \qquad \textbf{Equation 1.25}$$

where λ_p includes contributions from the solvent dipole and quadrupole moments, λ_{ind} includes contributions from the induction forces, and λ_{disp} includes contributions from the dispersion forces. The explicit expression of each term is more complicated than Equation 1.24 and they can be found in literature.[107] It has been shown that this model is suitable for a wide range of solvents, including nonpolar and weakly dipolar aromatic solvents.[30,107]

1.4.2 Electronic Coupling Calculation.

Compared to energy calculations, electronic coupling calculation is the most unique part that distinguishes electron transfer calculation from other conventional tasks in computational chemistry. It is harder than the energy calculations in the sense that most quantum chemistry packages do not provide automatic tools for such analysis. Thus one has to look deeper into the results and cannot simply treat the software packages as black boxes, as in the energy calculation. One of the reasons for this situation is that almost all modern quantum chemistry calculations are based on the adiabatic representations (for example, conical molecular orbitals and their eigenvalues are computed for Hartree-Fock level calculations), while rigorous electronic coupling calculations require a diabatic representation. However, one cannot create a strictly diabatic basis from a give adiabatic basis,[25] therefore approximations must be used. Until now, there is still no "universal" method for any electron transfer systems and one needs to choose the best suitable method with caution. Another difficulty arises from the fact that the "molecular orbitals" in the popular DFT method lack physical meaning, therefore a lot of fast DFT methods cannot be used

and one often has to choose more "expensive" (that is more time and CPU power consuming) post-Hartree-Fock methods.

A simple method is to partially diagonalize the Fock matrix by using a "double diagonalization" method, see Equation 1.26.[108,109] First, one partitions the full Fock matrix (that is, the Hartree-Fock Hamiltonian) to $\mathbf{H}$ a donor part ($\mathbf{H_{DD}}$) an acceptor part ($\mathbf{H_{AA}}$), and their couplings. Then one diagonalizes the $\mathbf{H_{DD}}$ and $\mathbf{H_{AA}}$ separately. In this step two unitary matrixes are obtained. Next, one can construct a block diagonal matrix from the unitary matrixes. Applying the transformation to the full Hamiltonian $\mathbf{H}$, one obtains the partially diagonalized $\mathbf{H'}$. Note that the diagonal elements in $\mathbf{H'}$ will be different from the matrix elements in the diagonalized $\mathbf{H_{DD}}$ and $\mathbf{H_{DD}}$. Those values will be used if a third "bridge" part is included but is of no particular importance for a two-state approximation discussed here. What is important is that, in $\mathbf{H'}$ the off-diagonal matrix elements are the couplings between the corresponding localized MOs of the donor part and the acceptor part. For example, the coupling between the donor HOMO and the acceptor LUMO can be viewed as the coupling for thermal electron transfer, while the coupling between the donor LUMO and the acceptor LUMO might be viewed as the coupling for photoinduced electron transfer. As mentioned earlier, this method can also be generalized to include the bridge partition and the details can be found in various reports.[108,110,111]

$$\mathbf{H} = \begin{pmatrix} \mathbf{H_{DD}} & \mathbf{H_{DA}} \\ \mathbf{H_{AD}} & \mathbf{H_{AA}} \end{pmatrix} = \begin{pmatrix} H_{D_1D_1} & H_{D_1D_2} & \cdots & H_{D_1A_{n-1}} & H_{D_1A_n} \\ H_{D_2D_1} & H_{D_2D_2} & & H_{D_2A_{n-1}} & H_{D_2A_{n-1}} \\ \vdots & & \ddots & \vdots & \\ H_{A_{n-1}D_1} & H_{A_{n-1}D_2} & \cdots & H_{A_{n-1}A_{n-1}} & H_{A_{n-1}A_n} \\ H_{A_nD_1} & H_{A_nD_2} & & H_{A_nA_{n-1}} & H_{A_nA_n} \end{pmatrix}$$

Equation 1.26

$$\Longrightarrow \begin{pmatrix} \varepsilon_{D_1} & 0 & \cdots & V_{1,n-1} & V_{1,n} \\ 0 & \varepsilon_{D_2} & & V_{2,n-1} & V_{2,n} \\ \vdots & & \ddots & \vdots & \\ V_{n-1,1} & V_{n-1,2} & \cdots & \varepsilon_{A_{n-1}} & 0 \\ V_{n,1} & V_{n,2} & & 0 & \varepsilon_{A_n} \end{pmatrix} \equiv \mathbf{H}'$$

However, it should be noted that as in Equation 1.7, $\mathbf{H}_D$ corresponds to state DA (reactant, denoted as $|D\rangle$) and $\mathbf{H}_A$ corresponds to state D^+A^- (product, denoted as $|A\rangle$), and the basis set for the **H** is not molecular orbitals but electronic states (or Slater determinants).[7] Therefore the above Fock matrix based method implicitly assumes Koopmans' theorem (or one-electron approximation) for both the donor part and acceptor part,[128-130,176] and the donor-acceptor couplings must be small enough to ensure that the adiabatic states are close enough to the diabatic states. These restrictions limit the usefulness of the simple method and various more rigorous methods have had to be developed.

1.4.2.1 Koopmans' Theorem based Energy Splitting calculation

As discussed previously, the results of Hartree-Fock calculations are "naturally" expressed in adiabatic (eigen) states. To get the electronic coupling of the two diabatic states, one can use Equation 1.8 and calculate the adiabatic energy gap at the transition state as shown in Figure 1.4A. However, the search for a transition state is far from trivial, especially when the molecule is ionized. For symmetrical systems, Koopmans' theorem drastically reduces the complexity of the calculation.[27,112] The electronic configurations for the ground and excited surfaces at the transition state geometry is shown in Figure 1.4B. Note that we use hole transfer (that is, the donor-acceptor

complex is a cation) as the example. If Koopmans' theorem holds for this system, the energy gap between the two states equals the energy difference between the two changed molecular orbitals (HOMO and HOMO-1 in Figure 1.4B). This statement is true at any nuclear coordinate. The remaining problem is how to reach the transition state. Again one can use Koopmans' theorem and start with the neutral state. As shown in Figure 1.4A, the nuclear configuration of the cation transition state must be at the minimum of the neutral molecule potential curve because of the symmetry. One great advantage of the Koopmans' theorem method is that the electron transfer pathway analysis can be easily performed within this framework, see Chapter 3 for the details.

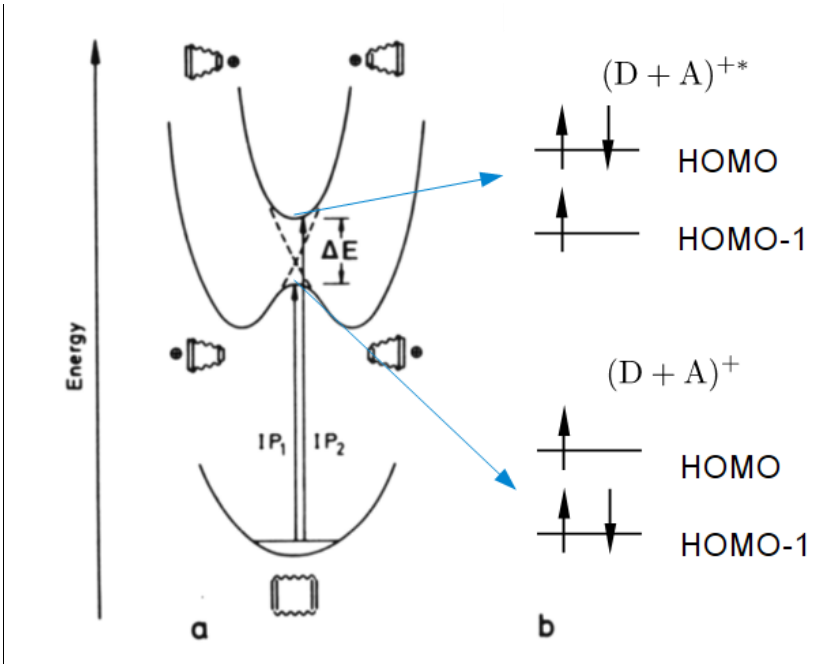

Figure 1.4. Panel A: Diabatic (dashed lines) and adiabatic (solid lines) potentials relevant for ionization of a symmetrical ethylene-bridge-ethylene system. Panel B: Electronic configurations for the two adiabatic state. Adapted with permission from *Chem. Rev.* 1992, *92*, 395-410. Copyright (1992) American Chemical Society.

Although the original Koopmans theorem based energy splitting calculation can only deal with symmetric systems, asymmetric systems can also be treated with the help of an external field.[113,114] The applied external electric field will change the energy of the diabatic states and the adiabatic energy gap reaches the minimum when $E_D = E_A$. Note however, that recent experiments

have shown that external electric fields might affect the couplings[115] and one might want to apply Koopmans' theorem to asymmetric system with caution.

1.4.2.2 GMH and FCD

Although strictly diabatic states cannot be constructed from adiabatic states, it is still possible to construct the 'best' diabatic states once a criterion is given. That is, one uses some unitary matrix to transform the adiabatic representation to a diabatic representation. The most widely used methods of this type are the generalized Mulliken-Hush (GMH) and fragment charge difference (FCD) methods. FCD can be viewed as a variant of GMH, hence GMH is discussed first.

GMH theory is a generalization of the Mulliken-Hush model,[116,117] which was developed to describe the charge transfer transition (optical electron transfer). Within the Condon approximation, the optical oscillator strength can be related to the transition dipole and eventually the electronic coupling. Here we will only focus on the relationship between the molecular dipole and the electronic coupling. A quick derivation[118] of MH results is to assume that the two adiabatic states $|1\rangle$ and $|2\rangle$ (e.g., the neutral ground state and the charge separated excited state at the crossing point of Figure 1.1) can be written in a basis of two degenerate states $|D\rangle$ and $|A\rangle$ as:

$$\begin{cases} |1\rangle = c|D\rangle + d|A\rangle, E_1 = E_D + \dfrac{d}{c}H_{DA} \\ |2\rangle = d|D\rangle - c|A\rangle, E_2 = E_D - \dfrac{c}{d}H_{DA} \end{cases} \qquad \textbf{Equation 1.27}$$

using the normalization condition ($c^2 + d^2 = 1$). As in Equation 1.7 and Equation 1.26, $|D\rangle$ denotes the reactant state and $|A\rangle$ denotes the product. Because dipole moments will be calculated later, it might be better to visualize $|D\rangle$ as D^-A where the excess charge is localized on the donor and $|A\rangle$ as DA^- where the excess charge is localized on the acceptor, although GMH can be applied

independently of whether $|D\rangle$ is neutral or negatively/positively charged. From Equation 1.27, the energy gap is given by

$$\Delta E_{12} = E_1 - E_2 = \frac{H_{DA}}{cd} \qquad \textbf{Equation 1.28}$$

Next we connect this result to the transition dipole between the ground ($|1\rangle$) state and the excited ($|2\rangle$) state. The (transition) dipole is defined as

$$\boldsymbol{\mu}_{kl} \equiv \langle k|\vec{r}|l\rangle, k, l = 1{,}2 \text{ or } D, A \qquad \textbf{Equation 1.29}$$

so that

$$\boldsymbol{\mu}_{12} \equiv \langle 1|\vec{r}|2\rangle = cd\{\langle D|\vec{r}|D\rangle - \langle A|\vec{r}|A\rangle\} = cd(\boldsymbol{\mu}_{DD} - \boldsymbol{\mu}_{AA}) \qquad \textbf{Equation 1.30}$$

Combining Equation 1.28 and Equation 1.30, the product cd can be eliminated and the electronic coupling is

$$H_{DA} = \frac{|\boldsymbol{\mu}_{12}|\,\Delta E_{12}}{|\boldsymbol{\mu}_{DD} - \boldsymbol{\mu}_{AA}|} \qquad \textbf{Equation 1.31}$$

The dipoles $\boldsymbol{\mu}_{DD}$ and $\boldsymbol{\mu}_{AA}$ are expressed in the diabatic basis and they cannot be measured directly. In the MH model an "effective" donor-acceptor length r_{DA} is defined to replace the denominator in Equation 1.31, and the final expression is

$$H_{DA} = \frac{|\boldsymbol{\mu}_{12}|\ \Delta E_{12}}{e \cdot r_{DA}} \qquad \textbf{Equation 1.32}$$

where r_{DA} has typically been estimated on the basis of molecular structure data. Note however that r_{DA} is not well-defined in the sense of a distance in real space, because the actual charge distribution is never a δ function.

To obtain Equation 1.30 (and eventually Equation 1.32), one assumes that the inter-site diabatic transition dipole $\boldsymbol{\mu}_{DA}$ is negligibly small. That is,

$$\boldsymbol{\mu}_{DA} \approx 0 \qquad \textbf{Equation 1.33}$$

The reason for this assumption is quite obvious: diabatic states are charge localized states in electron transfer so that it is expected that $|D\rangle$ and $|A\rangle$ are not only orthogonal, but also have only a negligibly small charge density overlap. Therefore their dipole matrix element $\boldsymbol{\mu}_{DA}$ ($\equiv \langle D|\, \vec{r}\, |A\rangle$) should also be small. However, this assumption turns out to be unnecessary to derive Equation 1.32, as shown by Newton *et al.* upon re-examination of the Mulliken-Hush model and development of the GMH theory.[119,120] Instead of assuming two diabatic states, one constructs $|D\rangle$ and $|A\rangle$ stepwise in GMH.[16,121] First, one calculates all of the dipole matrix elements of state $|1\rangle$ and $|2\rangle$. Second, one calculates the direction $\vec{v}_0$ of the dipole moment of state $|1\rangle$ minus the dipole moment of state $|2\rangle$ (that is, $\vec{v}_0 = (\vec{\mu}_{11} - \vec{\mu}_{12})/|\vec{\mu}_{11} - \vec{\mu}_{12}|$) and projects all dipole matrix elements onto that direction. Finally, one diagonalizes the dipole matrix and a transition matrix (sometimes also called as a "rotation matrix" because it is a 2×2 matrix, similar to a rotation matrix for a 2-D vector in real space) is obtained. This step is crucial because by diagonalizing a dipole matrix one actually finds a representation in which the off-diagonal transition dipole matrix elements are zero. That is, one can replace the "≈" in Equation 1.33 with $=$ in this representation. We can define this representation as an approximate diabatic representation. The Hamiltonian in this diabatic representation is:

$$\begin{pmatrix} H_{DD} & H_{DA} \\ H_{AD}(=H_{DA}) & H_{AA} \end{pmatrix} = \mathbf{C}^{-1} \begin{pmatrix} H_{11} & 0 \\ 0 & H_{22} \end{pmatrix} \mathbf{C} \qquad \textbf{Equation 1.34}$$

where $\mathbf{C}$ is the transition matrix. We are interested in the off-diagonal matrix element which is the electronic coupling between the diabatic states, and its expression is:

$$H_{DA} = \frac{|\boldsymbol{\mu}_{12}|\ \Delta E_{12}}{|\boldsymbol{\mu}_{AA} - \boldsymbol{\mu}_{DD}|} \qquad \textbf{Equation 1.35}$$

Because the transformation matrix is known, the matrix elements in the diabatic representation ($\boldsymbol{\mu}_{AA}$ and $\boldsymbol{\mu}_{DD}$) can be transformed back into the adiabatic representation ($\boldsymbol{\mu}_{11}$ and $\boldsymbol{\mu}_{22}$) and the final expression is

$$H_{DA} = \frac{|\boldsymbol{\mu}_{12}|\ \Delta E_{12}}{\sqrt{|\boldsymbol{\mu}_{11} - \boldsymbol{\mu}_{22}|^2 - 4|\boldsymbol{\mu}_{12}|^2}} \qquad \textbf{Equation 1.36}$$

The general idea behind the preceding steps is straightforward: We choose $\boldsymbol{\mu}_{DA} = 0$ as the criterion for diabatic states and this can be ensured by using a transformation matrix that diagonalizes the dipole matrix. Therefore, no extra assumption is needed in GMH. Besides, comparing with Equation 1.32, all variables in Equation 1.36 are well defined in the adiabatic basis. Another advantage of GMH theory is that multi-state models can be calculated as well.[16,121,122] However, this further generalization is beyond the scope of the dissertation and will not be discussed.

In actual calculations, the most time consuming part of the GMH method is to obtain the two adiabatic states, e.g., the ground state and the first excited state. Once the adiabatic states are obtained, GMH calculations can be finished almost immediately and it has been incorporated into a few quantum chemistry packages as an additional feature for excited state calculations such as CI Singles (CIS), which is probably the simplest and cheapest method to obtain excited states.[123,124] Wavefunctions are not used in Equation 1.36, thus TD-DFT can be used for GMH calculations, in principle. However, many commonly used exchange-correlation functionals cannot treat charge transfer transitions properly and one must choose functionals carefully.[125–127] In some applications, a high accuracy of the absolute value of H_{DA} is not required and GMH can be combined with Koopmans' theorem to simplify the calculation. On the basis of Koopmans' theorem, the dipole moment and energy difference between adiabatic states (Equation 1.36) can be replaced by variables for the corresponding molecular orbitals.[128–130] This method is especially useful when calculating H_{DA} for a large ensemble of conformations.[131]

Following a similar spirit to GMH but with a more straightforward criterion, Voityuk *et al.* developed the fragment charge difference (FCD) method.[132,133] In contrast to GMH, one needs to partition the molecule into the donor and acceptor part ("fragments") explicitly. A 2×2 donor-acceptor charge difference matrix is defined with elements calculated as:

$$\Delta q_{kl} \equiv q_{kl}^{\mathrm{Dn}} - q_{kl}^{\mathrm{Acc}}$$
$$= \int_{\vec{r} \in \mathrm{Dn}} \rho_{kl}(\vec{r}) \ \mathrm{d}\vec{r} - \int_{\vec{r} \in \mathrm{Acc}} \rho_{kl}(\vec{r}) \ \mathrm{d}\vec{r} \qquad \textbf{Equation 1.37}$$

where "Dn" and "Acc" denote donor and acceptor (not $|D\rangle$ or $|A\rangle$), respectively. $\rho_{mn}(\vec{r})$ is the matrix element of the density operator between states $|k\rangle$ and $|l\rangle$. In actual calculations a Mulliken population or other population analysis can be used for the integrations in Equation 1.37. According to such a definition, the diagonal elements Δq_{kk} and Δq_{ll} correspond to the charge difference between the donor and acceptor in state $|k\rangle$ and $|l\rangle$. The charge transfer and charge localization (that is, $|\Delta q_{kk} - \Delta q_{ll}|$) are maximized after the diagonalization of the charge difference matrix. Using the rotation matrix to define the diabatic states, the FCD method yields the donor-acceptor coupling in a form very similar to that of GMH, namely

$$H_{DA} = \frac{|\Delta q_{12}| \ \Delta E_{12}}{\sqrt{|\Delta q_{11} - \Delta q_{22}|^2 - 4|\Delta q_{12}|^2}} \qquad \textbf{Equation 1.38}$$

Like GMH, FCD can also be applied to multi-state models. It is claimed that FCD is more robust than GMH especially when the charge separation is strong and multiple states are involved.[123,132] Besides this feature, the explicit partition of the donor and acceptor gives the users more control and thus more benefits in the electronic coupling calculations. For example, the results of GMH would be hard to explain if $|1\rangle$ and $|2\rangle$ are delocalized. In such a case the "donor" and "acceptor" will be ambiguous in GMH but they are still well defined in FCD.

1.4.2.3 Direct coupling and Constrained DFT

In GMH and FCD the adiabatic states are calculated, and exited state calculations are required for high-accuracy results. However the excited states are troublesome in many cases and an alternative route to calculate the diabatic states without the calculation of adiabatic states would be helpful. Several strategies exist for this purpose. When the donor and acceptor are different molecules (such as the dimers discussed in 1.4.2.1) or well-separated fragments, one can calculate the neutral/charged states for the donor and charged/neutral states for the acceptor separately and simply combine the real space wavefunctions into two states and "pretend" they are diabatic. The couplings can then be calculated from the diabatic states directly.[104,123,134] A small problem in the direct coupling scheme is that these "pretend" diabatic states are often not orthonormal, however one can use the Löwdin transformation[135] to orthogonalize them so that they are closer to the real diabatic states.[2,123]

In one-electron assumption, the frontier orbitals of each natural fragment (donor or acceptor) can be used in the direct coupling scheme instead of charged states (Slater determinants) used in the above strategy.[128-130] Take hole transfer between the two fragments in a dimer as an example; the electronic coupling is expressed as:

$$H_{DA} = \frac{H_{12} - \frac{1}{2}(H_{11} + H_{22})S_{12}}{1 - S_{12}} \qquad \textbf{Equation 1.39}$$

where $H_{12} = \langle \phi^1_{\mathrm{HOMO}} | \mathbf{H} | \phi^2_{\mathrm{HOMO}} \rangle$, $H_{11} = \langle \phi^1_{\mathrm{HOMO}} | \mathbf{H} | \phi^1_{\mathrm{HOMO}} \rangle$, $H_{22} = \langle \phi^2_{\mathrm{HOMO}} | \mathbf{H} | \phi^2_{\mathrm{HOMO}} \rangle$, $H_{22} = \langle \phi^1_{\mathrm{HOMO}} | \phi^2_{\mathrm{HOMO}} \rangle$. ϕ^1_{HOMO} and ϕ^2_{HOMO} are the HOMOs of the first and second isolated molecules of the dimer respectively. The Löwdin orthogonalization has been used to obtain Equation 1.39 and therefore the fragment orbitals do not need to be orthogonal.[177,178] Note that at the self-consistent field level, **H** is the single-electron Fock operator and the matrix elements are evaluated

iteratively by quantum chemistry software packages. For example, ADF that can utilize the orbitals of isolated fragments as the basis set in subsequent calculations and extract the matrix elements from the final Fock matrix.[179]

The above strategies may fail for intramolecular charge transfer because the donor and acceptor are chemically bonded and corresponding fragment orbitals or states may not be well defined. Fortunately, in many cases, diabatic states can be clearly identified based on their electron density distributions. For example, $|D^+A^-\rangle$ will have excess electron density on the acceptor side of the molecule. Thus, suitable diabatic states can be obtained by optimizing the wavefunction subject to a constraint on the density without calculating the excited adiabatic curve. This concept is the basis of the constrained DFT (CDFT) approach.[25] The origin of CDFT can be traced back to the 1980s[136] but it was not widely accepted until the recent robust implementation and the demonstration of its power in electron transfer calculations by Van Voorhis *et al.*[97,98,137] Note that in CDFT the $|D\rangle$ and $|A\rangle$ states are calculated in parallel; they can be viewed as both "ground state", just with different charge constraints; hence no excited state technique such as TD-DFT is needed. Therefore a major difficulty in charge transfer transition calculations are avoided and the choice of exchange-correlation functionals becomes much larger. In principle the CDFT calculations can be both faster and more accurate than GMH in electronic coupling calculations. One cannot only calculate $|H_{DA}|$ at the transition state, but one can also calculate its change along the Marcus parabolas to test the Condon approximation. Such work has been reported and the validity of the Condon approximation is confirmed for several systems.[97,138]

1.4.2.4 Application: Pathway Analysis

One of the most interesting applications of electronic coupling calculations is the pathway analysis for electron transfer in the superexchange regime.[118] It was initiated more than two

decades ago and is still an active field. The Koopmans' theorem based pathway analysis will be discussed in detail in Chapter 3; GMH and FCD can be used in pathway analyses if the multiple state models are employed. There are also other quantum-mechanical methods.[111,139] However, a pathway analysis based on CDFT has not been reported so far. This is probably because the current implementation of CDFT is only based on the two-state model. Beratan *et al.* realized that the electron tunneling parameters are transferrable for a large range of peptides and proteins and summarized it in their empirical *Pathways* model.[140,141] It was implanted as a plugin in VMD recently, and the pathway analysis is now almost fully automatic.[142] and has been used in protein electron transfer studies.[143]

A very typical electron transfer pathway analysis is shown in Figure 1.5.[144] In a $Ru(byp)_2(im)$-His83 azurin, a combined QM and MD simulation showed that very rapid and large fluctuations exist in the electronic coupling between the Ru(II) donor and Cu(II) acceptor.[145] However, the origin of the fluctuations was not clear in the original report. By performing a pathway analysis, two main pathways were revealed. The routes look similar but one is largely destructive and has small coupling, while the other is constructive and has large coupling. Therefore a small fluctuation in geometry might lead to a large change in the electronic coupling. These studies predict the importance of the dynamical effects that will be discussed more in section 1.4.4. In Chapter 4 such an effect is observed by electrochemistry, and in Chapter 5 a very similar donor-acceptor pair is used and the fluctuations are observed in photoinduced electron transfer.

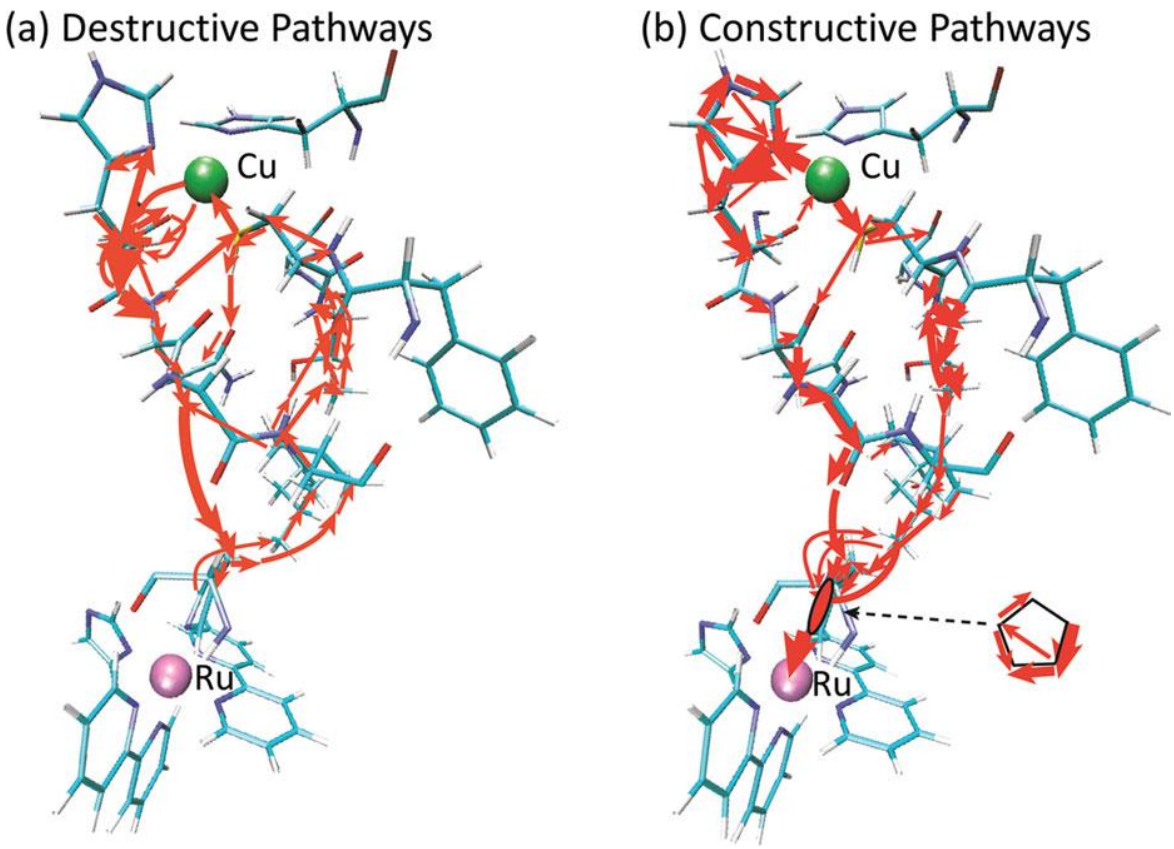

Figure 1.5. The tunneling pathways of Ru(byp)$_2$(im)-His83 azurin calculated using tunneling current analysis. Left: Destructive pathways. $|\boldsymbol{H_{DA}}| = \mathbf{1.7 \times 10^{-6}}$ eV. (b) Constructive pathways. $|\boldsymbol{H_{DA}}| = \mathbf{7.6 \times 10^{-5}}$ eV.[144] Reprinted with permission from *J. Phys. Chem. B* 2002, *106*, 11356–11366. Copyright (2002) American Chemical Society.

1.4.3 Conductance Calculations

1.4.3.1 Semiclassical models

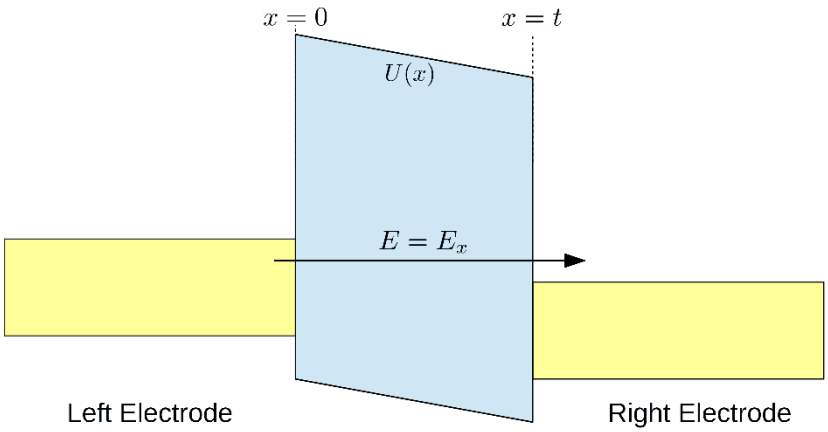

Figure 1.6. A basic semiclassical molecular junction model with rectangular barrier that can be calculated by the Wentzel-Kramers-Brillouin (WKB) approximation. Electron transfer along the *x*-axis and the width of the barrier is $\boldsymbol{d}$.

Semiclassical models are among the simplest models to describe charge transport and SAM conductance in the tunneling regime. For one-dimensional problems such as the barrier shown in Figure 1.6, the WKB (Wentzel-Kramers-Brillouin) approximation is the most commonly used approach.[146,147] The transmission factor T for electrons transferring along the *x*-axis is expressed as:

$$T(E_x) = g \exp\left(-\frac{2\sqrt{2m}}{\hbar}\int_0^d \mathrm{d}x\ \sqrt{U(x) - E_x}\right) \qquad \textbf{Equation 1.40}$$

$$g = 1\ (\text{if } U(x) \text{ varies slowly})$$

where E_x is the kinetic energy, and m is the mass of an electron. Taking the electrons moving in all directions into account and considering the Fermi distributions of electrons in the left and right electrode, one obtains an expression for the current density:

$$J(V) = \frac{2e\rho}{h}\left[eV\int_0^{\mu-eV} T(E_x,V)\ \mathrm{d}E_x + \int_{\mu-eV}^{\mu} T(E_x,V)\ (\mu - E_x)\ \mathrm{d}E_x\right] \qquad \textbf{Equation 1.41}$$

where ρ is the density of states (DOS) of the electrode. To use Equation 1.41 $U(x)$ must be known and it is usually not feasible to measure. Simmons used an effective barrier height to replace $U(x)$ (Figure 1.7) and in this approximation Equation 1.41 can be simplified to[148–150]

$$J(V) = \frac{e}{4\pi^2\hbar d^2}\left\{\left(\varphi_0 - \frac{eV}{2}\right)\exp\left[-\frac{2d\sqrt{2m}}{\hbar}\left(\varphi_0 - \frac{eV}{2}\right)^{\frac{1}{2}}\right]\right. \qquad \textbf{Equation 1.42}$$
$$\left. -\left(\varphi_0 + \frac{eV}{2}\right)\exp\left[-\frac{2d\sqrt{2m}}{\hbar}\left(\varphi_0 + \frac{eV}{2}\right)^{\frac{1}{2}}\right]\right\}$$

where V is the bias between the left and right electrode and d is the width of the barrier.

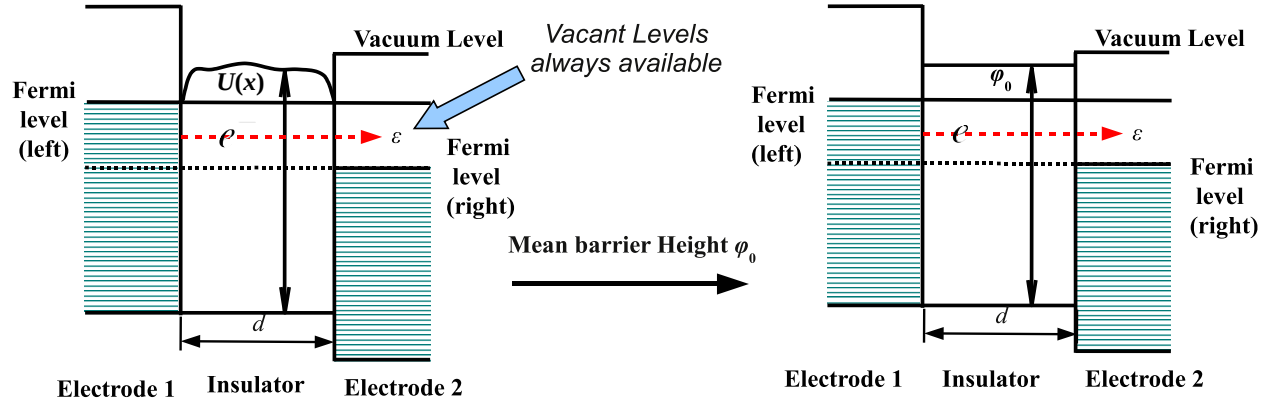

Figure 1.7. A barrier with arbitrary shape is replaced with an effective rectangular barrier with mean barrier height φ_0.

Note that at low bias, Equation 1.42 can be further simplified to an exponential decay form:

$$J = \frac{V}{d}\sqrt{\frac{2me\varphi_0}{h}}\ \exp\left[-\frac{2d\sqrt{2m\varphi_0}}{\hbar}\right] \qquad \textbf{Equation 1.43}$$

Such a distance dependence is well known. It also predicts a linear *J*-*V* relationship at low bias and is confirmed by STM experiments.[146] Another property of Simmons model is that it always predicts symmetrical *J*-*V* curves. The symmetry is *not* introduced in the "smoothing" step when

an effective flat barrier is used. Actually, the symmetry of *J-V* curves comes from the symmetry of the WKB approximation (Equation 1.40). As long as Equation 1.40 is employed, the transmission factor will be the same from left to right or from right to left at the same bias, no matter how asymmetric the barrier might be. People have tried to extended Simmons model to explain some asymmetrical *J-V* curves that are observed at the semiclassical level, and it required that they either introduce asymmetrical electrodes or assume asymmetrical potential drops when the bias is reversed.[151–153] Clearly, if one wants to study charge transport through possible molecular rectifiers[69] by numerical simulation, a more advanced formulism is needed.

1.4.3.2 Non-Equilibrium Green's Function Formalism

The Non-Equilibrium Green's Function (NEGF) method is now a standard paradigm for molecular and nanoscale charge transport problems.[70,154–157] Green's functions were originally developed as an important mathematical tool to solve inhomogeneous differential equations. Suppose we need to solve the following equation for $a(x)$:

$$\left(E - \widehat{H}\right)a(x) = b(x) \qquad \textbf{Equation 1.44}$$

where E is a parameter and $\widehat{H}$ is an Hermitian operator. The Green's function $G(x, x', E)$ associated with $\widehat{H}$ then satisfies

$$\left(E - \widehat{H}\right)G(x, x', E) = \delta(x - x') \qquad \textbf{Equation 1.45}$$

where $\delta(x - x')$ is the Dirac δ function. Now a specific solution to Equation 1.44 can be written in terms of the Green's function as

$$a(x) = \int_{-\infty}^{+\infty} G(x, x', E)\ b(x')\ \mathrm{d}E \qquad \textbf{Equation 1.46}$$

In quantum chemistry, wave functions are usually expanded on a basis set and the matrix version of Green's function is more convenient. Consider the solution to the following equation for $\{a\}$:

$$[E\mathbf{I} - \mathbf{H}]\{a\} = \{b\} \qquad \textbf{Equation 1.47}$$

where E is a parameter, $\mathbf{I}$ is the identity matrix, $\mathbf{H}$ is an Hermitian matrix, and $\{a\}$ and $\{b\}$ are column vectors. The Green's function for $\mathbf{H}$ is then defined as:

$$\begin{aligned} &\mathbf{G}(E) = [E\mathbf{I} - \mathbf{H}]^{-1} \\ &\Longrightarrow [E\mathbf{I} - \mathbf{H}]\mathbf{G}(E) = \mathbf{I} \end{aligned} \qquad \textbf{Equation 1.48}$$

The above equation is a matrix analog of Equation 1.45. Note that if $\mathbf{b} = 0$, $\mathbf{H}$ is the single particle Hamiltonian of the system, the physical meaning of E would be the energy of the single particle. A *spectral function* $\mathbf{A}(E)$, which has the physical meaning of density of states (DOS), can be defined as:

$$\mathbf{A}(E) = i[\mathbf{G}^R(E) - \mathbf{G}^A(E)] \qquad \textbf{Equation 1.49}$$

where $\mathbf{G}^R(E)$ is the retarded Green's function and $\mathbf{G}^A(E)$ is the advanced Green's function:

$$\begin{aligned} \mathbf{G}^R(E) &= [(E + i0^+)\mathbf{I} - \mathbf{H}]^{-1} \\ \mathbf{G}^A(E) &= [(E - i0^+)\mathbf{I} - \mathbf{H}]^{-1} \end{aligned} \qquad \textbf{Equation 1.50}$$

where 0^+ denotes a positive infinitesimal. It is introduced here to break the symmetry of the matrix. The names of the above two functions come from the fact that their Fourier transforms describe the evolution of the system after and before an impulse of perturbation respectively. $\mathbf{G}^A$ is the conjugate transpose of $\mathbf{G}^R$**;** the superscript of $\mathbf{G}^R$ is usually dropped when no confusion can be made. Therefore Equation 1.49 can be re-written as

$$\mathbf{A}(E) = i[\mathbf{G}(E) - \mathbf{G}^+(E)] \qquad \textbf{Equation 1.51}$$

Equation 1.51 can be rationalized by the corresponding Green's functions of pure numbers:

$$i[G(E) - G^{+}(E)] = i\left[\frac{1}{E - \varepsilon_\alpha + i0^{+}} - \frac{1}{E - \varepsilon_\alpha - i0^{+}}\right]$$

$$= \left[\frac{2\eta}{(E - \varepsilon_\alpha)^2 + \eta^2}\right]_{\eta \to 0} \qquad \textbf{Equation 1.52}$$

$$= 2\pi\, \delta(E - \varepsilon_\alpha) \equiv A(E)$$

where ε_α denotes any of the eigenvalues of $\widehat{H}$. With $\mathbf{A}(E)$, the correlation function or the "lesser" Green's function can be defined as

$$\mathbf{G}^{<}(E) = i\ f(E)\ \mathbf{A}(E) \qquad \textbf{Equation 1.53}$$

where $f(E)$ is the Fermi function. $\mathbf{G}^{<}(E)$ has the meaning of the matrix version of the electron density per unit energy.

It seems that the Green's function is only a trivial mathematical transformation of known results for isolated molecular systems at the Hartree-Fock level. However, the Hartree-Fock Hamiltonian (denoted as "$\mathbf{H}_0$") does not contain any correlation interactions and a better Hamiltonian can be written as:

$$\mathbf{H} = \mathbf{H}_0 + \mathbf{\Sigma} \qquad \textbf{Equation 1.54}$$

where $\mathbf{\Sigma}$ is the *self-energy* matrix containing (some) correlation interactions. The Green's function $\mathbf{G}$ for $\mathbf{H}$ can be calculated by the Dyson equation (the variable *E* is dropped for clarity):

$$\mathbf{G} \equiv [E\mathbf{I} - \mathbf{H_0} - \mathbf{\Sigma}]^{-1} = \mathbf{G_0} + \mathbf{G_0 \Sigma G} \qquad \textbf{Equation 1.55}$$

where $\mathbf{G_0}$ is the Green's function for $\mathbf{H}_0$. One can imagine that by improving $\mathbf{\Sigma}$ or adding more self-energy terms, the Green's function method can provide a systematic framework to solve the Schrödinger equation of isolated systems by using Equation 1.55. Hence it is very widely used in many-body theories and other post-Hartree-Fock methods.[158,159] More importantly for us, it provides a (if not "the") way to study the transport problem for an open system based on the results of isolated systems; see below.

Consider a molecule that is attached to an electrode. In this case, the Hamiltonian may be written as

$$\mathbf{H}_{Full} \equiv \begin{pmatrix} \mathbf{H}_{El} & \beta \\ \beta^{+} & \mathbf{H}_0 \end{pmatrix} \qquad \textbf{Equation 1.56}$$

where $\mathbf{H}_{El}$ is the Hamiltonian of the isolated electrode, $\mathbf{H}_0$ is the Hamiltonian of the isolated molecule, and β and β^{+} are the couplings. It is obvious that the dimension of $\mathbf{H}_{El}$ is much larger than the dimension of **H,** and $\mathbf{H}_{Full}$ cannot be evaluated on any computer. Fortunately we can still focus on the molecule in the Green's function formalism by adding a "correction" to $\mathbf{H}_0$, that is:

$$[E\mathbf{I} - \mathbf{H}_0 - \beta \mathbf{G}_{El} \beta^{+}]\{\psi_0\} = \{S\} \qquad \textbf{Equation 1.57}$$

where $\{\psi_0\}$ is the wavefunction for the isolated molecule, $\mathbf{G}_{El}$ is the retarded Green's function for the isolated electrode, and $\{S\}$ is some non-zero column vector because now $\{\psi_0\}$ is not a eigenvector of $[\mathbf{H}_0 - \beta \mathbf{G}_{El} \beta^{+}]$. Compared with Equation 1.54, $\beta \mathbf{G}_{El} \beta^{+}$ is just another type of *self-energy* (although now it is anti-Hermitian instead of Hermitian, as in Equation 1.54). Equation 1.57 can be re-written as:

$$[E\mathbf{I} - \mathbf{H}_0 - \mathbf{\Sigma}]\{\psi_0\} = \{S\} \quad \text{with} \quad \mathbf{\Sigma} \equiv \beta \mathbf{G}_{El} \beta^{+} \qquad \textbf{Equation 1.58}$$

Note that Equation 1.58 has the same form as Equation 1.47 or Equation 1.44 and Equation 1.54. However, our purpose is quite different here: $\{\psi_0\}$ is already known and we are interested in obtaining other properties of the open system. If we define the Green's function of the molecule in contact with the electrode,

$$\mathbf{G} \equiv [E\mathbf{I} - \mathbf{H}_0 - \mathbf{\Sigma}]^{-1} \qquad \textbf{Equation 1.59}$$

then $\mathbf{G}\{S\} = \{\psi_0\}$. Although no positive infinitesimal is explicitly used, the Green's function defined in the above equation is indeed a retarded Green's function, because $\mathbf{G}_{El}$ is a retarded Green's function. Consequently, the spectral function $\mathbf{A}(E)$ and correlation function $\mathbf{G}^{<}(E)$ can be expressed by using Equation 1.51 and Equation 1.53. That is, one can obtain the most useful

information without solving for the wavefunctions for the open system. Comparing with isolated molecules, $\mathbf{A}(E)$ now has the physical meaning of a "local" DOS because only the states on the molecular bridge are counted.

To further simply the calculation, a *broadening matrix* can be defined as:

$$\mathbf{\Gamma} \equiv i[\mathbf{\Sigma} - \mathbf{\Sigma}^{+}]^{-1} = \beta \mathbf{A}^{El} \beta^{+} \qquad \textbf{Equation 1.60}$$

where $\mathbf{A}^{El}$ is the spectral function of the isolated electrode. The spectral function of the molecule in contact with the electrode $\mathbf{A}(E)$ can be expressed as:

$$\mathbf{A} \equiv i[\mathbf{G} - \mathbf{G}^{+}]^{-1} = \mathbf{G\Gamma G}^{+} = \mathbf{G}^{+}\mathbf{\Gamma G} \qquad \textbf{Equation 1.61}$$

$\mathbf{\Gamma}$ is called the "broadening matrix" because the effect of the coupling broadens $\mathbf{A}(E)$ from a sum of Dirac δ functions, for isolated systems, to a multiple modal distribution with finite width for each peak, for open systems.

The above discussion can be easily generalized to open systems with two electrodes. The (retarded) Green's function is

$$\mathbf{G} = [E\mathbf{I} - \mathbf{H}_0 - \mathbf{\Sigma}_L - \mathbf{\Sigma}_R]^{-1} \qquad \textbf{Equation 1.62}$$

where L and R denote the left and right electrode, respectively. The spectral function and correlation function are

$$\begin{aligned} \mathbf{\Gamma} &= \mathbf{\Gamma}_L + \mathbf{\Gamma}_R = \beta_L \mathbf{A}_L^{El} \beta_L^{+} + \beta_R \mathbf{A}_R^{El} \beta_R^{+} \\ \mathbf{A} &= \mathbf{G}[\mathbf{\Gamma}_L + \mathbf{\Gamma}_R]\mathbf{G}^{+} = \mathbf{G\Gamma}_L\mathbf{G}^{+} + \mathbf{G\Gamma}_R\mathbf{G}^{+} \equiv \mathbf{A}_L + \mathbf{A}_R \qquad \textbf{Equation 1.63} \\ [\mathbf{G}^{<}] &= [\mathbf{A}_L] f_L + [\mathbf{A}_R] f_R \end{aligned}$$

with the above equations, the current flow can be calculated. The basic idea is to use the time-dependent Schrödinger equation associated with $\mathbf{H}_{Full}$ to get the net charge injection rate at a given electrode/molecule interface at energy *E*; see chapter 9 of Datta 2005[70] and chapter 8 of Datta 1995[154]. The overall current will be proportional to the integral of the charge injection rate. In this

process the electrode wavefunction can be eliminated by using the self-energy matrix, and the final expression of the electric current is (left electrode/molecule interface as example):

$$J = J_L = \frac{q}{h}\int_{-\infty}^{+\infty} (\mathrm{Trace}[\mathbf{\Gamma}_L \mathbf{A}] f_L - \mathrm{Trace}[\mathbf{\Gamma}_L \mathbf{G}^<]) \, \mathrm{d}E \qquad \textbf{Equation 1.64}$$

Insertion of Equation 1.61 and Equation 1.63 into Equation 1.64 gives the Landauer formula:

$$J = \frac{q}{h}\int T(E) \, [f_L(E-\mu_L) - f_R(E-\mu_R)] \, \mathrm{d}E \qquad \textbf{Equation 1.65}$$

where $T(E)$ is the transmission function and

$$\begin{aligned} T(E) &= \mathrm{Trace}[\mathbf{\Gamma}_L \mathbf{A}_R] = \mathrm{Trace}[\mathbf{\Gamma}_R \mathbf{A}_L] \\ &= \mathrm{Trace}[\mathbf{\Gamma}_L \mathbf{G} \mathbf{\Gamma}_R \mathbf{G}^+] = \mathrm{Trace}[\mathbf{\Gamma}_R \mathbf{G} \mathbf{\Gamma}_L \mathbf{G}^+] \end{aligned} \qquad \textbf{Equation 1.66}$$

Equation 1.65 and Equation 1.66 give the formal solution of the coherent current. In Chapter 3 and 4 these equations are applied to real molecular systems. There are some additional remarks about the applications I would like to make. First, orthogonal basis sets are assumed in the above derivation. Although non-orthogonal basis sets can be used theoretically, additional care must be taken.[160–162] To avoid such troubles, one can do electronic structure calculations with an orthogonal basis set directly (such as INDO/S calculation in Chapter 4), or change the representation of the final Fock matrix to an orthogonal basis set representation, such as the NAO Fock matrix used in Chapter 3. Second, the above protocol is not self-consistent, because we do not calculate the wavefunctions of the open system and therefore the electron density of the molecule is frozen to its isolated state. To reach a self-consistent solution, one needs to solve Poisson's equation ($\nabla^2 U(\vec{r}) = \rho(\vec{r})/\varepsilon_0$, where $\rho(\vec{r})$ is the net charge density) for the electric potential $U(\vec{r})$ with boundary conditions connecting the electric potentials of the left and right electrode. The calculated U will be used in solving the Schrödinger equation for the molecule to

get a new $\rho(\vec{r})$. This procedure will be performed iteratively until self-consistency is reached. Commercial packages such as ATK can perform such calculations, but it is too complicated to be implemented in a MATLAB script. Therefore we will limit our calculation to weak coupling and near zero conductance limit where the self-consistency is not required. Third, Equation 1.65 and Equation 1.66 do not cover the incoherent current. Incoherent current is important for hopping. However, it is difficult to implement it in molecular systems and even commercial packages cannot reproduce the distance dependence, because of the lack of incoherent current.[163] Dephasing can be included phenomenologically but additional parameters which cannot be measured directly by experiments must be introduced.[164] Thus, it might be better to stick to coherent calculations if the experiments can be explained in this way. Finally, the NEGF method cannot only be applied to molecular systems, it can also be used to calculate *J*-*V* curves of semi-classical models where the potential barrier can be in arbitrary shape, see the examples in Reference [70]. Different from the Simmons model discussed in section1.4.3.1, the WKB approximation (which requires $U(x)$ to vary slowly with distance) is not assumed and no "effective" barrier height is used in the NEGF formalism. Therefore a thin but tall barrier or a barrier with potential "spikes" can be calculated and the intrinsic asymmetry in the barrier might be captured.

1.4.4 A Dynamic Picture: Molecular Dynamics and Conformational Gating

In previous sections the Condon approximation (e.g. electronic coupling is independent of the nuclear coordinates) is always assumed. Note, however, that this does not imply that all charge transfer reactions occur from a unique nuclear configuration. This picture is far from the truth, especially in liquid solvents and for flexible molecules such as peptide nucleic acids.[131,165] The

Condon approximation assumes that there is a timescale separation between the nuclear motion(s) and the electronic transition, such that the electron tunneling event occurs rapidly compared to the nuclear motions. For a given ensemble of donor and acceptor molecules a range of distances and configurations may exist and they will have different electronic couplings and reaction rates. Even for a donor-bridge-acceptor supermolecule, the donor to acceptor distance, r_{DA}, might change with bridge vibrations and this will lead to a change in H_{DA} in the superexchange regime (see Equation Equation 1.12). Such effects have been observed in several systems.[166–168]

To obtain a full picture of charge transfer in computational chemistry, we need to generate an ensemble of conformations instead of just focusing on one optimized structure. This can be done by molecular dynamics (MD), see chapter 4 and 5. In our implementation, thousands of snapshots were taken from the equilibrium MD trajectories. The Condon approximation only applies to individual conformation snapshots but not the whole trajectory. That is, we can draw a pair of Marcus parabolas as Figure 1.1 for each snapshot. They will have similar λ and the coupling H_{DA} will be kept unchanged within each pair of parabolas. They will have similar λ and the coupling H_{DA} will be kept unchanged within each pair of parabolas. However, H_{DA} may vary a lot among different pairs (or different snapshots). Note that the actual position of each snapshot on its Marcus parabolas is arbitrary, and we are not interested in reaching any particular position such as the crossing point within the Condon approximation. Actually, depending on the activation energy, reaching the correct donor/acceptor and solvent molecule nuclear configuration of transition state (crossing point) of any pair of the Marcus parabolas could be a very rare event in equilibrium MD and may only be obtained by special techniques such as transition path sampling[169–171]; or even go beyond Born-Oppenheimer molecular dynamics.[172,173174]

The Condon approximation could eventually be problematic in some cases. Very recently Beratan *et al.* found that H_{DA} is very sensitive to the molecular geometries in near resonance tunnelings for some nucleic acids so that the non-Condon effects dominate, and the charge transfer mechanism changes to "flickering resonance".[175] This effect is beyond the scope of this dissertation but it is worth noting and might become an important direction in future electron transfer studies.

1.5 DISSERTATION OUTLINE

The work described in this dissertation employs a wide range of experimental and theoretical methods discussed above to address some fundamental problems in nanoscale charge transfer. Electrochemical measurement is probably the most feasible experimental mothed for most labs and its application in the "hopping" regime is discussed in Chapter 2. As mentioned in section 1.3.1, the traditional electrochemical analysis is based single-step non-adiabatic electron tunneling models and the validity of applying this model to "hopping" regime was never rigorously tested before. Chapter 2 describes a three-step kinetic scheme to model charge transfer in this regime. Some of the features of the three-step model are probed experimentally by changing the chemical composition of the SAM. As an example, the charge injection barrier for a SAM composed of a 10-mer peptide nucleic acid (PNA) is extracted by using the three-step model and a temperature dependence of the charge transfer rate.

Starting from Chapter 3, experimental and theoretical methods are combined to explore nanoscale objects. In Chapter 3, single molecule conductance measurements on alkanedithiols and alkoxydithiols (dithiolated oligoethers) were performed using the STM-controlled Break Junction

method (STM-BJ, see section 1.3.2) to ascertain how the oxygen heteroatoms in saturated linear chains impact the molecular conductance. The results show that the conductance of the oligoethers is lower than that of alkane chains with the same length. These experimental findings are substantiated by computational studies. First, the experimental trend were reproduced by NEGF formulism (see section 1.4.3) and explained by the differences in the spatial distribution of the molecular orbitals that contribute most to the conductance. Second, a pathway analysis was performed and the trend is discussed in terms of the electronic couplings in the Marcus theory of non-adiabatic electron transfer. The consistency between the two methods corroborates Nitzan's results on the relationship between molecular conductance and charge transfer rate (see section 1.3.2).

Chapter 4 focuses on the dynamic effects of the charge transfer. Peptide nucleic acid with an aminoethylglycine backbone (aeg-PNA) and that with a γ-methylated backbone (γ-PNA) have been studied. The common aeg-PNA has a flexible structure, whereas γ-PNA has significantly more rigid structure than aeg-PNA. Experimental electrochemical measurements show that the charge transfer rate through an aeg-PNA bridging unit is twice the charge transfer rate through a γ-PNA bridge unit. Theoretical NEGF conductance calculations of PNA electronic properties, which are based on a molecular dynamics structural ensemble, reveal that the difference in the charge transfer rate results from the difference in the extent of backbone fluctuations of aeg- and γ-PNA. The greater flexibility of the aeg-PNA gives rise to more broadening and a more frequent appearance of highly-conductive conformations, as compared to γ-PNA. This finding has implications for the design of nucleic acid-based molecular electronics components.

Finally, a new scaffold for studying photoinduced charge transfer has been constructed by connecting a $[Ru(Bpy)_3]^{2+}$ donor to a bis(8-hydroxyquinolinate)$_2$ copper $[CuQ_2]$ acceptor through

a peptide nucleic acid (PNA) bridge in Chapter 5. Intramolecular electron transfer from $[Ru(Bpy)_3]^{2+*}$ to $[CuQ_2]$ has been observed in time-resolved photoluminescence (TCSPC, see section 1.3.3). Depending on the positions of the donor, the conformational effects might be important and the power of lifetime distribution analysis to resolve the charge transfer details has been demonstrated. Molecular dynamics simulations are used to explore the donor-PNA-acceptor structure and the resulting conformational distribution provides a possible explanation for the distribution of electron transfer rates.

1.6 REFERENCES

(1) *Electron Transfer in Chemistry*; Balzani, V., Ed.; Wiley-VCH Verlag GmbH: Weinheim, Germany, 2001.

(2) Hsu, C. *Acc. Chem. Res.* **2009**, *42*, 509.

(3) Giese, B.; Graber, M.; Cordes, M. *Curr. Opin. Chem. Biol.* **2008**, *12*, 755.

(4) Cordes, M.; Giese, B. *Chem. Soc. Rev.* **2009**, *38*, 892.

(5) Warren, J. J.; Ener, M. E.; Vlček, A.; Winkler, J. R.; Gray, H. B. *Coord. Chem. Rev.* **2012**, *256*, 2478.

(6) Fukuzumi, S.; Ohkubo, K.; Suenobu, T. *Acc. Chem. Res.* **2014**, *1464*.

(7) Zhao, Y.; Liang, W. *Chem. Soc. Rev.* **2012**, *41*, 1075.

(8) Chen, R.; Wu, R.; Zhang, G.; Gao, Y.; Xiao, L.; Jia, S. *Sensors (Basel).* **2014**, *14*, 2449.

(9) Hines, D. a; Kamat, P. V *ACS Appl. Mater. Interfaces* **2014**, *6*, 3041.

(10) Lewis, F. D. *Isr. J. Chem.* **2013**, *53*, 350.

(11) Kirk, M. L.; Shultz, D. A. *Coord. Chem. Rev.* **2013**, *257*, 218.

(12) Natali, M.; Campagna, S.; Scandola, F. *Chem. Soc. Rev.* **2014**, *43*, 4005.

(13) Heckmann, A.; Lambert, C. *Angew. Chem. Int. Ed. Engl.* **2012**, *51*, 326.

(14) Aguirre-Etcheverry, P.; O'Hare, D. *Chem. Rev.* **2010**, *110*, 4839.

(15) Marcus, R. A. *J. Chem. Phys.* **1956**, *24*, 966.

(16) Newton, M. D. In *Electron Transfer in Chemistry*; Balzani, V., Ed.; Wiley-VCH Verlag GmbH: Weinheim, Germany, 2001; pp. 3–63.

(17) Nitzan, A. *Chemical Dynamics in Condensed Phases: Relaxation, Transfer and Reactions in Condensed Molecular Systems*; Oxford University Press, 2006.

(18) May, V.; Kühn, O. *Charge and Energy Transfer Dynamics in Molecular Systems*; Wiley-VCH Verlag GmbH & Co. KGaA: Weinheim, Germany, 2011.

(19) Barbara, P. F.; Meyer, T. J.; Ratner, M. A. *J. Phys. Chem.* **1996**, *100*, 13148.

(20) Miller, J. R.; Calcaterra, L. T.; Closs, G. L. *J. Am. Chem. Soc.* **1984**, *106*, 3047.

(21) Miller, J. R.; Beitz, J. V; Huddleston, R. K. *J. Am. Chem. Soc.* **1984**, *106*, 5057.

(22) Marcus, R. *Discuss. Faraday Soc.* **1960**, 21.

(23) Bard, A. J.; Faulkner, L. R. *Electrochemical Methods: Fundamentals and Applications*; 2nd ed.; John Wiley & Sons, Inc., 2000.

(24) Marcus, R. *Biochim. Biophys. Acta - Rev. Bioenerg.* **1985**, *811*, 265.

(25) Van Voorhis, T.; Kowalczyk, T.; Kaduk, B.; Wang, L.-P.; Cheng, C.-L.; Wu, Q. *Annu. Rev. Phys. Chem.* **2010**, *61*, 149.

(26) Sidis, V. In *Advances in Chemical Physics*; Baer, M.; Ng, C.-Y., Eds.; Advances in Chemical Physics; John Wiley & Sons, Inc.: Hoboken, NJ, USA, 1992; Vol. 82, pp. 73–134.

(27) Jordan, K. D.; Paddon-Row, M. N. *Chem. Rev.* **1992**, *92*, 395.

(28) Jortner, J.; Bixon, M. *J. Chem. Phys.* **1988**, *88*, 167.

(29) Jortner, J. *J. Chem. Phys.* **1976**, *64*, 4860.

(30) Zimmt, M. B.; Waldeck, D. H. *J. Phys. Chem. A* **2003**, *107*, 3580.

(31) Gray, H. B.; Ellis, W. R. In *Bioinorganic Chemistry*; Bertini, I.; Gray, H. B.; Lippard, S. J.; Valentine, J. S., Eds.; University Science Books: Mill Valley, CA, 1994; pp. 315–363.

(32) Khoshtariya, D. E.; Dolidze, T. D.; Shushanyan, M.; Davis, K. L.; Waldeck, D. H.; van Eldik, R. *Proc. Natl. Acad. Sci. U. S. A.* **2010**, *107*, 2757.

(33) McConnell, H. M. *J. Chem. Phys.* **1961**, *35*, 508.

(34) Núñez, M. E.; Hall, D. B.; Barton, J. K. *Chem. Biol.* **1999**, *6*, 85.

(35) Giese, B.; Amaudrut, J.; Köhler, A. K.; Spormann, M.; Wessely, S. *Nature* **2001**, *412*, 318.

(36) Paul, A.; Watson, R. M.; Wierzbinski, E.; Davis, K. L.; Sha, A.; Achim, C.; Waldeck, D. H. *J. Phys. Chem. B* **2010**, *114*, 14140.

(37) *Longe-Range Charge Transfer in DNA I*; Schuster, G. B., Ed.; Topics in Current Chemistry; Springer Berlin Heidelberg: Berlin, Heidelberg, 2004; Vol. 236.

(38) *Long-Range Charge Transfer in DNA II*; Schuster, G. B., Ed.; Topics in Current Chemistry; Springer Berlin Heidelberg: Berlin, Heidelberg, 2004; Vol. 237.

(39) Petrov, E. G.; May, V.; Hänggi, P. *Chem. Phys.* **2005**, *319*, 380.

(40) Petrov, E. G.; Shevchenko, Y. V.; Teslenko, V. I.; May, V. *J. Chem. Phys.* **2001**, *115*, 7107.

(41) Kawai, K.; Majima, T. *Acc. Chem. Res.* **2013**, *46*, 2616.

(42) Jortner, J.; Bixon, M.; Langenbacher, T.; Michel-Beyerle, M. E. *Proc. Natl. Acad. Sci.* **1998**, *95*, 12759.

(43) Renaud, N.; Berlin, Y. a; Lewis, F. D.; Ratner, M. a *J. Am. Chem. Soc.* **2013**, *135*, 3953.

(44) Jortner, J.; Bixon, M.; Voityuk, A. A.; Rösch, N. *J. Phys. Chem. A* **2002**, *106*, 7599.

(45) Li, X.-Q.; Zhang, H.; Yan, Y. *J. Phys. Chem. A* **2001**, *105*, 9563.

(46) Berlin, Y. A.; Burin, A. L.; Ratner, M. A. *Chem. Phys.* **2002**, *275*, 61.

(47) Berlin, Y. A.; Hutchison, G. R.; Rempala, P.; Ratner, M. A.; Michl, J. *J. Phys. Chem. A* **2003**, *107*, 3970.

(48) Finklea, H. O. In *Electroanalytical Chemistry: A Series of Advances, Vol 19*; Bard, A. J.; Rubinstein, I., Eds.; Dekker: New York, 1996; Vol. 19, pp. 109–335.

(49) Scherer, J.; Vogt, M. R.; Magnussen, O. M.; Behm, R. J. *Langmuir* **1997**, *13*, 7045.

(50) Xiao, X.; Hu, J.; Charych, D. H.; Salmeron, M. *Langmuir* **1996**, *12*, 235.

(51) Kim, H. I.; Graupe, M.; Oloba, O.; Koini, T.; Imaduddin, S.; Lee, T. R.; Perry, S. S. *Langmuir* **1999**, *15*, 3179.

(52) Smith, R. K.; Lewis, P. A.; Weiss, P. S. *Prog. Surf. Sci.* **2004**, *75*, 1.

(53) Wei, J.; Liu, H.; Dick, A. R.; Yamamoto, H.; He, Y.; Waldeck, D. H. *J. Am. Chem. Soc.* **2002**, *124*, 9591.

(54) Chidsey, C. E. *Science* **1991**, *251*, 919.

(55) Weber, K.; Creager, S. E. *Anal. Chem.* **1994**, *66*, 3164.

(56) Honeychurch, M. J. *Langmuir* **1999**, *15*, 5158.

(57) Dogonadze, R. R. In *Reactions of Molecules at Electrodes*; Hush, N. S., Ed.; Wiley Interscience, 1971; pp. 135–227.

(58) Dogonadze, R. R.; Kuznetsov, A. M. *Prog. Surf. Sci.* **1975**, *6*, 1.

(59) Gerischer, H. In *Advances in Electrochemistry and Electrochemical Engineering*; Paul, D., Ed.; Interscience Publishers, Inc.: New York, N.Y., 1961; Vol. 1, pp. 139–232.

(60) Mishra, A. K.; Waldeck, D. H. *J. Phys. Chem. C* **2011**, *115*, 20662.

(61) Mishra, A. K.; Waldeck, D. H. *J. Phys. Chem. C* **2009**, *113*, 17904.

(62) Zhao, L.-B.; Mishra, A. K.; Waldeck, D. H. *J. Phys. Chem. C* **2013**, *117*, 20746.

(63) Napper, A. M.; Liu, H.; Waldeck, D. H. *J. Phys. Chem. B* **2001**, *105*, 7699.

(64) Chen, F.; Hihath, J.; Huang, Z.; Li, X.; Tao, N. J. *Annu. Rev. Phys. Chem.* **2007**, *58*, 535.

(65) Reed, M. A. *Science* **1997**, *278*, 252.

(66) Xu, B.; Tao, N. J. *Science* **2003**, *301*, 1221.

(67) Kuhn, H.; Möbius, D. *Angew. Chemie Int. Ed. English* **1971**, *10*, 620.

(68) Mann, B. *J. Appl. Phys.* **1971**, *42*, 4398.

(69) Aviram, A.; Ratner, M. A. *Chem. Phys. Lett.* **1974**, *29*, 277.

(70) Datta, S. *Quantum Transport: Atom to Transistor*; Cambridge, 2005, 2005.

(71) *Introducing Molecular Electronics*; Cuniberti, G.; Richter, K.; Fagas, G., Eds.; Lecture Notes in Physics; Springer Berlin Heidelberg, 2005; Vol. 680.

(72) Jortner, J.; Nitzan, A.; Ratner, M. *Lect. Notes Phys.* **2005**, *680*, 13.

(73) Nitzan, A. *J. Phys. Chem. A* **2001**, *105*, 2677.

(74) Nitzan, A. *Isr. J. Chem.* **2002**, *42*, 163.

(75) Wierzbinski, E.; Venkatramani, R.; Davis, K. L.; Bezer, S.; Kong, J.; Xing, Y.; Borguet, E.; Achim, C.; Beratan, D. N.; Waldeck, D. H. *ACS Nano* **2013**, *7*, 5391.

(76) Gray, H. B.; Winkler, J. R. *Annu. Rev. Biochem.* **1996**, *65*, 537.

(77) Winkler, J. R.; Gray, H. B. *Chem. Rev.* **2014**, *114*, 3369.

(78) Kelley, S. O.; Barton, J. K. *Science* **1999**, *283*, 375.

(79) Arkin, M. R.; Stemp, E. D. A.; Holmlin, R. E.; Barton, J. K.; Hormann, A.; Olson, E. J. C.; Barbara, P. F. *Science* **1996**, *273*, 475.

(80) Genereux, J. C.; Barton, J. K. *Chem. Rev.* **2010**, *110*, 1642.

(81) Hall, D. B.; Holmlin, R. E.; Barton, J. K. *Nature* **1996**, *382*, 731.

(82) Lewis, F. D.; Liu, X.; Liu, J.; Miller, S. E.; Hayes, R. T.; Wasielewski, M. R. *Nature* **2000**, *406*, 51.

(83) Lewis, F. D.; Wu, T.; Zhang, Y.; Letsinger, R. L.; Greenfield, S. R.; Wasielewski, M. R. *Science* **1997**, *277*, 673.

(84) Lewis, F. D.; Letsinger, R. L.; Wasielewski, M. R. *Acc. Chem. Res.* **2001**, *34*, 159.

(85) Chernick, E. T.; Mi, Q.; Kelley, R. F.; Weiss, E. a; Jones, B. a; Marks, T. J.; Ratner, M. a; Wasielewski, M. R. *J. Am. Chem. Soc.* **2006**, *128*, 4356.

(86) Chakrabarti, S.; Liu, M.; Waldeck, D. H.; Oliver, A. M.; Paddon-Row, M. N. *J. Phys. Chem. A* **2009**, *113*, 1040.

(87) Shephard, M. J.; Paddon-Row, M. N.; Jordan, K. D. *Chem. Phys.* **1993**, *176*, 289.

(88) Nadeau, J. M.; Liu, M.; Waldeck, D. H.; Zimmt, M. B. *J. Am. Chem. Soc.* **2003**, *125*, 15964.

(89) Zeng, Y.; Zimmt, M. B. *J. Phys. Chem.* **1992**, *96*, 8395.

(90) Becker, W. *Advanced Time-Correlated Single Photon Counting Techniques*; Castleman, A. W.; Toennies, J. P.; Zinth, W., Eds.; Springer Series in Chemical Physics; Springer Berlin Heidelberg: Berlin, Heidelberg, 2005; Vol. 81.

(91) Kumar, K.; Kurnikov, I. V.; Beratan, D. N.; Waldeck, D. H.; Zimmt, M. B. *J. Phys. Chem. A* **1998**, *102*, 5529.

(92) Rehm, D.; Weller, A. *Isr. J. Chem.* **1970**, *8*, 259.

(93) Matyushov, D. V.; Schmid, R. *J. Chem. Phys.* **1995**, *103*, 2034.

(94) Rosso, K. M.; Dupuis, M. *J. Chem. Phys.* **2004**, *120*, 7050.

(95) Nelsen, S. F.; Blackstock, S. C.; Kim, Y. *J. Am. Chem. Soc.* **1987**, *109*, 677.

(96) Zhang, W.; Zhu, W.; Liang, W.; Zhao, Y.; Nelsen, S. F. *J. Phys. Chem. B* **2008**, *112*, 11079.

(97) Wu, Q.; Van Voorhis, T. *J. Chem. Theory Comput.* **2006**, *2*, 765.

(98) Kaduk, B.; Kowalczyk, T.; Van Voorhis, T. *Chem. Rev.* **2012**, *112*, 321.

(99) Liang, W.; Zhao, Y.; Sun, J.; Song, J.; Hu, S.; Yang, J. *J. Phys. Chem. B* **2006**, *110*, 9908.

(100) Marcus, R. A. *J. Phys. Chem.* **1989**, *93*, 3078.

(101) Blumberger, J. *Phys. Chem. Chem. Phys.* **2008**, *10*, 5651.

(102) Tipmanee, V.; Oberhofer, H.; Park, M.; Kim, K. S.; Blumberger, J. *J. Am. Chem. Soc.* **2010**, *132*, 17032.

(103) Blumberger, J.; Lamoureux, G. *Mol. Phys.* **2008**, *106*, 1597.

(104) Marcus, R. A. *Annu. Rev. Phys. Chem.* **1964**, *15*, 155.

(105) Marcus, R. A. *J. Chem. Phys.* **1965**, *43*, 679.

(106) Matyushov, D. V.; Voth, G. a. *J. Chem. Phys.* **1999**, *111*, 3630.

(107) Read, I.; Napper, A.; Zimmt, M. B.; Waldeck, D. H. *J. Phys. Chem. A* **2000**, *104*, 9385.

(108) Löwdin, P.-O. *J. Chem. Phys.* **1951**, *19*, 1396.

(109) Scholes, G. D. *Annu. Rev. Phys. Chem.* **2003**, *54*, 57.

(110) Löwdin, P.-O. *J. Mol. Spectrosc.* **1963**, *10*, 12.

(111) Evenson, J. W.; Karplus, M. *J. Chem. Phys.* **1992**, *96*, 5272.

(112) Jordan, K. D.; Paddon-Row, M. N. In *Encyclopedia of Computational Chemistry*; John Wiley & Sons, 1998; pp. 826–835.

(113) Prytkova, T. R.; Beratan, D. N.; Skourtis, S. S. *Proc. Natl. Acad. Sci. U. S. A.* **2007**, *104*, 802.

(114) Prytkova, T. R.; Kurnikov, I. V; Beratan, D. N. *J. Phys. Chem. B* **2005**, *109*, 1618.

(115) Wang, Y.; Liu, K.; Mukherjee, P.; Hines, D. a; Santra, P.; Shen, H. Y.; Kamat, P.; Waldeck, D. H. *Phys. Chem. Chem. Phys.* **2014**, *16*, 5066.

(116) Hush, N. S. *Electrochim. Acta* **1968**, *13*, 1005.

(117) Mulliken, R. S. *J. Am. Chem. Soc.* **1952**, *74*, 811.

(118) Kawatsu, T. *Biopolymers* **2013**, *100*, 100.

(119) Cave, R. J.; Newton, M. D. *Chem. Phys. Lett.* **1996**, *249*, 15.

(120) Cave, R. J.; Newton, M. D. *J. Chem. Phys.* **1997**, *106*, 9213.

(121) Subotnik, J. E.; Yeganeh, S.; Cave, R. J.; Ratner, M. A. *J. Chem. Phys.* **2008**, *129*, 244101.

(122) Toutounji, M. M.; Ratner, M. A. *J. Phys. Chem. A* **2000**, *104*, 8566.

(123) Lee, S.-J.; Chen, H.-C.; You, Z.-Q.; Liu, K.-L.; Chow, T. J.; Chen, I.-C.; Hsu, C.-P. *Mol. Phys.* **2010**, *108*, 2775.

(124) Shao, Y.; Molnar, L. F.; Jung, Y. *et al. Phys. Chem. Chem. Phys.* **2006**, *8*, 3172.

(125) Dreuw, A.; Head-Gordon, M. *J. Am. Chem. Soc.* **2004**, *126*, 4007.

(126) Zhao, Y.; Truhlar, D. G. *J. Phys. Chem. A* **2006**, *110*, 13126.

(127) Zhao, Y.; Truhlar, D. G. *Acc. Chem. Res.* **2008**, *41*, 157.

(128) Voityuk, A. A. *J. Chem. Phys.* **2005**, *123*, 34903.

(129) Voityuk, A. A. *J. Chem. Phys.* **2006**, *124*, 64505.

(130) Voityuk, A. A. *Chem. Phys. Lett.* **2007**, *439*, 162.

(131) Hatcher, E.; Balaeff, A.; Keinan, S.; Venkatramani, R.; Beratan, D. N. *J. Am. Chem. Soc.* **2008**, *130*, 11752.

(132) Voityuk, A. A.; Rösch, N. *J. Chem. Phys.* **2002**, *117*, 5607.

(133) Yang, C.-H.; Hsu, C.-P. *J. Chem. Phys.* **2013**, *139*, 154104.

(134) Newton, M. *Annu. Rev. Phys. Chem.* **1984**, *35*, 437.

(135) Löwdin, P.-O. *J. Chem. Phys.* **1950**, *18*, 365.

(136) Dederichs, P.; Blügel, S.; Zeller, R.; Akai, H. *Phys. Rev. Lett.* **1984**, *53*, 2512.

(137) Wu, Q.; Van Voorhis, T. *Phys. Rev. A* **2005**, *72*, 7.

(138) Wu, Q.; Van Voorhis, T. *J. Chem. Phys.* **2006**, *125*, 164105.

(139) Kurnikov, I. V.; Beratan, D. N. *J. Chem. Phys.* **1996**, *105*, 9561.

(140) Onuchic, J. N.; Beratan, D. N.; Winkler, J. R.; Gray, H. B. *Annu. Rev. Biophys. Biomol. Struct.* **1992**, *21*, 349.

(141) Beratan, D.; Betts, J.; Onuchic, J. *Science* **1991**, *252*, 1285.

(142) Balabin, I. A.; Hu, X.; Beratan, D. N. *J. Comput. Chem.* **2012**, *33*, 906.

(143) Consani, C.; Auböck, G.; van Mourik, F.; Chergui, M. *Science* **2013**, *339*, 1586.

(144) Kawatsu, T.; Kakitani, T.; Yamato, T. *J. Phys. Chem. B* **2002**, *106*, 11356.

(145) Daizadeh, I.; Medvedev, E. S.; Stuchebrukhov, a a *Proc. Natl. Acad. Sci. U. S. A.* **1997**, *94*, 3703.

(146) E. L. Wolf *Principles of Electron Tunneling Spectroscopy*; 2nd ed.; Oxford University Press, 2012.

(147) Schatz, G. C.; Ratner, M. A. *Quantum Mechanics in Chemistry*; Dover Publications, Inc.: Mineola, New York, 2002.

(148) Simmons, J. G.; Unterkofler, G. J. *J. Appl. Phys.* **1963**, *34*, 1828.

(149) Simmons, J. G. *J. Appl. Phys.* **1963**, *34*, 1793.

(150) Simmons, J. G. *J. Appl. Phys.* **1963**, *34*, 238.

(151) Hartman, T. E. *J. Appl. Phys.* **1964**, *35*, 3283.

(152) Brinkman, W. F.; DYNES, R. C.; ROWELL, J. M. *J. Appl. Phys.* **1970**, *41*, 1915.

(153) Ferraris, J.; Cowan, D. O.; Walatka, V.; Perlstein, J. H. *J. Am. Chem. Soc.* **1973**, *95*, 948.

(154) Datta, S. *Electronic Transport in Mesoscopic Systems*; Cambridge University Press, 1995.

(155) Ordejo, P.; Taylor, J.; Stokbro, K.; Brandbyge, M.; Mozos, J.-L.; Ordejón, P. *Phys. Rev. B* **2002**, *65*, 1.

(156) Taylor, J.; Guo, H.; Wang, J. *Phys. Rev. B* **2001**, *63*, 1.

(157) Wang, C.-K.; Fu, Y.; Luo, Y. *Phys. Chem. Chem. Phys.* **2001**, *3*, 5017.

(158) Szabo, A.; Ostlund, N. S. *Modern Quantum Chemistry*; Dover Publications, Inc.: Mineola, New York, 1996.

(159) Hirata, S.; He, X.; Hermes, M. R.; Willow, S. Y. *J. Phys. Chem. A* **2014**, *118*, 655.

(160) Reuter, M. G.; Harrison, R. J. *J. Chem. Phys.* **2013**, *139*, 114104.

(161) Reuter, M. G.; Harrison, R. J. *J. Chem. Phys.* **2014**, *140*, 177104.

(162) Brandbyge, M. *J. Chem. Phys.* **2014**, *140*, 177103.

(163) Liu, H.; Zhao, Z.; Wang, N.; Yu, C.; Zhao, J. *J. Comput. Chem.* **2011**, *32*, 1687.

(164) Venkatramani, R.; Davis, K. L.; Wierzbinski, E.; Bezer, S.; Balaeff, A.; Keinan, S.; Paul, A.; Kocsis, L.; Beratan, D. N.; Achim, C.; Waldeck, D. H. *J. Am. Chem. Soc.* **2011**, *133*, 62.

(165) Paul, A.; Bezer, S.; Venkatramani, R.; Kocsis, L.; Wierzbinski, E.; Balaeff, A.; Keinan, S.; Beratan, D. N.; Achim, C.; Waldeck, D. H. *J. Am. Chem. Soc.* **2009**, *131*, 6498.

(166) Khoshtariya, D. E.; Wei, J.; Liu, H.; Yue, H.; Waldeck, D. H. *J. Am. Chem. Soc.* **2003**, *125*, 7704.

(167) Davis, W. B.; Ratner, M. A.; Wasielewski, M. R. *J. Am. Chem. Soc.* **2001**, *123*, 7877.

(168) Balabin, I.; Beratan, D.; Skourtis, S. *Phys. Rev. Lett.* **2008**, *101*, 158102.

(169) Dellago, C.; Bolhuis, P. G.; Csajka, F. S.; Chandler, D. *J. Chem. Phys.* **1998**, *108*, 1964.

(170) Dellago, C.; Bolhuis, P. G.; Chandler, D. *J. Chem. Phys.* **1998**, *108*, 9236.

(171) Dellago, C.; Bolhuis, P. G.; Chandler, D. *J. Chem. Phys.* **1999**, *110*, 6617.

(172) Duncan, W. R.; Stier, W. M.; Prezhdo, O. V *J. Am. Chem. Soc.* **2005**, *127*, 7941.

(173) Abuabara, S. G.; Rego, L. G. C.; Batista, V. S. *J. Am. Chem. Soc.* **2005**, *127*, 18234.

(174) Woiczikowski, P. B.; Steinbrecher, T.; Kubař, T.; Elstner, M. *J. Phys. Chem. B* **2011**, *115*, 9846.

(175) Zhang, Y.; Liu, C.; Balaeff, A.; Skourtis, S. S.; Beratan, D. N. *Proc. Natl. Acad. Sci. U. S. A.* **2014**, *111*, 10049.

(176) Newton, M. D. *Chem. Rev.* **1991**, *91*, 767–792.

(177) Valeev, E. F.; Coropceanu, V.; da Silva Filho, D. A.; Salman, S.; Brédas, J.-L. *J. Am. Chem. Soc.* **2006**, *128*, 9882–6.

(178) Coropceanu, V.; Cornil, J.; da Silva Filho, D. A; Olivier, Y.; Silbey, R.; Brédas, J.-L. *Chem. Rev.* **2007**, *107*, 926–52.

(179) Senthilkumar, K.; Grozema, F. C.; Bickelhaupt, F. M.; Siebbeles, L. D. A. *J. Chem. Phys.* **2003**, *119*, 9809.

2.0 A THREE-STEP KINETIC MODEL FOR ELECTROCHEMICAL CHARGE TRANSFER IN THE HOPPING REGIME

This work has been published as Yin, X.; Wierzbinski, E.; Lu, H.; Bezer, S.; de Leon, A. R.; Davis, K. L.; Achim, C.; Waldeck, D. H. J. Phys. Chem. A 2014, 118, 7579–89. The author of the dissertation proposed the model, performed the electrochemical measurement of the 10-mer PNA and did subsequent analysis. E.W. provided data of other PNA strands and H.L. performed the measurement of the C11. S.B. and A.R.L. synthesized the PNA strands. K.L.D. provided data of mismatched PNAs. All authors participated in the writing and revision of the manuscript.

Single-step non-adiabatic electron tunneling models are widely used for analyzing electrochemical rates through self-assembled monolayer films (SAMs). For some systems, such as nucleic acids, long-range charge transfer can occur in a "hopping" regime that involves multiple charge transfer events and intermediate states. This report describes a three-step kinetic scheme to model charge transfer in this regime. Some of the features of the three-step model are probed experimentally by changing the chemical composition of the SAM. This work uses the three-step model and a temperature dependence of the charge transfer rate to extract the charge injection barrier for a SAM composed of a 10-mer peptide nucleic acid that operates in the "hopping" regime.

2.1 INTRODUCTION

A number of theoretical studies have addressed the detailed mechanism of charge transfer through nucleic acids, which can range from the superexchange (tunneling) limit to incoherent hopping.[1–8] For the incoherent limit, the application of simple random walk models[1,2] provides a weak (or 'soft') length dependence, similar to that observed experimentally. More detailed models distinguish the hopping through A:T base pairs from that through G:C base pairs.[3] The elementary steps of such hopping could be either direct tunneling/superexchange or thermally activated.[4] Those models all assume the presence of localized holes on a single site (nucleobase); however delocalized models, such as polaron hopping, can also explain the dependence of the rate constant on the length.[5,6] Besides analytical models, *ab initio*/DFT and semi-empirical approaches are widely used, and they can provide valuable insight into the parameters used in analytical models, which cannot be obtained easily from experiments.[7,8]

Several studies have used electrochemistry to probe charge transfer through self-assembled monolayers (SAMs) of nucleic acids, including DNA[9–16] and more recently peptide nucleic acid (PNA),[17,18] on gold electrodes. As a DNA analog with similar Watson-Crick base pairing but a neutral backbone,[19–24] PNA forms more compact SAMs than DNA.[25–27] Electrochemical studies of long-range charge transfer through SAMs of PNA duplexes show that charge transfer through PNA takes place through a multi-step "hopping" mechanism[25,28,29] similar to that reported for DNA.[30–37]

Often, it is not possible to determine all the observables in the above models from electrochemical measurements. To interpret the results of electrochemical experiments of nucleic acid SAMs, workers still rely on a single-step Marcus theory based analysis;[38–40] however this analysis assumes direct tunneling or single-step charge transfer from the electrode to the

electroactive reporter, an assumption that is not consistent with the multi-step hopping mechanism. In this work, a general three-step model is proposed, and it is parameterized from the results of a temperature dependence study of a typical 10-mer PNA duplex. The three-step model is then tested by application to several experiments.

2.2 THEORETICAL CONSIDERATIONS

The charge transfer rate constant can be extracted from cyclic voltammetry data; however the value of the rate constant depends on the electrochemical model used in the analysis. This section begins by reviewing the single-step non-adiabatic electron tunneling model, then proceeds to defining a more realistic kinetic scheme of long-range charge hopping, and ends by developing a simplified three-step kinetic model for the voltammetry.

2.2.1 Single-Step Approximation

In the single step approximation, the electron transfer between an electroactive reporter, e.g. ferrocene (Fc), and an electrode through the self-assembled monolayer (SAM) can be represented by Equation 2.1:

$$\text{Electrode} \underset{k^{red}}{\overset{k^{ox}}{\rightleftharpoons}} \text{Fc} \qquad \textbf{Equation 2.1}$$

This approximation is appropriate if the electron transfer occurs by direct superexchange (e.g., the process k_{SE} in Figure 2.1A is the dominant pathway). The rate law for the formation of ferrocenium (oxidized ferrocene) may be written as

$$\frac{d}{dt}P_{Fc} = k^{ox}(1 - P_{Fc}) - k^{red}P_{Fc} \qquad \textbf{Equation 2.2}$$

where P_{Fc} is the population of ferrocenium. Using a density-of-states treatment and assuming a Marcus (Gaussian) density of states,[39,41,42] the rate constant for charge transfer with the electrode can be written in as

$$k = \frac{2\pi}{\hbar}|V|^2 \frac{1}{\sqrt{4\pi\lambda k_B T}} \int_{-\infty}^{\infty} \rho(\varepsilon)\, f(\varepsilon)\, \exp\left[-\frac{(\lambda + (\varepsilon_F - \varepsilon) + e\eta)^2}{4\lambda k_B T}\right] d\varepsilon \qquad \textbf{Equation 2.3}$$

The $(\varepsilon_F - \varepsilon) + e\eta$ term corresponds to the Gibbs free energy of the reaction, where ε is the energy of an electronic state in the electrode, η is the overpotential, and ε_F is the energy of the Fermi level. $\rho(\varepsilon)$ is the density of electronic states of the electrode, $f(\varepsilon)$ is the Fermi-Dirac distribution, and *V* is the effective electronic coupling between the electrode and the redox probe states. Given that η is a function of time (*t*) and scan rate (v) in cyclic voltammetry, the rate constants for oxidation k^{ox} and reduction k^{red} depend on the time and scan rate, namely $k^{ox} = k\big(\eta(t,v)\big)$ and $k^{red} = k\big(-\eta(t,v)\big)$.

Lastly, we note that the standard heterogeneous rate constant k^0, which is defined as the rate constant at η=0 V, is given by

$$k^0 = \frac{2\pi}{\hbar}|V|^2 \frac{1}{\sqrt{4\pi\lambda k_B T}} \int_{-\infty}^{\infty} \rho(\varepsilon) f(\varepsilon) \exp\left[-\frac{\big(\lambda + (\varepsilon_F - \varepsilon)\big)^2}{4\lambda k_B T}\right] d\varepsilon \qquad \textbf{Equation 2.4}$$

By using Equation 2.2 through Equation 2.4, the cyclic voltammograms can be simulated for different k^0 values and voltage sweep rates *v*, and the potential of the faradaic current peak can be assigned. These calculations allow one to make plots of the faradaic current peak shift versus $\log(v)$ for different k^0 values. These calculated curves (or working curves) can be compared to

plots of the experimental faradaic current peak shifts versus voltage scan rate to extract a k^0 value from the experiment.[38,40,43,48]

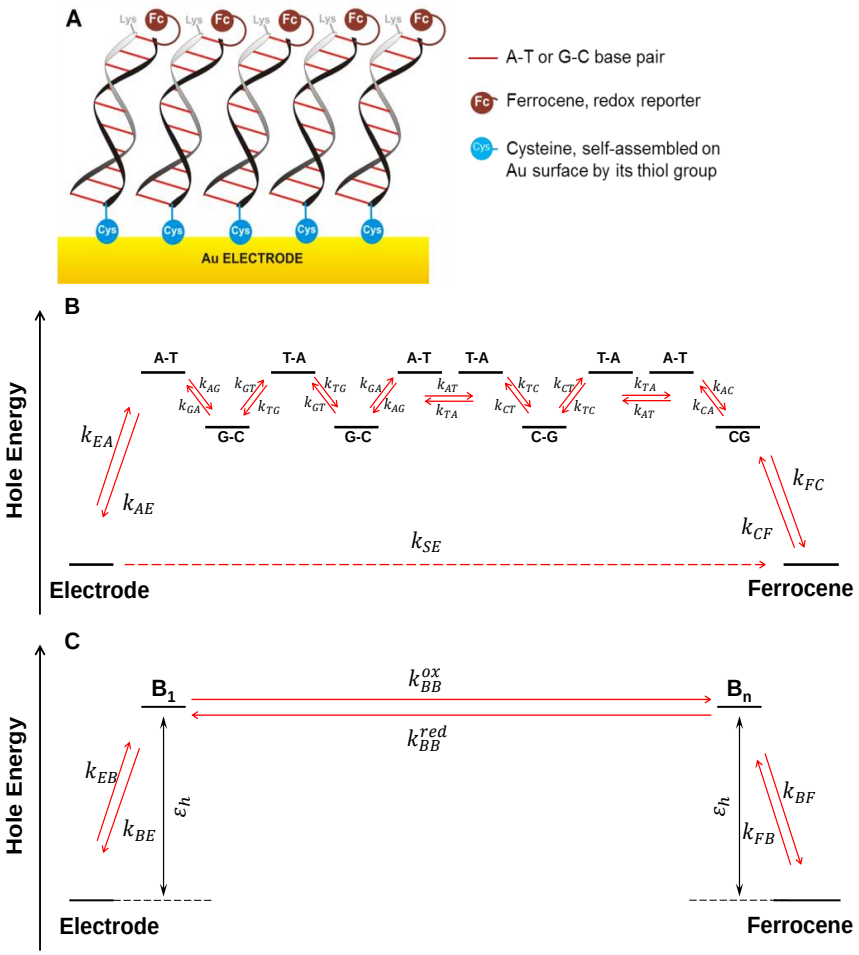

Figure 2.1. Panel A shows the structure of the SAM made of the 10-mer PNA duplex 1; 1 is Cys-TCACTAGATG-Fc:Lys-CATCTAGTGA. Panel B shows the energy levels 1. The base pair bridge energy levels are assigned based on the HOMO level of the base with the lower oxidation potential. The rate constants for nearest neighbor coupling are labeled, and k_{SE} is the rate for direct superexchange. Panel C shows the kinetic picture of the three-step model; which uses three kinetic steps: charge injection (k_{EB} and k_{BE}), charge hopping (k_{BB}^{ox} and k_{BB}^{red}), and the redox reaction of the terminal probe (k_{BF} and k_{FB}). The direct superexchange tunneling is neglected in the hopping regime. B1 and Bn are respectively the first and the last hopping site on the molecular bridge. In the model system, they do not have to represent a particular nucleobase pair of the molecular bridge, but may represent an effective site.

2.2.2 Multiple-Step Charge Transfer Process at Equilibrium

Figure 2.1B shows an energy diagram for charge transfer by incoherent hopping transport from an electrode to ferrocene through a nucleic acid duplex. The molecular oxidation levels are shown for the sequence of the 10-mer peptide nucleic acid (PNA) duplex used as a model molecule in this study (further referred to as duplex '**1**'). [44] For the oxidation reaction discussed here, the electrode is the hole donor and ferrocene is the hole acceptor. The rate constants are shown only for the nearest neighbor charge transfer pathway. It is worth noting that the actual picture is much more complicated because many non-nearest neighbor pathways can contribute to the overall charge transfer in long chains.[4,39,45] This scheme is chosen because the length dependence of charge transfer in a PNA duplex has been shown to be consistent with a sequential, superexchange-mediated, hopping mechanism.[25] To facilitate the comparison with experiments, the above picture can be simplified as suggested by Petrov *et al.*[46] That is, for a general hopping (electron or hole) process in a donor-bridge-acceptor system, one can replace the detailed scheme in Figure 2.1B with a scheme that uses a single effective energy barrier ε_h for all bridge units, and non-nearest neighbor pathways can be ignored. Different charge transfer rate constants between base pairs are replaced by a single average rate constant k_{BP}. The sum of the charge transfer rate of the hopping pathway and that of the direct superexchange pathway (k_{SE}), gives the overall charge transfer rate and its length dependence with reasonable parameters. For example, comparison of this model to photoinduced charge transfer through proline oligomers gives an ε_h of 0.2-0.4 eV.[46,47] However, in G-C and A-T base pairs, the energy difference is larger than between the units in peptide bridges and one must be careful when applying Petrov's approximation. For example, one may need to treat the charge transfer between neighboring G-C base pairs instead of any two adjacent base pairs as the elementary hopping step,[4] or use effective hopping sites instead of particular base pairs.

Even after simplification of the real system by Petrov's approximation, the kinetic scheme remains too detailed for meaningful comparison with the PNA-mediated electrochemical charge transfer rates that are measured. Specifically, the residence time of the charge on the bridge and the charge transfer rate of each elementary hopping step must be explicitly considered in this approximation. Recent bridge-only simulations[28,48,49] provide useful insights as to appropriate parameter values for PNAs, such as duplex **1**. Because the electrochemical charge transfer occurs between ground electronic states and is significantly slower than that found for photo-induced electron transfer, the residence time of charge on the bridge is not expected to be rate limiting. Hence, the rate limiting steps are likely to be the charge injection onto or off of the bridge and a more coarse grained view of the bridge will be acceptable. That is, the overall charge transfer scheme of Figure 2.1B can be simplified further to the approximate scheme in Figure 2.1C. Note that as shown later in the paper, the charge hopping on the bridge is unlikely to be a conventional rate limiting step no matter how small the absolute k_{BB} value would be. In reality, even if the k_{BB} limited hopping does exist, it is unlikely to happen within several tens of base pairs, considering soft length dependence in the hopping regime; thus we believe the model should be applicable to all current measureable systems. Also, because of the coarse grained nature of the model, it is not sensitive to the static or dynamic disorders of the film as long as the charge transfer rate is approximated homogeneous for all molecules. A strong inhomogeneity in the charge transfer rate will lead to severe broadening of the redox peaks of the cyclic voltammetry,[38] which is not observed either. If that happens in other systems, the model can be easily expanded to a linear combination of a serious of the primitive three-step models with different k_{BB} and/or other parameters which will be discussed through the whole paper.

The kinetics of the redox reaction given by the scheme shown in Figure 2.1C may be written as

$$\text{Elec} \underset{k_{BE}}{\overset{k_{EB}}{\rightleftharpoons}} \text{B}_1 \underset{k_{BB}^{red}}{\overset{k_{BB}^{ox}}{\rightleftharpoons}} \text{B}_n \underset{k_{FB}}{\overset{k_{BF}}{\rightleftharpoons}} \text{Fc} \qquad \textbf{Equation 2.5}$$

This mechanism uses three steps: charge injection with the electrode (k_{EB} and k_{BE}), an effective hole hopping rate on the bridge (k_{BB}^{ox} and k_{BB}^{red}), and the redox reaction of Fc (k_{BF} and k_{FB}). The direct superexchange tunneling from the electrode to the redox reporter (k_{SE}) is neglected because we are modeling a long PNA duplex and the direct superexchange is too slow to contribute significantly to the overall charge transfer.[a] In a tight binding description, B_1 is the bridge site that is directly coupled to the electrode, and B_n is the bridge site that is directly coupled to the ferrocene redox reporter. By comparison to the multiple-step hopping scheme (Figure 2.1B), the charge transfer rate constants k_{BB}^{ox} and k_{BB}^{red} are effective (or apparent) rate constants that replace the detailed kinetics of hopping between bridge sites, which are not directly coupled to the termini, electrode and ferrocene.[46] Similar ideas (simplifying multiple-step hopping on the bridge to an effective single step) have been proposed for photoinduced electron transfer, but have not been applied for electrochemical systems.[50]

[a] It is straightforward to add k_{SE} back by including more parameters when modeling a short duplex.

2.2.3 The Three-Step Model and Cyclic Voltammetry

2.2.3.1 Kinetic Equations of the Three-Step Model

The three step charge transfer mechanism represented by the diagram shown in Figure 2.1C and Equation 2.5 can be described by the following set of kinetic equations:

$$\frac{dP_{B1}}{dt} = k'_{EB}(1 - P_{B1})[h^+] - k'_{BE}P_{B1}[e^-] - k_{BB}^{ox}P_{B1}(1 - P_{Bn}) + k_{BB}^{red}\,P_{Bn}(1 - P_{B1})$$

$$\frac{dP_{Bn}}{dt} = k_{BB}^{ox}P_{B1}(1 - P_{Bn}) - k_{BB}^{red}P_{Bn}(1 - P_{B1}) - k_{BF}P_{Bn}(1 - P_{Fc}) + k_{FB}P_{Fc}(1 - P_{Bn}) \quad \textbf{Equation 2.6}$$

$$\frac{dP_{Fc}}{dt} = k_{BF}P_{Bn}(1 - P_{Fc}) - k_{FB}P_{Fc}(1 - P_{Bn})$$

where P_{B1}, P_{Bn}, and P_{Fc} are the normalized fractions of holes on corresponding sites, and $[h^+]$ and $[e^-]$ are the concentration of holes and electrons on the electrode. Note that the population on each of the bridge sites is usually much smaller than unity and $[h^+]$ or $[e^-]$ can be incorporated into the rate constant expression for an electrochemical process (see Equation 2.3). Hence the oxidation/reduction of B_1 is quasi-first order and the Eq. 6 can be simplified as follows:

$$\frac{dP_{B1}}{dt} = k_{EB} - k_{BE}\,P_{B1} - k_{BB}^{ox}P_{B1} + k_{BB}^{red}\,P_{Bn}$$

$$\frac{dP_{Bn}}{dt} = k_{BB}^{ox}P_{B1} - k_{BB}^{red}P_{Bn} - k_{BF}P_{Bn}\cdot(1 - P_{Fc}) + k_{FB}P_{Fc} \quad \textbf{Equation 2.7}$$

$$\frac{dP_{Fc}}{dt} = k_{BF}P_{Bn}\cdot(1 - P_{Fc}) - k_{FB}P_{Fc}$$

If all the rate constants are independent of time, this set of equations describes completely the reaction system. However, the rate constants are dependent on the potential profile through the

SAM, and it changes with time in cyclic voltammetry, as the applied potential is scanned. Thus a numerical method is needed to solve these equations and their solution is presented in the "Results and Discussion" section.

2.2.3.2 The Overall Rate Constant for Charge Transfer k_{tot}^{0}

While the single-step model uses a single rate constant k^0 to simulate the voltammograms, the three-step model uses several different rate constants to describe the overall charge transfer process. Because several rate constants are not convenient to use and can be difficult to quantify separately, it is desirable to understand how the k^0 from an analysis using the single-step model can be related to the parameters in the three-step model.

We define an effective overall rate constant k_{tot}^{0} by the rate of charge exchange with the electrode in the steady state limit. This definition reduces to the traditional one for k^0 in a single step model.[51] Thus we can numerically propagate the equations in time, at the formal potential, from the initial condition until it converges to steady state and define an (effective) overall rate constant by the condition $k_{tot}^{ox} = k_{tot}^{red} \Rightarrow k_{tot}^{0} = k_{tot}^{ox} = k_{tot}^{red}$. An apparent k_{tot}^{0} can be found by considering the "formal" rate equation for the single-step model, in which

$$\begin{aligned} \frac{dP_{Fc}}{dt} &= k_{tot}^{ox}(1 - P_{Fc}) - k_{tot}^{red}P_{Fc} \\ &= k_{tot}^{0}(1 - P_{Fc}) - k_{tot}^{0}P_{Fc} \\ &= k_{tot}^{0} - 2k_{tot}^{0}P_{Fc} \\ \Rightarrow k_{tot}^{0} &= \frac{dP_{Fc}}{dt}/(1 - 2P_{Fc}) \end{aligned}$$

Equation 2.8

where P_{Fc} (as a function of time) is obtained by way of Equation 2.7. In contrast to the cyclic voltammetry simulation, all rate constants in Equation 2.7 are held at their formal potential values.

This apparent k_{tot}^{0} is independent of time in a one-step electron transfer process, but changes with time in a multi-step process and converges to the final k_{tot}^{0} as equilibrium is approached. In the analysis below, the calculation is stopped after the time iteration at which the change in apparent k_{tot}^{0} becomes smaller than 10^{-5} s^{-1}, which is well within the precision of the experimental measurements.

2.2.3.3 Simplified Expression for k_{tot}^{0}

Besides the direct numerical simulation, an approximate analytical expression for k_{tot}^{0} can be obtained through the overall *forward* rate constant k_{tot}^{ox} for the following reaction:

$$\text{Elec} \underset{k_{BE}}{\overset{k_{EB}}{\rightleftharpoons}} \text{B}_1 \underset{k_{BB}}{\overset{k_{BB}}{\rightleftharpoons}} \text{B}_n \xrightarrow{k_{BF}} \text{Fc} \qquad \textbf{Equation 2.9}$$

Because charge hopping occurs thermo-neutrally at the formal potential (see Figure 2.1C), we have made the approximation that $k_{BB}^{ox} \sim k_{BB}^{red} = k_{BB}$. The overall rate constant for ferrocene oxidation is given by

$$k_{tot}^{ox} \equiv \frac{dP_{Fc}}{dt} = k_{BF} P_{Bn} \qquad \textbf{Equation 2.10}$$

and at steady-state,

$$0 = \frac{dP_{B1}}{dt} = k_{EB} \cdot 1 - k_{BE}\, P_{B1} - k_{BB} P_{B1} + k_{BB} P_{Bn}$$

$$0 = \frac{dP_{Bn}}{dt} = k_{BB} P_{B1} - k_{BB} P_{Bn} - k_{BF} P_{Bn} \qquad \textbf{Equation 2.11}$$

Solving these equations leads to

$$k_{tot}^{0} = k_{tot}^{ox} = \frac{k_{EB}}{\frac{k_{BE}}{k_{BB}} + \frac{k_{BE}}{k_{BF}} + 1} \qquad \textbf{Equation 2.12}$$

Because charge transfer from the bridge to the electrode and to the ferrocene is exergonic and because the hopping occurs thermoneutrally and proceeds through multiple sites,[46] one expects that $k_{BE} \gg k_{BB}$ and $k_{BF} \gg k_{BB}$. In these limits k_{BE}/k_{BB} is the dominant term in the denominator of Equation 2.12, and k_{tot}^0 can be approximated as:

$$k_{tot}^0 \approx \frac{k_{EB}}{k_{BE}} \cdot k_{BB} \qquad \textbf{Equation 2.13}$$

As the charge injection from the electrode and from the ferrocene are symmetric at the formal potential, as shown in Figure 2.1C, k_{tot}^0 becomes

$$k_{tot}^0 = k_{tot}^{red} \approx \frac{k_{FB}}{\frac{k_{BF}}{k_{BB}} + \frac{k_{BF}}{k_{BE}} + 1} \approx \frac{k_{FB}}{k_{BF}} \cdot k_{BB} \qquad \textbf{Equation 2.14}$$

Although Equation 2.13 and Equation 2.14 may appear different, they take the same form when the effective barrier ε_h is used. At electrochemical equilibrium, the principle of detailed balance requires that:

$$k_{EB} \cdot P_{Elec} = k_{BE} \cdot P_{B1} \qquad \textbf{Equation 2.15}$$

Using $P_{B1}/P_{Elec} \propto \exp(-\varepsilon_h/k_B T)$, we find that

$$k_{tot}^0 \propto \exp\left(-\frac{\varepsilon_h}{k_B T}\right) \cdot k_{BB} \qquad \textbf{Equation 2.16}$$

Aside from a constant, Equation 2.16 shows that the absolute value of k_{tot}^0 is determined by two parameters, the electrode-bridge energy barrier ε_h and k_{BB}. A charge hopping process that can be described by Equation 2.16 will be called in the "normal" hopping regime because the overall charge transfer rate is proportional to the charge hopping rate on the molecular bridge.

Note that Equation 2.16 only holds if $k_{BE} \gg k_{BB}$ and $k_{BF} \gg k_{BB}$. In the case that k_{BE} is the smallest among the three rate constants, Equation 2.12 reduces to

$$k_{tot}^{0} \approx k_{EB} \qquad \textbf{Equation 2.17}$$

and the overall reaction is *charge-injection limited* and becomes independent of the charge hopping rate on the molecular bridge.

If k_{BF} is the smallest, Equation 2.12 reduces to

$$k_{tot}^{0} \approx \frac{k_{BF}}{k_{BE}} \cdot k_{EB} = \frac{k_{EB}}{k_{BE}} \cdot k_{BF} \qquad \textbf{Equation 2.18}$$

In the derivation of Equation 2.16 we have shown that $\frac{k_{EB}}{k_{BE}} = \frac{k_{FB}}{k_{BF}}$. Inserting this result into Equation 2.18, we find that

$$k_{tot}^{0} \approx k_{FB} \qquad \textbf{Equation 2.19}$$

and the overall reaction is *redox reporter limited*. The same conclusion can be drawn directly from Equation 2.14 as well; see Supporting Information for a detailed discussion of the transition from k_{BB} independent region to k_{BB} depenent regions.

As we will show in the last part of the discussion section, charge transfer through the duplex **1** is not charge injection or redox reporter limited; the more general result (Eq. 2.12 or 2.14) will be used in further discussion regarding duplex **1**. Note the steady-state approximation used to obtain Equation 2.12 requires small change in the hole population on the bridge, which means the hopping site should not be oxidized drastically before the completed oxidation of ferrocene. This requirement can be tested in cyclic voltammetry easily because a large change in the hole population will result in additional peaks or distortion of the ferrocene peak. The three-step model should apply as long as no such distortion is observed. Since there are indeed no additional peaks or distortion for duplex **1** (*vide infra*), it is expected that model should be applicable within the range of at least several tens of base pairs because of the soft length dependence of charge hopping.

2.3 RESULTS AND DISCUSSION

2.3.1 Numerical Simulations of Cyclic Voltammograms

2.3.1.1 Potential Drop in Hopping

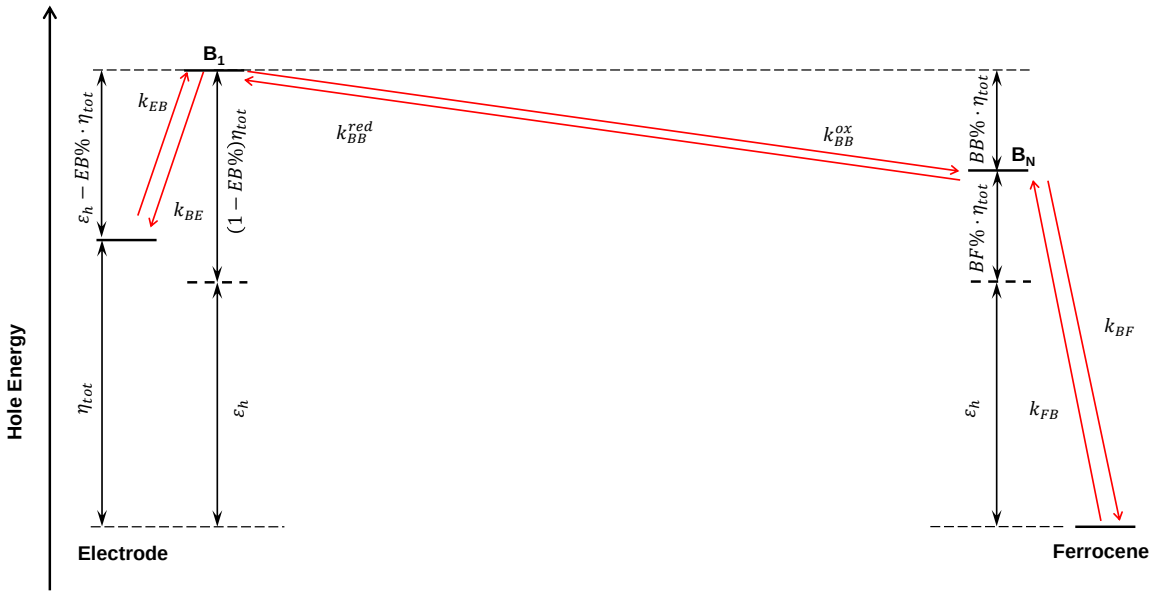

Figure 2.2. The energy diagram for the three step model shown here is similar to that shown in Figure 2.1C, but it includes an applied overpotential η_{tot}. The parameters $EB\%$, $BF\%$, and $BB\%$ are introduced to account for a variable potential drop through the SAM (see text for more details).

Because the potential profile of the electrode-bridge-ferrocene system[52] and consequently the overpotential at each of the sites B_1, B_n, and Fc, is not known, the time evolution and the kinetic rates between these sites, which are required for simulating the voltammograms, are not known either. One only knows the value of the overall bias, or total overpotential η_{tot} relative to the formal potential of ferrocene. Although a few theoretical and experimental studies have addressed this issue,[53–59] it is not yet clear how to realistically model the applied potential drops through a SAM assembly. To simulate the voltammograms, we introduce three new parameters that

correspond to the contributions of local potential drops (change in the energy of the Fermi level of the electrode and the energy of sites B_1 and B_n when out of equilibrium) to the total potential drop across the interface (equal to η_{tot}); see Figure 2.2. $EB\%$ is the percentage of the potential drop at the electrode-bridge interface; $BB\%$ is the percentage of the potential drop across the bridge itself; and $BF\%$ corresponds to the potential drop at the bridge-ferrocene interface. Equation 2.20 is the constraint applied to the three parameters:

$$EB\% + BB\% + BF\% = 100\% \qquad \textbf{Equation 2.20}$$

If values for these parameters are known, the overpotential for each step in the kinetic model is defined, and the Marcus theory can be applied. Some evidence indicates that the potential drop occurs over the whole charge transfer pathway for insulating films such as alkyl monolayers.[1] However, a π-stack structure is presumed to be more 'conductive' than alkyl chains, and it may be the most 'conductive' part along the charge transfer pathway (*i.e.,* the hopping rates are assumed to be much faster than the injection rates, *vide supra*). Thus $BB\%$ is taken to be the smallest. Another important constraint is that the oxidation and reduction waves are often found to be symmetric, or nearly so, in the experiments. Thus, the relative magnitudes of $BB\%$, $EB\%$, and $BF\%$ were adjusted to generate the most symmetric voltammograms.

2.3.1.2 Comparison of Simulated Voltammograms Based on Single-Step and Three-Step Models

Because the long range charge transfer through nucleic acids is widely studied, we have adapted parameters from those studies[60,61] and from earlier peptide nucleic acid (PNA) experiments[25] to simulate voltammograms and to compare the three-step model with the traditional single-step model. The numerical simulations were performed using MATLAB. Based on earlier studies of

ferrocene-terminated SAMs of alkanethiols[29,39] and the findings for the ferrocene-terminated undecanethiol (C11) SAMs reported here (*vide infra*), the reorganization energy λ was set to 0.8 eV for the ferrocene oxidation in both the single-step and the three-step model. For the single-step model only the parameter k^0 remained to be adjusted; whereas for the three-step model, the energy barrier ε_h, the site-to-site hopping rate constant k_{BB}, and the potential drop profile were adjusted. For each model voltammograms were simulated and compared with the experimental data (*vide infra*). For the molecular bridge sites in the three-step model, the effective energy difference between the ferrocene and the bridge state, ε_h, was chosen to be 0.24 eV, by systematically comparing the experimental temperature dependence of k_{tot}^0(*vide infra*) and the simulated one. Once ε_h was chosen, the rate constant for the site-to-site hopping constant, k_{BB}, was adjusted to obtain a good agreement between the calculated k_{tot}^0 and the apparent charge transfer rate from experiment. It is found that if the k_{BB} value is $1.5 \times 10^3 s^{-1}$, then k_{tot}^0 is 0.23 s^{-1}, which is similar to the k^0 values found for duplex **1** when a single-step model is used. The value of k_{BB} is also consistent with literature reports for similar systems.[32,50,62,63] The potential drop parameters $BB\% = 5\%$, $EB\% = 20\%$, and $BF\% = 75\%$ generated the highest symmetry for the simulated voltammograms.

With the parameter values given above, cyclic voltammograms for ferrocene were simulated. Figure 2.3A shows the simulations obtained using the three-step model. Note that the simulated peak shifts and peak heights are not totally symmetric as seen most clearly in the trumpet plot in the lower panel of the figure. In addition, single-step (Equation 2.2) simulations were performed to reproduce the oxidation peak shift (panel B) and the reduction peak shift (panel C) of the trumpet plot in panel A for the three-step simulation. The k^0 values for the single step simulations, 0.13 s^{-1} for the oxidation and 0.28 s^{-1} for the reduction, differ significantly from the

0.24 s^{-1} value that is used in the three-step model simulation; however the average of the two rate constants, 0.21 s^{-1}, differs from it by only $\approx 10\%$. The difference between the oxidation and reduction peak shifts arise from using different charge injection rates at the electrode-bridge interface (r_{inj}^{ox}) and the ferrocene-bridge interface (r_{inj}^{red}). These results indicate that the single-step analysis (used to find k^0) provides a reasonable approximation for the overall rate (k_{tot}^0) in the multi-step charge transfer process, considering current experimental precision; however, the use of the single-step model masks some important features of the process, *vide infra*.

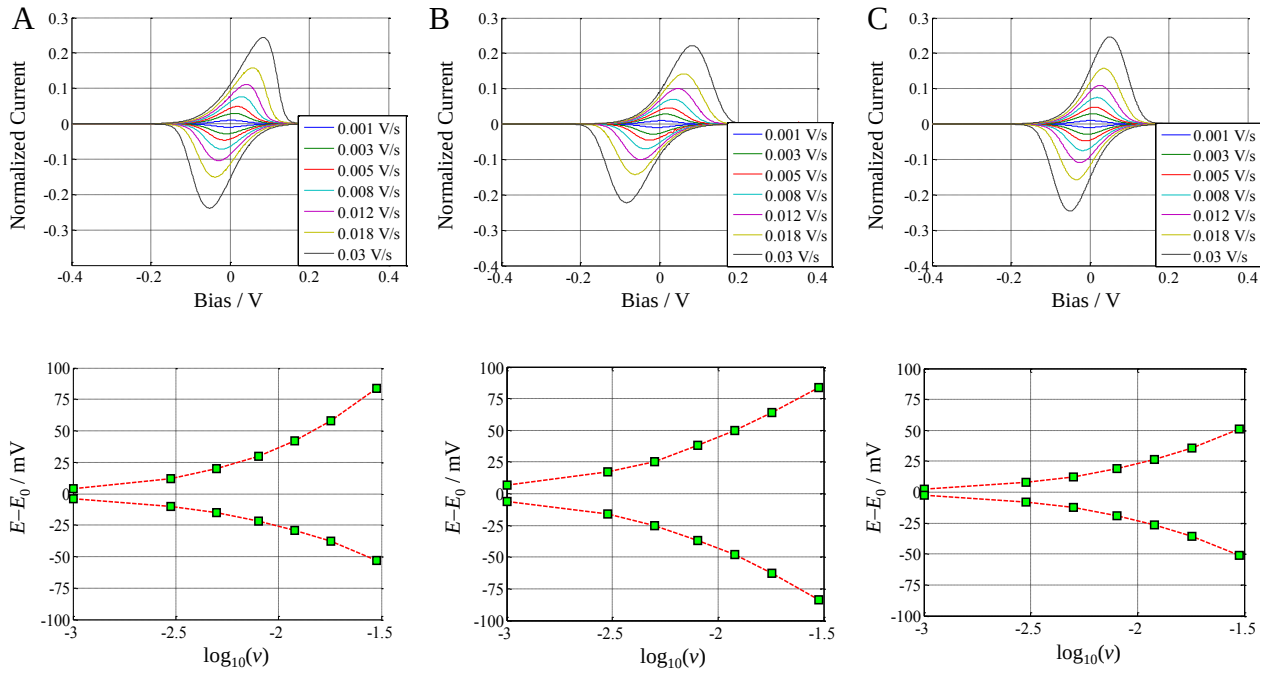

Figure 2.3. Simulated voltammograms and peak shifts from the formal potential E_0 are shown as a function of the potential scan rate. A) These simulations are for the three-step model with $\varepsilon_h = 0.24$ eV , $BB\% = 5\%$, $BB\% = 5\%$ and $BF\% = 75\%$, and $k_{tot}^0 = 0.23$ s^{-1}. In panel B) the simulations use the single-step model with a lower limit of k^0 (0.13 s^{-1}), and in panel C they use the single-step model with an upper limit of k^0 (0.28 s^{-1}); see text for details T is taken to be 298 K.

2.3.2 Electrochemistry Results

2.3.2.1 Cyclic Voltammetry Measurements

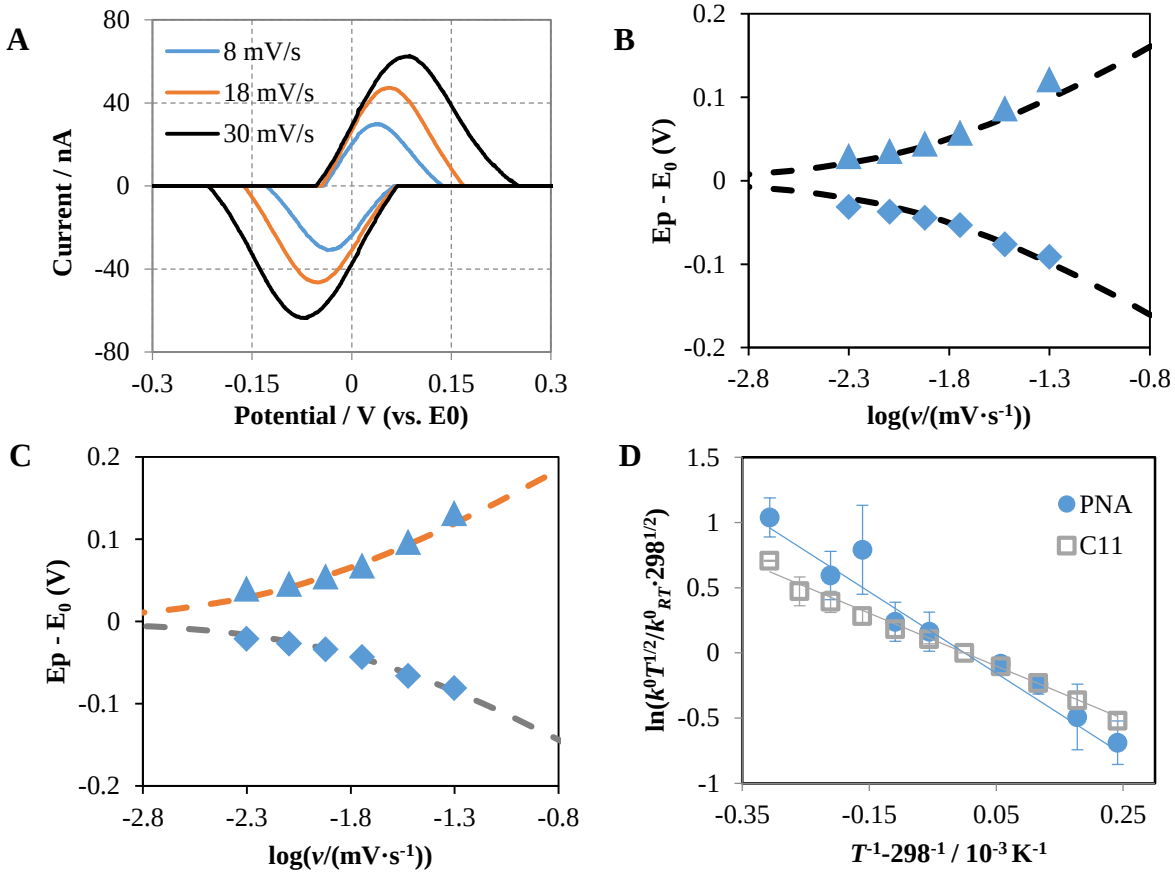

Figure 2.4. Panel A: Typical cyclic voltammgrams of the PNA duplex 1 (background substracted) are shown for a temperature of 298K. The asymmetry of the anodic and cathodic current, e.g. the currents at formal potential, can be observed. Panel B: k^0 was found to be 0.15 s^{-1} by using a fit of both the anodic and cathodic peak shifts with a single rate constant. Panel C: If the oxidation and reduction peak shifts are treated seperately, the k^0 that is extracted from the shift of oxidation peaks is 0.10 s^{-1} and the k^0 that is extracted from the shift of reduction peaks is 0.20 s^{-1}. Panel D: The temperature dependence of k^0 for ferrocene tethered to SAMs of the PNA duplex 1 and C11 alkanes are plotted for comparison. The k^0s were obtained from the best fit to a single rate constant and normalized to the rate constant k^0_{RT} at room temperature (298 K).

Cyclic voltammetry measurements at different temperatures were performed to determine the temperature dependence of the electrochemical rate constant through SAMs of the 10-bp PNA duplex **1** and of an alkane (C11). The observed redox potential of the ferrocene is the same for the two different bridges, however the cyclic voltammograms of the PNA duplex **1** showed an asymmetry (see Figure 2.4A). Figure 2.4B shows a fit of the data with a single $k^0 = 0.15\ s^{-1}$, however the fitting is improved if different rate constants are used for the shifts of the oxidation ($0.1\ s^{-1}$) and reduction peaks ($0.2\ s^{-1}$) – see Figure 2.4C. The average of the oxidation and reduction rate constants from the fit in Figure 2.4C coincides with the k^0 obtained in Figure 2.4B. Note that the asymmetry, whi ch is apparent for the trumpet plot of 1, is not observed for the case of the C11 SAM.

Figure 2.4D plots the logarithm of the electron transfer rate constants k^0 versus 1/T for both 1 and C11 SAMs. A linear least squares fit to the $\ln\left(k^0 \cdot \sqrt{T}/k^0_{RT} \cdot \sqrt{298}\right)$ as a function of T^{-1} was performed to extract the apparent reorganization energy:

$$\ln\left(\frac{k^0 \cdot \sqrt{T}}{k^0_{RT} \cdot \sqrt{298}}\right) = -\frac{\lambda}{4k_B} \cdot \left(\frac{1}{T} - \frac{1}{298}\right) \qquad \textbf{Equation 2.21}$$

The temperature dependence for the C11 SAM is softer than that of the 10-bp PNA. Using a Marcus model and assuming that the temperature dependence arises solely from the reorganization energy, a best fit is obtained for C11 with a λ value of 0.80 eV, in agreement with other work,[29,39] and for the 10-bp PNA with a λ of 1.1 eV. The detailed differences in the SAMs is unlikely to cause such a large difference in the reorganization energy of the ferrocene, hence the three-step model was fit to the experimental temperature dependence with λ constrained to be 0.80 eV.

2.3.2.2 Obtaining ε_h from the temperature dependence of k^0

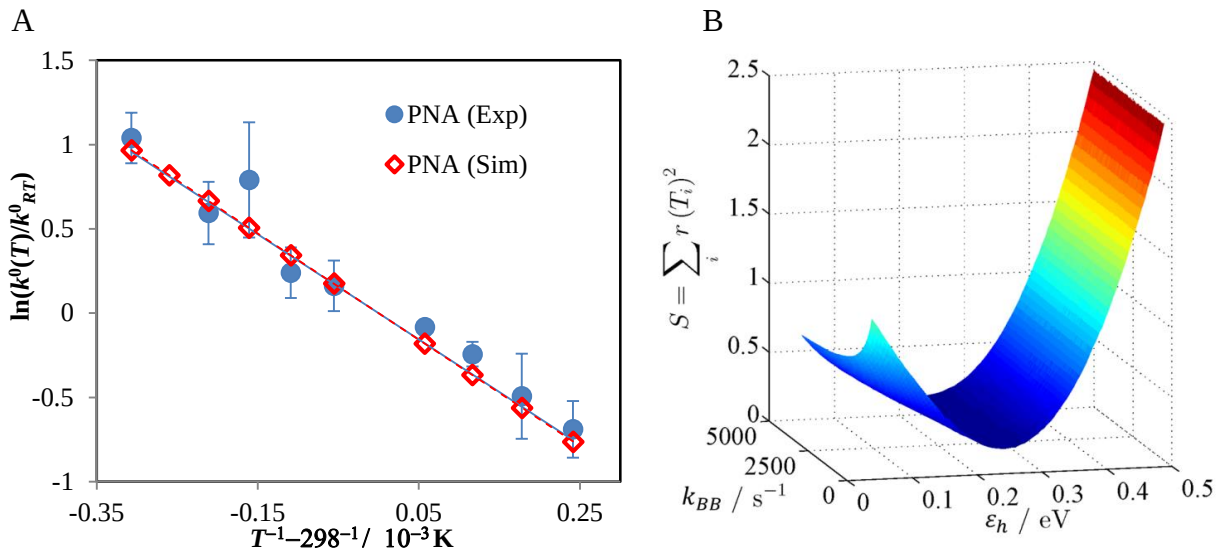

Figure 2.5. Panel A shows the dependence of the standard electrochemical rate constant k^0 on the temperature for the experimental PNA data and for the three-step simulation; the k^0 values are normalized to k^0_{RT}. Panel B shows a two-dimensional plot for the goodness-of-fit; the two significat parameters are the effective charge injection barrier ε_h, and the charge transfer rate across the bridge k_{BB}.

The temperature dependence of the electrochemical rate constant k^0 for the PNA duplex **1** was simulated by the three-step model to extract the energy barrier ε_h. As shown in Equation 2.16, the overall rate constant k^0_{tot} mainly depends on k_{BB} and ε_h. Because the temperature induced change of k_{BB} and the effect of ε_h cannot be distinguished in current electrochemical experiments, all of the temperature dependence was assumed to arise from ε_h and k_{BB} was taken to be temperature independent in the simulation.[a] Figure 2.5A shows a plot of the experimental rate constant observed for the duplex **1** with that found from the simulations by Equation 2.8 using the same parameters as for the voltammograms in Figure 2.3. The good agreement between the simulation

[a] The dependence of k^0_{tot} on k_{BB} is somewhat weaker than that implied by the approximate expression Equation 2.16; see the Supplemental Information for a discussion.

and the experiment reveals that the activation energy can be explained in terms of the three-step model and its effective energy barrier ε_h. The best fit curve that is shown in Figure 2.5A has an ε_h of 0.24 eV. Figure 2.5B shows a plot of how the goodness of fit, $\sum_i [k_{tot}^0(T_i) - k^0(T_i)]^2$, depends on the two parameters k_{BB} and ε_h. This plot shows that the best agreement between the simulated results and the PNA data are found for $\varepsilon_h \approx 0.24$ eV, and it is not very sensitive to k_{BB} in the tested range.

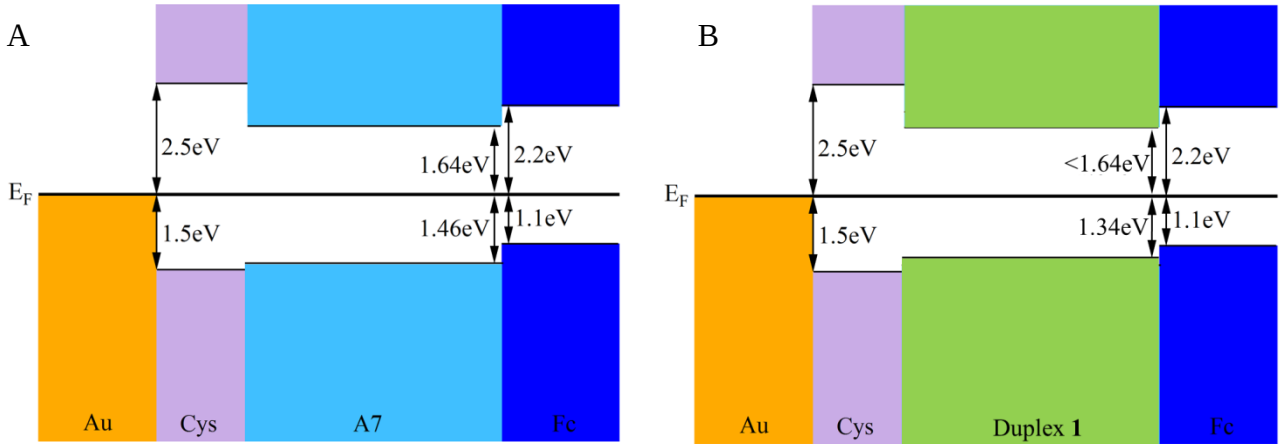

Figure 2.6. Panel A shows an energy diagram for the molecular levels of Cys-A7-Fc. The energy barrier is calculated from the HOMO of A7 (1.46 eV) and the HOMO of ferrocene (1.1 eV). Panel B shows an energy diagram that may be appropriate for duplex 1 based on our knowledge from electrochemical experiments.

The charge injection barrier of 0.24 eV is consistent with the 0.36 eV energy offset between the HOMO of ferrocene and that of adenine, recently reported by Schlaf and coworkers[64] for single-strand Cys-A7-Fc (see Figure 2.6A). Figure 2.6B shows a sketch of what the energy profile might look like for the duplex, assuming that the Au, cysteine, and ferrocene offsets are at the same place as that in Panel A. The duplex nucleotide energies are taken to lie at 1.34 eV. Note that the energy levels in the ferrocene modified PNA bridges lay closer to gold Fermi level than the levels in ferrocene-free PNAs.[64] For duplex **1**, several effects may cause the actual energy barrier to be lower than the 0.36 eV value found for Cys-A7-Fc. First, the guanines in duplex **1** have a

much lower oxidation level (and thus higher HOMO energy) than adenine and thymine,[44] which should lower the effective barrier. Second, the formation of base pairs and the enhanced π-stack in duplexes may facilitate some delocalization of the HOMOs and further reduce the effective energy barrier. Lastly, the broadening of molecular levels by thermal fluctuation and other factors could play a role in determining the energy offsets.[48,49] Although a quantitative analysis is not possible at this time, the small upper limit that is set on the energy barrier by the photoemission measurements is consistent with the ε_h value extracted from the electrochemical data.

2.3.3 PNA Linkage/Bridge Scheme and Kinetic Terms of the Model

The rate constant k_{tot}^0 has contributions from the elementary steps of charge injection to the bridge, charge hopping along the bridge, and the oxidation of the redox probe. Here we use chemical changes of the PNA duplex **1** and its terminal groups (e.g. linker between the duplex and the gold electrode, or redox probe) to vary these elementary steps. While it is not rigorously possible to adjust them independently in this way, a judicious choice of which groups to change can make it approximately so. Table 2.1 shows k_{tot}^0 values for different PNA duplexes used to test the predictions of the three-step model.

Table 2.1. k^0 and surface coverages for PNA SAMs with different linkage/bridge schemes at room temperature.

Linker-PNA Sequence-Redox Probe	k^0 / s^{-1}	Coverage (pmol/cm^{-2})
Cys-PNA(TA)-Fc (duplex **1**)	0.23 ± 0.10	42 ± 15
Sec-PNA(TA)-Fc (see SI)	0.18 ± 0.05	16 ± 3
Cys-PNA(CA)-Fc[65]	0.05 ± 0.02	52 ± 33
Cys-Ala-PNA(TA)-Fc (see SI)	0.13 ± 0.04	30 ± 10

In the previous discussion, we have assumed that the charge transfer in duplex **1** is in the "normal" hopping regime, *i.e.*, $k_{BE} \gg k_{BB}$, $k_{BF} \gg k_{BB}$, and that Equation 2.16 holds. These

assumptions were tested experimentally. First, a selenocysteine (Sec) was used to replace cysteine as the anchoring linker. The electronic coupling between the Se-Au bond is reported to be stronger than that of S-Au[66] and thus k_{BE} is expected to be higher for Sec-PNA(TA)-Fc than for duplex **1**. The use of a Se linker does not cause a dramatic boost in the overall k^0; rather the two rates are within experimental error of each other. This result implies that duplex **1** is not *charge injection limited*; see Equation 2.17. Second, the influence of the charge hopping rate was evaluated by comparing the k^0 for the fully complementary PNA duplex **1** to that for the PNA duplex with a single CA base pair mismatch (Cys-PNA(CA)-Fc). In these duplexes, both systems are attached to the gold electrode through a cysteine linker, and they have similar coverages on the electrode. The comparison shows that the overall rate of the charge transfer is affected strongly by the disruption of the base pair stacking, and the experimental k^0 value is five times higher for the fully complementary sequence. This result implies that the rate constant expression for duplex **1** should have a form in which k_{BB} plays a role; i.e., Equation 2.16.

To explore further the *charge injection limited* regime, the duplex Cys-Ala-PNA(TA)-Fc was synthesized, in which an alanine spacer is inserted between the cysteine and the duplex, k^0 is a factor of two smaller than for **1.** Because k_{tot}^0 in Equation 2.16 does not change with k_{BE}, it may be that the additional alanine reduces k_{BE} so that it is comparable to k_{BB} and k_{tot}^0 is affected. This result suggests that the Cys-Ala-PNA(TA)-Fc may be close to the *charge injection limited* regime.

Although current data do not warrant a detailed quantitative analysis, the results show that the injection rates at the electrode-bridge interface and bridge-redox reporter interface can contribute significantly to the overall rate. The effective energy barrier is mainly determined by the bridge-redox reporter interface and the overall charge transfer rate is determined by both ε_h and k_{BB} (duplex **1**, Cys-PNA(CA)-Fc and Sec-PNA(TA)-Fc). In summary, the overall charge

transfer rate depends on the charge injection barrier at the electrode bridge interface, the hopping rate through the bridge, and the oxidation/reduction of the redox probe to varying degrees, and it can be manipulated by the functional design of the studied molecules.

2.3.4 Comparison with Photoinduced Charge Transfer Rates

Another fact that can be explained by the three-step model is the difference between the absolute charge transfer rates measured in photoinduced charge transfer and those measured in electrochemical experiments. The absolute values of the charge transfer rates for DNA bridges have been measured by a number of different groups[67] using spectroscopic methods. The spectroscopic rate constant k_{tot}^{0} is usually about 10^3 to 10^5 times larger than those reported for PNA molecules by electrochemistry,[29] even though both of the mechanisms are believed to be charge hopping through π-stacks. It seems unlikely that the detailed differences in the structures themselves can lead to such a large difference. The difference does not seem to arise from the reaction free energy $\Delta_r G$ either, because the difference can still be observed when the hopping sites are all the same (thus the $\Delta_r G$ (hopping) is usually taken as zero).[67,68] In fact, the main difference between the spectroscopic and electrochemical experiments is that the spectroscopic experiments[32,37,63,67,68] have no electrodes and the photoinduced charge injection step is very fast, causing the overall reaction to be k_{BB} limited. Therefore the photoinduced electron transfer rate at $\Delta_r G = 0$ is mainly k_{BB}; not k_{tot}^{0} as in electrochemical experiments. In contrast, Equation 2.16 shows that k_{tot}^{0} depends strongly on ε_h for the electrochemical rate. At room temperature, ε_h is about 8~10 times larger than $k_B T$, leading to the result that k_{BB} is about $10^3 \sim 10^4$ times larger than k_{tot}^{0}, which can account for most of the difference in the two types of measurements.

2.4 CONCLUSIONS

In this work, the multi-step charge hopping through PNA SAMs was examined and a new three-step phenomenological model was developed to simulate the charge transfer process and interpret the electrochemical measurements. A temperature dependence study of a 10-basepair PNA duplex was performed and compared with the predictions of the three-step model. The importance of the energy barriers between the molecular bridge and the electrochemical reporter was revealed by applying the three-step model to the experimental results. An injection barrier of 0.24 eV was extracted by comparing the simulation with the experimental data, and it is in reasonable agreement with the results from photoelectron spectroscopy. Although designed for electrochemical measurements, the model may be used in a broader context such as comparing electrochemical data with spectroscopic results.

2.5 EXPERIMENTAL METHODS

2.5.1 Electrochemical Measurements

2.5.1.1 Electrode Preparation

A gold wire (0.5 mm diameter, 99.999%, Alfa Aesar, MA) was cleaned by immersion in "piranha" solution (1:3 H_2O_2 and 98% H_2SO_4) for at least 30 min and then washed with deionized water (>18 MΩ · cm). (*CAUTION! The piranha solution is a very strong oxidizing agent and extremely dangerous. Eye protection and gloves should be used during handling.*) The wire was sealed in a soft-glass capillary tube with the tip exposed. The tip of the gold wire was heated to form a ball.

The gold ball was reheated in a flame until glowing, then slowly cooled, and finally quenched in deionized water. This annealing process was repeated more than fifteen times until a smooth ball electrode was obtained. The area of the electrode was determined electrochemically[69] and found to be typically ~0.1 cm^2.

2.5.1.2 Preparation of Self-Assembled Monolayers

SAMs of PNA were prepared by incubating gold ball electrodes in 300 μL of a 20 μM ds-PNA solution for 40 h at 27 °C.[33-35] After incubation, the gold electrodes were washed with deionized water and directly used in the electrochemical studies.

SAMs of $Fc(CH_2)_{11}SH$ were prepared by incubating gold ball electrodes in 500 μL of an ethanol solution of $Fc(CH_2)_{11}SH$ and $CH_3(CH_2)_9SH$ for 24 h at 27 °C. The total thiol concentration was 1 mM and the mole ratio of $Fc(CH_2)_{11}SH$ to $CH_3(CH_2)_9SH$ was 1 to 9. After the initial incubation, the electrodes were rinsed with ethanol and transferred to 1mM $CH_3(CH_2)_9SH$ ethanol solution for another 24 h to remove weakly bounded $Fc(CH_2)_{11}SH$. The electrodes were then removed from the incubation solution, washed sequentially with ethanol and deionized water and directly used in the electrochemical studies.

2.5.1.3 Cyclic Voltammetry

Cyclic voltammetry was carried out with a CH Instrument Electrochemical Analyzer 430 (Austin, TX). The three-electrode electrochemical cell consisted of an Ag/AgCl (1 M KCl) reference electrode, a platinum wire as a counter electrode, and a SAM-coated gold ball electrode as the working electrode. All experiments were performed in a 1 M $NaClO_4$ (pH 6-7) aqueous electrolyte solution. The uncompensated solution resistance of a similar system was measured by AC impedance and found to be less than 5 Ω, so that the iR drop was not important for the

measurements. The coverage of the PNA ferrocene SAM was calculated by integrating the charge under the voltammetric peaks. k^0 was obtained by fitting the peaks shifts with working curves from the traditional single step model.[29,38]

The whole electrochemical cell was placed in a water jacket. The temperature was monitored by an Omega 44006 thermistor (precision $\pm$0.2 K), which was sealed in a Teflon cap and inserted into the solution beside the electrodes, and it was adjusted by a circulating water Endocal RTE-4 refrigerated circulating bath system. Measurements were performed at 298K first, then the system was heated or cooled and the measurements were carried out after the system stabilized at the desired temperature. The temperatures were controlled to be within a precision of $\pm$0.5 K.

2.6 SUPPORTING INFORMATION

2.6.1 PNA Synthesis and Characterization

The A, G, C, and T PNA monomers were purchased from ASM Research Chemicals and were used without further purification. The Tpy PNA monomer was synthesized by a previously published method.[70] All other reagents were commercially available, analytical grade quality, and used without further purification. PNA was manually synthesized by solid phase peptide synthesis using the Boc-protection strategy, as previously described.[71] The PNA was cleaved off the resin, ether precipitated, dried, dissolved in water, and purified by reverse phase HPLC on a Symmetry C18 300 5 μm 4.6 mm × 250 mm column. A 30 min linear gradient from 0.1% TFA in water to acetonitrile at 1 mL/min was used for elution. The PNA absorbance was monitored at 260 nm with

a Waters 2996 Photodiode Array Detector. Collected fractions were characterized on an Applied Biosystems Voyager Biospectrometry Workstation with Delayed Extraction (Applied Biosystems, Foster City, CA) using an R-cyano-4-hydroxycinnamic acid matrix (10 mg/mL in 1:1 water/acetonitrile, 0.1% TFA). The fractions with correct molecular weight were lyophilized and then resuspended in water. The concentration of PNA oligomers in water was determined by UV absorption at 90°C using the sum of the extinction coefficients of the constituent PNA monomers at 260 nm taken from the literature. ε_{260} used in the calculation of the PNA concentration were 8600 $M^{-1}cm^{-1}$ for T, 6600 8600 $M^{-1}cm^{-1}$ for C, 13700 $M^{-1}cm^{-1}$ for A, and 11700 $M^{-1}cm^{-1}$ for G.[72] The extinction coefficient for the Tpy monomer at 260 nm was 9750 $M^{-1}cm^{-1}$. [70]

Table 2.2. PNA sequences and molecular masses.

PNA sequence	**calculated *m/z***	**experimental *m/z***
Cys-TCACTAGATG-Fc	3043	3044
Lys-CATCTAGTGA	2855	2856
Sec-TCACTAGATG-Fc	3088.7	3087.5
Cys-Ala-TCACTAGATG-Fc	3113	3113

2.6.2 The effect of k_{BB} on k_{tot}^0

The approximate expression, Equation 2.16, overstates the dependence of k_{tot}^0 on k_{BB}, which is more rigorously found by numerical solution of the following equation (Equation 2.8 in the manuscript):

$$\frac{dP_{Fc}}{dt} = k_{tot}^{ox}(1 - P_{Fc}) - k_{tot}^{red}P_{Fc}$$

$$= k_{tot}^{0}(1 - P_{Fc}) - k_{tot}^{0}P_{Fc}$$

$$= k_{tot}^{0} - 2k_{tot}^{0}P_{Fc}$$

$$\Rightarrow k_{tot}^{0} = \frac{dP_{Fc}}{dt}/(1 - 2P_{Fc})$$

Equation 2.22

For the calculations shown in Figure 2.7, we set k_{BF} to be 4000 and varied k_{BB} from 0 to 5000; these values are similar to that found for duplex **1** is in the normal hopping regime. P_{Fc} (as a function of time) was obtained by numerical simulation of the three-step model, as described in the manuscript. As Figure 2.7A, a ten-fold change in k_{BB} from 500 to 5000 gives rise to only a factor of three change in k_{tot}^{0}. The numerical derivative of k_{tot}^{0} is also calculated and plotted in Figure 2.7B. Instead of being a constant, the derivate decreases as approaching the *redox reporter limited* region, clearly showing a sub-linear dependence of k_{tot}^{0} on k_{BB}.

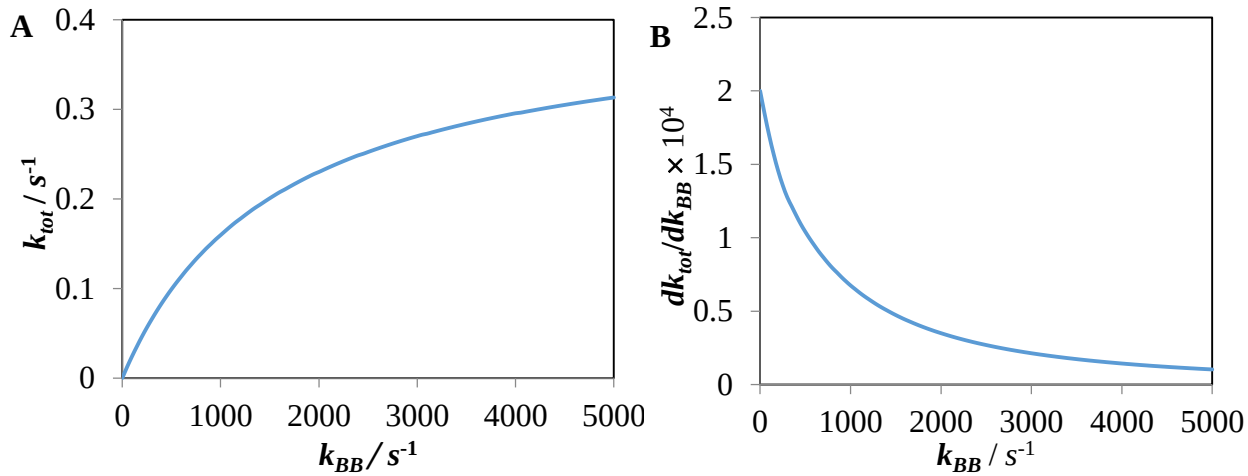

Figure 2.7. Panel A shows the simulation results of k_{tot}^{0} as a function of k_{BB}. Panel B shows the numerical derivatives of k_{tot}^{0}. Its decreasing clearly shows a sub-linear dependence of k_{tot}^{0} on k_{BB}.

A more quantitative analysis can be obtained by using the numerical derivative. Suppose k_{tot}^{0} and k_{BB} are related by a general power law $k_{tot}^{0} = A \cdot (k_{BB})^{\alpha}$, then

$$\ln k_{tot} = A + \alpha \cdot \ln k_{BB}$$ **Equation 2.23**

Take the derivative on both sides:

$$\frac{d \ln k_{tot}}{dk_{BB}} = \alpha \frac{d \ln k_{BB}}{dk_{BB}}$$ **Equation 2.24**

The expression of α is obtained as follows:

$$\alpha = \frac{k_{BB}}{k_{tot}} \cdot \frac{dk_{tot}}{dk_{BB}}$$ **Equation 2.25**

The soothed results of α calculated using Equation 2.25 are plotted in Figure 2.8A. Obviously, the linear relationship ($\alpha \approx 1$) only hold when k_{BB} is very small, see the logarithmic scale plot in Figure 2.8B. A sub-linear relationship is expected as k_{BB} increases and eventually k_{tot}^0 will become independent of k_{BB} as k_{BB} tend to infinity (i.e. $\lim_{k_{BB} \to \infty} \alpha = 0$ in the *redox reporter* or *charge-injection* limited region).

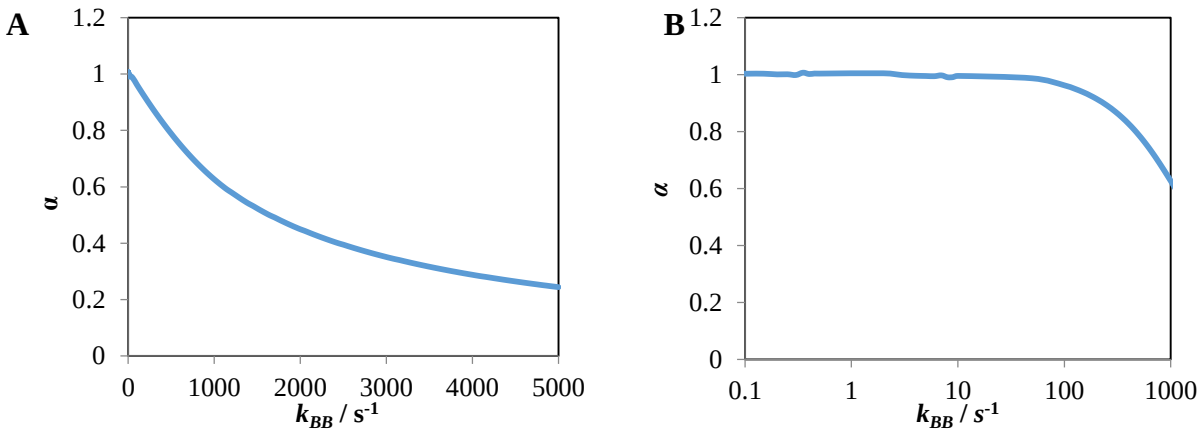

Figure 2.8. Panel A: α (defined in Equation 2.23) plotted as a function of k_{BB}. It approaches unity (linear relationship) when k_{BB} approaches 0 and approaches zero as k_{BB} tend to infinity. Panel B: Same as panel A but plotted in logarithmic scale, showing the quasi-linear relationship as $k_{BB} \to 0$.

2.6.3 Additional Cyclic Voltammograms

The cyclic voltammograms of Sec-PNA(TA)-Fc (Figure 2.9), Cys-Ala-PNA(TA)-Fc (Figure 2.10), are presented below. The SAM modified electrodes were prepared by using the same method as for duplex **1**. All measurements were performed in 1 M $NaClO_4$ (pH 6-7) aqueous electrolyte solution at room temperature.

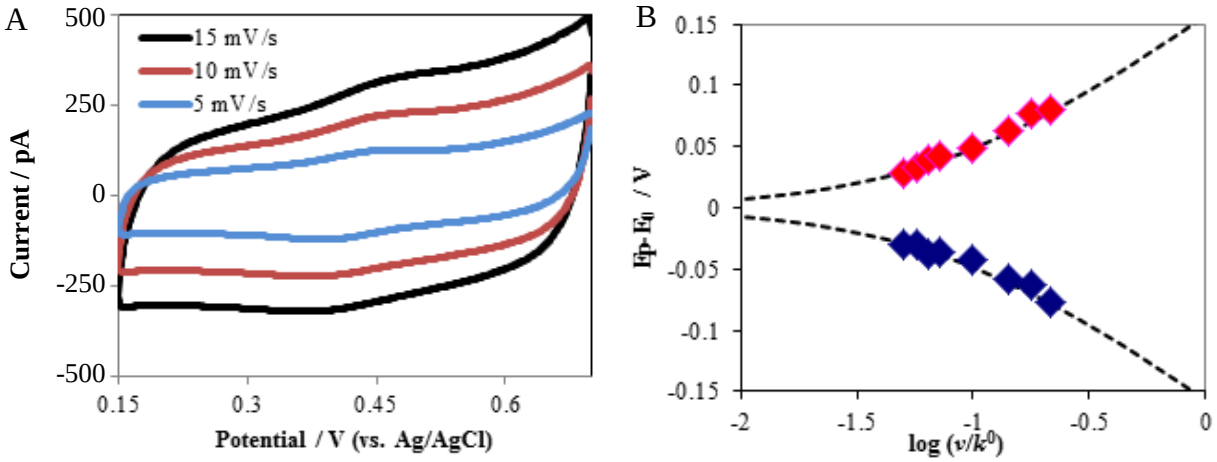

Figure 2.9. Panel A shows cyclic voltammograms for Sec-PNA(TA)-Fc at three different scan rates. Panel B shows a plot of the faradaic peak shift versus the logarithm of the voltage scan rate (scaled to k^0). The dashed curve shows a fit to the data with a $\boldsymbol{k^0}$ of $\boldsymbol{0.20\ s^{-1}}$.

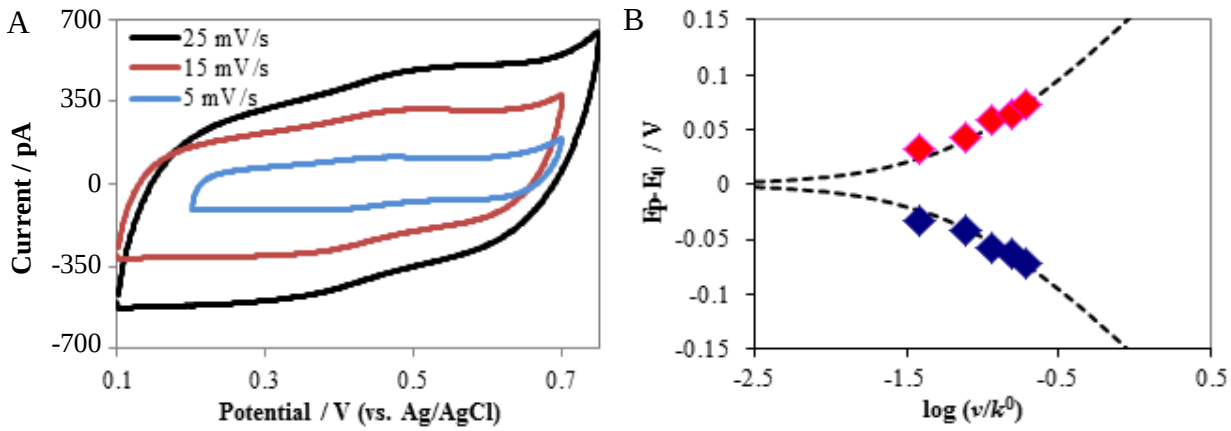

Figure 2.10. Panel A shows cyclic voltammograms for Cys-Ala-PNA(TA)-Fc at three different scan rates. Panel B shows a plot of the faradaic peak shift versus the logarithm of the voltage scan rate (scaled to k^0). The dashed curve shows a fit to the data with a k^0 of 0.13 s^{-1}.

2.7 REFERENCES

(1) Bar-Haim, A.; Klafter, J. *J. Chem. Phys.* **1998**, *109*, 5187.

(2) Wang, X.; Nau, W. M. *ChemPhysChem* **2001**, *2*, 761.

(3) Giese, B. In *Longe-Range Charge Transfer in DNA I*; 2004; pp. 27–44.

(4) Berlin, Y. A.; Burin, A. L.; Ratner, M. A. *Chem. Phys.* **2002**, *275*, 61.

(5) Conwell, E. *Top. Curr. Chem.* **2004**, *237*, 73.

(6) Genereux, J. C.; Barton, J. K. *Chem. Rev.* **2010**, *110*, 1642.

(7) Berlin, Y. A.; Kurnikov, I. V.; Beratan, D.; Ratner, M. A.; Burin, A. L. *Top. Curr. Chem.* **2004**, *237*, 1.

(8) Kubař, T.; Elstner, M. *Phys. Chem. Chem. Phys.* **2013**, *15*, 5794.

(9) Casero, E.; Darder, M.; Díaz, D. J.; Pariente, F.; Martín-Gago, J. a.; Abruña, H.; Lorenzo, E. *Langmuir* **2003**, *19*, 6230.

(10) Hartwich, G.; Caruana, D. J.; de Lumley-Woodyear, T.; Wu, Y.; Campbell, C. N.; Heller, A. *J. Am. Chem. Soc.* **1999**, *121*, 10803.

(11) Zhang, R.-Y.; Pang, D.-W.; Zhang, Z.-L.; Yan, J.-W.; Yao, J.-L.; Tian, Z.-Q.; Mao, B.-W.; Sun, S.-G. *J. Phys. Chem. B* **2002**, *106*, 11233.

(12) Kelley, S. O.; Jackson, N. M.; Hill, M. G.; Barton, J. K. *Angew. Chemie Int. Ed.* **1999**, *38*, 941.

(13) Kelley, S. O.; Holmlin, R. E.; Stemp, E. D. A.; Barton, J. K. *J. Am. Chem. Soc.* **1997**, *119*, 9861.

(14) Drummond, T. G.; Hill, M. G.; Barton, J. K. *J. Am. Chem. Soc.* **2004**, *126*, 15010.

(15) Gorodetsky, A. A.; Barton, J. K. *J. Am. Chem. Soc.* **2007**, *129*, 6074.

(16) Gorodetsky, A. A.; Buzzeo, M. C.; Barton, J. K. *Bioconjug. Chem.* **2008**, *19*, 2285.

(17) Egholm, M.; Buchardt, O.; Christensen, L.; Behrens, C.; Freier, S. M.; Driver, D. A.; Berg, R. H.; Kim, S. K.; Norden, B.; Nielsen, P. E. *Nature* **1993**, *365*, 566.

(18) Egholm, M.; Nielsen, P. E.; Buchardt, O.; Berg, R. H. *J. Am. Chem. Soc.* **1992**, *114*, 9677.

(19) Ramakrishnan, V.; D'Costa, M.; Ganesh, K. N.; Sastry, M. *Langmuir* **2002**, *18*, 6307.

(20) Petersson, B.; Nielsen, B. B.; Rasmussen, H.; Larsen, I. K.; Gajhede, M.; Nielsen, P. E.; Kastrup, J. S. *J. Am. Chem. Soc.* **2005**, *127*, 1424.

(21) Hatcher, E.; Balaeff, A.; Keinan, S.; Venkatramani, R.; Beratan, D. N. *J. Am. Chem. Soc.* **2008**, *130*, 11752.

(22) Rasmussen, H.; Kastrup, J. S.; Nielsen, J. N.; Nielsen, J. M.; Nielsen, P. E. *Nat. Struct. Biol.* **1997**, *4*, 98.

(23) Rasmussen, H.; Liljefors, T.; Petersson, B.; Nielsen, P. E.; Kastrup, J. S. *J. Biomol. Struct. Dyn.* **2004**, *21*, 495.

(24) Wittung, P.; Nielsen, P. E.; Buchardt, O.; Egholm, M.; Nordén, B. *Nature* **1994**, *368*, 561.

(25) Paul, A.; Watson, R. M.; Wierzbinski, E.; Davis, K. L.; Sha, A.; Achim, C.; Waldeck, D. H. *J. Phys. Chem. B* **2010**, *114*, 14140.

(26) Anne, A.; Demaille, C. *J. Am. Chem. Soc.* **2006**, *128*, 542.

(27) Anne, A.; Demaille, C. *J. Am. Chem. Soc.* **2008**, *130*, 9812.

(28) Paul, A.; Bezer, S.; Venkatramani, R.; Kocsis, L.; Wierzbinski, E.; Balaeff, A.; Keinan, S.; Beratan, D. N.; Achim, C.; Waldeck, D. H. *J. Am. Chem. Soc.* **2009**, *131*, 6498.

(29) Paul, A.; Watson, R. M.; Lund, P.; Xing, Y.; Burke, K.; He, Y.; Borguet, E.; Achim, C.; Waldeck, D. H. *J. Phys. Chem. C* **2008**, *112*, 7233.

(30) Giese, B.; Amaudrut, J.; Köhler, A. K.; Spormann, M.; Wessely, S. *Nature* **2001**, *412*, 318.

(31) Kawai, K.; Hayashi, M.; Majima, T. *J. Am. Chem. Soc.* **2012**, *134*, 9406.

(32) Takada, T.; Kawai, K.; Fujitsuka, M.; Majima, T. *Proc. Natl. Acad. Sci. U. S. A.* **2004**, *101*, 14002.

(33) O'Neill, M. A.; Barton, J. K. *J. Am. Chem. Soc.* **2004**, *126*, 11471.

(34) Daublain, P.; Thazhathveetil, A. K.; Shafirovich, V.; Wang, Q.; Trifonov, A.; Fiebig, T.; Lewis, F. D. *J. Phys. Chem. B* **2010**, *114*, 14265.

(35) Fiebig, T.; Wan, C.; Kelley, S. O.; Barton, J. K.; Zewail, a H. *Proc. Natl. Acad. Sci. U. S. A.* **1999**, *96*, 1187.

(36) Wan, C.; Fiebig, T.; Schiemann, O.; Barton, J. K.; Zewail, A. H. *Proc. Natl. Acad. Sci. U. S. A.* **2000**, *97*, 14052.

(37) Kawai, K.; Kodera, H.; Majima, T. *J. Am. Chem. Soc.* **2010**, *132*, 627.

(38) Weber, K.; Creager, S. E. *Anal. Chem.* **1994**, *66*, 3164.

(39) Napper, A. M.; Liu, H.; Waldeck, D. H. *J. Phys. Chem. B* **2001**, *105*, 7699.

(40) Honeychurch, M. J. *Langmuir* **1999**, *15*, 5158.

(41) Mishra, A. K.; Waldeck, D. H. *J. Phys. Chem. C* **2009**, *113*, 17904.

(42) Mishra, A. K.; Waldeck, D. H. *J. Phys. Chem. C* **2011**, *115*, 20662.

(43) Finklea, H. O. In *Electroanalytical Chemistry: A Series of Advances, Vol 19*; Bard, A. J.; Rubinstein, I., Eds.; Dekker: New York, 1996; Vol. 19, pp. 109–335.

(44) Seidel, C. A. M.; Schulz, A.; Sauer, M. H. M. *J. Phys. Chem.* **1996**, *100*, 5541.

(45) Shephard, M. J.; Paddon-Row, M. N.; Jordan, K. D. *J. Am. Chem. Soc.* **1994**, *116*, 5328.

(46) Petrov, E. G.; Shevchenko, Y. V; May, V. *Chem. Phys.* **2003**, *288*, 269.

(47) Isied, S. S.; Ogawa, M. Y.; Wishart, J. F. *Chem. Rev.* **1992**, *92*, 381.

(48) Wierzbinski, E.; de Leon, A.; Yin, X.; Balaeff, A.; Davis, K. L.; Rappireddy, S.; Venkatramani, R.; Keinan, S.; Ly, D. H.; Madrid, M.; Beratan, D. N.; Achim, C.; Waldeck, D. H. *J. Am. Chem. Soc.* **2012**, *134*, 9335.

(49) Venkatramani, R.; Davis, K. L.; Wierzbinski, E.; Bezer, S.; Balaeff, A.; Keinan, S.; Paul, A.; Kocsis, L.; Beratan, D. N.; Achim, C.; Waldeck, D. H. *J. Am. Chem. Soc.* **2011**, *133*, 62.

(50) Wenger, O. S. *Acc. Chem. Res.* **2011**, *44*, 25.

(51) Bard, A. J.; Faulkner, L. R. *Electrochemical Methods: Fundamentals and Applications*; 2nd ed.; John Wiley & Sons, Inc., 2000.

(52) Liang, G.; Ghosh, A.; Paulsson, M.; Datta, S. *Phys. Rev. B* **2004**, *69*, 115302.

(53) Yue, H.; Khoshtariya, D.; Waldeck, D. H.; Grochol, J.; Hildebrandt, P.; Murgida, D. H. *J. Phys. Chem. B* **2006**, *110*, 19906.

(54) Newton, M. D.; Smalley, J. F. *Phys. Chem. Chem. Phys.* **2007**, *9*, 555.

(55) Mujica, V. *Chem. Phys.* **2002**, *281*, 147.

(56) Zhao, J.; Uosaki, K. *Appl. Phys. Lett.* **2003**, *83*, 2034.

(57) Xue, Y.; Ratner, M. *Phys. Rev. B* **2003**, *68*, 1.

(58) Datta, S.; Tian, W.; Hong, S.; Reifenberger, R.; Henderson, J.; Kubiak, C. *Phys. Rev. Lett.* **1997**, *79*, 2530.

(59) Zhao, J.; Yu, C.; Wang, N.; Liu, H. *J. Phys. Chem. C* **2010**, *114*, 4135.

(60) *Longe-Range Charge Transfer in DNA I*; Schuster, G. B., Ed.; Topics in Current Chemistry; Springer Berlin Heidelberg: Berlin, Heidelberg, 2004; Vol. 236.

(61) *Long-Range Charge Transfer in DNA II*; Schuster, G. B., Ed.; Topics in Current Chemistry; Springer Berlin Heidelberg: Berlin, Heidelberg, 2004; Vol. 237.

(62) Taniguchi, M.; Tsutsui, M.; Shoji, K.; Fujiwara, H.; Kawai, T. *J. Am. Chem. Soc.* **2009**, *131*, 14146.

(63) Kawai, K.; Kodera, H.; Osakada, Y.; Majima, T. *Nat. Chem.* **2009**, *1*, 156.

(64) Schlaf, R. *In Preparation*.

(65) Wierzbinski, E.; de Leon, A.; Davis, K. L.; Bezer, S.; Wolak, M. A.; Kofke, M. J.; Schlaf, R.; Achim, C.; Waldeck, D. H. *Langmuir* **2012**, *28*, 1971.

(66) Yokota, K.; Taniguchi, M.; Kawai, T. *J. Am. Chem. Soc.* **2007**, *129*, 5818.

(67) Kawai, K.; Osakada, Y.; Sugimoto, A.; Fujitsuka, M.; Majima, T. *Chem. - A Eur. J.* **2007**, *13*, 2386.

(68) Takada, T.; Kawai, K.; Fujitsuka, M.; Majima, T. *Chem. - A Eur. J.* **2005**, *11*, 3835.

(69) Sawyer, D. T.; Sobkowiak, A.; Roberts(Jr.), J. L. *Electrochemistry for Chemists*; 2nd Ed.; John Wiley & Sons, Inc.: New York, 1995.

(70) Bezer, S.; Rapireddy, S.; Skorik, Y. a; Ly, D. H.; Achim, C. *Inorg. Chem.* **2011**, *50*, 11929.

(71) Nielsen, P. E. *Peptide Nucleic Acids: Protocols and Applications*; Peter Nielson, Ed.; 2nd ed.; Horizon Bioscience, 2004.

(72) Dueholm, K. L.; Egholm, M.; Behrens, C.; Christensen, L.; Hansen, H. F.; Vulpius, T.; Petersen, K. H.; Berg, R. H.; Nielsen, P. E.; Buchardt, O. *J. Org. Chem.* **1994**, *59*, 5767.

3.0 THE EFFECT OF OXYGEN HETEROATOMS ON THE SINGLE MOLECULE CONDUCTANCE OF SATURATED CHAINS

This work has been published as Wierzbinski, E.; Yin, X.; Werling, K.; Waldeck, D. H. J. Phys. Chem. B 2013, 117, 4431–41. The author of this dissertation performed the theoretical analysis.

Single molecule conductance measurements on alkanedithiols and alkoxydithiols (dithiolated oligoethers) were performed using the STM-controlled Break Junction method in order to ascertain how the oxygen heteroatoms in saturated linear chains impact the molecular conductance. The results show that the conductance of the oligoethers is lower than that of alkane chains with the same length, and the difference in conductance increases with chain length, over the range studied. These experimental findings are substantiated by computational studies. Electronic structure calculations allow the difference in the conductance of these two families of molecules to be traced to differences in the spatial distribution of the molecular orbitals that contribute most to the conductance. A pathway analysis of the electronic coupling through the chain is used to explain the dependence of the electronic coupling difference on the chain length.

3.1 INTRODUCTION

Since the concept of molecular electronics first appeared,[1,2] progress in the development of experimental methods for determining the charge transfer properties of organic molecules (as prospective elements of electronic devices) has evolved to allow measurements on individual molecules.[3–7] Single molecule conductance measurements have been used to quantify the charge

transport properties for a diverse array of molecules, including saturated and unsaturated hydrocarbons,[6,8–14] conjugated oligomers,[15–18] fullerenes,[19] metal complexes,[20,21] porphyrins,[22–25] peptides,[26,27] and nucleic acids.[4,28–33] Saturated hydrocarbons are often used as model molecular bridges,[8–14] because of the simplicity of their chemical structure and the establishment of superexchange as their charge transfer mechanism for chains of twenty methylenes and less. This work compares the conductance of methylene chains (-CH_2-CH_2-CH_2) to oligoethers (-CH_2-CH_2-O-) of corresponding length. The STM-controlled break junction method[6] was used to measure the single molecule conductance of three alkanedithiols, containing five, eight, and eleven methylene units, and the three corresponding dithiolated oligoethers, in which every third methylene unit is replaced by an oxygen. Comparison of these two sets of organic compounds provides a way to probe how the local electronic differences between carbon and oxygen affect the conductance of saturated chains. Presumably, the construction of molecular electronic devices would require binding several molecules or functional groups together. Hence knowledge about the influence of various kinds of chemical bonds on the charge transfer properties is necessary in order to produce functional electrical circuits. Similar concerns were addressed recently by Whitesides and coworkers, who studied the impact of introducing amide bonds into hydrocarbon chains on the conductance of self-assembled monolayers (SAMs).[34] The findings reported here demonstrate that the conductance of the saturated chains can be decreased below the level found for saturated hydrocarbon chains, and that an ether-type linkage may be used as an alternative to hydrocarbons in situations where one wishes to decrease the electronic coupling between different fragments of a complex molecular structure.

Comparison of the charge transfer properties of saturated hydrocarbon and ether chains has been probed by Napper *et al.* using electroactive SAMs.[35] That report used alkanethiol and

alkoxythiol SAMs, in which a small fraction (circa 5%) of the chains were appended with a terminal ferrocene as a redox reporter group, and measured the electrochemical rate constant. They reported a four to five-fold decrease in the rate constant for the ether-linked ferrocene as compared to the alkyl linked ferrocene. The electrochemical rate constant is sensitive to a combination of the properties of the molecular bridge, as well as the quality of the monolayer[36,37] and intermolecular interactions.[35,36,38–40] Napper's study also varied the diluent molecules between ferrocenated alkanethiols and alkoxythiols in order to quantify the influence of the electrical dipole in the monolayer on the measured rate constant. They found that thirty to forty percent lower rate constants were measured whenever ferrocenated molecules with the same covalent linkage to the electrode were embedded in the ether monolayer. These studies showed that the effects produced by the environment (overall dipole moment in the monolayer) were dramatically smaller than the through-bond electronic coupling in determining electrochemical rate constant.[41] The electrochemical through-bond unimolecular rate constant was predicted to be proportional to the molecular conductance of the same molecular bridge;[42–44] thus Napper's results imply that the single molecule conductances of alkanes should be higher than that of ethers.

Computational studies were used to understand the origin of the differences in the experimental conductance of the hydrocarbon and oligoether chains. The trend in the calculated conductance, hydrocarbon chain more conductive than the alkoxy chain, agrees with experiment. Furthermore, the trend in the delocalization level of the calculated molecular orbitals (MOs) in these two families of molecules agrees with the experimental trend in their single molecule conductances. To quantify the degree of the delocalization of the MOs, the concept of normalized localization factors is introduced, and it shows a higher delocalization of the MOs for the hydrocarbon chains than for the ether-linked chains. In order to better understand the role of the

oxygen atoms in the saturated chains, an analysis of electronic coupling pathways based on natural bond orbitals (NBO) was used.[35,45] A perturbation treatment[46] is used to assess the relative contribution from each pathway to the overall coupling, in the limits of hole-mediated superexchange and electron-mediated superexchange. This procedure shows that non-nearest neighbor couplings are a dominant contributor to the overall coupling for long chains. To understand the impact of the oxygen on the electronic coupling (and in consequence on the molecular conductance) and its length dependence, the pool of the orbital interactions used in the perturbation treatment was expanded to accommodate additional electronic interactions that arise from the presence of multiple oxygen atoms in the oligoether chains. This analysis shows how the oxygen atoms affect the electronic couplings differently in the short and long molecular chains.

3.2 EXPERIMENTAL SECTION

3.2.1 Compounds.

The STM break junction method was used to measure the conductance of three alkoxy dithiolated saturated linear molecules [2-mercaptoethyl ether (5-O), 2,2′-(ethylenedioxy)diethanethiol (8-O), and tetra(ethylene glycol) dithiol (11-O)] and three alkanedithiols of corresponding length [1,5-pentanedithiol (5-C), 1,8-octanedithiol (8-C), and 1,11-undecanedithiol (11-C)]. All compounds were purchased from Sigma-Aldrich in the highest available purity grade and were used without additional purification.

3.2.2 Single Molecule Conductance (STM-Controlled Break Junction) Measurements.

The conductance of the single dithiolated molecules was measured using the STM-controlled break-junction method.[6] In this experiment, the molecules of interest are occasionally trapped between the substrate and an STM tip by periodic modulation of the tip-substrate separation. During this process, the tunneling current is monitored as a function of the tip-substrate distance at a constant bias voltage. The conductance is determined by analysis of the current-distance characteristics. All measurements were performed with an Agilent 5500 system equipped with an environmental chamber. The STM head was placed in a homemade, acoustically isolated Faraday cage, which was mounted on an active antivibrational system (Table Stable) located on an optical table. A brief description of the STM-BJ measurements is presented below.

Experiments were performed using freshly cut gold STM tips (0.25 mm, 99.999% gold wire, Alfa Aesar). Typically, 5-10 tips were used to collect sufficient data for each molecule. 100 nm thick gold films on silicon (Sigma-Aldrich) were used as the substrates. Typically, at least three independent substrates were used to collect 2000 - 3000 current-distance characteristics for each studied compound. Prior to the measurements, the substrates were cleaned for 10-20 s in piranha solution, rinsed solely with deionized water, and dried under a stream of argon. Measurements were performed in 2 mM solutions in mesitylene under an argon atmosphere. A 10 nA/V preamplifier was used in the measurements. Current-distance curves were recorded under 0.5 V bias. Curves that displayed current plateaus (20-30% of the total data set) were manually selected for further analysis. Measured conductances were plotted in the form of normalized histograms on a logarithmic scale, with 25 bins per decade. For each of the studied molecules, a Gaussian function was fitted to the conductance distribution to determine the position of the conductance peak. The conductance distributions are plotted on a linear scale together with the

fitted Gaussian functions in the Supporting Materials. Conductance results are expressed in the units of the quantum conductance, $G_0 = 2e^2/h \approx 77\ \mu S$.

In order to plot two dimensional (2-D) conductance-displacement distributions it is necessary to determine a zero distance in a constant and meaningful way. For each-current-distance curve, the beginning of the drop of measured current from its maximum value of 100 nA ($\sim 2.5 \times 10^{-3}\ G_0$) was taken to define the zero of distance. This part of the curve represents the moment at which direct contact between the gold tip and gold substrate breaks, and thus measured current rapidly decreases to zero. The distributions were built with a bin size in the displacement scale of 0.24 Å.

3.2.3 Theoretical Calculations of the Conductance.

A nonequilibrium Green's function (NEGF) method, which has been verified in the weak coupling limit[47,48] was employed to calculate the conductance. First, the geometries of all six molecules were optimized at the RHF/6-31G(d) level using Gaussian 03.[49] Next, the Fock matrix from the last SCF calculation was transformed into a fully localized natural atomic orbitals (NAOs) [50,51] through Gaussian's NBO 3.1 routine[52] and used in the following Green's function:

$$G(\varepsilon) = \frac{1}{\varepsilon \mathbf{I} - \mathbf{F} - \mathbf{\Sigma}_{\mathrm{L}} - \mathbf{\Sigma}_{\mathrm{R}}} \qquad \textbf{Equation 3.1}$$

where **F** is the NAO Fock matrix, and ε is the energy variable. The self-energy matrix **Σ**, which describes the molecular orbital (eigenstates of the NAO Fock matrix) broadening that arises from the coupling to left (L) and right (R) electrodes, was calculated using the broadening matrix **Γ** through $\mathbf{\Gamma} = i[\mathbf{\Sigma} - \mathbf{\Sigma}^{+}]$. The values of the matrix elements of **Γ** represent the coupling between corresponding NAOs and electrodes. A 0.1 eV electrode-NAO coupling strength, which is the

same value used previously,[32,48] was set for the terminal sulfur NAOs. Because linkers are always present in experiments, the terminal carbon atoms were included in the broadening matrix to get the correct trend of conductance. The method for the weak coupling limit is optimized for model molecules without a "linker". For the models with linkers, the coupling was kept weak enough between the electrode and terminal carbon NAOs so that the molecular bridge states are not significantly perturbed. The transmission was computed by the way of Eqn 3.2,

$$T(\varepsilon) = \mathbf{Tr}[\boldsymbol{\Gamma}_L \boldsymbol{G} \boldsymbol{\Gamma}_R \boldsymbol{G}] \qquad \textbf{Equation 3.2}$$

and the conductance was calculated by way of Landauer's formula,

$$\sigma = \frac{q^2}{h} \int T(\varepsilon)\, F_T\,(\varepsilon - E_F)\, \mathrm{d}\varepsilon \qquad \textbf{Equation 3.3}$$

where q is the elementary charge, h is Planck's constant. The function F_T is the difference between the Fermi functions of the left and right electrode,[32] namely

$$F_T(\varepsilon - E_F) = \frac{1}{4k_B T} \mathrm{sech}^2\left(\frac{\varepsilon - E_F}{2k_B T}\right) \qquad \textbf{Equation 3.4}$$

E_F is the Fermi level, which was set to -5.5eV to reflect the value for Au.[53] Because of the strong decrease in the value of F_T as the energy ε moves away from E_F, the dominant contribution to the conductance σ is from $T(\varepsilon = E_F)$. By defining a scoring factor,[47] the transmission (and the current) was decomposed into contributions from specific orbitals: $T(\varepsilon = E_F) = \sum_m \mathrm{SF}_m$. The scoring factor is expressed as

$$\mathrm{SF}_m = \sum_n \frac{\Gamma^{\mathrm{L}}_{\mathrm{mn}} \Gamma^{\mathrm{R}}_{\mathrm{nm}}}{(E_F - \varepsilon_m)(E_F - \varepsilon_n)} \qquad \textbf{Equation 3.5}$$

in which Γ^L_{mn} and Γ^R_{nm} are the corresponding elements of matrixes $\boldsymbol{\Gamma}_L$ and $\boldsymbol{\Gamma}_R$. ε_m is the energy of molecular orbital m.

3.3 RESULTS AND DISCUSSION

3.3.1 Single Molecule Conductance.

The single molecule conductance was studied using the STM-BJ[6] method, in which a gold STM tip serves as one electrode and the gold substrate serves as a second electrode of the junction (Figure 3.1A). During retraction of the tip from the substrate, the current was measured as a function of the distance between the electrodes. In pure solvent, the current-distance curves are characterized by an exponential decay, such as the black curves presented in Figure 3.1C. If thiol functionalized molecules are present in the solvent, they can be trapped between the tip and the substrate and contribute to the overall conductance of the junction. Figure 3.1C shows sample experimental curves (presented in conductance scale) with step-like features that result from the conduction of the different molecules studied in this work. The structures of the molecules are given in Figure 3.1B.

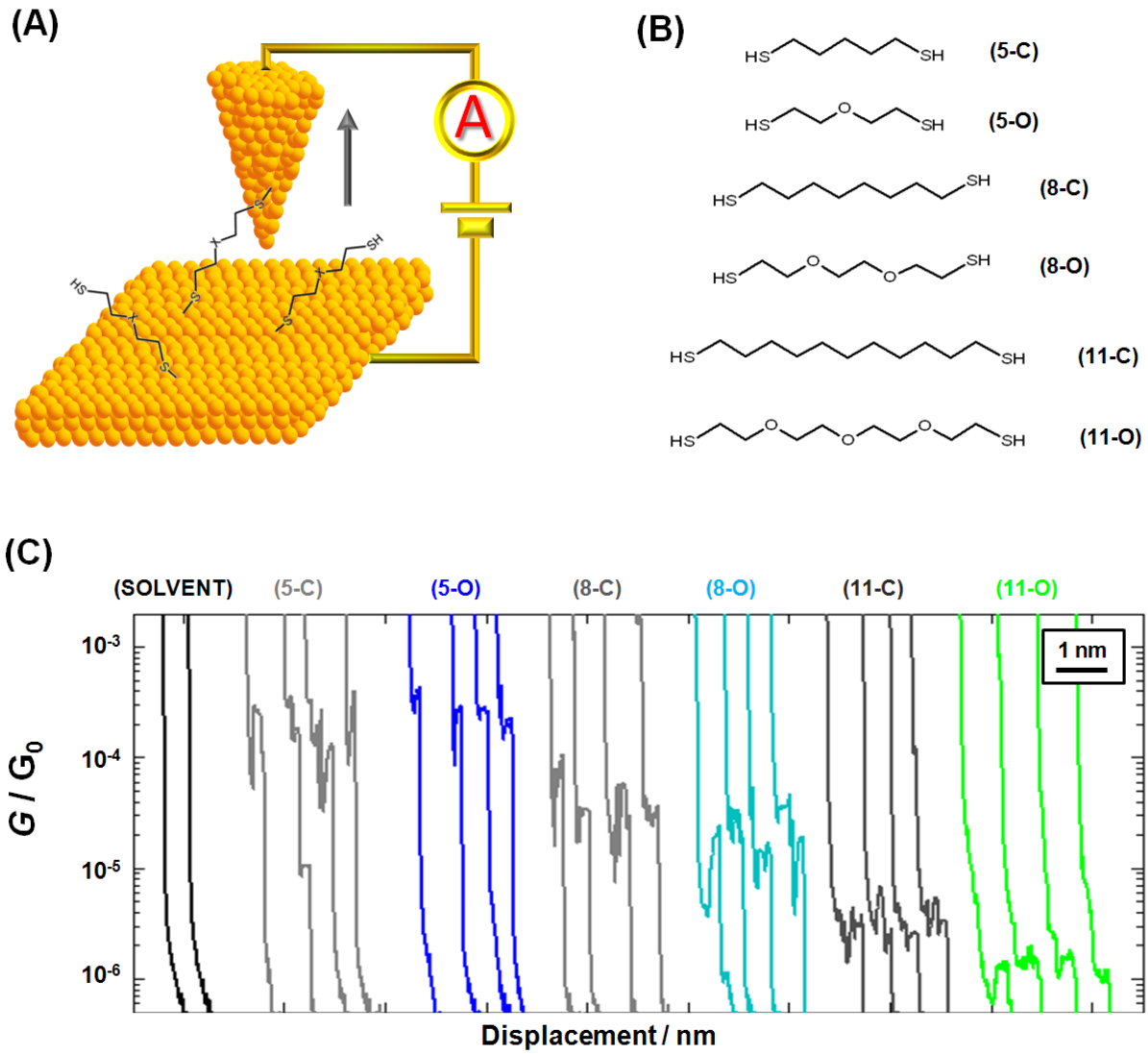

Figure 3.1. Panel A shows a cartoon representation of the STM break junction. Panel B shows the molecular structures of 1,5-pentanedithiol (5-C), 2-mercaptoethyl ether (5-O), 1,8-octanedithiol (8-C), 2,2′-(ethylenedioxy)diethanethiol (8-O), 1,11-undecanedithiol (11-C), and tetra(ethylene glycol) dithiol (11-O). Panel C shows sample conductance-distance curves recorded in the presence of the molecules in the junction. For comparison typical curves recorded in pure mesitylene (solvent) are shown also.

Because the conformations of the molecules and their binding geometries can vary, the measured conductance varies from trace to trace;[10–12] nevertheless its distribution is characteristic for each studied compound. Figure 3.2 shows two-dimensional conductance - displacement

distributions constructed from the many conductance - distance curves recorded for each compound. The displacement axis reflects the distance at which the STM tip is withdrawn after the direct contact between the tip and the substrate is broken.

For each compound, the measured conductance varied by less than an order of magnitude, and the conductance for a family of compounds became smaller with the increasing length of the molecule. The values of the conductances that were determined for the alkanedithiol chains (5-C, 8-C, and 11-C) are in good agreement with the values reported by others for the single molecule conductance of alkanedithiols[11,12] (more details are provided in the Supporting Materials, see section 3.5). The average distances at which the junctions break are dependent on the length of the molecules, and it varies from 2 to 3 Å for 5-C and 5-O, to 3 to 5 Å for 8-C and 8-O, and 6 to 8 Å for 11-C and 11-O. Other than a shift in the conductance values of the steps, no significant difference in overall shape of the conductance-distance dependencies (Figure 3.1C) and in the average length of the conductance steps (Figure 3.2) were observed between the hydrocarbon and oligoether chains with the same number of bridge units (sum of $-CH_2$ and oxygen atoms in the chain). Furthermore, a comparison of the conductance distributions constructed for the 5-C and 5-O chains show very similar conductances for these two compounds. Nonetheless, the situation changes when longer molecules, with a larger number of oxygen atoms in the chain, are compared with their hydrocarbon analogs.

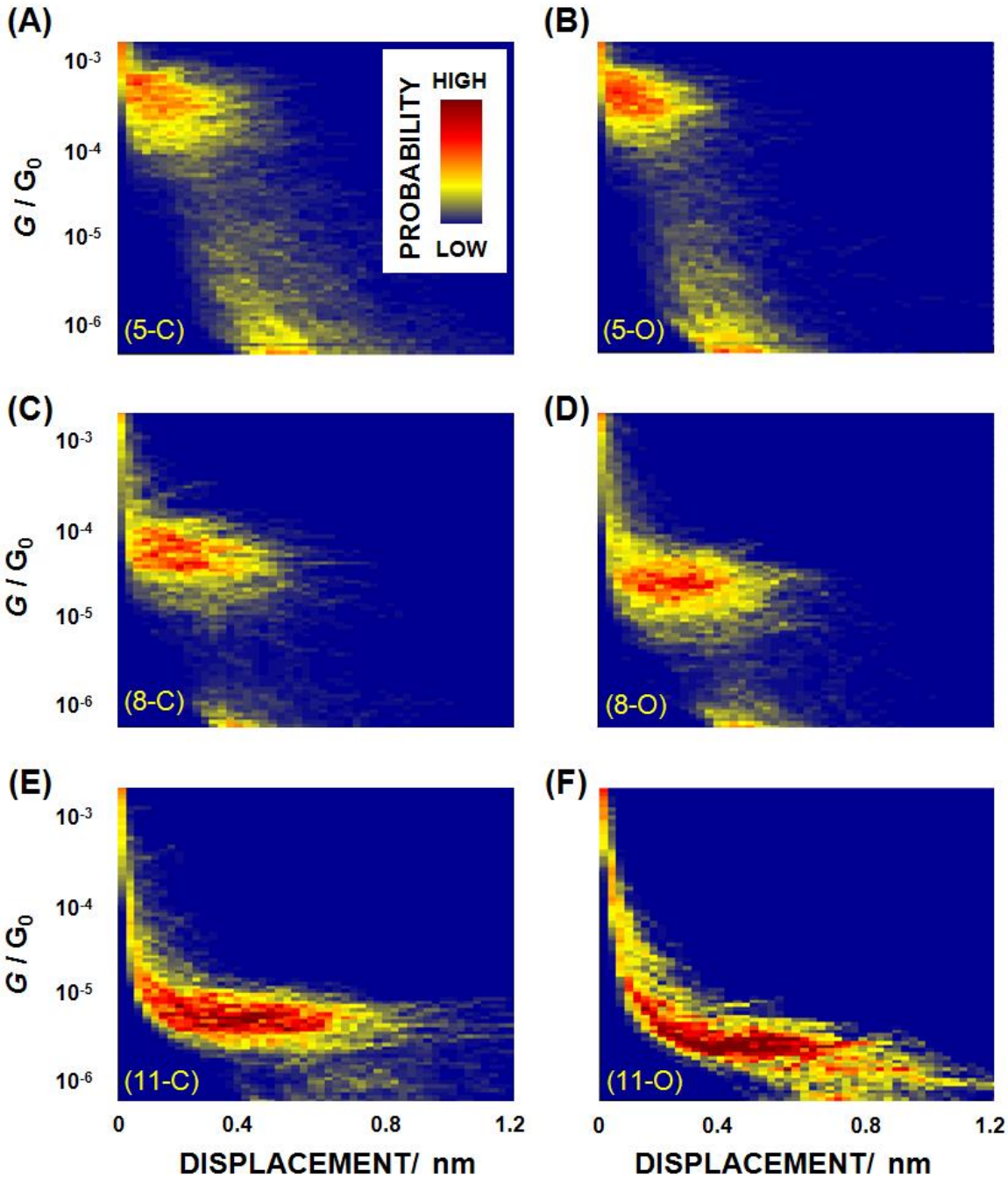

Figure 3.2. Two dimensional conductance-displacement distributions are shown for 1,5-pentanedithiol (A), 2-mercaptoethyl ether (B), 1,8-octanedithiol (C), 2,2′-(ethylenedioxy)diethanethiol (D), 1,11-undecanedithiol (E), and tetra(ethylene glycol) dithiol (F). The color bar in panel A is common for all compounds.

Figure 3.3 shows a direct comparison between the conductance distributions constructed for alkanedithiol (5-C, 8-C, and 11-C) and oligoether (5-O, 8-O, and 11-O) molecules. Evaluation

of the conductance distributions for 5-C and 5-O indicates that replacing a single carbon atom in the hydrocarbon chain by an oxygen reduces the average conductance of the chain by several percent. If each third methylene unit in the chain is replaced by an oxygen (compounds 8-O and 11-O, see Figure 1B), the effect becomes stronger and leads to about a fifty percent decrease of the average conductance when compared to the hydrocarbon counterparts (8-C and 11-C). The increasing influence of the oxygen atoms on the conductance of the longer oligoether chains, which is observed in the single molecule conductance experiments, were confirmed by theoretical calculations with the NEGF method. Both measured and calculated conductances are given in Table 3.1.

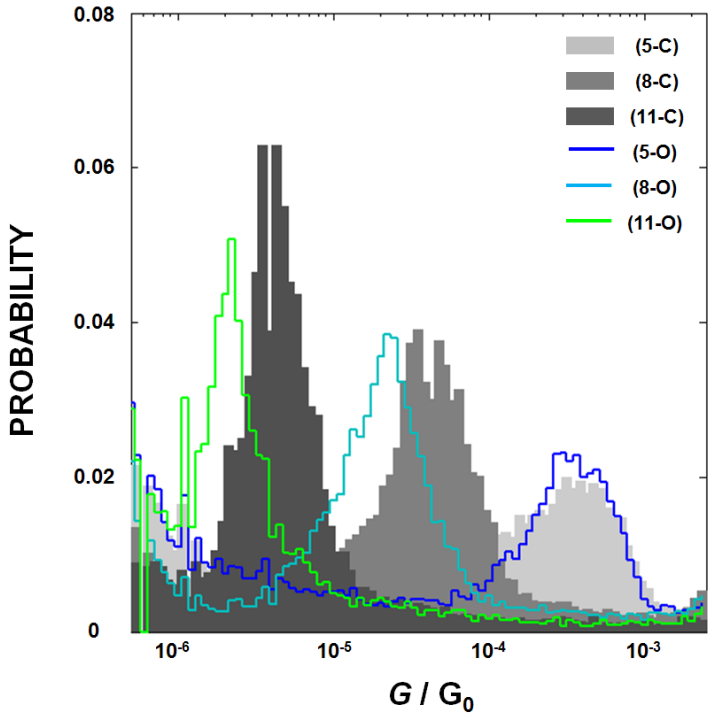

Figure 3.3. The plot compares the conductance distributions of dithiolated hydrocarbons (5-C, 8-C, 11-C) and oligoethers (5-O, 8-O, 11-O). The shaded distributions represent the hydrocarbon chains and the colored curves sketch the distributions for the corresponding oligoethers (green is 11-O, aqua is 8-O, and blue is 5-O).

Table 3.1. The average experimental conductance of studied compounds and the calculated conductance of the model compounds.

MOLECULE	CONDUCTANCE / G_0	
	MEASURED	**CALCULATED**
5-C	$(4.6 \pm 2.9) \times 10^{-4}$	2.6×10^{-9}
5-O	$(4.2 \pm 2.3) \times 10^{-4}$	1.9×10^{-9}
(5-O/5-C)	0.91	0.74
8-C	$(5.2 \pm 2.5) \times 10^{-5}$	7.0×10^{-11}
8-O	$(2.5 \pm 1.2) \times 10^{-5}$	4.1×10^{-11}
(8-O/8-C)	0.48	0.59
11-C	$(4.7 \pm 1.9) \times 10^{-6}$	2.2×10^{-12}
11-O	$(2.1 \pm 0.7) \times 10^{-6}$	1.3×10^{-12}
(11-O/11-C)	0.45	0.58

[a] The NEGF methods used here are not expected to reproduce the absolute values of the experimental conductances for this system. Simplifications about the nature of the electrode-molecule coupling and the exact position of the metal Fermi levels can strongly shift the absolute values. The approach is believed to capture relative charge transport trends between systems, however.[32,47,48]

3.3.2 Relationship between Electronic Structure and Calculated Conductance.

Figure 3.4 compares the contributions of particular molecular orbitals (MOs) to the calculated conductance for the 8-C and 8-O molecules, by plotting scoring factors SF versus the molecular orbital energy (top row in Figure 4).[47] Values of scoring factors can be positive or negative. Hence constructive and deconstructive interference between different MOs is important in determining the overall conductance of the molecule, which is proportional to the sum of all SFs (∑SFs). The bottom panel in Figure 4 compares the summation of SFs for occupied and unoccupied levels, beginning from the frontier molecular orbitals. That is, the sum is taken from the highest occupied molecular orbital (HOMO) downward in energy, and a corresponding sum is taken from the lowest unoccupied molecular orbital (LUMO) upward in energy. Three major conclusions can be deduced from this comparison: i) SFs are typically higher for HOMOs than LUMOs, suggesting hole-

mediated charge transfer, ii) ∑SFs s are higher for the alkane chains, as compared to the alkoxy chains, iii) for both alkoxy and alkyl chains, the contributions of particular MO's to the conductance become important below the HOMO-1 level. The comparisons of SFs and ΣSFs for these molecules plotted versus energy, and versus MO index, are given in the Supporting Materials (Figures S4 to S6).

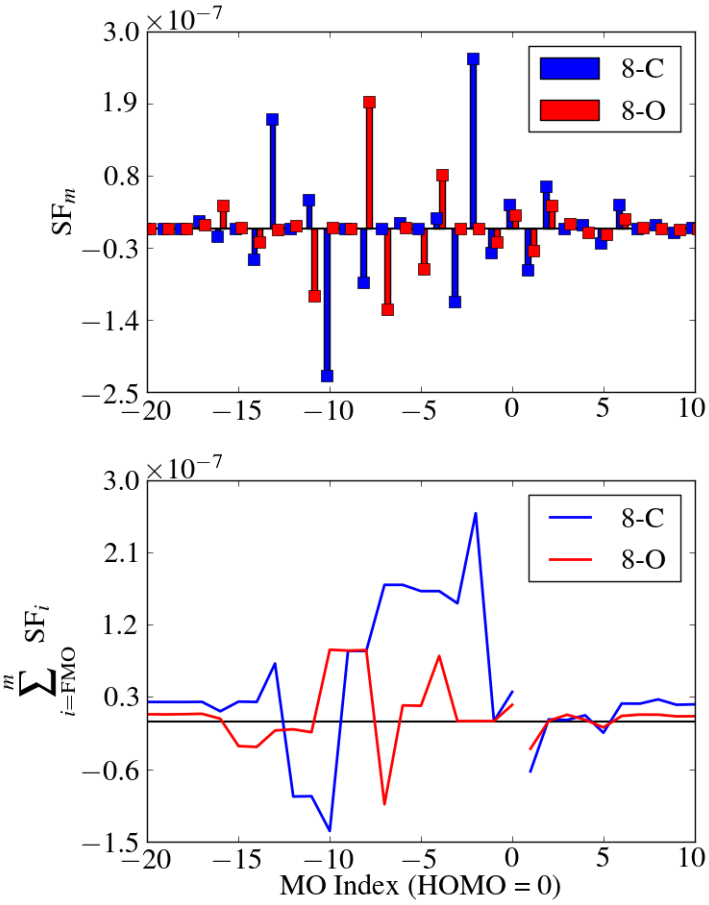

Figure 3.4. Comparison of scoring factors (top row) and their sums (bottom row) for 8-C (blue) and 8-O (red) molecules, plotted versus MO Index. The sums are calculated separately for HOMO and LUMO levels starting from frontier molecular orbitals.

Starting from the HOMO-2 level the differences in SF values, and consequently in ∑SFs, becomes apparent with a high contribution of this level to the conductance of the 8-C molecule,

but a negligible value for 8-O. Table 3.2 gives some energies for some selected MOs with respect to the vacuum level. The differences in energy of levels listed in Table 3.2 are less than 0.2 eV in all molecules. In particular, the energy of the HOMO-2 level in 8-C and in 8-O is similar, thus the molecular conductance of 8-C and 8-O cannot be explained exclusively by their orbital energetics.

Table 3.2. Energies of selected molecular orbitals for the dithiol molecules.

MOLECULAR ORBITAL	ENERGY / eV					
	5-C	**5-O**	**8-C**	**8-O**	**11-C**	**11-O**
HOMO	-9.68	-9.83	-9.63	-9.81	-9.60	-9.80
HOMO-1	-9.69	-9.85	-9.63	-9.81	-9.60	-9.80
HOMO-2	-12.00	-11.96	-11.76	-11.74	-11.55	-11.64

[a] Note that the HOMO and HOMO-1 are primarily thiol nonbonding electrons (see text).

Figure 3.5 shows the spatial distributions of selected MOs for 8-C and 8-O. One can see that the HOMO and HOMO-1 levels are fully localized at the terminal sulfur atoms, and are very similar for the alkyl and oligoether chains. This localization indicates little contribution from carbons on the bridge, and indicates that these orbitals can be viewed primarily as symmetric and antisymmetric combinations of the sulfur lone pair orbitals. The longer molecular bridge minimizes direct coupling between the two terminal atoms further. Together with the symmetry of these molecules, this leads to an interesting result that the HOMO and HOMO-1 levels are nearly degenerate and their total contributions to the conductance almost cancel each other in the weak coupling limit.

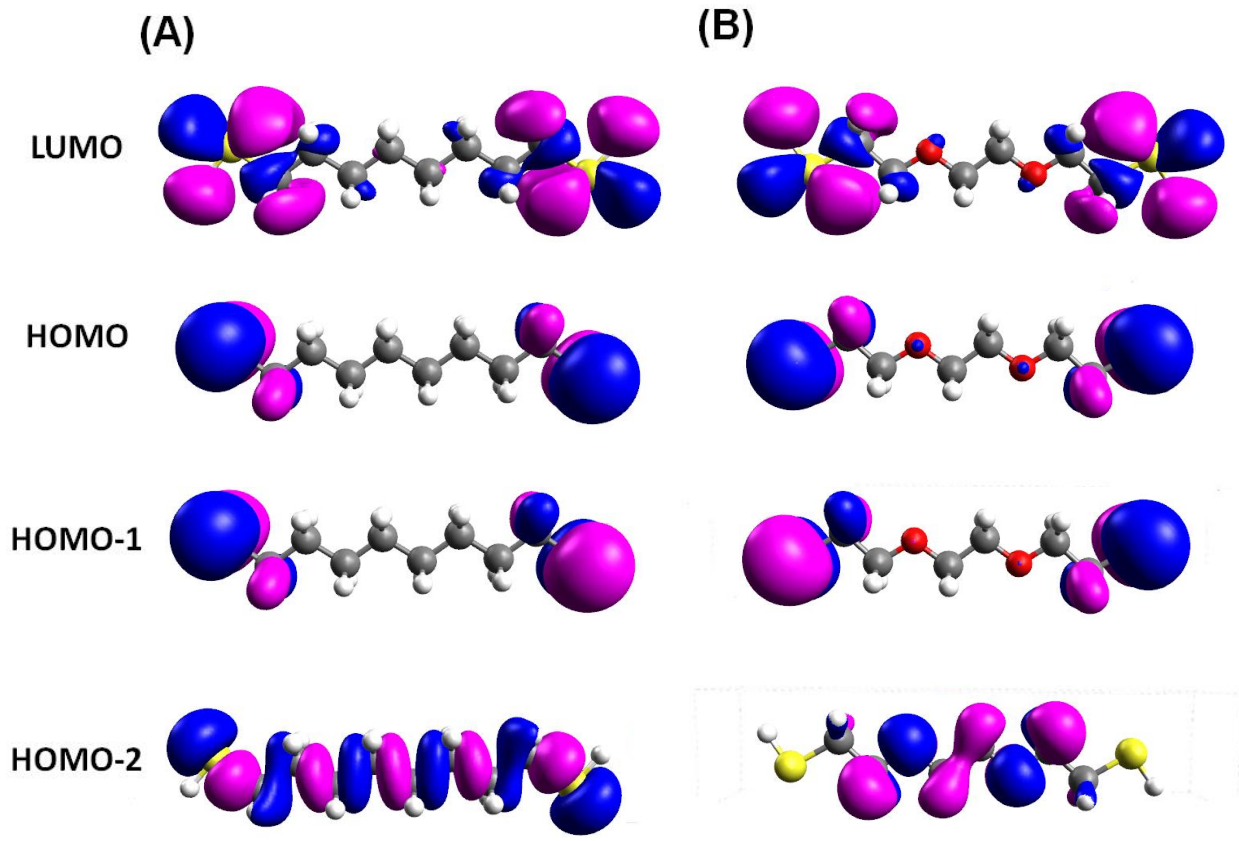

Figure 3.5. Spatial distributions are shown for selected molecular orbitals in 8-C (A) and 8-O (B).

The spatial distribution of probability amplitude for the HOMO-2 level in these molecules is qualitatively different. In the case of 8-C, the HOMO-2 is delocalized along the entire molecule, while in the case of 8-O it is more localized on the oxygen atoms. Similar differences in the localization of the HOMO-2 levels have been found for the shorter and longer chains also, see Figure 3.6.

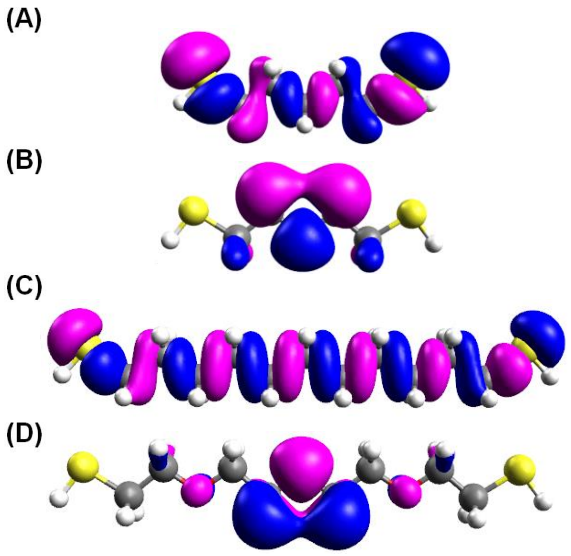

Figure 3.6. Spatial distributions of the HOMO-2 orbital are shown for 5-C (A), 5-O (B), 11-C (C), and 11-O (D). Spatial distributions of LUMO, HOMO, and HOMO-1 levels for these molecules can be found in the Supporting Materials.

The degree of localization of the MOs was quantified by defining a normalized localization factor (NLF) for each MO. Because the MOs have been transformed into the natural atomic orbital (NAO) basis (*vide supra*), each MO can be decomposed into a linear combination of NAOs:

$$\mathrm{MO}_m = \sum_{i=1}^{n} c_{m,i}\,\mathrm{NAO}_i \qquad \textbf{Equation 3.6}$$

where $c_{m,i}$ is a coefficient and $\left|c_{m,i}\right|^2$ is the contribution of the i^{th} NAO to the m^{th} MO. A localization factor for MO_m can be defined as the coefficient of variation of the corresponding MO coefficients:

$$\mathrm{LF}_m = \frac{\mathrm{std}(c_m)}{\langle c_m \rangle} \qquad \textbf{Equation 3.7}$$

where $\mathrm{std}(c_m)$ is the standard deviation of the series of c_m and $\langle c_m \rangle$ is the mean. To compare molecules with a different number of NAOs, LF is normalized to its highest possible value for

each molecular orbital and the normalized localization factor (NLF) is used in the following discussion.

$$\mathrm{NLF}_m = \frac{\mathrm{LF}_m}{\mathrm{LF}_{max}} \qquad \textbf{Equation 3.8}$$

The NLF values can vary between 0 and 1, where '0' means that the MO is fully delocalized (all of the chain's heavy atom orbitals contribute equally to the MO) and '1' means that the MO is localized on a single atomic orbital. Some of the calculated NLF values are presented in Table 3.3. The HOMO, and HOMO-1 levels are strongly localized on the terminal sulfur atoms (see Figure 3.5), and the same high NLF value of 0.66 was calculated for these MOs in all the molecules. For both alkanes and oligoethers the LUMO is delocalized along the chain, however the contribution of this orbital to the overall conductance is small (see Figure 3.4, and Figures 3.12 and 3.13) because of its position with respect to the Fermi level. On the other hand, NLF values calculated for the HOMO-2 show a strong difference in the localization. The oligoethers have NLF values that are nearly as high as that of the HOMO and HOMO-1,[54] whereas the alkyl chains show delocalization that is more similar to the LUMO orbitals. The contribution of each MO to the conductance (scoring factors) depends not only on the localization factor, but also on the MO's energy relative to the Fermi level and on how much the terminal atomic orbital (which is coupled with the electrode) contributes to the MO. Other than the HOMO-2 level, the NLFs of the hydrocarbons and oligoethers are quite uniform. This feature suggests that the differences in the HOMO-2 are largely responsible for the differences in the conductance.

Table 3.3. Normalized localization factors (NLFs) for selected molecular orbitals.

MOLECULE	MOLECULAR ORBITAL				Filled States[a]
	HOMO-2	HOMO-1	HOMO	LUMO	
5-C	0.30	0.66	0.66	0.29	0.34
5-O	0.60	0.66	0.66	0.30	0.38
8-C	0.27	0.66	0.66	0.29	0.28
8-O	0.46	0.66	0.66	0.30	0.32
11-C	0.27	0.66	0.66	0.30	0.25
11-O	0.60	0.66	0.66	0.30	0.30

[a] The average NLF of all MOs formed from the valence atomic orbitals.

3.3.3 Analysis of the Charge Transfer Pathways.

Although the MO based conductance analysis explains the general trend, analyzing the MOs directly masks how the local bonding and site energy changes affect the conductance. To further explore these effects, a pathway analysis based on fully localized natural bond orbitals (NBO)[35,45] was performed. Six symmetric, model molecules: •$CH_2(CH_2)_3CH_2$•, •$CH_2CH_2OCH_2CH_2$•, •$CH_2(CH_2)_6CH_2$•, •$CH_2(CH_2OCH_2)_2CH_2$•, •$CH_2(CH_2)_9CH_2$•, and •$CH_2(CH_2OCH_2)_3CH_2$•, were used as model donor-bridge-acceptor representations of 5-C, 5-O, 8-C, 8-O, 11-C, and 11-O molecules, respectively. The terminal radicals played the role of the donor or the acceptor for each model molecule. Terminal sulfurs were not included in order to explore better the molecular bridge charge transfer properties of the chains. Following Lewis,[42] the single molecule conductance in the superexchange regime can be approximated as

$$\sigma = |V|^2 \frac{2\pi e^2}{\hbar}\left[\left(\frac{\pi}{6}\right)^{2/3} \frac{\mathrm{D_{m,L}} l_{\mathrm{m,L}}}{{d_{m,\mathrm{L}}}^{2/3}} \frac{\mathrm{D_{m,R}} l_{\mathrm{m,R}}}{{d_{m,\mathrm{R}}}^{2/3}}\right] \qquad \textbf{Equation 3.9}$$

where V is the electronic coupling through the molecular bridge, D_m is the density of electronic states in the metal, d_m is atomic density of the metal (atoms cm^{-3}), l_m is the effective coupling length of the bridge's wavefunction into the metal (in cm), and the R (L) index indicates the right

(left) metal contact. The other symbols have their usual meanings. Because the electronic coupling is the only variable that depends on the molecular structure of the bridge, the conductance analysis is reduced to an electronic coupling analysis. The geometry and electronic structure of the triplet diradicals were calculated at the UHF/3-21G level using Gaussian 03,[49] which is accurate enough for this NBO analysis – see Refs. [35,45,55]. The Fock matrixes obtained from the *ab initio* calculation were transformed into the NBO basis using Gaussian 03's NBO option.[52]

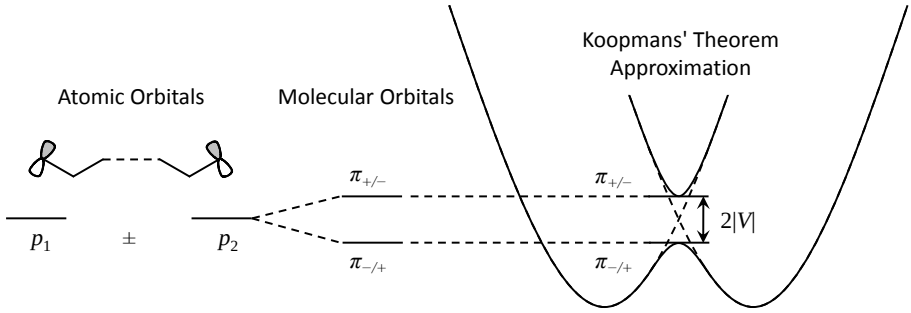

Figure 3.7. This schematic diagram shows how the electronic coupling relates to the orbital splitting. The two unpaired electrons (shown here as *p* atomic orbital's) form frontier molecular orbitals (FMOs) that can be labeled as "+" or "−" based on their parities. The sign of the splitting depends on the order of the two FMOs. We follow the convention defined in Ref. 56.

Both the radical cation coupling (dominated by hole-mediated superexchange) and radical anion coupling (dominated by electron-mediated superexchange) can be determined from the neutral molecule NBO Fock matrix, when combined with Koopmans theorem.[56,57] The general procedure is to diagonalize the α and β NBO Fock matrices, from which the splitting of the α HOMO and HOMO-1 levels corresponds to $2|V|$ for the radical cation and the splitting of the β LUMO and LUMO+1 levels corresponds to $2|V|$ for the radical anion; see Figure 3.7. If all elements of the NBO Fock matrix are retained, then the splittings are the same as the ones obtained from the original canonical molecular orbitals, because the change of basis does not affect the

eigenvalues. The couplings obtained in this way are presented in Table 3.4 and labeled as "(full)". The trend of $|V|_{cation}$(full) reproduces the experimental conductance trends: i) ether chains have lower conductance than the corresponding alkyl chains; ii) the coupling difference between 5-C and 5-O is much smaller than the difference between the longer chains. Although $|V|_{anion}$ and $|V|_{cation}$ are almost the same for the shortest chain molecules, one must consider their energy level position with respect to the Fermi level to ascertain the relative importance of electron-mediated pathways versus hole-mediated pathways. The actual Fermi level is much closer to the filled molecular orbitals, which should make the hole-mediated charge-transfer more favorable. This inference is supported by the conductance calculation and the scoring factor analysis which show that the hole-mediated superexchange dominates the coupling.

The benefit of the NBO pathway analysis arises from the use of a "reduced" NBO Fock matrix. The NBO basis set can be divided into "occupied" core orbitals, bonding orbitals, (C-C, C-O or C-H σ bonds in our system), and non-bonding lone-pair orbitals (the two terminal radicals; note the occupancy is one per orbital instead of two), "unoccupied" antibonding and extra-valence-shell orbitals (Rydbergs). The diagonal elements of the NBO Fock matrix correspond to the self-energy of each orbital, and the off-diagonal elements correspond to the interaction between the orbitals. By setting the corresponding off-diagonal elements to zero, one obtains a reduced Fock matrix with certain interactions turned off. The reduced Fock matrix can be treated in the same way as the full matrix to calculate a $|V|$ that retains only the desired interactions. The last two rows in Table 3.4 show such calculations for the cation radical case where interactions involving core orbitals and unoccupied orbitals were zeroed out, so that $|V|$ only contains the interactions among valence orbitals. Those values are similar to the corresponding "full" coupling, suggesting that the core orbitals and unoccupied orbitals play a minor role in the conductance. This finding is

consistent with the earlier MO analysis and validates this approach. Note that the error for the anion coupling is larger than that for the cation coupling, because the unoccupied molecular orbitals were used in the anion cases, and they contain more contribution from the unoccupied NBOs in the full Fock matrix. This feature is neglected because the anion pathways are less important than the cation pathways. The discussion below focuses on $|V|_{cation}$ and valence orbitals.

Table 3.4. Electronic couplings (in cm^{-1}) for the radical cations and anions.

	5-C	5-O	8-C	8-O	11-C	11-O
$\|V\|_{cation}$(full)	4451	4238	1560	1172	613	333
$\|V\|_{anion}$(full)	4587	5349	940	1326	202	339
$\|V\|_{cation}$(only valence orbitals)	4517	4334	1715	1265	733	378
$\|V\|_{anion}$(only valence orbitals)	5479	6568	1223	1814	299	532

The NBO Fock matrix of valence orbitals can be further reduced to retain only the interactions of NBOs on a specific coupling pathway, and the $|V|_{cation}$ can be decomposed into a set of couplings for individual pathways. This calculation is similar to the scoring factor decomposition of the conductance that was discussed above, but from a more "local" perspective. The number of all possible pathways for all six molecules is too large to analyze one by one, but for the bridge length regime studied in this work, "forward" pathways through the C-C (and C-O for ether chains) backbone capture the main features of $|V|_{cation}$.[56–61] Figure 3.8 shows the dominant forward pathways for each of the six model molecules. The pairwise couplings are very similar from one matrix to another because of the portability of NBO interactions. The symbol *T* indicates the coupling element involving a donor or acceptor, and *t* is used for coupling interactions only involving backbone sigma bonds. Following the convention defined in Ref. 56, the superscript indicates the distance between the two NBOs with 0 corresponding to the nearest-neighbors. The

subscript indicates the atom types, O for O-C, and C for C-C in each bond. Note that the terminal lone pair orbital is perpendicular to the nearest sigma bond so ${}^{0}T$ is usually very small and ${}^{1}T$ can be viewed as the *de facto* "nearest-neighbor" interaction. The signs of V come from the parity of the MOs and whether the symmetric level is higher than the anti-symmetric level. As observed previously,[35,60] backbone only pathways are found to be constructive.

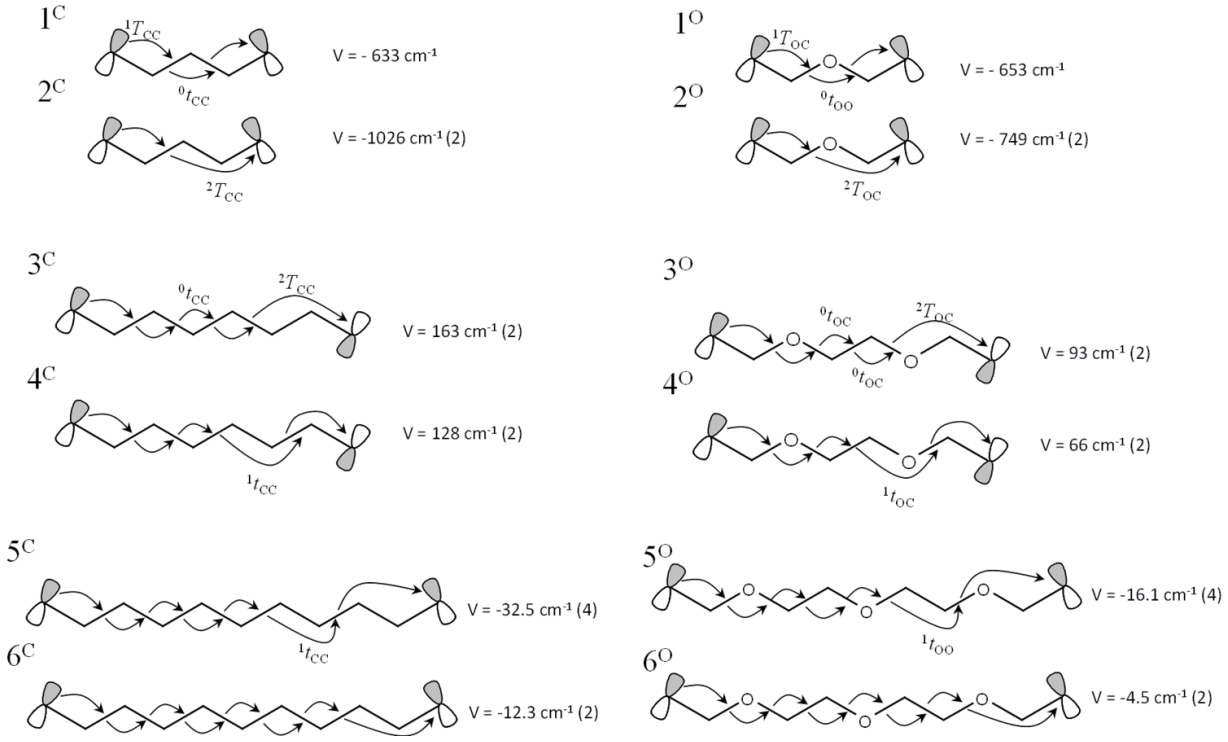

Figure 3.8. The diagrams show the dominant coupling pathways for the diradical model molecules. Couplings of identical pathways are combined together, and the number of the pathways is indicated in the parentheses.

From Figure 3.8, it is clear that the nearest neighbor pathway which is used in McConnell's model (see below) is no more important than other non-nearest neighbor pathways, and it will become less and less important to the overall conductance as the chain length increases because of the rapid growth of the total number of non-nearest pathways.[60] Another notable fact is that the McConnell pathways, 1^{C} and 1^{O}, have similar couplings, while the couplings of non-nearest pathways such as $4^{C}/4^{O}$ and $5^{C}/5^{O}$, are always larger for alkyl chains as compared to ether chains.

Thus, the larger number of possible non-nearest neighbor pathways and their dominant contribution to the overall charge transport in the longer chains (8-C, 8-O, and 11-C, 11-O) can explain the larger conductance difference between the longer alkane and ether chains than in the short chains, such as 5-O and 5-O.

Perturbation theory can be used to quantify this finding. The perturbation treatment decomposes the coupling strength of a pathway into the individual steps through the approximate expression[46]

$$V = \frac{\prod_{\mathrm{Dn}}^{\mathrm{Acc}} H_{i,j}}{\prod_{\mathrm{Bd}} \Delta_i} \qquad \textbf{Equation 3.10}$$

$H_{i,j}$ represents the coupling between adjacent NBOs, starting from the NBO of the donor to the NBO of the acceptor through the sigma bond NBOs of the chain. Δ_i is defined as $\Delta_i = \epsilon_i - \epsilon_{\mathrm{Dn}}$ in which ϵ_i is the self-energy of the NBOs, and ϵ_{Dn} is the self-energy of the lone pair NBO of the donor (which is equal to the self-energy of the lone pair NBO of the acceptor). If only the nearest-neighbor pathway is considered, the analysis reduces to the original McConnell superexchange model.[62] Because of the portability of NBO, the averaged values for the same type of interaction were used; see Table 3.5. All the parameters in Table 3.5 are normalized to the corresponding C-C bonds only interactions. The results of the perturbation treatment based on Table 3.5 are listed in Table 3.6.

Table 3.5. Values of the normalized parameters used in the perturbation calculations.

Subscript	Δ	${}^1T$	${}^2T$	${}^0t$	${}^1t$
CC	1	1	1	1	1
OC	1.52	0.99	1.09	0.94	0.88
OO	--	--	--	2.06	1.09

Table 3.6. Relative couplings that were calculated using the perturbation method for the most dominant charge transfer pathways are compared with the results obtained using MO splittings.

Pathway[a]	(No. $^0t_{OO}$)/(No. Δ_{OC})[b]	Vo/Vc(perturbation)	Vo/Vc
1^O	0.5	0.91	1.03
2^O	0	0.73	0.73
3^O	0.33	0.58	0.57
4^O	0.33	0.50	0.52
5^O	0.4	0.59	0.50
6^O	0.4	0.47	0.37

[a] The labels refer to the diagrams in Figure 3.8.

[b] Numbers of NBO interactions of each type in every pathway (see Figure 3.8) are tabularized in Table 3.7 in Supporting Materials.

As Table 3.6 shows, this analysis predicts a decrease in the ratio of V_O to V_C as the chain length increases, in qualitative argument with the experiment. Note that the errors are larger for the last two long pathways, which is probably caused by the accumulated deviation between the average values and the actual values of the NBO couplings.

The interactions in the last two rows of Table 3.5 can be divided into two types which compensate each other: Type I interactions decrease the coupling compared to alkyl chains, and Type II interactions increase the coupling compared to alkyl chains. Δ_{OC} is the strongest type I interaction, however others will play a role in the final coupling when a lot of them are included (that is, when the chain length is long enough). The strong "self-energy effect" (Δ_{OC}) can be compensated by type II interactions, of which $^0t_{OO}$ is the strongest. The effects compensate most when the ratio of the number of $^0t_{OO}$ couplings and the number of the self energy differences Δ_{OC} is as large as possible (see Table 6). The largest compensation exists for 1^O pathway, thus the overall coupling is close to that of 1^C. In contrast, when non-nearest neighbor pathways that skip a C-O bond are present then the ratio will decrease. Although $^1t_{OO}$ and other type II interactions can compensate, they are minor as compared to $^0t_{OO}$. The non-nearest neighbor pathways for 8-

C/O and 11-C/O are much more important than for 5-C/O. Also, type I interactions other than Δ_{OC} begin to play a role. The overall effect is that the conductance/coupling difference is larger in long chains, such as 8-C/O, and 11-C/O, than in the short 5-C/O.

The pathway analysis, which is described above, only focuses on the $|V|_{cation}$ in Table 3.4. If $|V|_{cation}$ is taken to be the only electronic coupling in the system, then the large electronic coupling difference for longer chains is similar to what Napper *et al.* found ($|V|_{cation}(C)/|V|_{cation}(O) \approx 0.6$ for a chain with 13 heavy atoms and one oxygen atom maximum),[35] but it is an overestimation when compared with the conductance experiments and calculation. This overestimation may result from not including the electron mediated $|V|_n$ in this latter analysis and suggests that hole-mediated tunneling may be more important in the electrochemical charge transfer than in the conductance measurements.

3.4 CONCLUSIONS

Single molecule conductance measurements showed that the molecular conductance of alkoxy chains is smaller than that of alkane chains. Computational methods were used to show that the contribution of the molecular orbitals to the conductance depend strongly on their delocalization, with higher contributions for more delocalized orbitals. Delocalization of the orbitals was found to be higher in the alkyl chains than in the oligoethers, a trend that is in agreement with that of the conductances determined experimentally. In addition, an NBO pathway analysis shows that the self-energy shift of due to the presence of oxygen atoms is compensated by an increased coupling for the shortest chains, 5-C and 5-O. For the longer chains, the non-nearest neighbor contributions

to the overall coupling decreases this compensation and the difference in couplings through the two chains is more strongly manifested.

3.5 SUPPORTING INFORMATION

3.5.1 Conductance Distributions

The conductance of the single dithiolated molecules was measured using the STM-controlled break-junction method.[6] In this experiment, the molecules of interest are occasionally trapped between the substrate and an STM tip by periodic modulation of the tip-substrate separation. During this process, the tunneling current is monitored as a function of the tip-substrate distance at a constant bias voltage. The conductance is determined by statistical analysis of current-distance characteristics.

Typically, 2000 - 3000 current-distance characteristics were collected to construct conductance distribution for each studied compound. A 10 nA/V preamplifier was used in measurements. Current-distance curves were recorded under 0.5 V bias. Curves attributed with current plateaus (20-30% of the total data set) were manually selected for further analysis. Measured conductances were plotted in the form of normalized histograms in logarithmic scale, with 25 bins per decade. For each of studied molecules, Gaussian function was fitted to the conductance distribution to determine position of the conductance peak. The conductance distributions plotted in linear scale together with fitted Gaussian functions are provided in Supporting Materials. Conductance results are expressed in quantum conductance units $G_0 = 2e^2/h \approx 77\ \mu S$.

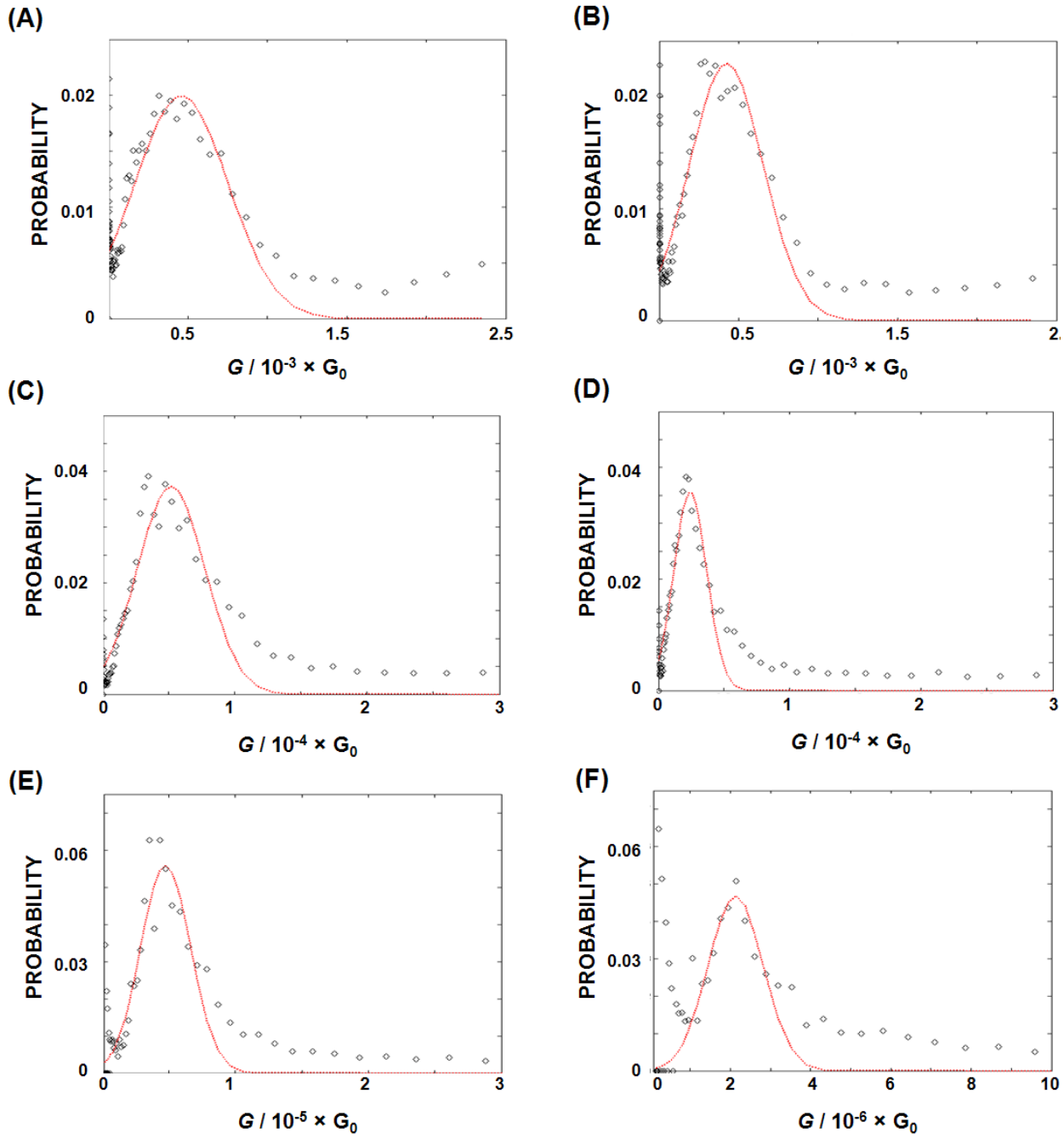

Figure 3.9. Conductance distributions (black diamonds) constructed for 1,5-pentanedithiol (A), 2-mercaptoethyl ether (B), 1,8-octanedithiol (C), 2,2′-(ethylenedioxy)diethanethiol (D), 1,11-undecanedithiol (E), and tetra(ethylene glycol) dithiol (F). Red dotted lines represent Gaussian distributions fitted to experimental data.

3.5.2 Comparison of Measured Conductance with Literature.

We note that several modes of conductance, resulted by variations in Au-S bond geometry, have been determined in single molecule measurements of dithiolated molecules, in particular alkanedithiols.[10–12] In Figure 3.10A is shown comparison of our experimental data obtained for alkanedithiols with the data adopted from Ref.12.This comparison indicates that the data presented in this manuscript corresponds to the "medium" mode of conductance data reported in Ref. 12. Comparison of the data obtained for 1,5-pentanedithiol molecule with preamplifiers characterized by different sensitivity and working range of currents is shown in Figure 3.10B. The "high" mode of conductance measured for that compound is in agreement with predictions given in Ref. 12, but it can be only measured with the preamplifier characterized by logarithmic characteristics, and it is too high for 10 nA/V preamplifier. Moreover, the "high" conductance peak is much smaller that of "medium" conductance, thus "high" conductance is hard to determine.

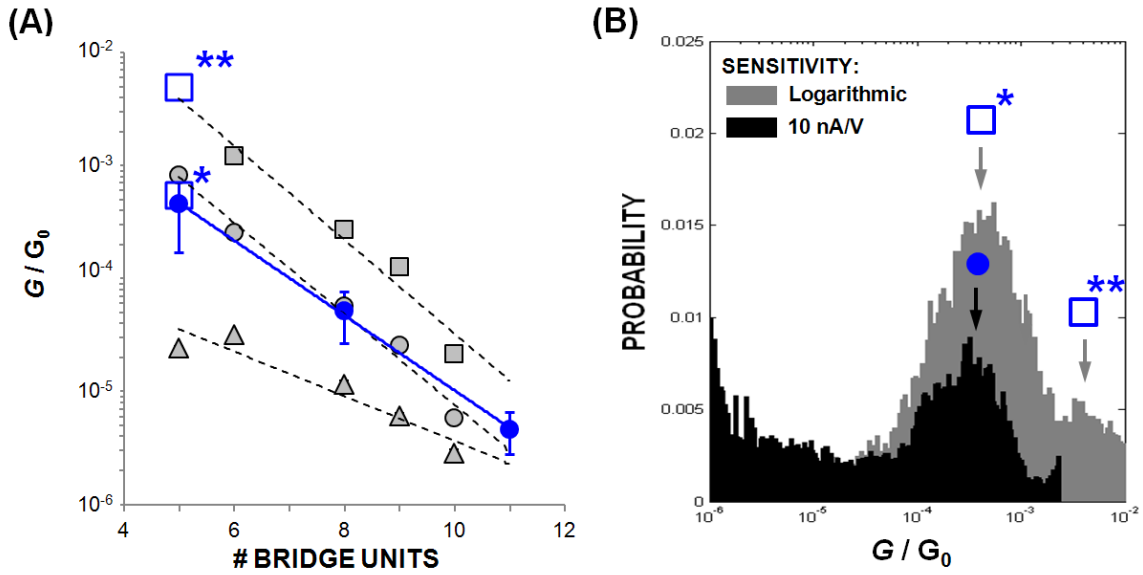

Figure 3.10. Panel (A) show comparison of length distance dependences based on the conductance measurements presented in this work (blue symbols) and the data adopted from work of Wandlowski, Evers and coworkers (grey

symbols).[11] Different grey symbols reflect different modes of conductance caused by the differences in the geometry of the thiol bond with gold. Blue circles represent experimental data obtained in this work using 10 nA/V preamplifier. Squares represent conductance values determined in this work using preamplifier with logarithmic characteristics. Asterisks point to the peaks in the conductance distributions presented in panel (B) that were obtained for 1,5-pentanedithiol using preamplifiers with 10 nA/V and logarithmic sensitivity.

Probing different contact geometries and their influence on the single molecule conductivity is out of the scope in this manuscript; therefore our results are limited to the data obtained using 10nA/V sensitivity, with main focus on the major peak in the conductance distributions.

3.5.3 Dependence of the Single Molecule Conductance on the Length of Studied Molecules.

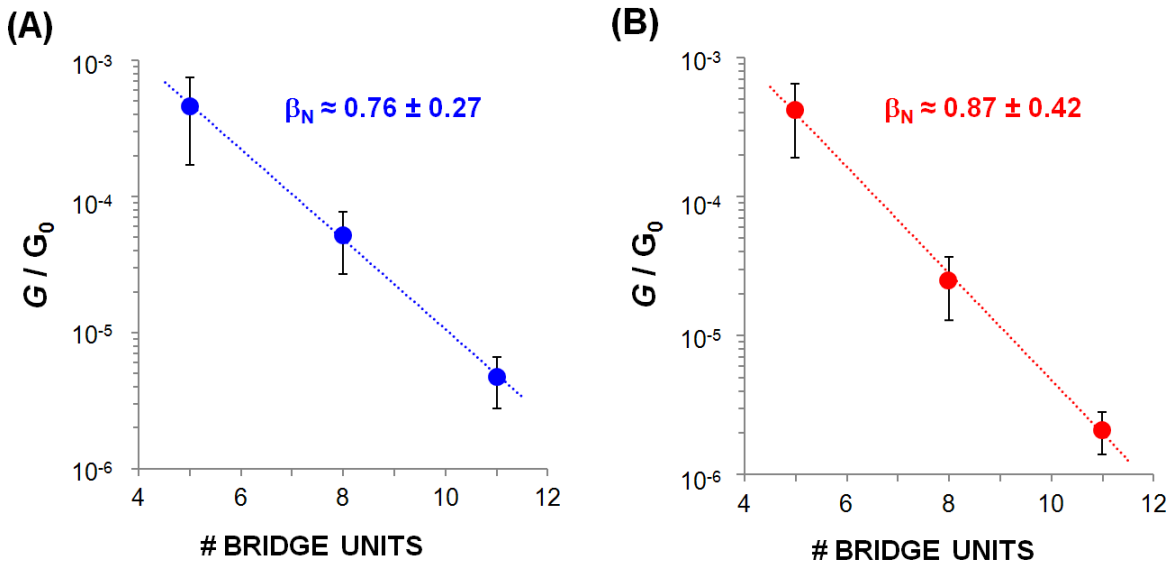

Figure 3.11. Dependence of the conductance on the length of the hydrocarbon (A) and oligoether (B) chains. Dotted lines show the least squares fits to experimental data by exponential function with decay constant β_N.

3.5.4 Contributions of Molecular Orbitals to Calculated Conductance.

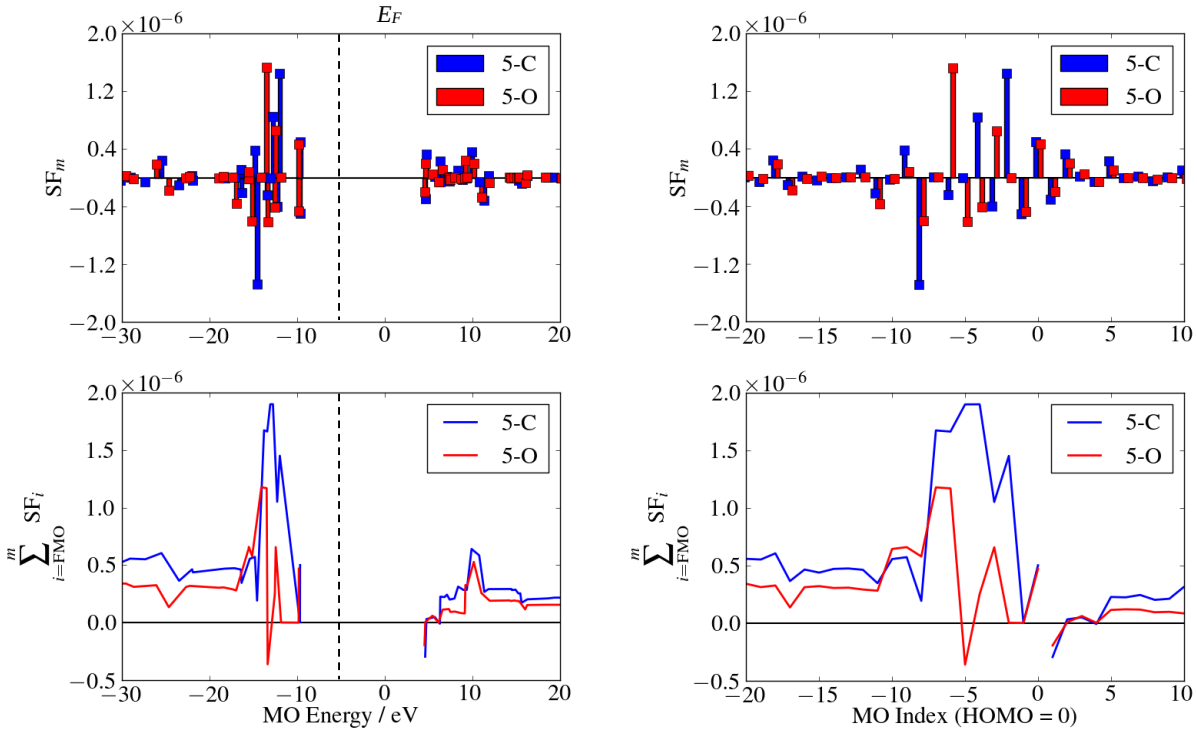

Figure 3.12. Left Panel: Comparison of scoring factors (top row) and their sums (bottom row) for 5-C (blue) and 5-O (red) molecules. The sums are calculated separately for HOMO and LUMO levels starting from frontier molecular orbitals. Energy of Fermi level E_F=-5.5 eV that was used in conductance calculations is indicated in graphs by dotted lines. Right Panel: The same comparison plotted versus MO Index.

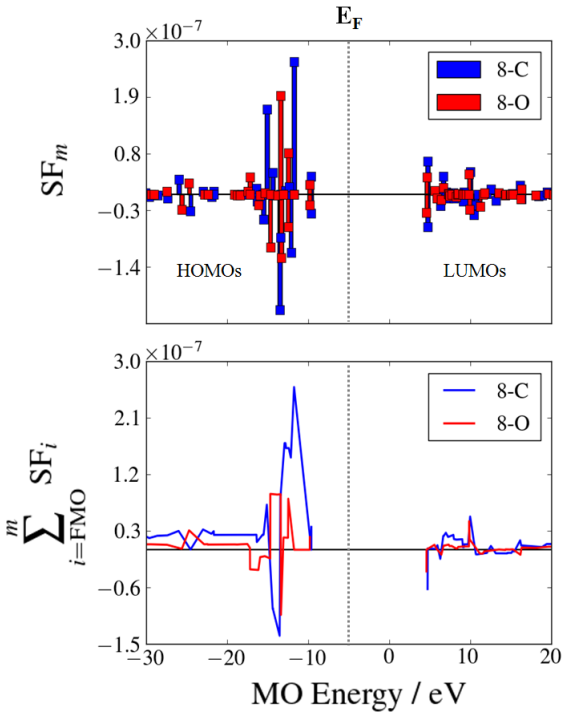

Figure 3.13. The scoring factors (top panel) and their partial sums (bottom panel) are shown for 8-C (blue) and 8-O (red) molecules. The sums are calculated separately for HOMO and LUMO levels starting from frontier molecular orbitals. The energy of Fermi level E_F=-5.5 eV that was used in conductance calculations is indicated in graphs by dotted lines.

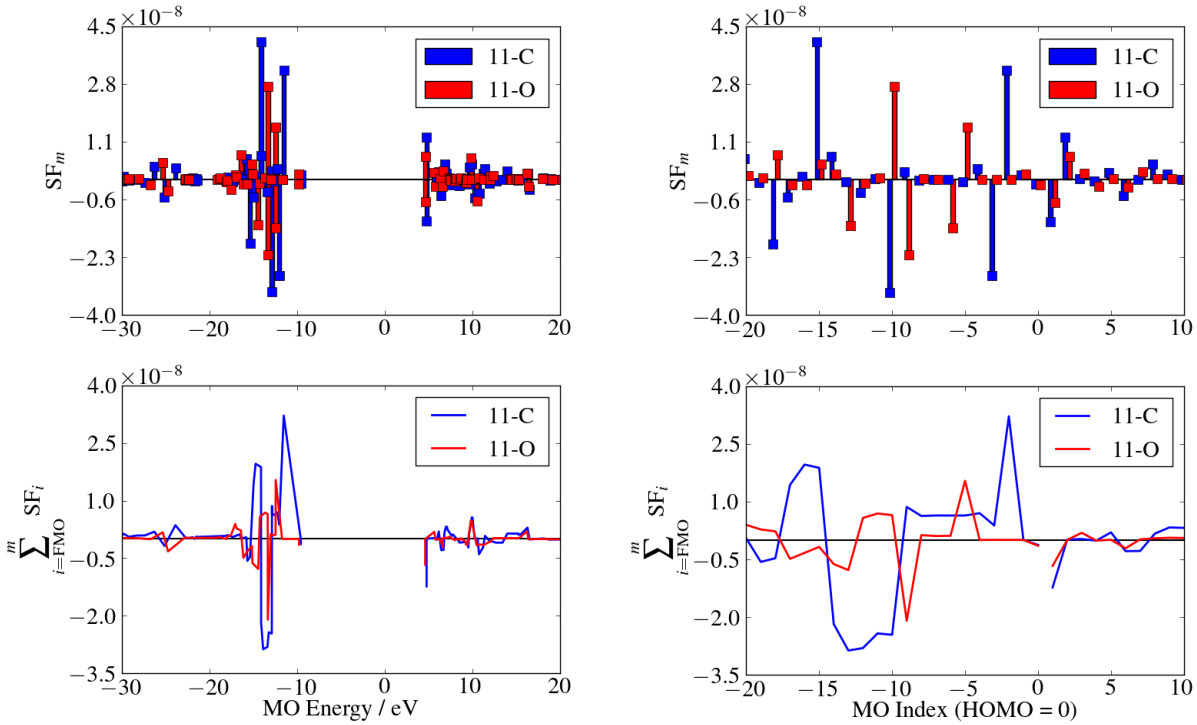

Figure 3.14. Left Panel: Comparison of scoring factors (top row) and their sums (bottom row) for 11-C (blue) and 11-O (red) molecules. The sums are calculated separately for HOMO and LUMO levels starting from frontier molecular orbitals. Energy of Fermi level E_F=-5.5 eV that was used in conductance calculations is indicated in graphs by dotted lines. Right Panel: The same comparison plotted versus MO Index.

3.5.5 Calculated Energies of the LUMO Levels.

We note that our calculations give, in all cases, a similar HOMO-LUMO gap of about 14 eV. The calculated position of the HOMO level is close to that determined from photoemission of alkanethiol self-assembled,[63] while the calculated LUMO level is about 4.5 eV above the vacuum level. The high energy of the LUMO level results in the calculated HOMO-LUMO gap higher than the gap of 8 - 9 eV reported for bulk polyethylene,[64,65] and 9-10 eV for alkanethiol SAMs.[63] In these experiments, LUMOs from numerous molecules formed a band what is measured is the edge (onset) of the band. Besides, deficiencies significantly decrease the band edge because it is very unfavorable for a fully saturated alkane chain to acceptor excess electrons. Thus, the experimental gap values from bulk or SAMs cannot be compared with the theoretical single molecule HOMO-LUMO gap directly. In the study presented in this manuscript, the relative position of the energy levels of the molecular orbitals in respect to the Fermi level of the gold electrodes for different chemical species (alkanes versus oligoethers) decides about the contribution of these MOs to the overall conductance, while the absolute value of the energy gap obtained in the calculations does not influence the conclusions.

3.5.6 Spatial Distributions of Selected Molecular Orbitals.

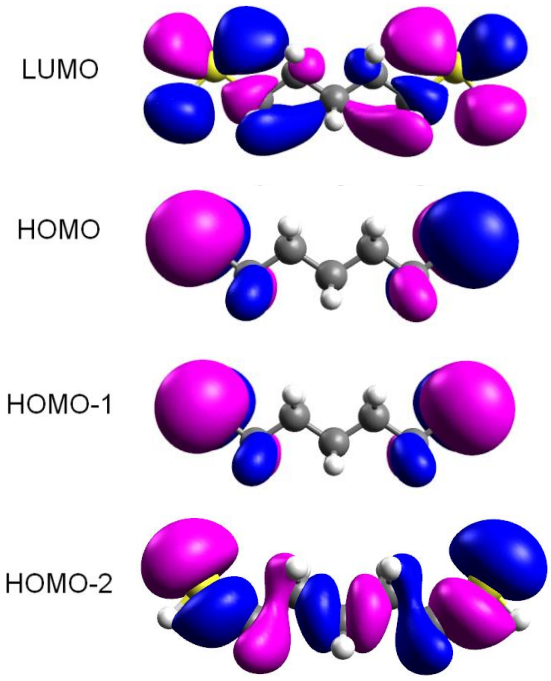

Figure 3.15. Spatial distributions of selected molecular orbitals in 5-C.

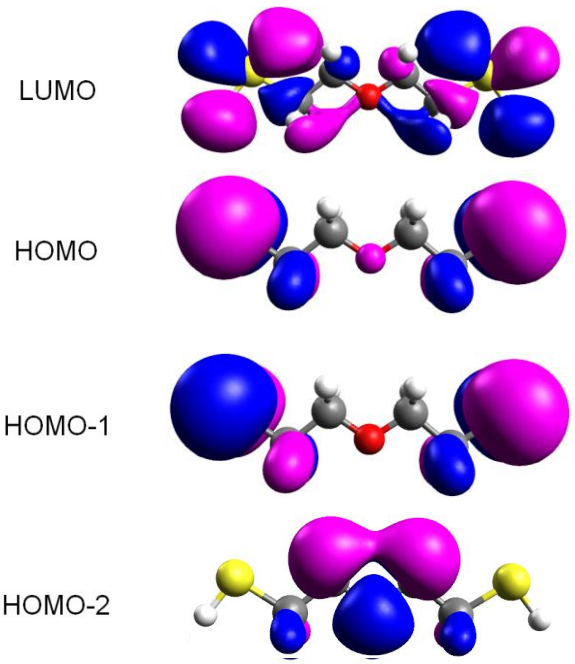

Figure 3.16. Spatial distributions of selected molecular orbitals in 5-O.

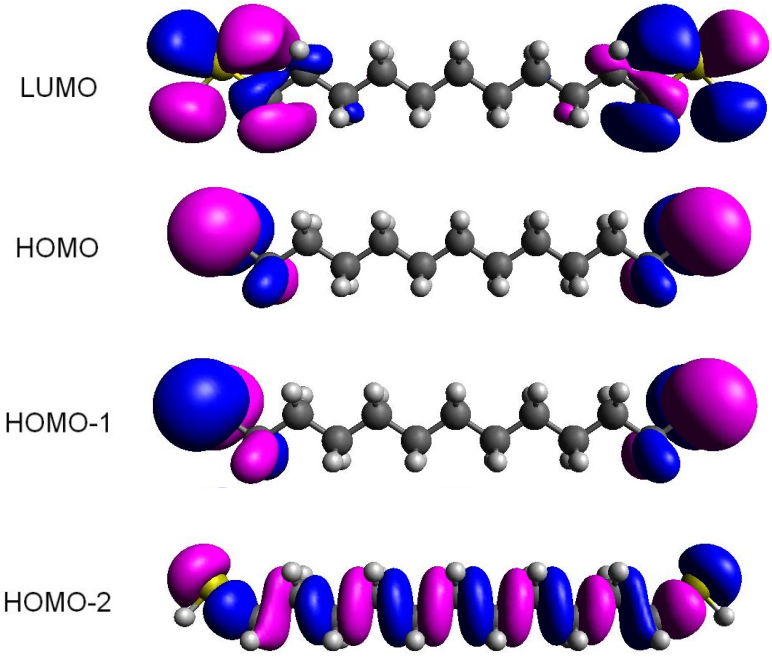

Figure 3.17. Spatial distributions of selected molecular orbitals in 11-C.

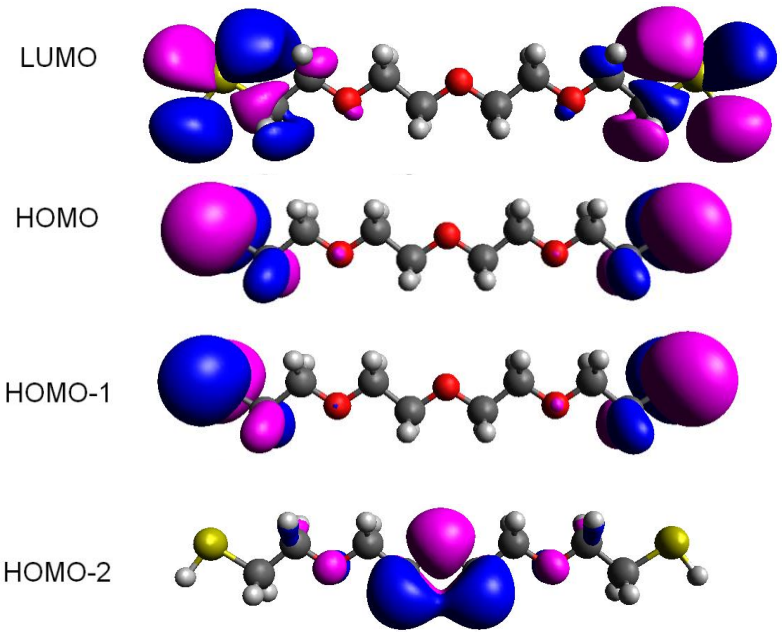

Figure 3.18. Spatial distributions of selected molecular orbitals in 11-O.

3.5.7 Number of the Most Dominant Pathways used in Perturbation Method.

Table 3.7. Number of NBO interactions of each type for the most dominant pathways used in the calculations in Table 3.6.

	Δ_{OC}	$^{1}T_{OC}$	$^{2}T_{OC}$	$^{0}t_{OC}$	$^{0}t_{OO}$	$^{1}t_{OC}$	$^{1}t_{OO}$
1^{O}	2	2	--	--	1	--	--
2^{O}	1	1	1	--	--	--	--
3^{O}	3	1	1	2	1	--	--
4^{O}	3	2	--	1	1	1	--
5^{O}	5	1	1	2	2	--	1
6^{O}	5	1	1	4	2	--	--

3.6 REFERENCES

(1) Mann, B.; Kuhn, H. *J. Appl. Phys.* **1971**, *42*, 4398.

(2) Aviram, A.; Ratner, M. A. *Chem. Phys. Lett.* **1974**, *29*, 277.

(3) Reed, M. A.; Zhou, C.; Muller, C. J.; Burgin, T. P.; Tour, J. M. *Science (80-.).* **1997**, *278*, 252.

(4) Porath, D.; Bezryadin, A.; de Vries, S.; Dekker, C. *Nature* **2000**, *403*, 635.

(5) Cui, X. D.; Primak, a; Zarate, X.; Tomfohr, J.; Sankey, O. F.; Moore, a L.; Moore, T. a; Gust, D.; Harris, G.; Lindsay, S. M. *Science* **2001**, *294*, 571.

(6) Xu, B.; Tao, N. J. *Science* **2003**, *301*, 1221.

(7) Guo, X.; Small, J. P.; Klare, J. E.; Wang, Y.; Purewal, M. S.; Tam, I. W.; Hong, B. H.; Caldwell, R.; Huang, L.; O'brien, S.; Yan, J.; Breslow, R.; Wind, S. J.; Hone, J.; Kim, P.; Nuckolls, C. *Science* **2006**, *311*, 356.

(8) Haiss, W.; Nichols, R. J.; van Zalinge, H.; Higgins, S. J.; Bethell, D.; Schiffrin, D. J. *Phys. Chem. Chem. Phys.* **2004**, *6*, 4330.

(9) Venkataraman, L.; Klare, J. E.; Tam, I. W.; Nuckolls, C.; Hybertsen, M. S.; Steigerwald, M. L. *Nano Lett.* **2006**, *6*, 458.

(10) Wierzbinski, E.; Slowinski, K. *Langmuir* **2006**, *22*, 5205.

(11) Li, X.; He, J.; Hihath, J.; Xu, B.; Lindsay, S. M.; Tao, N. *J. Am. Chem. Soc.* **2006**, *128*, 2135.

(12) Li, C.; Pobelov, I.; Wandlowski, T.; Bagrets, A.; Arnold, A.; Evers, F. *J. Am. Chem. Soc.* **2008**, *130*, 318.

(13) Martin, S.; Giustiniano, F. *J. …* **2009**, *113*, 18884.

(14) Parameswaran, R.; Widawsky, J. R.; Vázquez, H.; Park, Y. S.; Boardman, B. M.; Nuckolls, C.; Steigerwald, M. L.; Hybertsen, M. S.; Venkataraman, L. *J. Phys. Chem. Lett.* **2010**, *1*, 2114.

(15) Huber, R.; González, M. T.; Wu, S.; Langer, M.; Grunder, S.; Horhoiu, V.; Mayor, M.; Bryce, M. R.; Wang, C.; Jitchati, R.; Schönenberger, C.; Calame, M. *J. Am. Chem. Soc.* **2008**, *130*, 1080.

(16) Yamada, R.; Kumazawa, H.; Noutoshi, T.; Tanaka, S.; Tada, H. *Nano Lett.* **2008**, *8*, 1237.

(17) Kaliginedi, V.; Moreno-García, P.; Valkenier, H.; Hong, W.; García-Suárez, V. M.; Buiter, P.; Otten, J. L. H.; Hummelen, J. C.; Lambert, C. J.; Wandlowski, T. *J. Am. Chem. Soc.* **2012**, *134*, 5262.

(18) Diez-Perez, I.; Hihath, J.; Hines, T.; Wang, Z.-S.; Zhou, G.; Müllen, K.; Tao, N. *Nat. Nanotechnol.* **2011**, *6*, 226.

(19) Morita, T.; Lindsay, S. *J. Phys. Chem. B* **2008**, *112*, 10563.

(20) Shih, K.-N.; Huang, M.-J.; Lu, H.-C.; Fu, M.-D.; Kuo, C.-K.; Huang, G.-C.; Lee, G.-H.; Chen, C.; Peng, S.-M. *Chem. Commun. (Camb).* **2010**, *46*, 1338.

(21) Zhou, X.-S.; Liu, L.; Fortgang, P.; Lefevre, A.-S.; Serra-Muns, A.; Raouafi, N.; Amatore, C.; Mao, B.-W.; Maisonhaute, E.; Schöllhorn, B. *J. Am. Chem. Soc.* **2011**, *133*, 7509.

(22) Sedghi, G.; Sawada, K.; Esdaile, L. J.; Hoffmann, M.; Anderson, H. L.; Bethell, D.; Haiss, W.; Higgins, S. J.; Nichols, R. J. *J. Am. Chem. Soc.* **2008**, *130*, 8582.

(23) Kiguchi, M.; Takahashi, T.; Kanehara, M.; Teranishi, T.; Murakoshi, K. *J. Phys. Chem. C* **2009**, *113*, 9014.

(24) Perrin, M. L.; Prins, F.; Martin, C. A.; Shaikh, A. J.; Eelkema, R.; van Esch, J. H.; Briza, T.; Kaplanek, R.; Kral, V.; van Ruitenbeek, J. M.; van der Zant, H. S. J.; Dulić, D. *Angew. Chem. Int. Ed. Engl.* **2011**, *50*, 11223.

(25) Li, Z.; Park, T.-H.; Rawson, J.; Therien, M. J.; Borguet, E. *Nano Lett.* **2012**, *12*, 2722.

(26) Xiao, X.; Xu, B.; Tao, N. *J. Am. Chem. Soc.* **2004**, *126*, 5370.

(27) Sek, S.; Misicka, A.; Swiatek, K.; Maicka, E. *J. Phys. Chem. B* **2006**, *110*, 19671.

(28) Xu; Zhang; Li; Tao *Nano Lett.* **2004**, *4*, 1105.

(29) Hihath, J.; Xu, B.; Zhang, P.; Tao, N. *Proc. Natl. Acad. Sci. U. S. A.* **2005**, *102*, 16979.

(30) Van Zalinge, H.; Schiffrin, D. J.; Bates, A. D.; Haiss, W.; Ulstrup, J.; Nichols, R. J. *Chemphyschem* **2006**, *7*, 94.

(31) Wierzbinski, E.; Arndt, J.; Hammond, W.; Slowinski, K. *Langmuir* **2006**, *22*, 2426.

(32) Venkatramani, R.; Davis, K. L.; Wierzbinski, E.; Bezer, S.; Balaeff, A.; Keinan, S.; Paul, A.; Kocsis, L.; Beratan, D. N.; Achim, C.; Waldeck, D. H. *J. Am. Chem. Soc.* **2011**, *133*, 62.

(33) Wierzbinski, E.; de Leon, A.; Davis, K. L.; Bezer, S.; Wolak, M. A.; Kofke, M. J.; Schlaf, R.; Achim, C.; Waldeck, D. H. *Langmuir* **2012**, *28*, 1971.

(34) Thuo, M. M.; Reus, W. F.; Simeone, F. C.; Kim, C.; Schulz, M. D.; Yoon, H. J.; Whitesides, G. M. *J. Am. Chem. Soc.* **2012**, *134*, 10876.

(35) Napper, A. M.; Liu, H.; Waldeck, D. H. *J. Phys. Chem. B* **2001**, *105*, 7699.

(36) Chidsey, C. E. D.; Bertozzi, C. R.; Putvinski, T. M.; Mujsce, a. M. *J. Am. Chem. Soc.* **1990**, *112*, 4301.

(37) Paul, A.; Watson, R. M. R. M.; Lund, P.; Xing, Y.; Burke, K.; He, Y.; Borguet, E.; Achim, C.; Waldeck, D. H. D. H. *J. Phys. Chem. C* **2008**, *112*, 7233.

(38) Sek, S.; Misicka, A.; Bilewicz, R. *J. Phys. Chem. B* **2000**, *104*, 5399.

(39) Sek, S.; Palys, B.; Bilewicz, R. *J. Phys. Chem. B* **2002**, *106*, 5907.

(40) Wain, A. J.; Do, H. N. L.; Mandal, H. S.; Kraatz, H.-B.; Zhou, F. *J. Phys. Chem. C. Nanomater. Interfaces* **2008**, *112*, 14519.

(41) Slowinski, K.; Chamberlain, R. V.; Miller, C. J.; Majda, M. *J. Am. Chem. Soc.* **1997**, *119*, 11910.

(42) Traub, M. C.; Brunschwig, B. S.; Lewis, N. S. *J. Phys. Chem. B* **2007**, *111*, 6676.

(43) Venkatramani, R. *In Preparation.*

(44) Wierzbinski, E.; Venkatramani, R.; Davis, K. L.; Bezer, S.; Kong, J.; Xing, Y.; Borguet, E.; Achim, C.; Beratan, D. N.; Waldeck, D. H. *ACS Nano* **2013**, *7*, 5391.

(45) Jordan, K. D.; Paddon-Row, M. N. In *Encyclopedia of Computational Chemistry*; John Wiley & Sons, 1998; pp. 826–835.

(46) Ratner, M. A. *J. Phys. Chem.* **1990**, *94*, 4877.

(47) Paul, A.; Bezer, S.; Venkatramani, R.; Kocsis, L.; Wierzbinski, E.; Balaeff, A.; Keinan, S.; Beratan, D. N.; Achim, C.; Waldeck, D. H. *J. Am. Chem. Soc.* **2009**, *131*, 6498.

(48) Wierzbinski, E.; de Leon, A.; Yin, X.; Balaeff, A.; Davis, K. L.; Rapireddy, S.; Reppireddy, S.; Venkatramani, R.; Keinan, S.; Ly, D. H.; Madrid, M.; Beratan, D. N.; Achim, C.; Waldeck, D. H.; Rappireddy, S.; Venkatramani, R.; Keinan, S.; Ly, D. H.; Madrid, M.; Beratan, D. N.; Achim, C.; Waldeck, D. H. *J. Am. Chem. Soc.* **2012**, *134*, 9335.

(49) Frisch, M. J. .; Trucks, G. W. .; Schlegel, H. B. .; Scuseria, G. E. .; Robb, M. A. .; Cheeseman, J. R. .; Montgomery Jr, J. A.; Vreven, T. .; Kudin, K. N. .; Burant, J. C. .; Millam, J. M. .; Iyengar, S. S. .; Tomasi, J. .; Barone, V. .; Mennucci, B. .; Cossi, M. .; Scalmani, G. .; Rega, N. .; Petersson, G. A. .; Nakatsuji, H. .; Hada, M. .; Ehara, M. .;

Toyota, K. .; Fukuda, R. .; Hasegawa, J. .; Ishida, M. .; Nakajima, T. .; Honda, Y. .; Kitao, O. .; Nakai, H. .; Klene, M. .; Li, X. .; Knox, J. E. .; Hratchian, H. P. .; Cross, J. B. .; Bakken, V. .; Adamo, C. .; Jaramillo, J. .; Gomperts, R. .; Stratmann, R. E. .; Yazyev, O. .; Austin, A. J. .; Cammi, R. .; Pomelli, C. .; Ochterski, J. W. .; Ayala, P. Y. .; Morokuma, K. .; Voth, G. A. .; Salvador, P. .; Dannenberg, J. J. .; Zakrzewski, V. G. .; Dapprich, S. .; Daniels, A. D. .; Strain, M. C. .; Farkas, O. .; Malick, D. K. .; Rabuck, A. D. .; Raghavachari, K. .; Foresman, J. B. .; Ortiz, J. V. .; Cui, Q. .; Baboul, A. G. .; Clifford, S. .; Cioslowski, J. .; Stefanov, B. B. .; Liu, G. .; Liashenko, A. .; Piskorz, P. .; Komaromi, I. .; Martin, R. L. .; Fox, D. J. .; Keith, T. .; Al-Laham, M. A. .; Peng, C. Y. .; Nanayakkara, A. .; Challacombe, M. .; Gill, P. M. W. .; Johnson, B. .; Chen, W. .; Wong, M. W. .; Gonzalez, C. .; Pople, J. A. .; Montgomery J. A.;, J.; Vreven, T. .; Kudin, K. N. .; Burant, J. C. .; Millam, J. M. .; Iyengar, S. S. .; Tomasi, J. .; Barone, V. .; Mennucci, B. .; Cossi, M. .; Scalmani, G. .; Rega, N. .; Petersson, G. A. .; Nakatsuji, H. .; Hada, M. .; Ehara, M. .; Toyota, K. .; Fukuda, R. .; Hasegawa, J. .; Ishida, M. .; Nakajima, T. .; Honda, Y. .; Kitao, O. .; Nakai, H. .; Klene, M. .; Li, X. .; Knox, J. E. .; Hratchian, H. P. .; Cross, J. B. .; Bakken, V. .; Adamo, C. .; Jaramillo, J. .; Gomperts, R. .; Stratmann, R. E. .; Yazyev, O. .; Austin, A. J. .; Cammi, R. .; Pomelli, C. .; Ochterski, J. W. .; Ayala, P. Y. .; Morokuma, K. .; Voth, G. A. .; Salvador, P. .; Dannenberg, J. J. .; Zakrzewski, V. G. .; Dapprich, S. .; Daniels, A. D. .; Strain, M. C. .; Farkas, O. .; Malick, D. K. .; Rabuck, A. D. .; Raghavachari, K. .; Foresman, J. B. .; Ortiz, J. V. .; Cui, Q. .; Baboul, A. G. .; Clifford, S. .; Cioslowski, J. .; Stefanov, B. B. .; Liu, G. .; Liashenko, A. .; Piskorz, P. .; Komaromi, I. .; Martin, R. L. .; Fox, D. J. .; Keith, T. .; Al-Laham, M. A. .; Peng, C. Y. .; Nanayakkara, A. .; Challacombe, M. .; Gill, P. M. W. .; Johnson, B. .; Chen, W. .; Wong, M. W. .; Gonzalez, C. .; Pople, J. A. Gaussian 03, Revision E.01 **2004**.

(50) Reed, A. E.; Weinhold, F. *J. Chem. Phys.* **1983**, *78*, 4066.

(51) Reed, A. E.; Weinstock, R. B.; Weinhold, F. *J. Chem. Phys.* **1985**, *83*, 735.

(52) Glendening, E. D.; Reed, A. E.; Carpenter, J. E.; Weinhold, F. NBO Version 3.1.

(53) Ashcroft, N. W.; Mermin, N. D. *Solid State Physics*; Harcourt College Publishers, 1976.

(54) Gangamani, B. P.; Kumar, V. A.; Ganesh, K. N. *Synthesis (Stuttg).* **1997**, 1913.

(55) Shephard, M. J.; Paddon-Row, M. N.; Jordan, K. D. *Chem. Phys.* **1993**, *176*, 289.

(56) Liang, C.; Newton, M. D. *J. Phys. Chem.* **1992**, *96*, 2855.

(57) Liang, C.; Newton, M. D. *J. Phys. Chem.* **1993**, *97*, 3199.

(58) Curtiss, L.; Naleway, C.; Miller, J. *J. Phys. Chem.* **1993**, *97*, 4050.

(59) Curtiss, L. A.; Naleway, C. A.; Miller, J. R. *Chem. Phys.* **1993**, *176*, 387.

(60) Jordan, K. D.; Paddon-Row, M. N. *Chem. Rev.* **1992**, *92*, 395.

(61) Shephard, M. J.; Paddon-Row, M. N.; Jordan, K. D. *J. Am. Chem. Soc.* **1994**, *116*, 5328.

(62) McConnell, H. M. *J. Chem. Phys.* **1961**, *35*, 508.

(63) Boulas, C.; Davidovits, J.; Rondelez, F.; Vuillaume, D. *Phys. Rev. Lett.* **1996**, *76*, 4797.

(64) Fujihira, M.; Inokuchi, H. *Chem. Phys. Lett.* **1972**, *17*, 554.

(65) Less, K. J.; Wilson, E. G. *J. Phys. C Solid State Phys.* **1973**, *6*, 3110.

4.0 THE EFFECT OF BACKBONE FLEXIBILITY ON CHARGE TRANSFER RATES IN PEPTIDE NUCLEIC ACID DUPLEXES

This work has been published as Wierzbinski, E.; de Leon, A.; Yin, X.; Balaeff, A.; Davis, K. L.; Rapireddy, S.; Reppireddy, S.; Venkatramani, R.; Keinan, S.; Ly, D. H.; Madrid, M.; Beratan, D. N.; Achim, C.; Waldeck, D. H.; Rappireddy, S. J. Am. Chem. Soc. 2012, 134, 9335–9342. The author of this dissertation performed molecular dynamics simulation and conductance analysis.

Charge transfer (CT) properties are compared between peptide nucleic acid with an aminoethylglycine backbone (aeg-PNA) and that with a γ-methylated backbone (γ-PNA). The common aeg-PNA is an achiral molecule with flexible structure, whereas γ-PNA is a chiral molecule with a significantly more rigid structure than aeg-PNA. Electrochemical measurements show that the CT rate through an aeg-PNA bridging unit is twice the CT rate through a γ-PNA bridge unit. Theoretical calculations of PNA electronic properties, which are based on a molecular dynamics structural ensemble, reveal that the difference in the CT rate results from the difference in the extent of backbone fluctuations of aeg- and γ-PNA. In particular, fluctuations of the backbone affect the local electric field that broadens the energy levels of PNA nucleobases. The greater flexibility of the aeg-PNA gives rise to more broadening and a more frequent appearance of high-CT rate conformations, as compared to γ-PNA. This finding has implications for the design of nucleic acid-based molecular electronics components.

4.1 INTRODUCTION

DNA and its synthetic analogues are of great interest because of their potential applications as scaffolds for nanostructures[1–4] and as active elements in nanoelectronic devices.[3,5] In part, this promise arises from the fact that nucleic acids can form well-defined, supramolecular structures based on Watson Crick hybridization. Our interest lies in the long distance charge transfer (CT) properties of nucleic acids (NAs) and the dependence of these properties on nucleobase sequence and the backbone chemistry.[6–9] While the nucleobase effect on CT in nucleic acids is widely explored, the impact of the backbone's properties on the CT is not as well studied.[10,11] This work explores how the backbone rigidity affects the CT properties of nucleic acids.

Several CT mechanisms are known to operate in NAs (see Ref. 12 and references therein). In the short distance range, the CT is characterized by an exponential decrease of the rate constant with distance and is commonly understood to follow a superexchange dominated tunneling mechanism. Across longer distances, the thermally-induced hopping mechanism is assumed to operate, wherein the CT rate constant decreases as a power law. In addition to the distance, the CT mechanism depends on the NA sequence and the energy levels of the charge donor and acceptor (or the electrode Fermi energy). In certain situations, a near-resonant CT regime was identified, wherein the hopping and superexchange CT mechanisms coexist.[13]

The effect of the nucleobase sequence on the charge localization and transport is strongly correlated with the presence of guanine (G).[14–18] Because of its lower oxidation potential with respect to the other nucleobases, G can stabilize positive charge (hole) and thus dominate the CT mechanism.[19] The charge transport through DNA can also be accelerated by replacing adenine (A) in thymine-adenine (TA) base pairs by a lower oxidation potential base, such as 7-deazaadenine[18] or diaminopurine.[17,18] It is important to note that clusters of lower oxidation potential bases do not

accelerate the overall charge transport.[20–22] For example, Sugiyama and coworkers showed that adjacent G bases, GG or GGG, do not cause an increase in the rate constant of long-range charge transfer through DNA, but can act as hole trapping states.[23,24] Electronic structure calculations suggest that CT may be enhanced by extending the aromaticity of the nucleobases, as in size-extended DNA.[25–29] Another strategy to manipulate the charge transport in nucleic acids is to incorporate metal ions into the nucleic acid helix, resulting in the so-called M-DNA.[30,31] Finally, we note that CT through DNA can be significantly perturbed by "defects", such as base pair (bp) mismatches,[32–36] abasic sites,[33] and methylated or oxidized nucleobases.[37]

While earlier CT studies with NA's show unequivocally that nucleobase sequence is a major determinant of the mechanism and CT rate, the influence of the NA backbone on charge transfer is relatively poorly studied.[10,11] For example, Barton *et al.* showed that CT through DNA monolayers was not affected by a nick in the DNA backbone.[11] However, other studies find that the nucleobase geometry and fluctuations, which are determined by the NA backbone chemistry, have a noticeable effect on the CT rate and mechanism in NA's. For example, a theoretical study by Hatcher *et al.*[10] concluded that the CT through 4 bp-long DNA and PNA[38] duplexes was affected by the structural flexibility of the duplexes. In particular, the CT rate constant through PNA was predicted to be higher than that through DNA because larger fluctuations make PNA more likely to adopt conformations with stronger donor-acceptor couplings that favor CT. Notably, Hatcher *et al.* focused on charge mediation by the nucleobase stack only; the nucleic acid backbone was included in their geometry sampling but not in their quantum mechanical analysis of CT. This approximation has been standard in treating the NA electronic structure because the ground and the first excited states of the excess charge are localized mostly on the nucleobases.[10,12,39,40]

DNA analogues enable investigations of how the backbone structure and dynamics can affect the charge transfer rate through NAs. A wide variety of NA structures, such as locked nucleic acid (LNA),[41,42] threose nucleic acid (TNA),[43] glycol nucleic acid (GNA),[44] and PNA[45,46] are all available. Although these analogues hybridize according to the Watson-Crick rules, their helicoidal parameters and their conformational flexibility vary. Consequently, the electronic couplings among bases in different analogues of DNA vary as well. Additionally, the NA backbone structure and fluctuations affect those of the nucleobase stack and may have a gating effect on the CT through the nucleobases, as has been reported for DNA[47–50] and other molecules.[51–53] Apart from the direct conformational effect, the differences in the backbone structure and chemical composition between the NAs translate into differences in local electric field that the nucleobases experience. Hence, the polarization and broadening of nucleobase-localized charge states differ among the NAs, resulting in different CT properties.[39]

This study uses two different forms of ds PNA, aeg- and γ-methylated, to investigate how the backbone can affect charge transport, and hence the observed CT rate. Typically, the backbone of the PNA is based on the neutral and achiral 2-aminoethylglycine (aeg),[54–56] which is more flexible than the DNA backbone constrained by ribose rings and stiffened by the electric charge.[57,58] Incorporation of side chains at the γ position of the backbone makes γ-methylated (γ-PNA) more rigid than aeg-PNA (Figure 4.1). [46,59] Consequently, hybrid duplexes PNA/DNA and PNA/RNA,[54,55] and PNA/PNA duplexes that contain γ-PNA strands have greater thermal stability than the corresponding duplexes containing aeg-PNA strands.[56]

(A) (B)

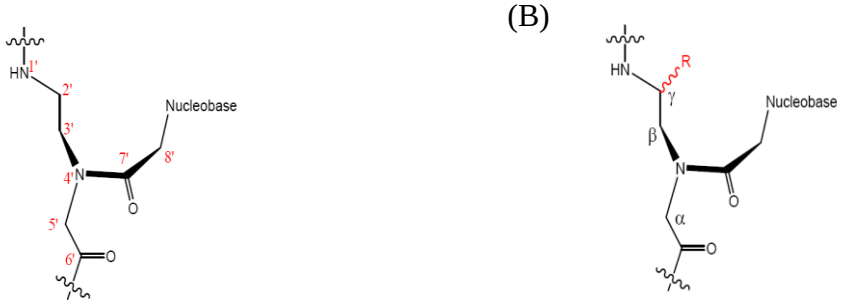

Figure 4.1. (a) Chemical structure of the backbone of aeg-PNA; (b) Chemical structure of the γ-PNA. In this study, R = methyl.

4.2 RESULTS AND DISCUSSION

The CT properties of two different 7 bp ds PNAs were investigated: one contained only TA base pairs while the other contained a central GC base pair (Table 4.1). Using the same methodology as in earlier work,[13,60–62] this study examined the oxidation and reduction of a ferrocene moiety (Fc) which was attached to a terminus of the PNA molecules assembled into a monolayer on a gold electrode. Cyclic voltammetry data were fitted by Marcus theory and used to determine the standard heterogeneous rate constant k^0.[63] The key finding of this study is that the electrochemical CT rate constants for γ-PNA duplexes are lower than those for aeg-PNA duplexes.

Table 4.1. Sequences and functional groups of PNA duplexes. The PNAs were assembled on gold electrodes via a C-terminal cysteine (Cys) group. The N-terminal ferrocene served as the redox reporter group.

Abbreviation	Sequence
aeg-PNA$_{(TA)}$ / γ -PNA$_{(TA)}$	Cys-T_3-**T**-T_3-Fc A_3-**A**-A_3-Lys
aeg-PNA$_{(GC)}$ / γ-PNA$_{(GC)}$	Cys-T_3-**G**-T_3-Fc A_3-**C**-A_3-Lys

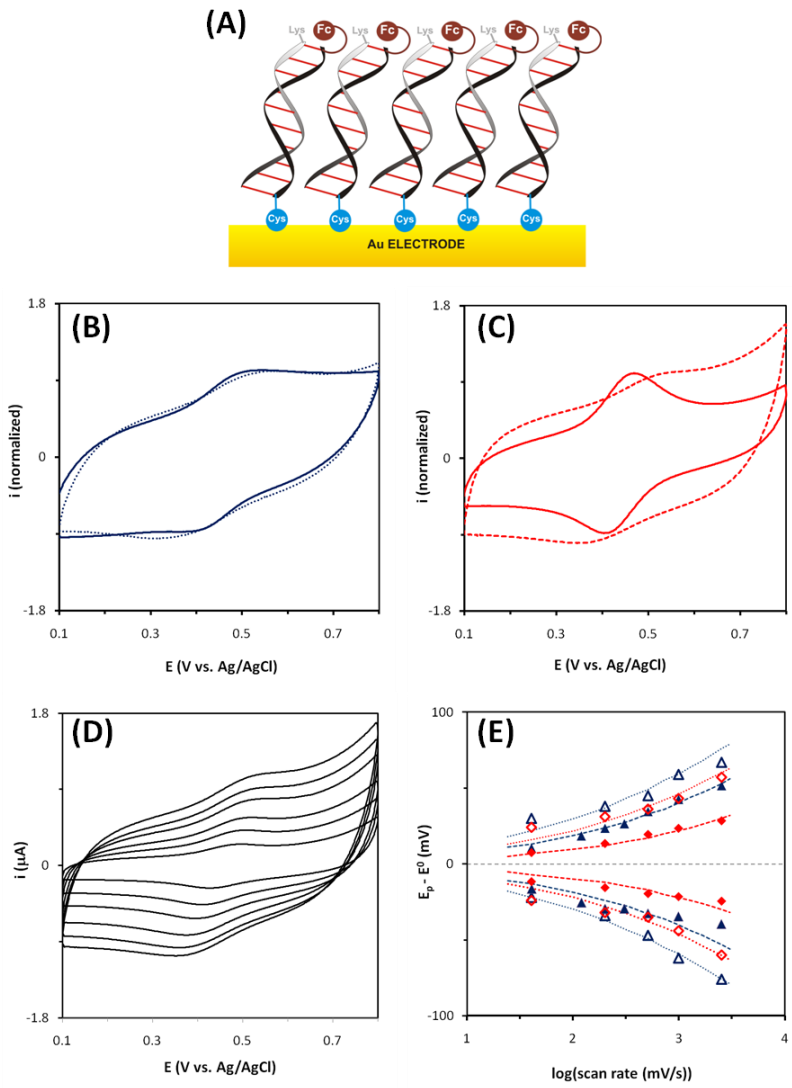

Figure 4.2. (A) Schematic representation of Fc-terminated PNA SAMs on gold electrodes used for electrochemical studies. (B) Voltammograms (normalized to the anodic peak current) taken at 30 mV/s for SAMs of aeg-$PNA_{(TA)}$ (blue, solid) and γ-$PNA_{(TA)}$ (blue, dashed) on gold electrodes. (C) Voltammograms (normalized to the anodic peak current) taken at 30 mV/s for SAMs of aeg-$PNA_{(GC)}$ (red, solid), and γ-$PNA_{(GC)}$ (red, dashed) on gold electrodes. (D) Voltammograms (non-normalized current) for a SAM of γ-$PNA_{(GC)}$ taken at scan rates from 5 to 30 mV/s (with 5mV/s increment). (E) Peak position relative to the formal potential ($E_p - E^0$) versus log (scan rate) for aeg- (filled symbols) and γ- (open symbols) $PNA_{(TA)}$ (blue triangles), and $PNA_{(GC)}$ (red diamonds) sequences, with corresponding Marcus theory fits: aeg- (dashed blue) and γ- (dotted blue) $PNA_{(TA)}$, and aeg- (dashed red) and γ- (dotted red) $PNA_{(GC)}$.

Surface coverage and thickness data for the PNA films are presented in Table 4.2. Self-assembled monolayers (SAMs) of Fc-terminated PNA molecules were adsorbed on gold electrodes as described in the methods section below (*cf.* Refs.13,61). The surface coverage of the SAMs was determined from the total amount of charge transferred, which was obtained by integrating the area of the Faradaic current peaks (Figure 4.2B-D). The surface coverage of aeg- and γ-PNA SAMs are similar and indicate that both PNAs form densely packed monolayers on Au (Table 4.2). This observation was confirmed by ellipsometry measurements of the PNA film thickness (see Table 4.2), which was found to be comparable to the thickness of 7 bp aeg-PNA monolayers reported earlier.[13,62]

Figure 2.2 shows representative cyclic voltammograms for SAMs of ds aeg-PNA and γ-PNA. Analysis of the voltammograms shows that the Fc redox couple is quasi-reversible. The relationship between the shift of the oxidation/reduction peak potential from the formal potential of the ferrocene ($E_p - E^0$) and the scan rate can be described by Marcus theory, as was found in prior studies.[13,60–62] The average standard heterogeneous rate constants determined for the ds PNA SAMs are presented in Table 4.2.

Table 4.2. Electrochemical CT rate constant k^0, surface coverage, and thickness of the ferrocene-terminated PNA films.

Sequence	k^0 / s^{-1}	Coverage / pmol×cm^{-2}	Film Thickness / nm
aeg-$PNA_{(TA)}$	0.25 ± 0.05	110 ± 40	2.8 ± 0.6
γ-$PNA_{(TA)}$	0.11 ± 0.06	68 ± 21	2.8 ± 0.7
aeg-$PNA_{(GC)}$	0.57 ± 0.14	120 ± 50	3.5 ± 0.2
γ-$PNA_{(GC)}$	0.22 ± 0.07	86 ± 27	3.0 ± 0.4

The data in Table 4.2 reveal two clear trends. First, replacement of a central TA base pair with a GC base pair causes an increase in the CT rate constant for both aeg- and γ–PNA by a factor

of about two. This effect demonstrates the sensitivity of the CT kinetics to the nucleobase identity: G has a higher oxidation potential than A, therefore, a GC pair presents a lower hole tunneling barrier than an AT pair.[19] Second, comparison of the rate constants for duplexes of the same sequence but different backbone chemistry shows that a change from the aeg- backbone to the γ-methylated backbone attenuates the CT rate constant by about a factor of two (Table 4.2). This effect is new and its origin is not immediately evident. Thus the central question of this manuscript arises: Why does the chemical change in the backbone cause the CT rate constant to change?

Several explanations can be ruled out. First, methylation of the backbone does not have a significant effect on the average geometry of the nucleobase stack, to which the CT rate is highly sensitive. Indeed, a molecular dynamics (MD) simulations employing NMR constraints indicates that γ-PNA adopts a general P-form helical structure that is very similar to the well documented structure of aeg-PNA.[59] Next, we can rule out the backbone effect on the structure of the PNA film. Because the CT rate constant measurements were performed on molecular monolayers, the number of the molecules and their arrangement in the SAMs might be expected to influence the overall CT rate constant. For example, CT in low-coverage films can be conformationally gated by bending of the DNA or PNA strand toward the electrode surface;[64,65] however, such motions are disfavored in the closely packed PNA films used here (see Table 4.2).[13,60–62] Besides, the trend in observed electrochemical CT rate with the measured PNA surface coverages (Table 4.2) is opposite to that expected for gating by large-scale molecular motions, i.e., the more densely packed films exhibit higher CT rates even though the large-scale molecular motions in those films are expectedly suppressed. Finally, the dependence of the rate constant on the PNA sequence provides another argument in favor of bridge-mediated CT, as opposed to the direct CT gated by PNA

bending motions. Thus, we are left to consider the effect of the backbone on the PNA structural fluctuations.

Appreciation of the importance of conformational fluctuations on CT kinetics and mechanism in NAs and proteins has been growing.[12,40,66] An important difference between aeg-PNA and γ-PNA is the extent of structural fluctuations and their impact on the conformational ensemble of the nucleobase stack. It is possible that aeg-PNA more often populates well-coupled, high-conductance conformations of the base pairs than does γ-PNA because aeg-PNA adopts a broader range of conformations than γ-PNA. A computational study of four base-pair, palindromic fragments of DNA and PNA[10] found that both the donor-acceptor coupling and the bridge hopping probability in NAs is linked to conformational flexibility. This result is consistent with the current experimental findings that the more flexible aeg-PNA has a larger CT rate constant than the rigidified γ-methylated PNA (Table 4.2).

In order to test the hypothesis that structural fluctuations affect the CT rate, computational studies of PNA were performed according to a protocol established previously (see the Methods section for details).[13,61] The MD simulations confirmed the *a priori* expectations that the flexibility and fluctuations of γ-PNA are smaller than those of aeg-PNA. For instance, the root mean square deviation (RMSD) of the aeg-PNA structure from its average is 25-30% higher than that found for γ-PNA (1.11±0.19 Å for aeg-$PNA_{(TA)}$ versus 0.81±0.15 Å for γ-$PNA_{(TA)}$ and 1.17±0.27 Å for aeg-$PNA_{(GC)}$ versus 0.80±0.17 Å for γ-$PNA_{(GC)}$). Next, the MD ensembles of PNA conformations were used to compute the near zero bias molecular conductance (which is assumed to be directly related to the molecular CT rate)[12,67,68] and analyze the distribution of computed conductance values.[13,61] The near-zero bias conductance σ was computed using the non-equilibrium Green's function formalism and Landauer's formula;

$$\sigma = \frac{q^2}{h} \int T(E) F_T(E - E_F) dE \qquad \textbf{Equation 4.1}$$

In Eqn. 4.1, E is the energy variable, $T(E)$ is the transmission function (*cf.* Eqn. 3 in the Methods section), q is the elementary charge, h is Planck's constant, and

$$F_T\,(E - E_F) \;=\; (1/4k_BT) \cdot \mathrm{sech}^2\big((E - E_F)/2k_BT\big) \qquad \textbf{Equation 4.2}$$

is the difference between the Fermi functions of the left and right electrode.[13,61] These calculations use a Fermi energy E_F = -6.7 eV. The value of -6.7 eV is inferred from the 0.8 eV difference in the measured oxidation potential of Fc and G[19] and the -7.5 eV average HOMO energy of G resulting from CNDO calculations.[10] Because $F_T\,(E - E_F)$ peaks strongly near E_F and is basically zero elsewhere, the main contribution to molecular conductance comes from the molecular orbitals (MOs) that lie near E_F (cf. Eqn. 4.3).

Two different models were used to calculate the conductance: one that only used the nucleobases and one that used the nucleobases, the backbone, and the water solvent (see the Methods section below). Figure 3 shows the calculated electronic density of states (DOS) for each of the four PNAs studied, and Table 4.3 shows the ratio between the median calculated conductances of aeg- and γ-PNA for each of the two studied sequences (cf. Table 4.7). If only the nucleobases are included in the calculations, then the DOS curves of aeg- and γ-PNA for each of the two studied sequences are very similar (Figure 3 top row). This result is consistent with the average geometries of the duplexes' nucleobase stack being similar, but the ratio between the calculated conductances of aeg- and γ-PNA nucleobase stacks does not match the experimental trends (Table 4.3). When the PNA backbone and water solvation shell are included in the calculation, the DOS curves of the aeg-PNAs and γ-PNAs become broadened and shifted with respect to each other along the energy axis (Figure 3 bottom row). As a result of the shift, the aeg-PNA ensemble has more electronic states (molecular orbitals) near E_F and, consequently, larger

$T(E_F)$ than the γ-PNA ensemble. The larger $T(E_F)$ translates into more MOs closer to the Fermi energy and a higher conductance for the aeg-PNAs (cf. Eqns. 4.1, 4.3). As shown in Table 4.3, inclusion of the backbone and the solvent in the calculations produces ratios between the calculated conductances of aeg- and γ-PNA that match the experimental trends well.

While it has been shown the nucleic acid backbone makes but an insignificant contribution to molecular conductance[39,69,70] there are several mechanisms by which the backbone and the solvent can affect the nucleobase-mediated CT. First and foremost, the fluctuations of the backbone geometry and the positions/orientations of the solvent molecules result in fluctuations in the electric field experienced by the nucleobases. Such fluctuations cause a broadening of the MO energy levels of the nucleobases, estimated to be as high as 1-2eV.[71,72] Because the more flexible aeg-PNA produces larger electric field fluctuations than γ-PNA, it pushes more MOs towards E_F, thereby increasing $T(E)$ in the vicinity of E_F, and increasing the resulting PNA conductance (*cf.* Eqns. (1-3) and Figure 4.6A).

Several other mechanisms of solvent/backbone-nucleobase interaction exist, and they appear to affect the PNA MOs, DOS, and molecular conductance in different ways (Figure 4.3, S3). First, the net electric field of the two backbone strands shifts the bases-only PNA DOS up the energy axis, thus increasing the PNA conductance.[72] This effect is compensated by solvent screening which shifts the DOS curve down the energy axis (Figure 4.6). Second, the solvent screening apparently reduces the dipolar repulsion between the nucleobases which arises from near-alignment of neighboring nucleobases in the PNA duplex, owing to the relatively small twist of the P-type helix (17-23 deg/bp).[46] This effect should shift the PNA DOS further down the energy axis. The cumulative result of all of these effects is a shift of the aeg-PNA DOS to higher energies than the γ-PNA DOS (Figure 4.3) and, consequently, a higher conductance for aeg-PNA than for

γ-PNA. A detailed analysis of the relative importance of the different mechanisms of nucleobase-backbone and nucleobase-solvent interactions is beyond the scope of this manuscript.

The effect of backbone electric field fluctuations on the nucleobase DOS distribution represents an important new consideration for quantitatively modeling charge transport through nucleic acids. Although, it has been shown before that the charge transfer rate in PNA is affected by the backbone flexibility, those studies focused on how fluctuations affected the DNA and PNA base stack geometry and hence the base-to-base overlap and molecular orbital delocalization.[10] In

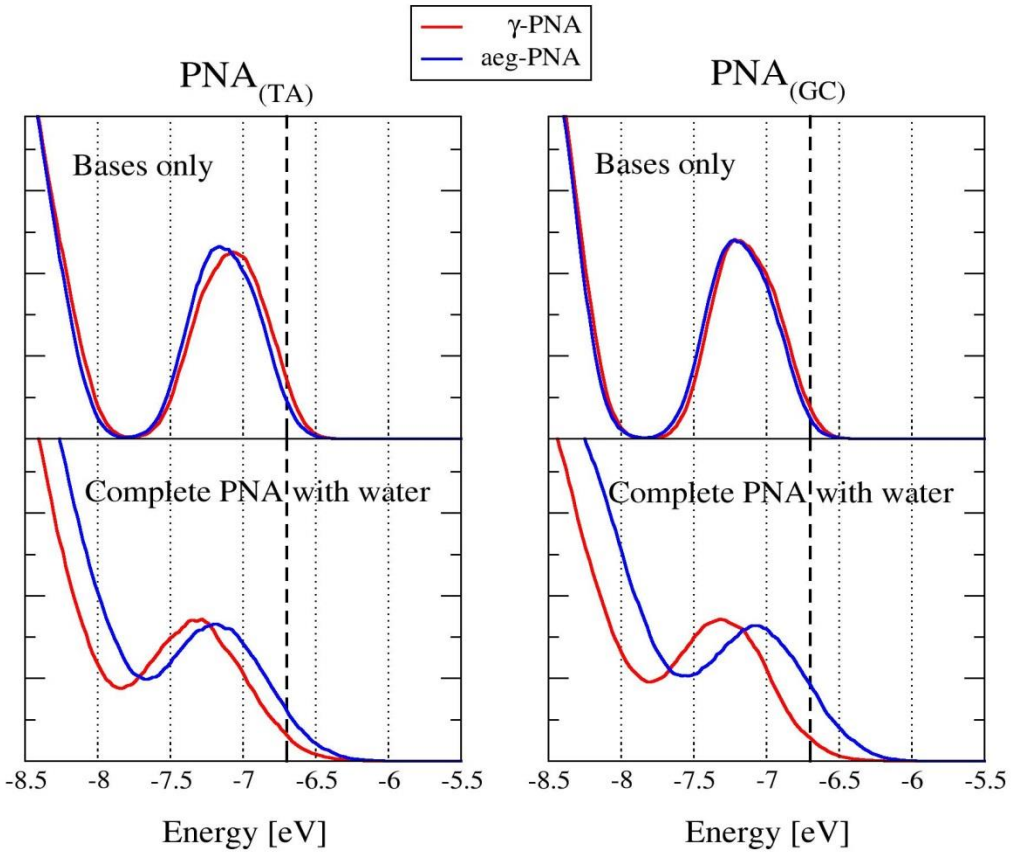

Figure 4.3. Electronic density of states (DOS) computed for the MD ensembles of the four studied PNA systems. Top row: DOS computed for nucleobases only. Bottom row: DOS computed for both bases and backbone, with the water included as point charges to account for the solvent screening of electrostatic interactions. The proximity of the DOS peaks to the Fermi level -6.7 eV, identified by the vertical dashed lines) puts the systems into a near-resonant regime.[13]

contrast, this study finds a significant difference in the CT rate for two types of PNA that share a

very similar geometry and fluctuations of the nucleobase stack, as well as the backbone geometry, but differ in the backbone flexibility. The results presented here indicate that the backbone fluctuations may affect the nucleobase-mediated molecular conductance by an amount comparable to those arising from structural fluctuations of the nucleobases themselves (*cf.* Figure 4.3),[10] or even nucleobase substitution (compare the average rate constants of γ-PNA$_{(GC)}$ and aeg-PNA$_{(TA)}$ in Table 4.2).

One should be cautious not to over-interpret the results of the theoretical calculations here. On the one hand, the amount of solvent in the shell surrounding the simulated PNA is likely different from the amount of solvent that saturates the experimental SAMs. In addition, the length of the MD simulation (2ns) is hardly sufficient for a comprehensive sampling of the PNA structural ensemble. It is telling that even though the experimental trends in charge transfer rates between the aeg- and γ-PNA have been reproduced, the trends between the different PNA sequences (PNA$_{(GC)}$ vs. PNA$_{(TA)}$) were not (*cf.* Tables 4.2 and S4). Such a discrepancy could be attributed to the neglect of the direct coupling between the model electrodes and the non-terminal nucleobases, including the central GC base where the HOMO is predominantly localized.[13] Yet, the qualitative conclusion that larger fluctuations cause larger MO broadening and increase the PNA molecular conductance is very general and likely to be valid regardless of the computational details.

Table 4.3. The ratio of aeg- and γ-PNA conductances resulting from the theoretical calculations. Median values for the calculated ensembles of conductances were used (*Cf.* Figure 4.6B, Figure 4.7, Table 4.7).

Sequence	$\sigma_{\text{aeg-PNA}}/\sigma_{\gamma\text{-PNA}}$	
	Bases only	**Whole PNA in water**
PNA$_{(TA)}$	0.06 ± 0.06	1.86 ± 1.74
PNA$_{(GC)}$	0.72 ± 0.44	2.13 ± 1.83

4.3 CONCLUSIONS

In summary, this study explored the influence of structural flexibility on the charge transfer rate constant through PNA. Both the experimental and theoretical components of this study indicate that charge transport in PNA can be suppressed by limiting the conformational flexibility of the PNA duplex, e.g., by changing the backbone chemistry. While the charge transfer occurs through the nucleobases, the fluctuations of the PNA backbone broaden the nucleobase energy levels and thus increase the charge transfer rate.

4.4 METHODS

4.4.1 PNA Synthesis

The synthesis of PNA oligomers with C-terminal cysteine and N-terminal ferrocene moieties was previously reported and discussed;[60,61] further details are found in the Supporting Information. Briefly, both the non-modified and γ-modified PNA oligomers were synthesized using solid phase peptide synthesis methods with a Boc protection strategy.[38,73,74] Ferrocene carboxylic acid (Aldrich) was coupled to the N-terminus; oligomers were cleaved from the resin using trifluoroacetic acid (TFA) and trifluoromethanesulfonic acid (TFMSA), precipitated in ethyl ether, and dried under nitrogen. The solid products were dissolved in aqueous solution and purified by reverse-phase HPLC. PNA oligomers were characterized by MALDI-TOF mass spectrometry on an Applied Biosystems Voyager-DE STR workstation. The observed mass of each synthesized PNA agreed well with the expected mass (Supporting Information). PNA solutions were prepared

in deionized water, and the PNA concentrations were determined by UV-Vis spectrophotometry assuming $\varepsilon(260)$ = 8600, 6600, 13700, and 11700 cm^{-1} M^{-1} for each T, C, A, and G monomer, respectively.[38] PNA duplexes were formed by slow cooling (from 95 °C to 10 °C) of solutions containing 1:1 mixtures of the complementary PNA strands.

4.4.2 Electrochemical Characterization of PNA SAMs

4.4.2.1 Electrode Preparation and SAM formation

Gold ball electrodes were prepared and annealed in a manner similar to earlier reports[60–62] and were coated with PNA SAMs via 28-40 h immersion at 27° C in 0.3-1 mL of a 20 μM PNA solution (1:1 v/v acetonitrile/pH 7.0 10 mM sodium phosphate buffer). Following incubation, electrodes were washed with deionized water and used directly in electrochemical experiments.

4.4.2.2 Electrochemical Measurements

Cyclic voltammetry (CV) was performed using a CH Instruments 618B or CHI430 electrochemical analyzer in 1 M $NaClO_4$ (pH ≈ 6-7), with a Ag/AgCl (1 M KCl) reference electrode, a platinum wire counter electrode and a PNA-modified gold wire electrode. Surface coverage was calculated by integrating the charge under voltammetric peaks. Kinetic data were obtained by plotting the peak separation versus scan rate and fitting the data by rate constants based on Marcus theory,[75,76] using a reorganization energy (λ) of 0.8 eV.[76] The rate constants so determined were unchanged with a ±0.2 eV variation in λ. Note that any changes in λ would systematically change all of measured k^0 values and the relative trends would remain the same.

4.4.3 Ellipsometric Measurements of PNA Film Thickness

Unmodified PNA was assembled on gold slides from EMF Corp. (Ithaca, NY) which consisted of a 100 nm Au layer over a 50 nm Ti binding layer on float glass. Gold slides for the γ-methylated PNA samples were obtained from Evaporated Coatings, Inc. (Willow Grove, PA), which consisted of a 150 nm Au layer over a 2 nm Ti binding layer on BK7 glass. The slides were cleaned by immersion in piranha solution for 2 min, and then rinsed with large amounts of deionized water, followed by ethanol rinsing and drying under nitrogen. The slides were then immersed in 1 mL 20 μM PNA solution in 1:1 (v:v) acetonitrile:10 mM sodium phosphate buffer for 28 hours at 27° C. Following incubation, the samples were rinsed with ethanol and deionized water, and then dried under nitrogen. A Gaertner L-117 Null Ellipsometer was used to measure the thickness of the PNA films.

4.4.4 Theoretical Calculations of PNA Structure and Conductance

4.4.4.1 Molecular Dynamics Simulations

The initial structures of left-handed aeg-PNA duplexes $(TA)_7$ and $(TA)_3(GC)(TA)_3$ were constructed based on the average helicoidal parameters of experimentally determined aeg-PNA duplexes (PDB ID: 2K4G).[46] The detailed protocol of initial structure construction is explained in Ref 13. To generate γ-PNAs, the hydrogens atoms in the R-configuration at the C2' positions along the PNA backbone were replaced with methyl groups. The force field ff99SB[77] in Amber 11[78] was complemented with the previously determined atomic partial charges for aeg-[46] and γ-methylated PNA.[59] The structures were solvated in a TIP3P water box, such that the distance between the walls of the box and the closest PNA atom was at least 17 Å. After energy minimization, the

solvated structures were subject to 2 ns of molecular dynamics using the module pmemd of Amber 11,[78] at T = 300 K and P = 1 atm, with periodic boundary conditions. 2,000 snapshots were saved every 1 ps for each trajectory and used for the subsequent electronic structure computations. The dynamics of PNA during the simulations was characterized by the root-mean square deviation (RMSD) and the helicoidal parameter distribution. The RMSDs of the PNA snapshots were computed with respect to the time-averaged structure after best-fit alignment of the heavy atoms. The helicoidal parameters were computed for the PNA base pairs with 3DNA[79] (see Supporting Information).

4.4.4.2 Analysis of the Electronic Structure

The quantum mechanical analysis of the PNA structures extracted from the MD ensemble was based on single point self-consistent field calculations with the INDO/s method implemented in the CNDO program.[80] The CNDO calculations were performed for either PNA nucleobases only (capped with hydrogens), or for the complete PNA including both the nucleobases and the backbone, or for the complete PNA surrounded by water. The waters were extracted from the MD simulation for each MD snapshot and were rearranged into a Voronoi cell centered on the PNA molecule to ensure even solvation of PNA on each side (see Ref. 39 for detail). The water atoms were included in the CNDO calculations as point charges, assigned according to the TIP3P water model. The calculated MOs were used as input to the molecular conductance calculations.

4.4.4.3 Conductance Calculations

The non-equilibrium Green's function (NEGF) method[81] used in previous studies[13,61] was employed here to calculate the molecular conductance of PNA. In the NEGF calculations, the non-hydrogen atoms of the A and T nucleobases of the terminal A:T base pairs were coupled to the

virtual electrodes. The conductance σ of a given PNA structure was computed using Eq. (1) (*vide supra*). The transmission function $T(E)$ was determined for every PNA structure as:[13,61]

$$T(E) = \sum_m \frac{\Gamma_{mm}^L \Gamma_{mm}^R}{(E - E_m)^2 + \frac{1}{4}(\Gamma_{mm}^L + \Gamma_{mm}^R)^2} + \sum_{m \neq n} \frac{\Gamma_{nm}^L \Gamma_{mn}^R}{\left[(E - E_m) - \frac{i}{2}(\Gamma_{mm}^L + \Gamma_{mm}^R)\right]\left[(E - E_n) - \frac{i}{2}(\Gamma_{nn}^L + \Gamma_{nn}^R)\right]} \quad \textbf{Equation 4.3}$$

Here, the indices *m* and *n* refer to the PNA MOs and $\Gamma_{mn}^{L/R}$ are elements of the broadening matrices $\mathbf{\Gamma^{L/R}}$ that describe the MO broadening due to the electrode coupling.[13,61]

4.5 SUPPORTING INFORMATION

4.5.1 Detailed PNA Synthesis

The aeg PNA oligomers were synthesized using solid phase peptide synthesis methods with a Boc protection strategy.[38,73,74] MBHA resin (Peptides International, Louisville, KY) with a loading of 0.18 mequiv/g was down-loaded[38] using Boc-L-Cys-(4-MeOBzl)-OH (NovaBiochem/Merck Biosciences, Switzerland) to an estimated loading of 0.04-0.06 mequiv/g. Thereafter, depending on sequence, Boc-T-OH/ Boc-(A-Z)-OH/ Boc-(G-Z)-OH/ Boc-(C-Z)-OH (Applied Biosystems, Foster City, CA) or *N*-(2-Boc-aminoethyl)-*N*-(methyl)-glycine were coupled using 1*H*-Benzotriazolium 1-[*bis*(dimethylamino)methylene]-5chloro-hexafluorophosphate(1),3-oxide (HCTU) (Peptides International) as a coupling agent. The γ-modified PNA oligomers were prepared in the same manner but using the γ-methylated monomers synthesized according to published procedures.[54] Finally, ferrocene carboxylic acid (Aldrich) was coupled to the N-terminus. This coupling was repeated twice to increase the yield of ferrocene-conjugated PNA. Oligomers were cleaved from the resin using trifluoroacetic acid (TFA) and

trifluoromethanesulfonic acid (TFMSA), precipitated in ethyl ether, and dried under nitrogen. The solid products were dissolved in aqueous solution and purified by reverse-phase HPLC using a solvent gradient, from 0% to 50% acetonitrile in water over 40 min on a Waters Delta 600 pump with a 2996 photodiode-array detector (Milford, MA). PNA oligomers were characterized by MALDI-TOF mass spectrometry on an Applied Biosystems Voyager-DE STR Workstation. PNA solutions were prepared in deionized water, and the PNA concentrations were determined by UV-vis spectrophotometry assuming $\varepsilon(260)$ = 8600, 6600, 13700, and 11700 $cm^{-1} \times M^{-1}$ for each T, C, A, and G monomer, respectively.[38] PNA solutions for electrode incubation were typically 20 μM ss-PNA in 1:1 (v/v) acetonitrile/10 mM pH 7.0 sodium phosphate buffer.

4.5.2 Properties of Studied Duplexes

4.5.2.1 Masses of the Duplexes

Table 4.4. Calculated masses of PNA molecules and corresponding m/z observed from MALDI-ToF MS (reflection mode, α-cyano-4-hydroxycinnamic acid matrix, laser intensity 1000).

Sequence	Expected Mass (Da)		Observed m/z (Da)	
	Aeg-PNA	γ-PNA	Aeg-PNA	γ-PNA
$PNA_{(TA)}$	2196.0 2072.1	2294.2 2170.3	2195.54 2071.61	2316.85 (+Na) 2168.9
$PNA_{(GC)}$	2221.1 2048.1	2319.2 2146.3	2220.7 2047.5	2321.11 2147.05

4.5.2.2 Melting Temperatures of ds-PNAs

Table 4.5. Approximate melting temperatures T_m determined from heating curves measured at 260 nm for aeg- and γ-PNA sequences.

Sequence	**T_m (°C)**	
	aeg-PNA	γ-PNA
$PNA_{(TA)}$	39	77
$PNA_{(GC)}$	40	60

4.5.2.3 Helical Parameters of Non-Modified and γ-Methylated PNAs

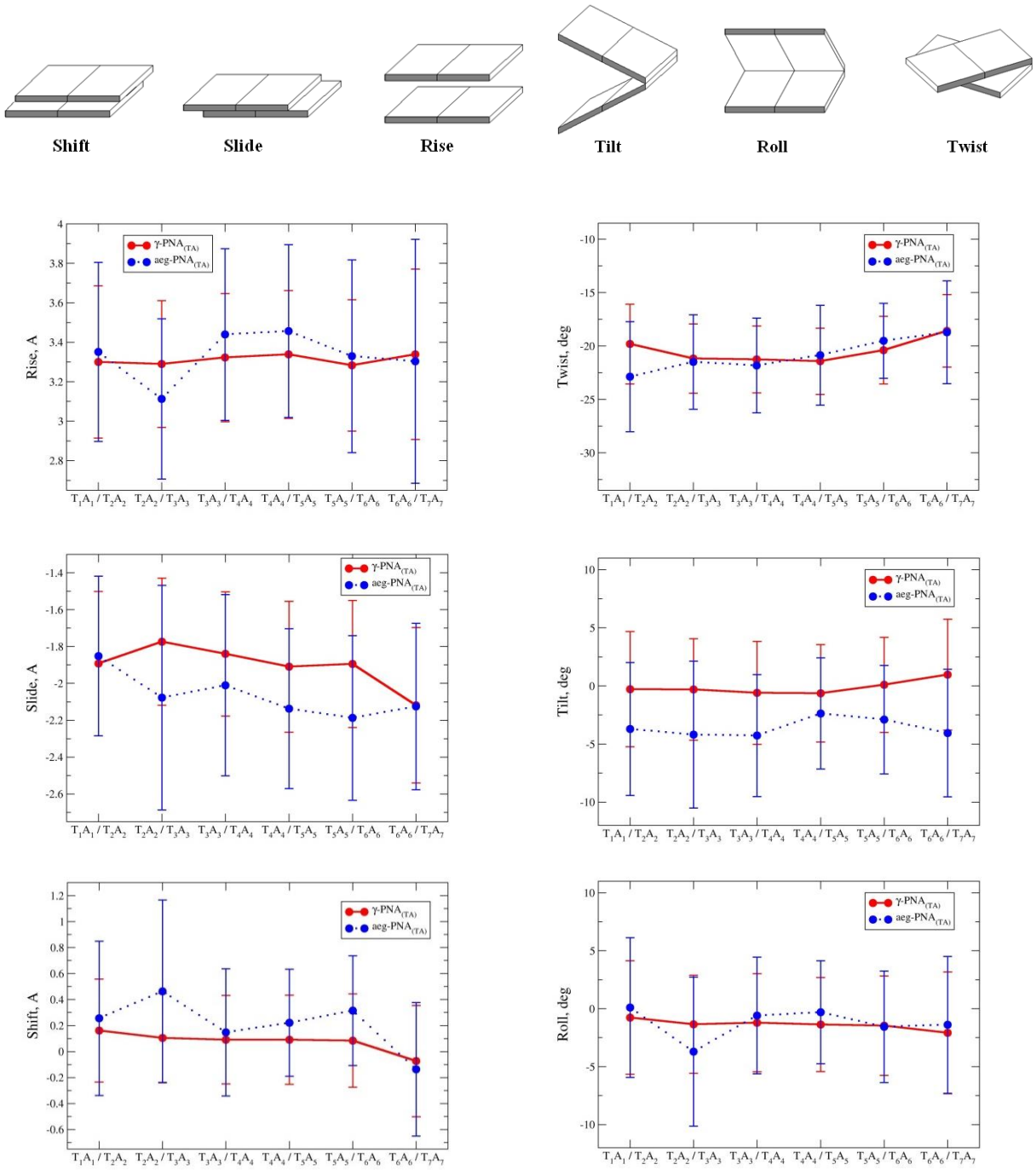

Figure 4.4. Helical parameters of the base pairs for $PNA_{(TA)}$ sequence with aeg- (blue) and γ-methylated (red) backbone.

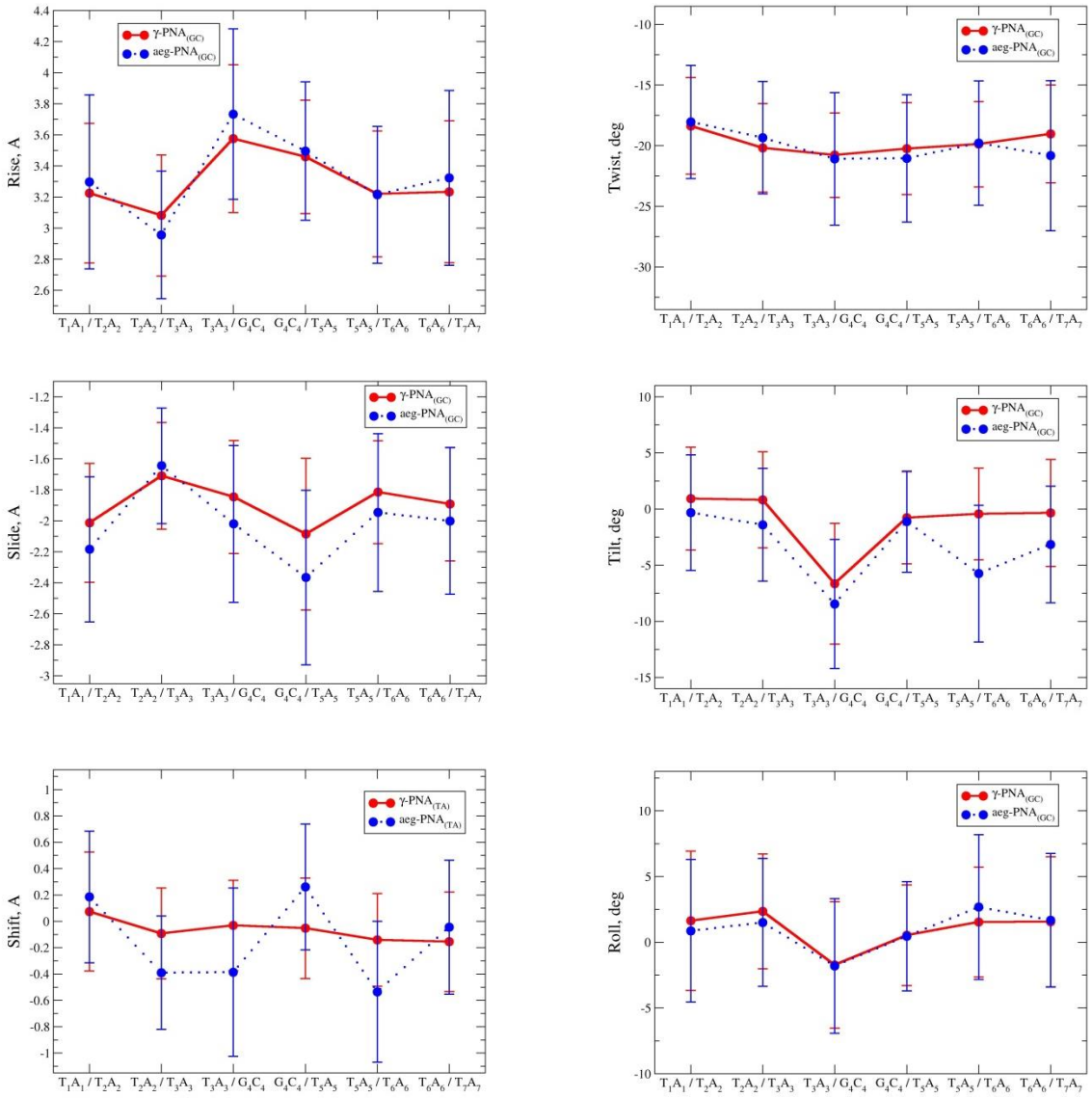

Figure 4.5. Helical parameters of the base pairs for $PNA_{(GC)}$ sequence with aeg- (blue) and γ-methylated (red) backbone.

4.5.2.4 Electronic Structure and Calculated Conductance of Model PNAs

(A)

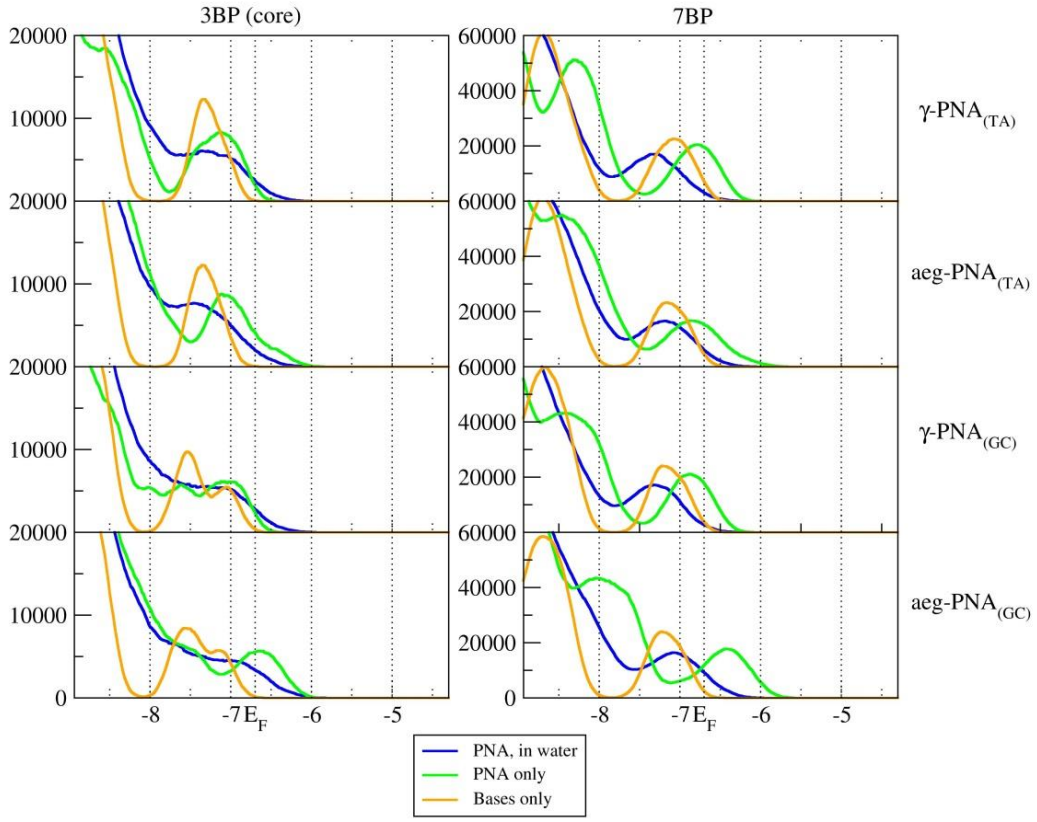

(B)

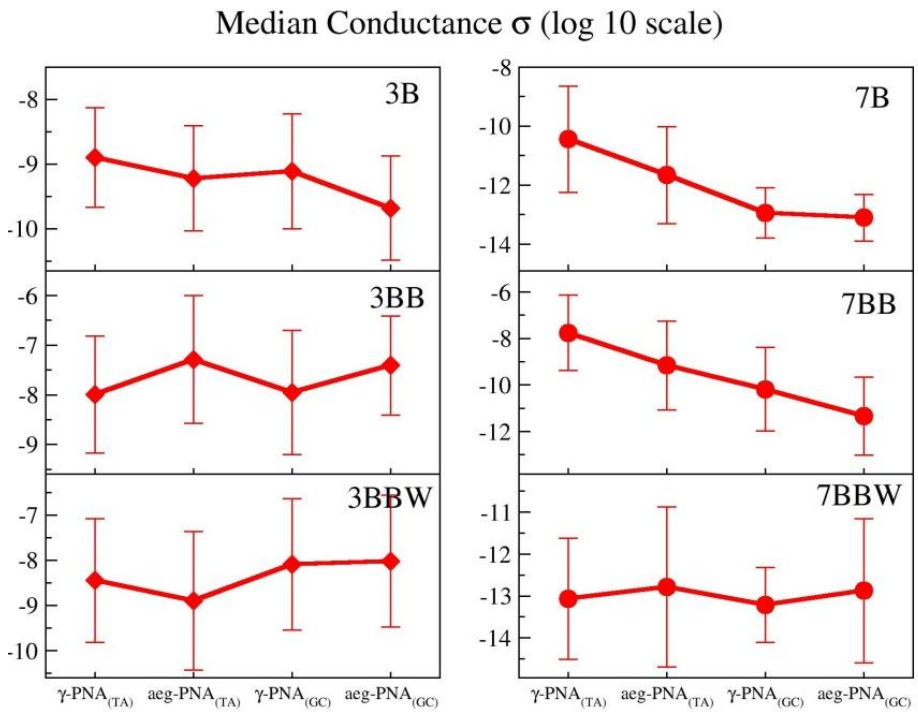

Figure 4.6. Dependence of the PNA electronic structure on sequence and the computational model. (A) Electronic density of states, plotted in the vicinity of the Fermi energy. (B) Resulting molecular conductance (shown is a median value of the calculated conductance, in arbitrary units), calculated for nucleobases 'B', whole PNA with included backbone 'BB', and whole PNA and solvating water 'BBW'.

Table 4.6. Energies of HOMO, HOMO-1 and HOMO-2 levels calculated for 7 bp long duplexes.

System		HOMO	HOMO-1	HOMO-2
Base pairs only	aeg-	-6.82 ± 0.11	-6.94 ± 0.09	-7.04 ± 0.08
	γ-	-6.77 ± 0.11	-6.89 ± 0.07	-6.99 ± 0.08
Whole PNA molecule	aeg-	-6.44 ± 0.25	-6.58 ± 0.23	-6.69 ± 0.22
	γ-	-6.48 ± 0.22	-6.61 ± 0.21	-6.71 ± 0.21
Whole PNA with Water	aeg-	-6.82 ± 0.25	-6.97 ± 0.24	-7.08 ± 0.23
	γ-	-6.95 ± 0.25	-7.11 ± 0.22	-7.22 ± 0.22

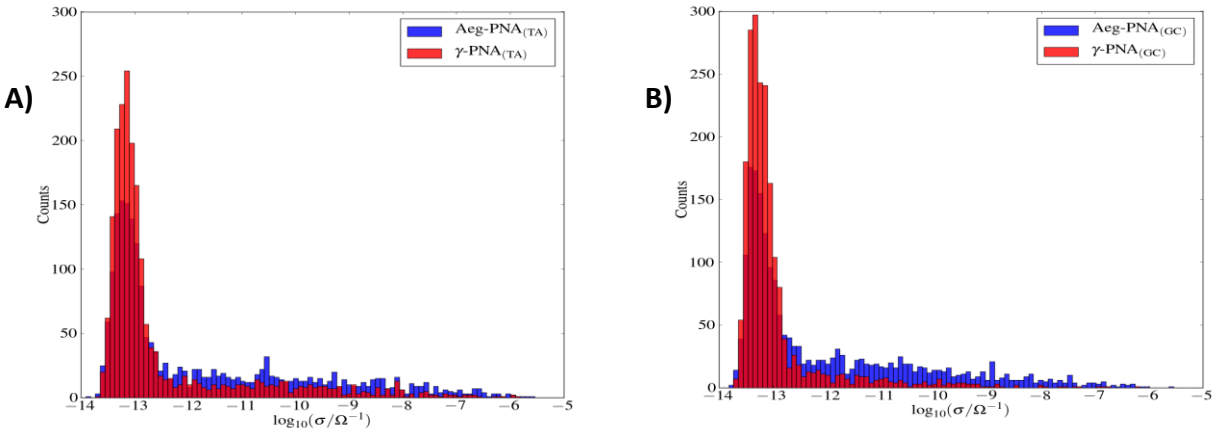

Figure 4.7. Conductance distribution calculated for $PNA_{(TA)}$ (A), and $PNA_{(GC)}$ (B).

Table 4.7. Median values and the median absolute deviations for the calculated conductance ensembles (*Cf.* Figure 4.6B, Figure 4.7).

Sequence	σ / S	
	Bases only	**Whole PNA in water**
aeg-$PNA_{(TA)}$	$(2.2 \pm 2.1) \times 10^{-12}$	$(1.6 \pm 1.3) \times 10^{-13}$
γ-$PNA_{(TA)}$	$(3.6 \pm 3.6) \times 10^{-11}$	$(8.6 \pm 4.0) \times 10^{-14}$
aeg-$PNA_{(GC)}$	$(7.9 \pm 3.3) \times 10^{-14}$	$(1.3 \pm 1.0) \times 10^{-13}$
γ-$PNA_{(GC)}$	$(1.1 \pm 0.5) \times 10^{-14}$	$(6.1 \pm 2.3) \times 10^{-14}$

4.6 REFERENCES

(1) Seeman, N. C. *J. Theor. Biol.* **1982**, *99*, 237.

(2) Seeman, N. C. *Nature* **2003**, *421*, 427.

(3) Braun, E.; Eichen, Y.; Sivan, U.; Ben-Yoseph, G. *Nature* **1998**, *391*, 775.

(4) Liu, D.; Park, S. H.; Reif, J. H.; LaBean, T. H. *Proc. Natl. Acad. Sci. U. S. A.* **2004**, *101*, 717.

(5) Endres, R.; Cox, D.; Singh, R. *Rev. Mod. Phys.* **2004**, *76*, 195.

(6) Uhlmann, E.; Peyman, A. *Chem. Rev.* **1990**, *90*, 543.

(7) Núñez, M. E.; Hall, D. B.; Barton, J. K. *Chem. Biol.* **1999**, *6*, 85.

(8) Angelov, D.; Barton, J. K.; Behrens, C.; Cadet, J.; Carell, T.; Cichon, M. K.; Douki, T.; Giese, B.; Grolle, F.; Hennecke, U.; Kawai, K.; Majima, T.; Landman, U.; Lewis, F. D.; Nakatani, K.; O'Neill, M. A.; Ravanat, J.-L.; Saito, I.; Schuster, G. B.; J.R.Wagner; Wasielewski, M. R. *Longe-Range Charge Transfer in DNA I*; Schuster, G. B., Ed.; Topics in Current Chemistry; Springer Berlin Heidelberg: Berlin, Heidelberg, 2004; Vol. 236.

(9) Berlin, Y. A.; Kurnikov, I. V.; Beratan, D.; Ratner, M. A.; Burin, A. L.; Rösch, N.; Voityuk, A. A.; Conwell, E.; Cai, Z.; Sevilla, M. D.; Shafirovich, V.; Geacintov, N. E.; Thorp, H. H.; Porath, D.; Cuniberti, G.; Felice, R. Di *Long-Range Charge Transfer in DNA II*; Schuster, G. B., Ed.; Topics in Current Chemistry; Springer Berlin Heidelberg: Berlin, Heidelberg, 2004; Vol. 237.

(10) Hatcher, E.; Balaeff, A.; Keinan, S.; Venkatramani, R.; Beratan, D. N. *J. Am. Chem. Soc.* **2008**, *130*, 11752.

(11) Liu, T.; Barton, J. K. *J. Am. Chem. Soc.* **2005**, *127*, 10160.

(12) Venkatramani, R.; Keinan, S.; Balaeff, A.; Beratan, D. N. *Coord. Chem. Rev.* **2011**, *255*, 635.

(13) Venkatramani, R.; Davis, K. L.; Wierzbinski, E.; Bezer, S.; Balaeff, A.; Keinan, S.; Paul, A.; Kocsis, L.; Beratan, D. N.; Achim, C.; Waldeck, D. H. *J. Am. Chem. Soc.* **2011**, *133*, 62.

(14) Nogues, C.; Cohen, S. R.; Daube, S.; Apter, N.; Naaman, R. *J. Phys. Chem. B* **2006**, *110*, 8910.

(15) Iqbal, S. M.; Balasundaram, G.; Ghosh, S.; Bergstrom, D. E.; Bashir, R. *Appl. Phys. Lett.* **2005**, *86*, 153901.

(16) Van Zalinge, H.; Schiffrin, D. J.; Bates, A. D.; Haiss, W.; Ulstrup, J.; Nichols, R. J. *Chemphyschem* **2006**, *7*, 94.

(17) Kawai, K.; Kodera, H.; Majima, T. *J. Am. Chem. Soc.* **2010**, *132*, 627.

(18) Kawai, K.; Kodera, H.; Osakada, Y.; Majima, T. *Nat. Chem.* **2009**, *1*, 156.

(19) Seidel, C. A. M.; Schulz, A.; Sauer, M. H. M. *J. Phys. Chem.* **1996**, *100*, 5541.

(20) Meggers, E.; Michel-Beyerle, M. E.; Giese, B. *J. Am. Chem. Soc.* **1998**, *120*, 12950.

(21) Lewis, F. D.; Letsinger, R. L.; Wasielewski, M. R. *Acc. Chem. Res.* **2001**, *34*, 159.

(22) Berlin, Y. A.; Burin, A. L.; Ratner, M. A. *Chem. Phys.* **2002**, *275*, 61.

(23) Sugiyama, H.; Saito, I. *J. Am. Chem. Soc.* **1996**, *118*, 7063.

(24) Saito, I.; Nakamura, T.; Nakatani, K.; Yoshioka, Y.; Yamaguchi, K.; Sugiyama, H. *J. Am. Chem. Soc.* **1998**, *120*, 12686.

(25) Fuentes-Cabrera, M.; Sumpter, B. G.; Wells, J. C. *J. Phys. Chem. B* **2005**, *109*, 21135.

(26) Fuentes-Cabrera, M.; Sumpter, B. G.; Lipkowski, P.; Wells, J. C. *J. Phys. Chem. B* **2006**, *110*, 6379.

(27) Liu, H.; Gao, J.; Lynch, S. R.; Saito, Y. D.; Maynard, L.; Kool, E. T. *Science (80-.).* **2003**, *302*, 868.

(28) Lu, H.; He, K.; Kool, E. T. *Angew. Chem. Int. Ed. Engl.* **2004**, *43*, 5834.

(29) Lee, A. H. F.; Kool, E. T. *J. Am. Chem. Soc.* **2006**, *128*, 9219.

(30) Rakitin, A.; Aich, P.; Papadopoulos, C.; Kobzar, Y.; Vedeneev, A. S.; Lee, J. S.; Xu, J. M. *Phys. Rev. Lett.* **2001**, *86*, 3670.

(31) Liu, S.; Clever, G. H.; Takezawa, Y.; Kaneko, M.; Tanaka, K.; Guo, X.; Shionoya, M. *Angew. Chem. Int. Ed. Engl.* **2011**, *50*, 8886.

(32) Kelley, S. O.; Jackson, N. M.; Hill, M. G.; Barton, J. K.; Giese, B.; Wessely, S.; Spormann, M.; Lindemann, U.; Meggers, E.; Michel-Beyerle, M. E. *Angew. Chemie Int. Ed.* **1999**, *38*, 941.

(33) Treadway, C. *Chem. Phys.* **2002**, *281*, 409.

(34) Hihath, J.; Xu, B.; Zhang, P.; Tao, N. *Proc. Natl. Acad. Sci. U. S. A.* **2005**, *102*, 16979.

(35) Wierzbinski, E.; Arndt, J.; Hammond, W.; Slowinski, K. *Langmuir* **2006**, *22*, 2426.

(36) Guo, X.; Gorodetsky, A. A.; Hone, J.; Barton, J. K.; Nuckolls, C. *Nat. Nanotechnol.* **2008**, *3*, 163.

(37) Boal, A. K.; Barton, J. K. *Bioconjug. Chem.* **2005**, *16*, 312.

(38) Nielsen, P. E. *Peptide Nucleic Acids: Protocols and Applications*; Peter Nielson, Ed.; 2nd ed.; Horizon Bioscience, 2004.

(39) Wolak, M. A.; Balaeff, A.; Gutmann, S.; Helmrich, H. J.; Vosloo, R.; Beerbom, M. M.; Wierzbinski, E.; Waldeck, D. H.; Bezer, S.; Achim, C.; Beratan, D. N.; Schlaf, R. *J. Phys. Chem. C* **2011**, *115*, 17123.

(40) Beratan, D. N.; Skourtis, S. S.; Balabin, I. A.; Balaeff, A.; Keinan, S.; Venkatramani, R.; Xiao, D. *Acc. Chem. Res.* **2009**, *42*, 1669.

(41) Koshkin, A. A.; Singh, S. K.; Nielsen, P.; Rajwanshi, V. K.; Kumar, R.; Meldgaard, M.; Olsen, C. E.; Wengel, J. *Tetrahedron* **1998**, *54*, 3607.

(42) Obika, S.; Nanbu, D.; Hari, Y.; Morio, K.; In, Y.; Ishida, T.; Imanishi, T. *Tetrahedron Lett.* **1997**, *38*, 8735.

(43) Schoning, K. U.; Scholz, P.; Guntha, S.; Wu, X.; Krishnamurthy, R.; Eschenmoser, A. *Science (80-.).* **2000**, *290*, 1347.

(44) Zhang, L.; Peritz, A.; Meggers, E. *J. Am. Chem. Soc.* **2005**, *127*, 4174.

(45) Egholm, M.; Buchardt, O.; Christensen, L.; Behrens, C.; Freier, S. M.; Driver, D. A.; Berg, R. H.; Kim, S. K.; Norden, B.; Nielsen, P. E. *Nature* **1993**, *365*, 566.

(46) He, W.; Hatcher, E.; Balaeff, A.; Beratan, D. N.; Gil, R. R.; Madrid, M.; Achim, C. *J. Am. Chem. Soc.* **2008**, *130*, 13264.

(47) Bruinsma, R.; Grüner, G.; D'Orsogna, M.; Rudnick, J. *Phys. Rev. Lett.* **2000**, *85*, 4393.

(48) O'Neill, M. A.; Becker, H.-C.; Wan, C.; Barton, J. K.; Zewail, A. H. *Angew. Chem. Int. Ed. Engl.* **2003**, *42*, 5896.

(49) O'Neill, M. A.; Barton, J. K. *J. Am. Chem. Soc.* **2004**, *126*, 13234.

(50) O'Neill, M. A.; Barton, J. K. *J. Am. Chem. Soc.* **2004**, *126*, 11471.

(51) Davis, W. B. W. B.; Ratner, M. A. M. A.; Wasielewski, M. R. *J. Am. Chem. Soc.* **2001**, *123*, 7877.

(52) Haiss, W.; van Zalinge, H.; Bethell, D.; Ulstrup, J.; Schiffrin, D. J.; Nichols, R. J. *Faraday Discuss.* **2006**, *131*, 253.

(53) Ghosh, A. W.; Rakshit, T.; Datta, S. *Nano Lett.* **2004**, *4*, 565.

(54) Dragulescu-Andrasi, A.; Rapireddy, S.; Frezza, B. M.; Gayathri, C.; Gil, R. R.; Ly, D. H. *J. Am. Chem. Soc.* **2006**, *128*, 10258.

(55) Englund, E. A.; Appella, D. H. *Angew. Chem. Int. Ed. Engl.* **2007**, *46*, 1414.

(56) He, G.; Rapireddy, S.; Bahal, R.; Sahu, B.; Ly, D. H. *J. Am. Chem. Soc.* **2009**, *131*, 12088.

(57) Brown, S.; Thomson, S.; Veal, J.; Davis, D. *Science (80-.).* **1994**, *265*, 777.

(58) Eriksson, M.; Nielsen, P. E. *Nat. Struct. Biol.* **1996**, *3*, 410.

(59) He, W.; Crawford, M. J.; Rapireddy, S.; Madrid, M.; Gil, R. R.; Ly, D. H.; Achim, C.; H, D. *Mol. Biosyst.* **2010**, *6*, 1619.

(60) Paul, A.; Watson, R. M. R. M.; Lund, P.; Xing, Y.; Burke, K.; He, Y.; Borguet, E.; Achim, C.; Waldeck, D. H. D. H. *J. Phys. Chem. C* **2008**, *112*, 7233.

(61) Paul, A.; Bezer, S.; Venkatramani, R.; Kocsis, L.; Wierzbinski, E.; Balaeff, A.; Keinan, S.; Beratan, D. N.; Achim, C.; Waldeck, D. H. *J. Am. Chem. Soc.* **2009**, *131*, 6498.

(62) Paul, A.; Watson, R. M.; Wierzbinski, E.; Davis, K. L.; Sha, A.; Achim, C.; Waldeck, D. H. *J. Phys. Chem. B* **2010**, *114*, 14140.

(63) Laviron, E. *J. Electroanal. Chem.* **1979**, *101*, 19.

(64) Anne, A.; Demaille, C. *J. Am. Chem. Soc.* **2006**, *128*, 542.

(65) Hüsken, N.; Gębala, M.; La Mantia, F.; Schuhmann, W.; Metzler-Nolte, N. *Chemistry* **2011**, *17*, 9678.

(66) Skourtis, S. S.; Waldeck, D. H.; Beratan, D. N. *Annu. Rev. Phys. Chem.* **2010**, *61*, 461.

(67) Nitzan, A. *J. Phys. Chem. A* **2001**, *105*, 2677.

(68) Nitzan, A. *Isr. J. Chem.* **2002**, *42*, 163.

(69) Venkatramani, R. *Publ. Prep.*

(70) Tong, G. S. M.; Kurnikov, I. V.; Beratan, D. N. *J. Phys. Chem. B* **2002**, *106*, 2381.

(71) Venkatramani, R. *In Preparation*.

(72) Balaeff, A. *Publ. Prep.*

(73) Anderson, G. W.; McGregor, A. C. *J. Am. Chem. Soc.* **1957**, *79*, 6180.

(74) McKay, F. C.; Albertson, N. F. *J. Am. Chem. Soc.* **1957**, *79*, 4686.

(75) Weber, K.; Creager, S. E. *Anal. Chem.* **1994**, *66*, 3164.

(76) Napper, A. M.; Liu, H.; Waldeck, D. H. *J. Phys. Chem. B* **2001**, *105*, 7699.

(77) Hornak, V.; Abel, R.; Okur, A.; Strockbine, B.; Roitberg, A.; Simmerling, C. *Proteins* **2006**, *65*, 712.

(78) Case, D. A.; Darden, T. A.; Cheatham T.E.,, I. I. I.; Simmerling, C. L.; Wang, J.; Duke, R. E.; Luo, R.; Walker, R. C.; Zhang, W.; Merz, K. M.; Roberts, B.; Wang, B.; Hayik, S.; Roitberg, A.; Seabra, G.; Kolossváry, I.; Wong, K. F.; Paesani, F.; Vanicek, J.; Liu, J.; Wu, X.; Brozell, S. R.; Steinbrecher, T.; Gohlke, H.; Cai, Q.; Ye, X.; Hsieh, M.-J.; Cui, G.; Roe, D. R.; Mathews, D. H.; Seetin, M. G.; Sagui, C.; Babin, V.; Luchko, T.; Gusarov, S.; Kovalenko, A.; Kollman, P. A. AMBER11. *AMBER11* **2010**.

(79) Lu, X.-J.; Olson, W. K. *Nucleic Acids Res.* **2003**, *31*, 5108.

(80) Zeng, J.; Hush, N. S.; Reimers, J. R. *J. Am. Chem. Soc.* **1996**, *118*, 2059.

(81) Datta, S. *Quantum Transport: Atom to Transistor*; Cambridge, 2005, 2005.

5.0 LUMINESCENCE QUENCHING BY PHOTOINDUCED CHARGE TRANSFER BETWEEN METAL COMPLEXES IN PEPTIDE NUCLEIC ACIDS

This work has been published as Yin, X.; Kong, J.; De Leon, A. R.; Li, Y.; Ma, Z.; Wierzbinski, E.; Achim, C.; Waldeck, D. H. J. Phys. Chem. B 2014, 118, 9037–45. The author of the dissertation is the lead author and performed the spectroscopic experiments and subsequent lifetime distribution and molecular dynamics analysis. J.K. and A.R.L. synthesized the PNAs. Y.L. provided the force field parameters. Z.M. developed the method to synthesize the $Ru(bpy)_3^{2+}$ *monomer. All authors participated in the writing and revision of the manuscript.*

A new scaffold for studying photoinduced charge transfer has been constructed by connecting a $[Ru(Bpy)_3]^{2+}$ donor to a bis(8-hydroxyquinolinate)$_2$ copper $[CuQ_2]$ acceptor through a peptide nucleic acid (PNA) bridge. The luminescence of the $[Ru(Bpy)_3]^{2+*}$ donor is quenched by electron transfer to the $[CuQ_2]$ acceptor. Photoluminescence studies of these donor-bridge-acceptor systems reveal a dependence of the charge transfer on the length and sequence of the PNA bridge and on the position of the donor and acceptor in the PNA. In cases where the $[Ru(Bpy)_3]^{2+}$ can access the π-base stack at the terminus of the duplex, the luminescence decay is described well by a single exponential; but if the donor is sterically hindered from accessing the π base stack of the PNA duplex, a distribution of luminescence lifetimes for the donor $[Ru(Bpy)_3]^{2+*}$ is observed. Molecular dynamics simulations are used to explore the donor-PNA-acceptor structure and the resulting conformational distribution provides a possible explanation for the distribution of electron transfer rates.

5.1 INTRODUCTION

Nucleic acids are interesting building blocks for supramolecular assemblies because of their predictable and programmable Watson-Crick base pairing, which in turn makes possible the encoding of specific three-dimensional architectures in the assemblies.[1–5] Hence nucleic acids have been studied extensively as a building block for nanotechnology applications.[6] Chemical synthesis has created either nucleic acid analogues, such as peptide nucleic acids (PNAs), or nucleic acids with functional groups, including redox centers and fluorophores, that impart functionality to the nucleic-acid-based nanostructures. This work reports on PNA, a synthetic analog of DNA that typically has a pseudo-peptide backbone composed of N-(2-aminoethyl)-glycine units.[7–9] PNA offers a number of advantages over DNA for nucleic acid based structures, such as higher thermal stability, superior chemical stability in biological media, and control over the chirality.[10,11] The PNA backbone and nucleobases have been chemically modified to confer desirable properties for specific applications, such as sequence specific binding to DNA, cell permeability, and others.[12,13] By substituting the PNA nucleobases with ligands that have a high affinity for metal ions, PNA duplexes that bind transition metal ions at specific positions can be created.[10,11]

While we and others have appended electroactive groups to PNA and reported the results of electrochemical and sensing studies of PNA attached to solid surfaces,[14–21] charge transfer through PNA duplexes in solution has not been reported. We have studied charge transfer through self-assembled monolayers (SAMs) of the PNAs by electrochemistry,[22,23] and more recently, we have measured the single molecule conductance of the PNAs by a break junction method and compared it to the electrochemical charge transfer rates.[24] Studies of unimolecular charge transfer in PNA, which is a synthetic analog of DNA with a neutral polyamide backbone rather than a diphosphate ester, polyanion backbone, provide insight into the fundamental features of long-range

charge transfer in nucleic acids, by making possible comparisons with existing work on DNA[25–40] and eventually with other nucleic acids.

In this work, photoinduced electron transfer through PNA is studied between a $[Ru(Bpy)_3]^{2+}$ electron donor and a [Cu(8-hydroxy-quinolinate)$_2$] ([CuQ_2]), which acts as an electron acceptor. A PNA monomer that contains a $[Ru(Bpy)_3]^{2+}$ complex tethered to the PNA backbone was synthesized (Monomer **Ru** in Figure 5.1) and introduced into PNA oligomers at different positions, either terminal or central, by solid phase peptide synthesis (Table 5.1 and 5.2). When $[Ru(Bpy)_3]^{2+}$ was situated in a central position of the duplex, an abasic PNA monomer in which the secondary amine of the Aeg was capped with an acetyl group (Monomer **B** in Figure 5.1) was introduced at the position complementary to $[Ru(Bpy)_3]^{2+}$. The acceptor was created by Cu^{2+} coordination to a pair of Q ligands situated in complementary positions in the duplexes (Monomer **Q** in Figure 5.1).[15]

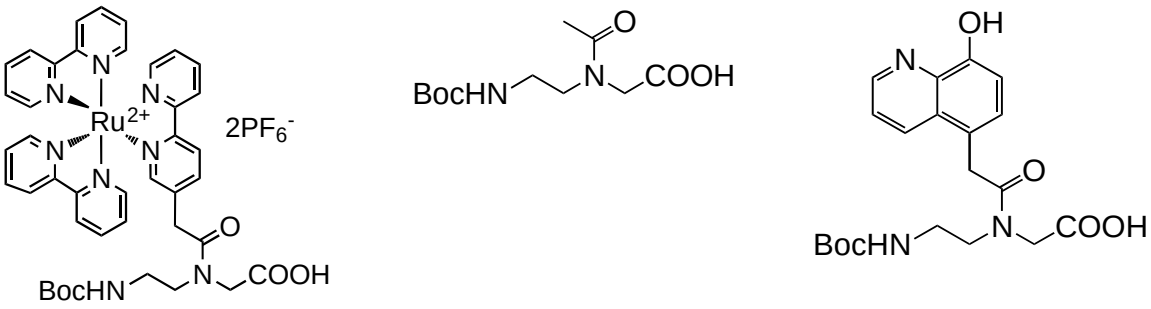

Ru **B** **Q**

Figure 5.1. The structure of PNA monomers. The nucleobase is replaced by $[Ru(Bpy)_3]^{2+}$ (Monomer **Ru**), formally, by a hydrogen atom (Monomer **B**), or by 8-hydroxyquinoline (Monomer **Q**).

5.2 METHODS

5.2.1 PNA Synthesis and Characterization

5.2.1.1 Materials

The Boc-protected 8-hydroxyquinolinyl PNA monomer 2-(N-(tert-butyloxycarbonyl-2-aminoethyl)-2-(8-hydroxyquinolin-5-yl)acetamido)acetic acid (**Q**, Figure 5.1C) and precursor 2,2'-bipyridyl PNA monomer **1** (Figure 5.2) 2-(N-(tert-butyloxycarbonyl-2-aminoethyl)-2-(2,2'-bipyridin-4-yl)acetamido)acetic acid, which are needed for synthesizing ruthenium(II) tris(bipyridyl) PNA monomer (**Ru**, Figure 5.1A), were synthesized as reported previously.[15,41] The ruthenium(II) tris(bipyridyl) PNA monomer **Ru**, namely 2-(N-(tert-butyloxycarbonyl-2-aminoethyl)-2-(2,2'-bipyridin-4-yl) acetic acid)-bis(2,2'-bipyridine)ruthenium(II), was synthesized from precursor **1**, Bpy PNA monomer.[42] The backbone monomer was synthesized from the coupling between tert-butyl 2-(2-(tert-butoxycarbonyl)ethylamino)acetate and acetic anhydride, followed by hydrolysis, as reported previously.[22] All other reagents were commercially available, analytical grade quality, and used without further purification.

5.2.1.2 Synthesis of $[Ru(Bpy)_3]^{2+}$-containing PNA monomer (Figure 5.2)

All manipulations were carried out under low light. Bpy PNA monomer **1** (415 mg, 1mmol) was suspended in 43 ml of a 70% ethanol solution. cis-Bis(2,2'-bipyridine)dichlororuthenium(II) hydrate (500 mg, 0.96 mmol) was added to the suspension. The reaction mixture was refluxed for 16 h and the solvent was removed by vacuum. The compound was purified by cation exchange chromatography using CM-sepharose resin, with an ammonium chloride step gradient. The desired product precipitated out of the solution upon addition of ammonium hexafluorophosphate. The

precipitate was filtered and washed several times with water and ether. An orange residue remained. Yield: 42% (447 mg). Mass Spectral data (ESI) calc./found 827.9/827.2. ^{1}H NMR (300 MHz, CD_3CN): δ 8.5 (m, 6H), 8.05 (m, 5H), 7.95 (m, 1H), 7.75 (m, 5H), 7.60 (m, 1H), 7.40 (m, 5H), 5.50 (βρ, 1H,NH), 4.0 (m, 2H, CH_2), 3.6 (m, 2H, CH_2), 3.30 (m, 2H, CH_2), 3.10 (m, 2H, CH_2), 1.40 (s, 9H, Boc).

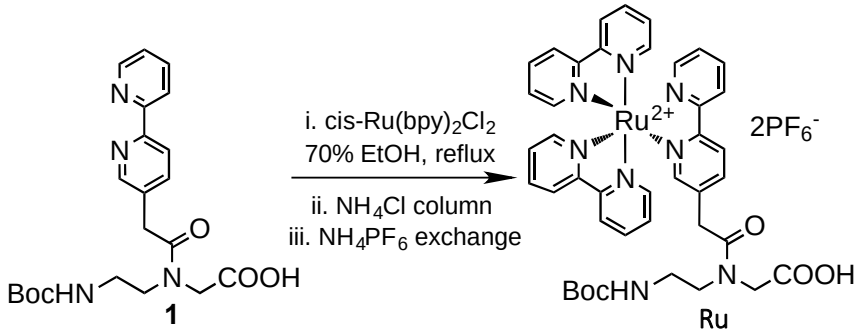

Figure 5.2. The synthesis scheme for the PNA monomer that contains $[Ru(Bpy)_3]^{2+}$ complex**.**

5.2.1.3 Solid Phase PNA Synthesis

PNA oligomers were synthesized with the Boc-protection strategy. PNA monomers were purchased from ASM Research Chemicals and were used without further purification. PNA was precipitated using diethyl ether after cleavage and was purified by reversed-phase HPLC using a C18 silica column on a Waters 600 model. Absorbance was measured at 260 nm with a Waters 2996 Photodiode Array Detector. The concentration of PNA oligomers was determined by UV absorption at 90°C using the sum of the extinction coefficients of the constituent PNA monomers at 260 nm taken from the literature. (ε_{260} were taken to be 8600 M^{-1} cm^{-1} for T, 6600 M^{-1} cm^{-1} for C, 13700 M^{-1} cm^{-1} for A, and 11700 M^{-1} cm^{-1} for G).[10] The extinction coefficient for the $[Ru(Bpy)_3]^{2+}$ at 260 nm is taken to be the same as that of $[Ru(Bpy)_3]Cl_2$ in water (ε_{260} = 13250 M^{-}

$^{1}cm^{-1}$). The extinction coefficient for 8-hydroxyquinoline ε_{260} = 2570 M^{-1} cm^{-1} (at pH 7.0) was determined from the slope of a plot of A_{260} versus concentration.

Characterization of the oligomers was performed by MALDI-ToF mass spectrometry on an Applied Biosystems Voyager Biospectrometry Workstation with Delayed Extraction and an R-cyano-4-hydroxycinnamic acid matrix (10 mg/mL in 1:1 water/acetonitrile, 0.1% TFA). m/z for $(M+H)^{+}$ were calculated and found to be **P-AA** α 3565.44/3568.05, **P-AA** β 2879.88/2882.03, **P-AG** α 3582.63/3582.39, **P-AG** β 2864.87/2864.95, **P-AGTGA** α 3582.63/3579.06, **P-AGTGA** β 2864.87/2863.12, **P-AA-P'** α 4390.71/4392.44, **P-AA-P'** β 3824.73/3824.83, **P-AG-P'** α 4415.82/4417.45, **P-AG-P'** β 3799.10/3800.87.

5.2.2 Photoluminescence Measurement

Steady-state emission spectra were measured on a HORIBA Jobin Yvon Fluoromax 3 fluorescence spectrophotometer. The luminescence decay data were collected using the time-correlated single photon counting (TCSPC) method with a PicoHarp 300 TCSPC module (PicoQuant GmbH). The samples were excited by light from a 440 nm pulsed diode laser (PIL043, ALS GmbH) operating at a 500 kHz repetition rate. Emission from the sample was collected at 620 nm using a monochromator. All PNA samples were dissolved in 10 mM phosphate buffer (pH=7) and measurements were performed with a duplex concentration of 20 μM. The concentration dependence was tested for P-AA/Cu, P-AA-P'/Cu, and P-AG-P'/Cu from 3 μM to 30 μM (see Table 5.1 for sequence of the PNAs). In each case, no concentration dependence of the luminescence lifetime was observed, indicating a unimolecular decay process. The instrument response function had a full-width-at-half-maximum (fwhm) of ~60ps, which is much shorter than

the luminescence lifetimes (> 250 ns); thus tail fitting (discarding the rising part of the decay) was employed in the exponential component and lognormal distribution analyses.

5.2.3 Lognormal Distribution Fitting of Luminescence Decays

A general form of the luminescence decay law may be written as

$$D(t) = C_0 \cdot \int_0^\infty A(\tau)\ \exp\left(-\frac{t}{\tau}\right)\ \mathrm{d}\tau + B_0 \qquad \textbf{Equation 5.1}$$

where $D(t)$ is the emission intensity at time t and $A(\tau)$ is the normalized distribution function of luminescence lifetimes τ. C_0 is a parameter that represents the experimental signal at time zero, and B_0 represents the background counts (noise level). $D(t)$ is a Laplace transform of $A(\tau)$ and to recover $A(\tau)$ one can perform an inverse Laplace transform. Several methods exist for this purpose, such as the maximum entropy method[43] and a method for the recovery of $A(\tau)$ from frequency domain data.[44–46] These methods do not require *a priori* knowledge about the shape of the distribution but they are usually very sensitive to noise and require very high counts (about 5×10^5 counts per channel)[47] because of the ill-conditioned nature of inverse Laplace transforms.[48]

Here we assume a lognormal shape[47] of the lifetime components and perform a direct fitting of the data which is much more robust with regard to noise. The lognormal distribution is used because it has the correct boundary behaviors.[49] Using symbols similar to those used for the normal distribution, the lognormal distribution $P(\tau)$ is defined as:

$$P(\tau) = \frac{1}{\tau \cdot \sigma\sqrt{2\pi}} \exp\left\{\frac{-(\ln\tau - \mu)^2}{2\sigma^2}\right\} \qquad \textbf{Equation 5.2}$$

where μ is a parameter related to the peak maximum and σ is a parameter controlling the peak width. Note that μ and σ are not the mean and standard deviation of the distribution. Equation 5.2 can be transformed to

$$P(\tau) = \frac{1}{\sigma\sqrt{2\pi}} \cdot \exp\left(\frac{\sigma^2}{2} - \mu\right) \cdot \exp\left\{\frac{-[\ln\tau - (\mu - \sigma^2)]^2}{2\sigma^2}\right\} \quad \textbf{Equation 5.3}$$

From the above equation, it is straightforward to show that the peak maximum (mode) is $\exp(\mu - \sigma^2)$ and the mean is $\exp(\mu + \sigma^2/2)$.

Another reason to choose the lognormal distribution is that a lognormal distribution of τ is equivalent to a lognormal distribution of k. Because $\tau = 1/k$, one finds that

$$P_\tau(\tau) = \exp\left\{\frac{-[\ln\tau - (\mu - \sigma^2)]^2}{2\sigma^2}\right\} = \exp\left\{\frac{-[\ln k - (\sigma^2 - \mu)]^2}{2\sigma^2}\right\} \quad \textbf{Equation 5.4}$$

where $P_\tau(\tau) = \sigma\sqrt{2\pi}\, P(\tau) \cdot \exp\left(\frac{-\sigma^2}{2} + \mu\right)$. If one defines $\mu' = 2\sigma^2 - \mu$, then one obtains:

$$P_\tau(\tau) = \exp\left\{\frac{-[\ln k - (\mu' - \sigma^2)]^2}{2\sigma^2}\right\} = P_k(k) \quad \textbf{Equation 5.5}$$

The overall distribution function $A(\tau)$ may contain more than one peak (two in the actual fitting used here) and it is defined as follows

$$A(\tau) = C_1 \cdot P_1(\tau) + C_2 \cdot P_2(\tau) + \cdots \quad \textbf{Equation 5.6}$$

where C_1 and C_2 are the normalized statistical weight of each peak. To fit $A(\tau)$ with experimental data, a set of discrete lifetimes (the number of lifetimes used is 200 in this work) from 1 ns to 1000 ns are used to convert the integral in Equation 5.1 to a summation; that is,

$$D(t) = C_0 \cdot \sum_n \left\{A_n \cdot \exp\left(-\frac{t}{\tau_n}\right)\right\} + B_0 \quad \textbf{Equation 5.7}$$

where $A_n = A(\tau_n)$ is the amplitude of lifetime τ_n. The $D(t)$ defined above is used for the fit with experimental data. Because TCSPC data follows a Poisson distribution, the fitting process varies the A_n parameters in order to minimize the reduced chi-square χ^2:

$$\chi^2 = \sum_t \frac{[D(t) - F(t)]^2}{N \cdot F(t)} \qquad \textbf{Equation 5.8}$$

where *N* is the number of TCSPC channels. χ^2 is set as the objective function and is optimized to a minimum by using the Optimization Toolbox in MATLAB. The final χ^2 is smaller than 1.05 for all lognormal distribution fittings.

5.2.4 Molecular Dynamics Simulation

The molecular dynamics (MD) simulation followed a protocol like that previously reported for PNAs.[50,51] The initial structures were constructed based on the average helicoidal parameters of experimentally determined PNA duplexes (PDB ID: 2K4G).[52] Because a force field is not available for the [CuQ_2] complex, an A:T base pair was used instead. The force field ff99SB[53] was complemented with the previously determined atomic partial charges[52] and the parameter set was adapted from another work[54] for $[Ru(Bpy)_3]^{2+}$. The structures were solvated in a TIP3P water box, such that the distance between the walls of the box and the closest PNA atom was at least 12 Å. After energy minimization and equilibration, the solvated structures were subjected to a 2 ns MD run using the module 'pmemd' of Amber 12[55] at T = 300 K and P = 1 atm, with periodic boundary conditions. A total of 2000 snapshots were saved for each trajectory (at every 1 ps) and used for the subsequent analyses.

5.3 RESULTS AND DISCUSSION

5.3.1 Duplex Characterization

The formation of the PNA duplexes and the binding of Cu^{2+} to the duplexes have been studied by thermal denaturation and by titrations using photoluminescence spectroscopy. Table 5.1 shows the sequence of several of the PNA duplexes that are studied in this work; see Table 5.2 for a more comprehensive list.[41,42] The sequence of the duplexes is related to that of the duplex named **P** in Table 5.1. The positions of the donor unit (labeled Ru) and of the ligands (labeled Q) that form the $[CuQ_2]$ acceptor on the PNA duplexes are varied between the different systems studied. In addition, the chemical nature of the base pairs has been varied (see **P-AG** and **P-AA** in Table 5.1). For example, PNA duplexes that contain a terminal Ru donor and can form the $[CuQ_2]$ acceptor have been synthesized with two or five nucleobases between the donor and acceptor positions. The name of these duplexes includes the names of the nucleobases situated between the donor and the acceptor; for example, duplex **P-AA** has two A nucleobases between the **Ru** monomer and Q ligand and can form two AT base pairs between the donor and the $[CuQ_2]$ acceptor. Duplexes that have only one Q ligand (instead of a pair of Q ligands) have been synthesized as control systems and are labeled with a **1Q**. In addition, duplexes that have a duplex 'tail' which sterically hinders the $Ru(Bpy)_3^{2+}$ donor from accessing the duplex terminus were synthesized, and they are identified by including the tail in the name of the duplex as **P'**.

Table 5.1. Sequences and melting temperatures T_m of the PNA duplexes with and without Cu^{2+}.[a]

Duplex	Sequence	T_m (ºC)[b]	
		without Cu^{2+}	with Cu^{2+}
P	H-AGTGATCTAC-H H_2N-Lys-TCACTAGATG-H	67	67
P-AG	H-**Ru**AG**Q**GATCTAC-Lys-NH_2 H_2N-Lys-TC**Q**CTAGATG-H	56	>75
P-AA	H-**Ru**AA**Q**GATCTAC-Lys-NH_2 H_2N-Lys-TT**Q**CTAGATG-H	56	>75
P-AG-1Q	H-**Ru**AG**Q**GATCTAC-Lys-NH_2 H_2N-Lys-TCACTAGATG-H	58	52
P-AA-1Q	H-**Ru**AA**Q**GATCTAC-Lys-NH_2 H_2N-Lys-TTACTAGATG-H	58	56
P-AGTGA	H-**Ru**AGTGA**Q**CTAC-Lys-NH_2 H_2N-Lys-TCACT**Q**GATG-H	47	>75
P-AT-P'	H-AGTGA**Ru**AT**Q**TCTAC-Lys-NH_2 H_2N-Lys-TCACT**B**TA**Q**AGATG-H	48	70
P-AG-P'	H-AGTGA**Ru**AG**Q**TCTAC-Lys-NH_2 H_2N-Lys-TCACT**B**TC**Q**AGATG-H	48	66

[a] Ru, Q, and B indicate the monomers in Figure 5.1; T, C, G, and A are the conventional nucleobase notations; and Lys indicates placement of a lysine;

[b] The Tm values are an average of 2 or 3 measurements on 5 μM solutions of ds PNA in a pH 7.0, 10 mM sodium phosphate buffer solution and are known within 1°C.

Melting curves of PNA duplexes in the absence and presence of Cu^{2+} are shown in panels A and B of Figure 5.3; the melting temperatures T_m for all the duplexes are reported in Table 5.1. The T_m of the non-modified, 10-base pair PNA duplex **P** is 67°C. The T_m of duplexes that contained one or two Q ligands was lower than that of **P** by 9-20°C. This decrease is similar to that caused by a base pair mismatch. In the presence of Cu^{2+}, the melting of the **P-AG**, **P-AA**, and **P-AGTGA** duplexes showed a hyperchromicity increase of more than 15% as the temperature was increased, but the hyperchomicity did not reach saturation. In these cases a two-state model cannot be used to determine the T_m but the increase in hyperchromicity indicates that the duplexes are

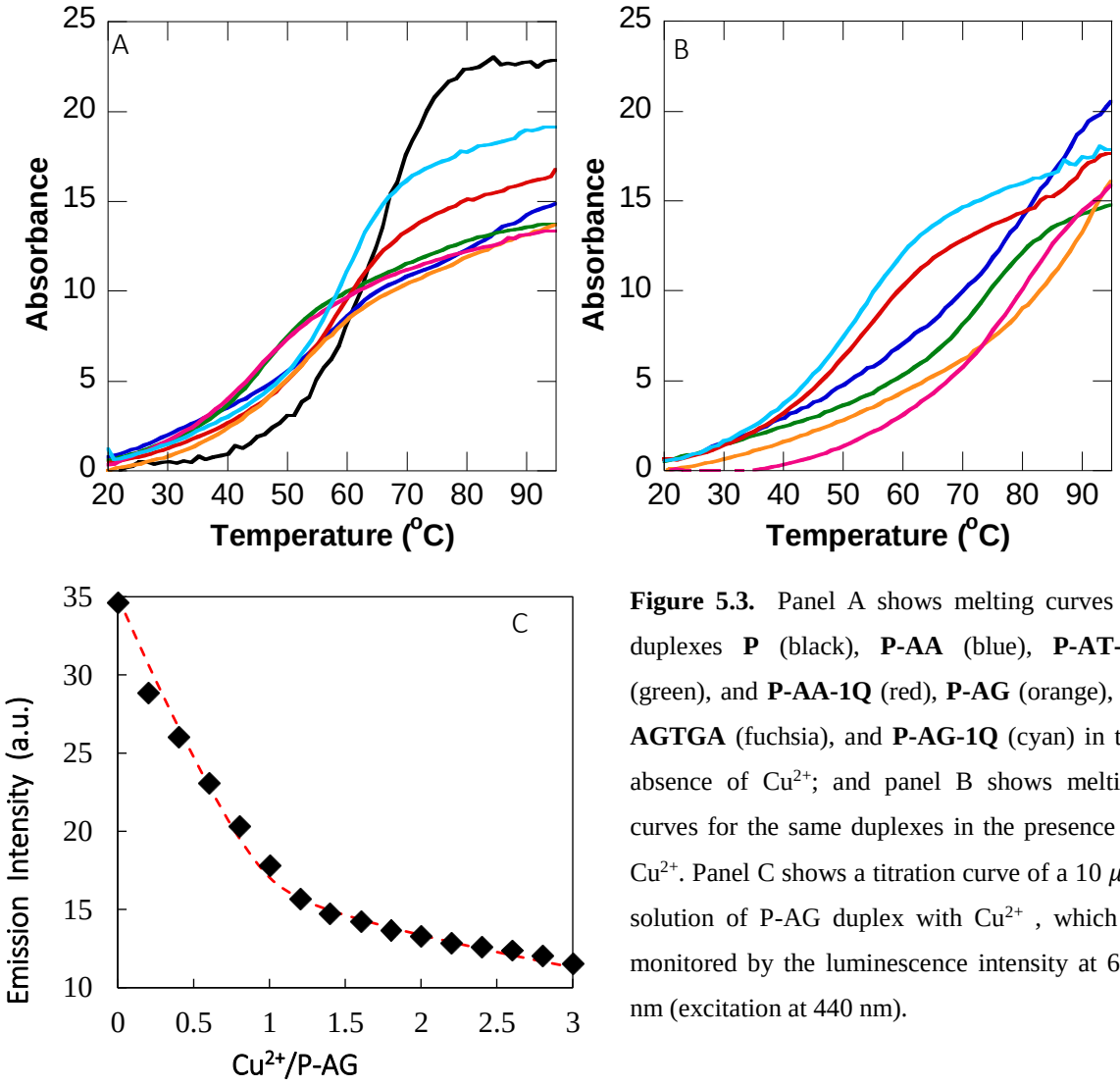

Figure 5.3. Panel A shows melting curves of duplexes **P** (black), **P-AA** (blue), **P-AT-P'** (green), and **P-AA-1Q** (red), **P-AG** (orange), **P-AGTGA** (fuchsia), and **P-AG-1Q** (cyan) in the absence of Cu^{2+}; and panel B shows melting curves for the same duplexes in the presence of Cu^{2+}. Panel C shows a titration curve of a 10 μM solution of P-AG duplex with Cu^{2+} , which is monitored by the luminescence intensity at 620 nm (excitation at 440 nm).

stabilized by Cu^{2+}. For the other PNA duplexes, the melting curves measured in the presence of Cu^{2+} reached saturation, and the T_m determined using a two-state model was higher than that of duplex **P** by more than 15°C.[56] This increase in stability in the presence of Cu^{2+} for all PNA duplexes that contain a pair of Q ligands could be attributed to the formation of a $[CuQ_2]$ complex that functions as an alternative base pair. This interpretation of the melting temperature data is supported by the fact that the T_m of the PNA duplexes that contain only one Q ligand and cannot form an intra-duplex $[CuQ_2]$ complex (**P-AG-1Q** and **P-AA-1Q**) was 9°C lower than that of **P** and was not stabilized by Cu^{2+}.

Photoluminescence titrations of the duplexes (Figure 5.3C and Figure 5.7) showed a decrease in the emission intensity of $[Ru(Bpy)_3]^{2+}$ as the Cu^{2+} concentration increased. This decrease can be described by a bimolecular equilibrium between the Cu^{2+}-free duplex and the duplex to which one equivalent of Cu^{2+} is coordinated (in which the luminescence of the Ru complex is quenched; see Supporting Information).[43,45–49,57–60] The equilibrium constant from this analysis was found to be larger than 10^6 M^{-1}.[a] The photoluminescence measurements described below were performed on 10 μM to 20 μM solutions of the PNA duplexes that contained two equivalents of Cu^{2+}; under these conditions a K~ 10^6 M^{-1} imples that 97% of the duplexes are fully coo ated with Cu^{2+}.

[a] The upper limit (which is larger than 10^{10}) of the equilibrium constant was studied by more accurate methods such as ITC and UV titrations and it will be published in another paper. This manuscript focuses on the charge transfer thus only the low limit (which obtained by fitting the photoluminescence data to the bimolecular equilibrium model) is needed.

5.3.2 Charge Transfer and the Duplex π-stack

The luminescence decay profiles for **P-AG** and **P-AGTGA** duplexes, which are presented in Figure 5.4, show the effect of the [CuQ_2] acceptor on the $[Ru(Bpy)_3]^{2+*}$ luminescence. In the absence of Cu^{2+}, the luminescence intensity of the $[Ru(Bpy)_3]^{2+*}$ complex in the **P-AG** and **P-AGCTA** duplexes (Figure 5.9) is similar to that of the "free" $[Ru(Bpy)_3]^{2+*}$ complex in solution (Figure 5.8). Addition of Cu^{2+} to the solution of the duplexes modified with **Ru**, but with no **Q** ligands, left the luminescence of $[Ru(Bpy)_3]^{2+*}$ unaffected (Figure 5.11). In contrast, the addition of one or more equivalents of Cu^{2+} to a solution of duplexes that contain two **Q** ligands quenches the $[Ru(Bpy)_3]^{2+*}$ luminescence (Figure 5.3). These results indicate that quenching of the $[Ru(Bpy)_3]^{2+*}$ in the **P-AG** or **P-AGCTA** involves the [CuQ_2] complex that is part of the PNA duplex. Energy transfer from $[Ru(Bpy)_3]^{2+*}$ to [CuQ_2] is discounted as a decay pathway because of the poor overlap between the emission spectrum of $[Ru(Bpy)_3]^{2+}$ (Figure 5.8 and Figure 5.9) and the absorption spectrum of [CuQ2] (Figure 5.10). On the other hand, the electron transfer reaction $[Ru(Bpy)_3]^{2+*}$+[CuQ_2] $\rightarrow$ $[CuQ_2]^-$ + $[Ru(Bpy)_3]^{3+}$ is thermodynamically favorable ($\Delta_r G < -0.6$ eV before Coulomb correction,[61,62] see SI). Hence, quenching of the $[Ru(Bpy)_3]^{2+*}$

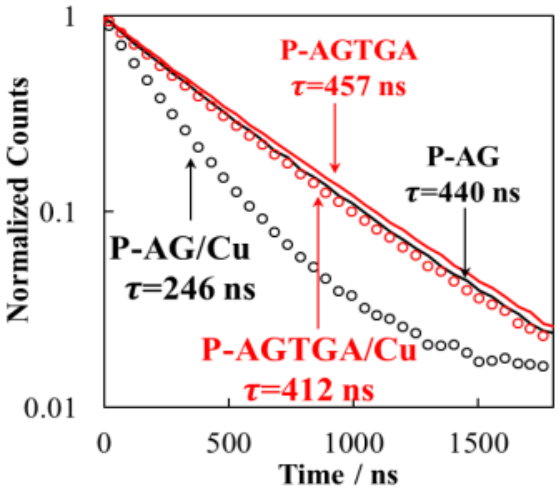

Figure 5.4. Luminescence decay for 20 μM solutions of **P-AG** (black) and **P-AGTGA** (red) in a pH 7.0, 10 mM phosphate buffer in the absence (solid lines) and presence (open circles) of two Cu^{2+} equiv. The time constants that are obtained from a best fit by a single exponential decay are shown in the figure. A support plane analysis (see supplemental information) indicates that they are accurate to ± 1 ns; however sample to sample variations display a standard deviation of ~ 1.5% in the lifetime value (see section 5 of the Supplementary Information).

occurs because of electron transfer to the acceptor [CuQ_2]. This conclusion was corroborated by the observation of strong luminescence with the redox inactive [ZnQ_2] in the **P-AG** duplex (see SI for details). Note that a conformational change between [CuQ_2] and [CuQ_2]$^{\square}$ may occur after charge transfer; however, the reduction potential of $[Ru(Bpy)_3]^{3+}$ is much more positive (+1.15 V vs. NHE) (See Supporting Information) than that of [CuQ_2] (+0.05 V vs. NHE)[61] and a fast back electron transfer in the ground state is expected to restore the planar structure of the [CuQ_2] complex. This interpretation is supported by the fact that the system showed no signs of photoinduced degradation over the course of the experiments.

The luminescence decays for $[Ru(Bpy)_3]^{2+*}$ in duplexes of **P-AG** and **P-AGTGA** were used to probe the length dependence of the charge transfer rate; see Figure 5.4. In each case the luminescence decay law could be described by a single exponential,[a] and the addition of Cu^{2+} caused a decrease of the luminescence lifetime of the $[Ru(Bpy)_3]^{2+*}$ for both duplexes. Assuming that the enhanced excited state decay rate of $[Ru(Bpy)_3]^{2+*}$ upon addition of Cu^{2+} is caused by electron transfer, the rate constant for electron transfer from $[Ru(Bpy)_3]^{2+*}$ to [CuQ_2] can be calculated as $k_{CT} = 1/\tau - 1/\tau_0$; one obtains a value of 1.8 μs^{-1} for **P-AG** and of 0.24 μs^{-1} for **P-AGTCA**. Although these values are for only two donor-acceptor distances, a decay parameter of $\beta \sim 0.2$ $Å^{-1}$ is obtained if one assumes that $k_{CT} \propto \exp(-\beta \cdot D_{DA})$, in which D_{DA} is the distance between $[Ru(Bpy)_3]^{2+*}$ and [CuQ_2] through the π-base stack. This value should be considered a lower limit however; as differences in $\Delta_r G$ for the **P-AG** than **P-AGTGA** duplexes that arise from differences in the Coulomb field stabilization of the different charge separated states also affect

[a] Although the luminescence decay of the Ru complex in **P-AG**/Cu can be fit with a single exponential decay, the goodness of the fit can be increased by using a single modal distribution. The origin of the distribution is discussed later.

the rate constant.[63,64] Accounting for these differences causes the value of β to increase to about 0.4 Å^{-1} (see section 5 of SI). Nevertheless, the value of β lies between the values reported for superexchange in single stranded PNAs (0.7∼0.8 Å^{-1})[23,61,65] and hole hopping in duplex PNAs (0.07 Å^{-1})[65] from electrochemistry. The difference between β measured by luminescence in solution and by electrochemistry in SAMs of PNA may be caused by differences in the PNA geometry and/or by the fact that the charge transfer is likely to be electron-mediated[66,67] in solution and hole-mediated[23,65] in the SAMs.

The distance dependence observed here for PNA is consistent with literature reports for DNA. The range of estimated β values (0.2 to 0.4) for PNA are somewhat smaller than those reported for DNA in the superexchange regime, which range from 0.6-0.8,[31,68–70] but are comparable to the range of β values (0.2-0.4) Å^{-1} reported for hole transfers in DNA when the donor and acceptor are separated by 3-6 base pairs.[71,72] Note that β in DNA becomes < 0.1 Å^{-1} once the hole transfer is in the hopping regime.[69] For reductive electron transfer in DNA, fewer studies are available and the mechanism is not yet wholly clear, but a number of groups have reported small β values for relatively short distances (less than 5 to 7 base pairs), ranging from 0.11 Å^{-1} to 0.26 Å^{-1}.[66,67,73–75] Thus, the distance dependence observed here for photoinduced electron transfer in PNA is not atypical of that found for charge transfer through □-stacked nucleobases in previous studies.

To examine the importance of the π-stack between the Ru donor and acceptor on the electron transfer, the effects (1) of a base pair mismatch and (2) of the chemical nature of the base pairs situated between the donor and acceptor were studied. To create a mismatch, a T nucleobase was replaced by a C nucleobase in one of the two AT base pairs situated between the $[Ru(Bpy)_3]^{2+}$ and the Q ligands in the **P-AA** duplex. The lifetime of Ru increased from 278 ns for the fully

matched **P-AA**/Cu^{2+} duplex to 300 ns for the mismatched duplex in the presence of Cu^{2+}. This slowing of the charge transfer (longer lifetime) occurs, even though the mismatch is expected to cause more 'fraying' on the end of the base stack and suggests that the $Ru(Bpy)_3^{2+}$ is not penetrating through to the $[CuQ_2]$. For the fully complementary duplexes **P-AA** and **P-AG**, the difference in luminescence lifetime (278 ns for **P-AA**/ Cu^{2+} and 265 ns for **P-AG**/ Cu^{2+}) is smaller than that found in the mismatch study. This weak dependence on sequence is consistent with previous work on DNA for excess-electron transfer and has been attributed to the very similar reduction potentials of the base pairs.[66,67,76] These findings are consistent with charge transfer through the π-stack that is 'electron mediated'. Given the small lifetime changes, this hypothesis was tested further by constructing PNA duplexes in which the Ru is centrally situated and thus its access to the base stack is sterically encumbered.

5.3.3 Electron Transfer in Sterically Hindered Duplexes

The luminescence decay of the $[Ru(Bpy)_3]^{2+*}$ complex depends on the position of the Ru complex in the duplex, *i.e.* terminal versus central, as can be seen by comparing the data for **P-AG** and **P-AG-P'** in the presence of Cu^{2+} (Figure 5.5A). The **P-AG** duplex has the $[Ru(Bpy)_3]^{2+}$ at the end of the base stack while the **P-AG-P'** duplex is elongated so that the $[Ru(Bpy)_3]^{2+}$ cannot access the top of the nucleobase stack. The excited state decay law of $[Ru(Bpy)_3]^{2+*}$ in the **P-AG-P'** duplex cannot be fit by a single exponential; it could be fit by a double exponential decay law, however.

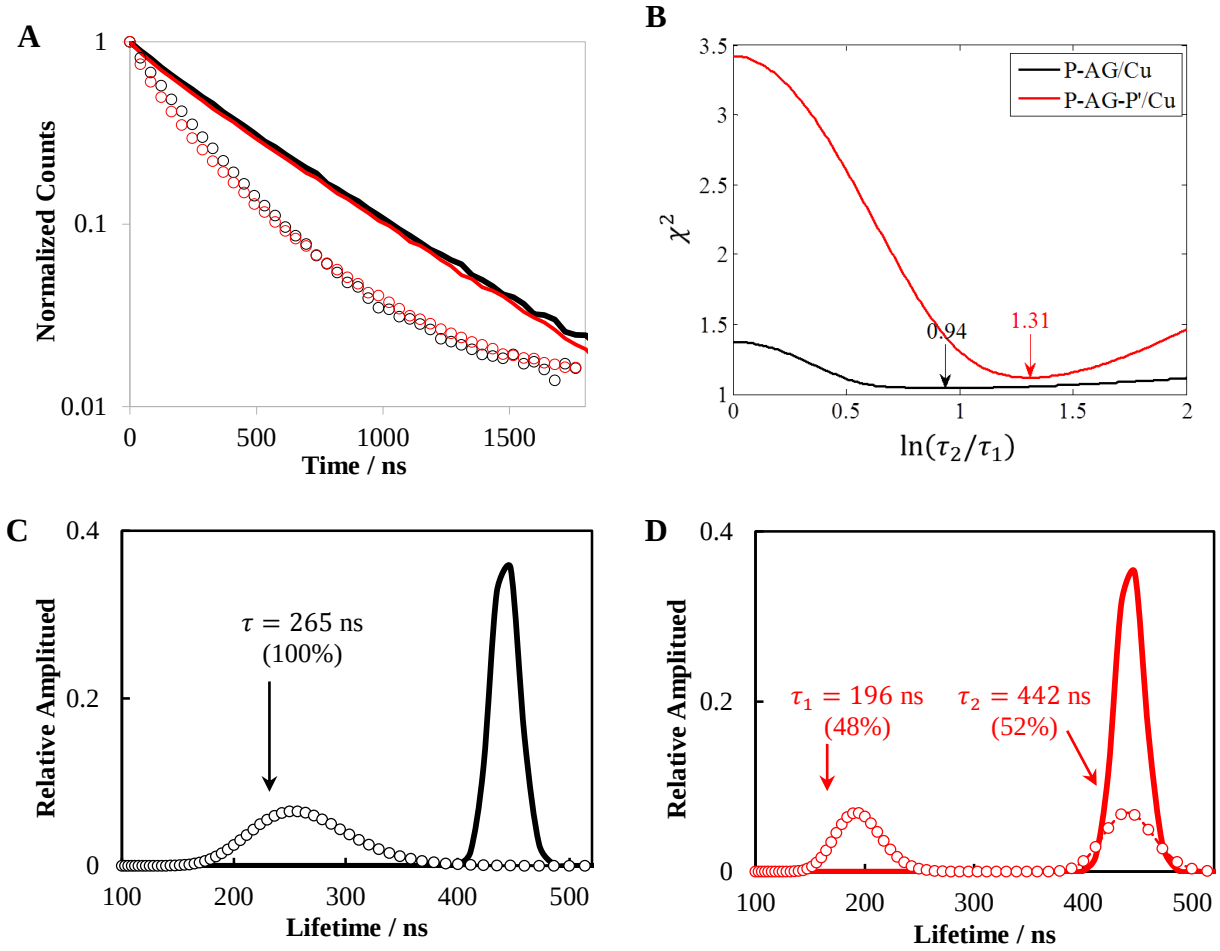

Figure 5.5. (A) Luminescence decays are shown for $[Ru(Bpy)_3]^{2+*}$ emission in duplexes **P-AG** (black) and **P-AG-P'** (red) in the absence (solid lines) and presence (open circles) of Cu^{2+}. Note that only every tenth data point is shown, so as to improve clarity of the image. (B) The optimized $\boldsymbol{\chi^2}$ of a double exponential fit is plotted versus $\boldsymbol{\ln(\tau_2/\tau_1)}$ for **P-AG** (black) and **P-AG-P'** (red) in the presence of Cu^{2+}. (C,D) The distribution of lifetimes are shown for the $[Ru(Bpy)_3]^{2+*}$ luminescence decay law. The color and symbol code is the same as panel A. Note that the distributions for the two duplexes in the absence of Cu^{2+} coincide and are centered at **442** ns. The mean value and the relative statistical weight of each peak are labeled for **P-AG**/Cu and **P-AG-P'**/Cu in panels C and D.

To quantify the difference between the **P-AG**/Cu and **P-AG-P'**/Cu decay laws, the χ^2 surface of a double exponential fit of the two decays was analyzed. In this analysis the ratio of the two lifetime components (τ_2/τ_1) was kept fixed while their absolute values and the relative

amplitudes of the two decay components were varied to minimize the χ^2. Figure 5B shows a plot of the optimized χ^2 for the two decay laws as a function of $\ln(\tau_2/\tau_1)$, where τ_1 and τ_2 are the two decay constants of the double exponential decay law. Note that when $\tau_2 = \tau_1$ (or $\ln(\tau_2/\tau_1) = 0$) a single exponential is recovered. It is clear from the plots that the **P-AG**/Cu system is better described by a single exponential (i.e., lower χ^2 value at $\ln(\tau_2/\tau_1) = 0$) than is the **P-AG-P'**/Cu system, and the χ^2 value of 1.4 for $\ln(\tau_2/\tau_1) = 0$ for **P-AG**/Cu is low enough to be considered acceptable for a single exponential fit. Moreover, the χ^2 versus $\ln(\tau_2/\tau_1)$ curve reaches a minimum at 0.94 for **P-AG**/Cu whereas it is 1.31 for the centrally-attached **P-AG-P'**/Cu; again suggesting that **P-AG**/Cu is closer to a single exponential decay.

The origin of the difference in χ^2 values (Figure 5B) is revealed by the lognormal lifetime distribution analysis (procedure described in the Methods section) as shown in Figs 5C and 5D. Note that without Cu^{2+} present the distribution of $[Ru(Bpy)_3]^{2+*}$ luminescence lifetimes in **P-AG** and **P-AG-P'** are well described by a single exponential decay law, and the distribution plots in Figure 5.5C and 5.5D provide a lower limit on the peak width that is available from this analysis. In the presence of Cu^{2+}, the luminescence decay of the $[Ru(Bpy)_3]^{2+*}$ in **P-AG-P'** requires a bimodal distribution, whereas **P-AG** can be fit by a single mode distribution (albeit with a somewhat larger peak width than shown for the Cu^{2+} free case). The mean value for the long lifetime component of **P-AG-P'** in the presence of Cu^{2+} is similar to the mean lifetime observed for **P-AG** and **P-AG-P'** in the absence of Cu^{2+}, but it has a larger width.

The observation of two different lifetimes for **P-AG-P'** and a single lifetime for **P-AG** could be caused by differences in the conformations available for the $[Ru(Bpy)_3]^{2+}$ in these duplexes. The bimodal distribution of luminescence lifetimes observed for **P-AG-P'** suggests that the PNA exists in (at least) two distinct conformations for which the charge transfer rates between

the $[Ru(Bpy)_3]^{2+*}$ and the $[CuQ_2]$ are significantly different and that the interchange between the two conformations is slow compared to the timescale of charge transfer. In contrast, the unimodal distribution for the luminescence decay of the $[Ru(Bpy)_3]^{2+*}$ complex **in P-AG** in the presence of Cu^{2+} indicates that the $[Ru(Bpy)_3]^{2+*}$ complex adopts one dominant conformation with respect to the $[CuQ_2]$ acceptor (or several ones that interconvert fast on the charge transfer timescale). This interpretation was corroborated by performing studies which showed that the luminescence decay of **P-AG -P'**/Cu^{2+}did not change when a mismatch was introduced between the $[Ru(Bpy)_3]^{2+*}$ and the $[CuQ_2]$.

In order to further test the conformation hypothesis, molecular dynamics (MD) simulations of the **P-AG** and **P-AG-P'** were performed. In these calculations, the $[CuQ_2]$ complex was replaced by an AT base pair because an accurate $[CuQ_2]$ force field is not yet available. Figure 6 shows the average structures of the duplexes that arise from typical trajectories and the distributions that were found for the donor-to-acceptor distance. Figure 6A shows the case of **P-AG** for which one of the three bipyridine ligands participates in a π-π interaction with a terminal base pair. This interaction may restrict the flexibility of the $[Ru(Bpy)_3]^{2+}$ and favor positions of the complex in which π-π stacking between pyridine ligands and the A-T base pair occurs. Note that the steric interactions between the two $[Ru(Bpy)_3]^{2+}$ enantiomers and the left-handed PNA duplex are somewhat different (See SI for distributions of individual trajectories for PNAs that contain (Λ)- and (Δ)-$[Ru(Bpy)_3]^{2+}$) and may contribute to broadening of the distribution; see Figure 6C. For the **P-AG-P'** duplex the π-π interaction is less important; presumably because of the large steric effect that prevents $[Ru(Bpy)_3]^{2+}$ from intercalating into the π-stack. In this latter system, the central $[Ru(Bpy)_3]^{2+}$ can be flipped toward either end of the duplexes, resulting in a more complicated conformational distribution.

To quantitatively characterize the distributions, the donor-acceptor distance D_{DA} was calculated for snapshots of each trajectory at every 0.2 ps. D_{DA} is defined as the distance between the Ru atom and the centroid of the "acceptor" AT base pair. As shown in the histogram of Figure

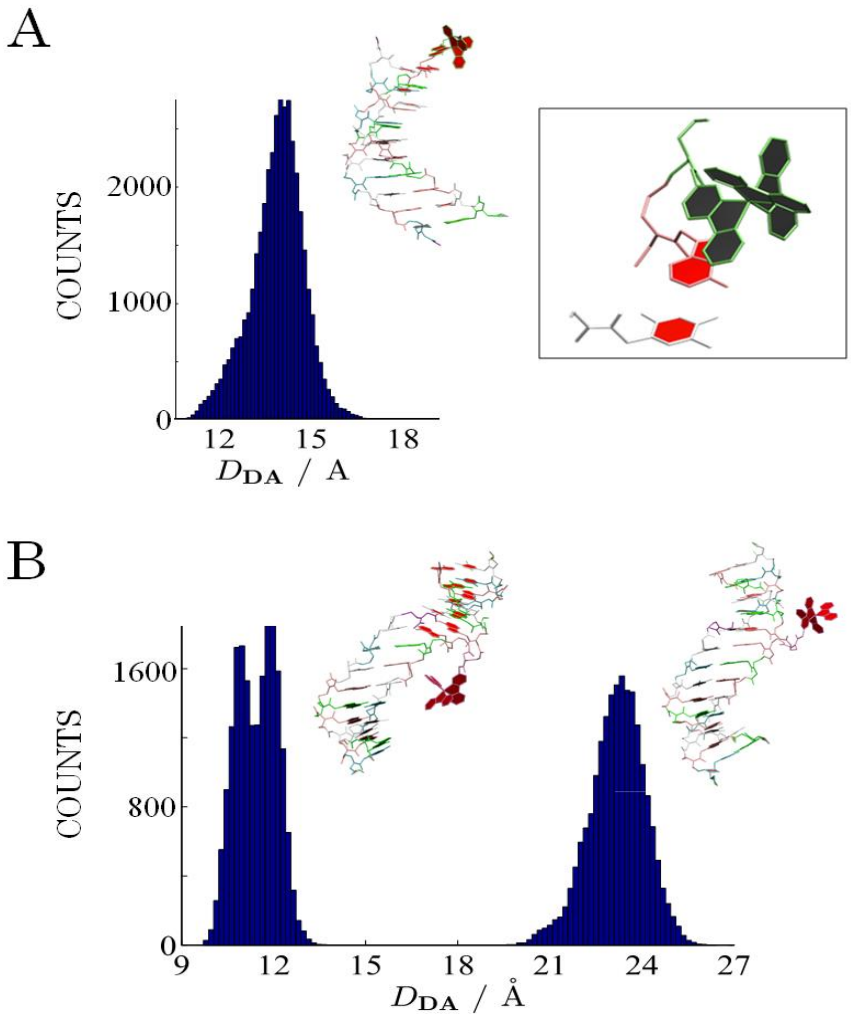

Figure 5.6. The D_{DA} distributions calculated using MD simulations for the analog of P-AG (A) and of P-AG-P' (B). The insets are the average structure for one MD trajectory. The aromatic rings of the Bpy in $[Ru(Bpy)_3]^{2+}$ are shown in green.

5.6A, the D_{DA} for the duplexes with a terminal $[Ru(Bpy)_3]^{2+}$ complex have a single mode distribution; while for the duplexes with a central $[Ru(Bpy)_3]^{2+}$ complex the distribution is bimodal (see Figure 5.6B). Moreover, the mean value of the short-distance peak in duplexes with a terminal $[Ru(Bpy)_3]^{2+}$ complex is larger than the corresponding value for duplexes with a central

$[Ru(Bpy)_3]^{2+}$ complex, indicating that the latter duplexes would have a shorter luminescence lifetime than the former ones, as observed in experiments. An alternative definition of D_{DA} was also considered but it gives rise to the same conclusions; see the Supporting Information for details.

5.4 CONCLUSIONS

In summary, this work demonstrates that $[Ru(Bpy)_3]^{2+*}$ can transfer an electron to a $[CuQ_2]$ complex incorporated into the nucleobase stack of a PNA duplex. If the $[Ru(Bpy)_3]^{2+}$ complex can access the terminus of the duplex and interact with the nucleobase π system, the electron transfer occurs through the nucleobase stack and is affected by mismatches and the number of nucleobase pairs between the donor and acceptor. If the $[Ru(Bpy)_3]^{2+}$ cannot access the PNA terminus, charge transfer can still proceed directly from the $[Ru(Bpy)_3]^{2+*}$ to the $[CuQ_2]$ if they are close enough, however the charge transfer rate does not depend on the mismatches or the intervening nucleobase pairs.

5.5 SUPPORTING INFORMATION

5.5.1 The Table of PNA Sequences

Table 5.2 provides a complete listing of the sequences of various PNA duplexes studied in this work.

Table 5.2. Sequences of PNA duplexes studied in this work.

Duplex	Sequence	Strand ID
P	H-AGTGATCTAC-H H_2N-Lys-TCACTAGATG-H	α β
P-AG	H-**Ru**AG**Q**GATCTAC-Lys-NH_2 H_2N-Lys-TC**Q**CTAGATG-H	α β
P-AA	H-**Ru**AA**Q**GATCTAC-Lys-NH_2 H_2N-Lys-TT**Q**CTAGATG-H	α β
P-AG-1Q	H-**Ru**AG**Q**GATCTAC-Lys-NH_2 H_2N-Lys-TCACTAGATG-H	α β
P-AA-1Q	H-**Ru**AA**Q**GATCTAC-Lys-NH_2 H_2N-Lys-TTACTAGATG-H	α β
P-AGTGA	H-**Ru**AGTGA**Q**CTAC-Lys-NH_2 H_2N-Lys-TCACT**Q**GATG-H	α β
P-AT-P'	H-AGTGA**Ru**AT**Q**TCTAC-Lys-NH_2 H_2N-Lys-TCACT**B**TA**Q**AGATG-H	α β
P-AG-P'	H-AGTGA**Ru**AG**Q**TCTAC-Lys-NH_2 H_2N-Lys-TCACT**B**TC**Q**AGATG-H	α β
P-AA/TC	H-**Ru**AA**Q**GATCTAC-Lys-NH_2 H_2N-Lys-TC**Q**CTAGATG-H	α β
P-AG/TT	H-**Ru**AG**Q**GATCTAC-Lys-NH_2 H_2N-Lys-TT**Q**CTAGATG-H	α β
P-AT/TC-P'	H-AGTGA**Ru**AT**Q**TCTAC-Lys-NH_2 H_2N-Lys-TCACT**B**TC**Q**AGATG-H	α β
P-AG/TA -P'	H-AGTGA**Ru**AG**Q**TCTAC-Lys-NH_2 H_2N-Lys-TCACT**B**TA**Q**AGATG-H	α β
P-R	H-**Ru**AGTGATCTAC-Cys-NH_2 H_2N-Lys-TCACTAGATG-H	α β

[a] **Ru**, **Q**, and **B** indicate the monomers in Figure 5.1; T, C, G, and A are the conventional nucleobase notations; and Lys indicates placement of a lysine.

5.5.2 More Photoluminescence Titrations of PNA duplexes with Cu^{2+}

Two additional steady-state luminescence titrations (**P-AA** and **P-AT-P'**) are shown in Figure 5.7.

A

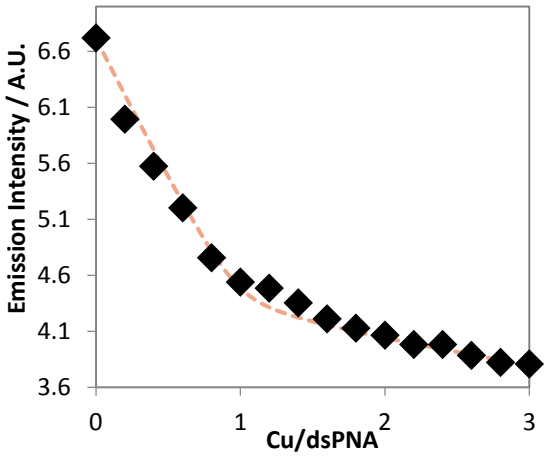

B

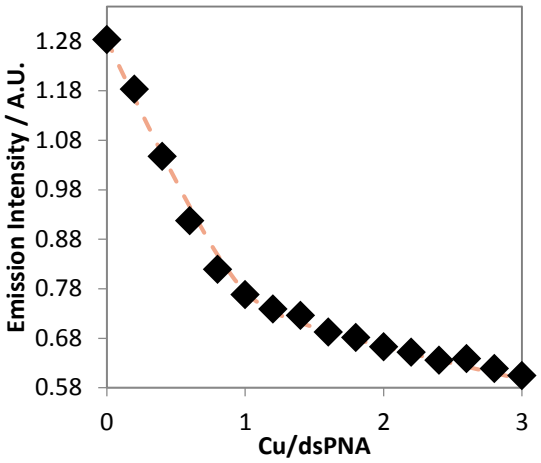

Figure 5.7. Panel A shows a titration curve for 10 μM **P-AA** with excitation wavelength at 440nm. Panel B shows a titration curve for 10 μM **P-AT-P'** with excitation wavelength at 480nm. All spectra were measured in 10 mM pH=7 phosphate buffer and the emissions were monitored at 620nm.

5.5.3 UV and Steady-State Photoluminescence Spectra of the Donor and Acceptor

Figure 5.8 shows steady state absorbance and luminescence spectra for $[Ru(Bpy)_3]^{2+}$ (donor) in water, and Figure 5.9 shows the luminescence spectra for $[Ru(Bpy)_3]^{2+}$ incorporated into PNA duplexes. Although the intensity of the emission spectra changes as Cu^{2+} is added to the solution, the shape of the spectra do not change. The emission spectra were collected on a Horiba Fluoromax 3 fluorescence spectrometer.

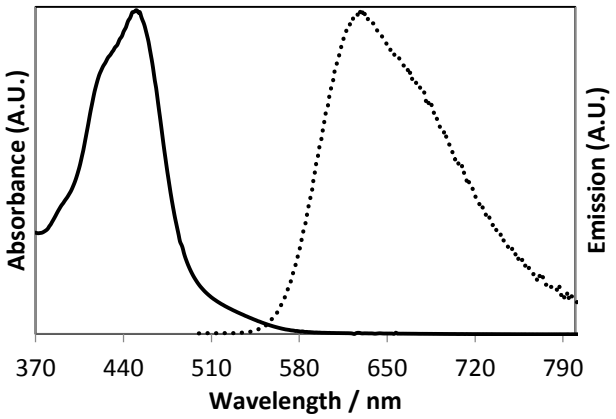

Figure 5.8. Absorption (solid line) and emission (dotted line) spectra of free $[Ru(Bpy)_3]^{2+}$ in water.

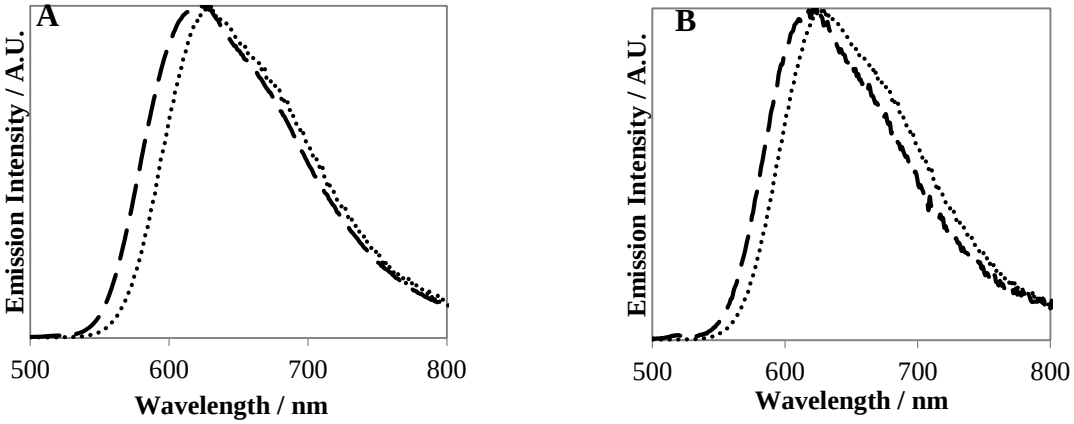

Figure 5.9. Panel A shows the emission spectrum of $[Ru(Bpy)_3]^{2+*}$ on 20μM **P-AG**, and panel B shows the emission spectrum of $[Ru(Bpy)_3]^{2+*}$ on 20μM P-AGTGA. The emission of free $[Ru(Bpy)_3]^{2+}$ in water is shown as a dotted line for reference. Both spectra were measured in 10 mM pH=7 phosphate buffer with an excitation wavelength at 450nm, and in each panel the emission spectrum of $[Ru(Bpy)_3]^{2+*}$ in water is plotted with a dotted line.

Figure 5.10 shows the UV spectra of hydroxyquinoline ligand and the metal complex $[CuQ_2]$ (acceptor) in solution.

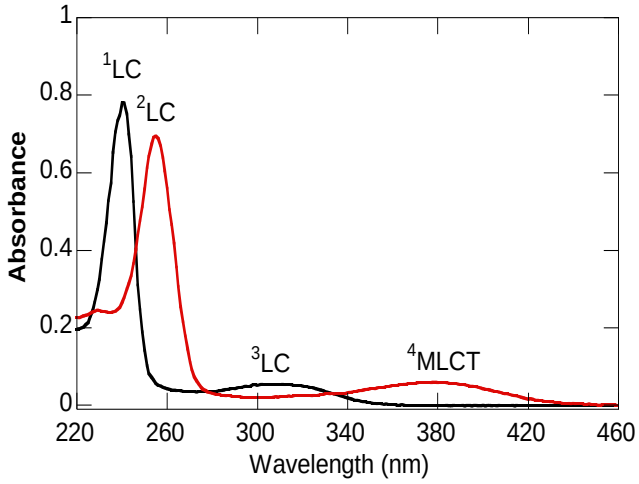

Figure 5.10. UV spectra are shown for a 40 μM solution of the hydroxyquinoline ligand (black) and a 40 micromolar solution of the complex $[CuQ_2]$ (red), in 25% MeCN and pH 7 10 mM phosphate buffer at 25°C. High-temperature spectrophotometric titrations of Q with $CuCl_2$ have shown that $[CuQ_2]$ is stable even when the temperature is as high as 95°C.[15]

Two systems without Q were tested in order to show the inefficient quenching of the ruthenium complex by free Cu^{2+} in solution. Figure 5.11A shows the luminescence decay of $[Ru(Bpy)_3]^{2+}$ when it is chemically attached at the end of the PNA duplex, **P-R** (see Table 5.2), both with and without added copper ion. The emission decay law does not change significantly after adding 10 equivalent of Cu^{2+} to 120 μL of the 10 μM **P-R** solution; the best fit decay lifetime changes from 457 ns to 455 ns, which is well within error of the measurement. Figure 5.11B shows the results for a similar study with 20 μM free $[Ru(Bpy)_3]^{2+}$ in buffer solution. In this latter case, the best fit emission lifetime changes slightly from 379 ns to 381 ns after adding 2 equivalents Cu^{2+} to the solution, well within experimental error of the fit. The results clearly show that no significant quenching occurs for the 40 μM of free Cu^{2+}. In experiments with Q, the concentration of excess Cu^{2+} is only half of 40 μM and the effect of free Cu^{2+} can be ignored.

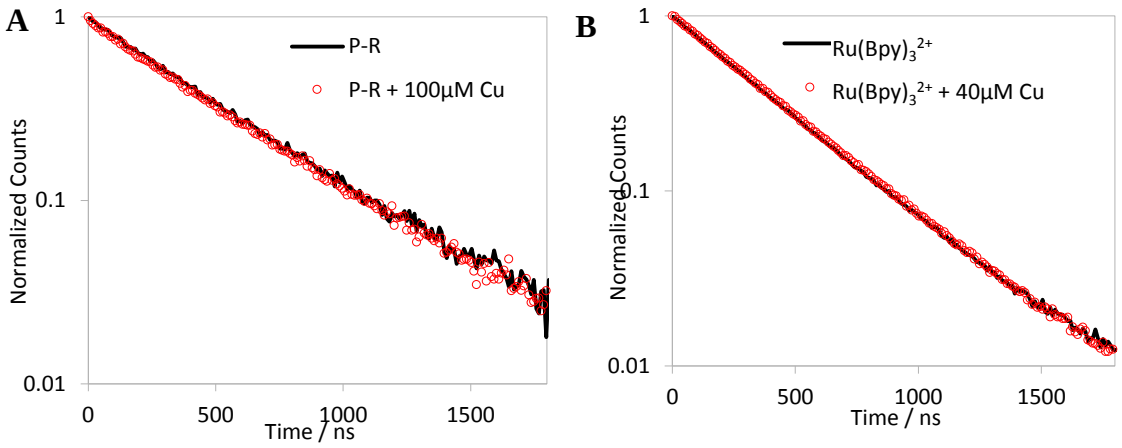

Figure 5.11. A) Time-resolved luminescence decays are shown for 10 μM **P-R**. B) Time-resolved luminescence decays are shown for 20 μM free $[Ru(Bpy)_3]^{2+}$. All spectra were measured in 10 mM pH=7 phosphate buffer with an excitation wavelength at 440nm.

5.5.4 Zn^{2+} as a Control for P-AG/Cu.

Hydroxyquinoline itself has a weak fluorescence with a nanosecond timescale lifetime and its short-lived fluorescence is enhanced significantly in the presence of Zn^{2+}. Figure 5.12A shows the steady-state photoluminescence titration curve of **P-AG**. When excited at 480nm where it is beyond the absorption peak of hydroxyquinoline, no inflection point is observed. However, an inflection point (maximum) around 0.6~0.7 was observed when monitored at 378nm where it is close to the maximum of hydroxyquinoline absorption peak. The increase of hydroxyquinoline emission clearly shows the binding of Zn^{2+} with **P-AG**. The binding is probably a two-step equilibrium because the inflection point is neither exactly 0.5 or 1. By using two-step equilibrium model fitting (where L stands for **P-AG**):

$$\mathrm{Zn} + 2\mathrm{L} \rightleftharpoons \mathrm{ZnL_2}, \qquad K_1 = \frac{[\mathrm{ZnL_2}]}{[\mathrm{Zn}][\mathrm{L}]^2}$$

$$ZnL_2 + L \rightleftharpoons 2ZnL, \qquad K_2 = \frac{[ZnL]^2}{[ZnL_2][L]}$$

We found that the effective bimolecular equilibrium constant $K = \sqrt{K_1 K_2}$ is larger than 10^7 mol^{-1}. When two equivalents of Zn^{2+} is added, there is less than 2% unbonded **P-AG** in solution and more than 80% of the **P-AG** exists in the form of ZnL_2.

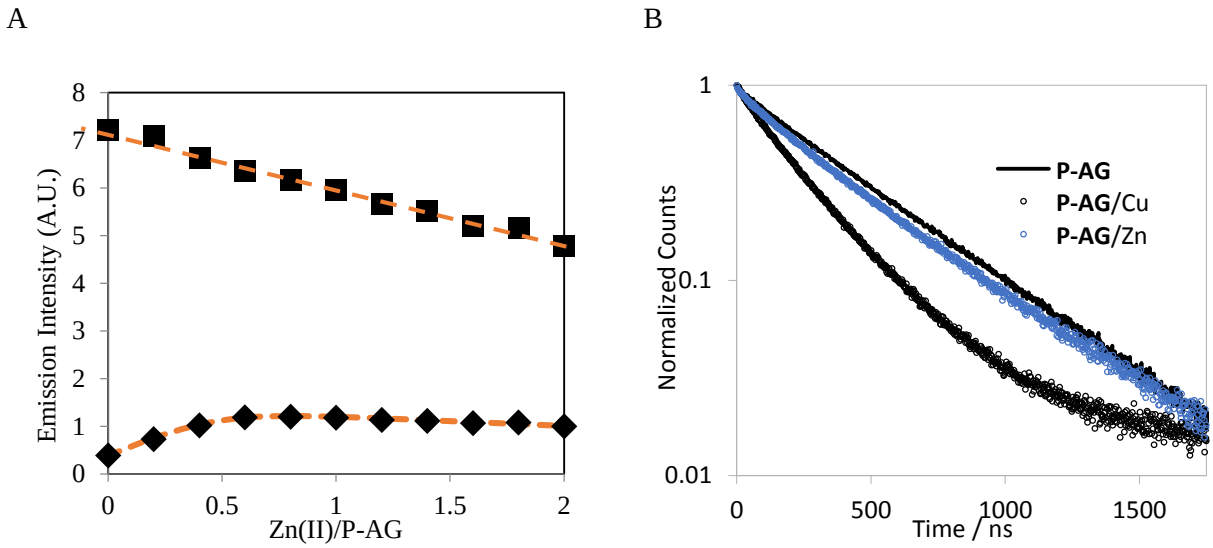

Figure 5.12. A) Steady-state photoluminescence titration of 20μM **P-AG** in 10mM pH=7 phosphate buffer with 500 μM Zn^{2+}. Squares: Excited at 480nm. Diamonds: Excited at 378nm. The emission was monitored at 620nm for both titrations. B) Luminescence decay curves are shown for 20μM **P-AG** (black solid line), **P-AG** with 2 equivalents of Cu^{2+}(black circles), and **P-AG** with 2 equivalents of Zn^{2+} (aqua circles) in 10mM pH=7 phosphate buffer.

The time-resolved results are shown Figure 5.12B. The fluorescence lifetime of Q is more than two orders of magnitude shorter and can be totally removed from the luminescence decay curves by discarding the first 10 ns. The long-lived component arises from the $[Ru(Bpy)_3]^{2+*}$ and the lifetime can be extracted from fitting the rest of the decay law. The best fit time constant for the $[Ru(Bpy)_3]^{2+*}$ emission data of the **P-AG** duplex is 440 ns and that for the **P-AG/Zn** duplex is 430 ns. The small change supports the conclusion that the large quenching observed in **P-AG**/Cu is caused by the charge transfer from Ru* to Cu(II).

5.5.5 The Estimation of k_{CT}^{0}

The charge transfer rate was determined by using the following equation:

$$k_{CT} = \frac{1}{\tau} - \frac{1}{\tau_0} \qquad \textbf{Equation 5.9}$$

This rate constant has contributions from the reorganization energy and the Gibbs free energy ($\Delta_r G$), as well as the electronic coupling. To compare with previous electrochemical data, the charge transfer rates k_{CT} should be converted to the rate constants k_{CT}^{0}, for which $\Delta_r G = 0$. According to the classical Marcus theory,

$$k_{CT} = \frac{2\pi}{\hbar} |H_{AB}|^2 \frac{1}{\sqrt{4\pi\lambda k_b T}} \exp\left(-\frac{\Delta G^{\ddagger}}{k_b T}\right) \qquad \textbf{Equation 5.10}$$

and

$$\Delta G^{\ddagger} = \frac{(\lambda + \Delta_r G)^2}{4\lambda} \qquad \textbf{Equation 5.11}$$

Thus, one finds that

$$k^{0} = k_{CT} \exp\left(\frac{4\Delta G^{\ddagger} - \lambda}{4 k_b T}\right) \qquad \textbf{Equation 5.12}$$

and Equation 5.11 can be written as

$$\lambda^2 + \left(2\Delta_r G - 4\Delta G^{\ddagger}\right)\lambda + (\Delta_r G)^2 = 0 \qquad \textbf{Equation 5.13}$$

where $\Delta G^{\ddagger}$ is the activation energy, λ is the reorganization energy and $\Delta_r G$ is the total Gibbs free energy change. $\Delta G^{\ddagger}$ can be measured in temperature dependence experiments and the result is 0.1 eV as shown in Figure 5.13.

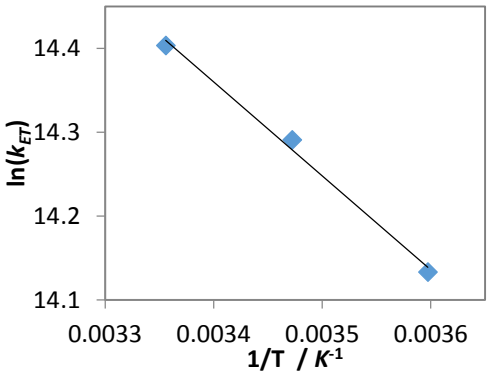

Figure 5.13. An Arrhenius plot is shown for the charge transfer rate in P-AG/Cu. $\boldsymbol{\Delta G^{\ddagger}} \approx 0.1$ eV from the fitting.

$\Delta_r G$ was estimated from literature values. The excited state energy of $[Ru(Bpy)_3]^{2+}$is taken to be 2.12 eV,[62] the oxidation potential of $[Ru(Bpy)_3]^{2+}$ monomer is measured to be about 1.15 V (See Supporting Information Section 9), and the reduction potential of CuQ_2 and the reduction potential of $[CuQ_2]$ is taken to be 0.05 V vs NHE.[61] If the Coulomb interaction between the donor and acceptor is neglected, then $\Delta_r G_\infty = 1.15 + 0.05 - 2.12 \text{ eV} = -1.08 \text{ eV}$. The Rehm-Weller equation[57] takes the correction of Coulomb interaction into account:

$$\Delta_r G = \Delta_r G_\infty - \frac{e^2}{4\pi\epsilon_0\epsilon_r D_{DA}} \qquad \textbf{Equation 5.14}$$

where ϵ_0 is the vacuum permittivity and ϵ_r is the relative dielectric constant. Because D_{DA} is very small ($\approx$ 1.4 nm), ϵ_r will become much smaller than the bulk solvent.[58,64,77] If $\epsilon_r \approx 2.5$ then the Coulomb interaction is about 0.4 eV and $\Delta_r G \approx -1.5$ eV.

Using the above values, λ could be 2.5 eV or 0.9 eV. 2.5 eV is far larger than most Ru complexes such as $Ru(NH_3)_4$L-(His33)-Zn-CytC (1.15 eV for L=NH_3, pyridine, or isonicotinamide) or $Ru(Bpy)_2$(im)(His33)-Fe-CytC (about 0.8 eV for im=imidazole).[59] Thus using 0.9 eV as the reorganization energy seems more reasonable, and Equation 5.12 becomes:

$$k^0(\mathbf{P-AG}/\text{Cu}) \approx 0.007 k_{ET} \qquad \textbf{Equation 5.15}$$

Thus, one estimates k^0 to be 1.3×10^4 s^{-1} for **P-AG**/Cu.

Using Eqn S6 to account for the shift in $\Delta_r G$ and the other parameters given, it is possible to estimate k^0 for **P-AGTGA**/Cu. From Eqn S6 and a D_{DA} of 2.4 nm, one finds that $\Delta_r G$ = -1.32 eV and

$$k^0(\mathbf{P-AGTGA}/\mathrm{Cu}) \approx 0.0009 k_{ET} \qquad \textbf{Equation 5.16}$$

so that k^0 is 210 s^{-1} for **P-AG**/Cu. These results are compiled in Table 5.3.

Table 5.3. Luminescence lifetimes and charge transfer rates in **P-AG**/Cu and **P-AGTGA**/Cu**.**

PNA	τ / ns	τ_0 /ns	k_{CT} / s^{-1}	k^0 / s^{-1}
P-AG/Cu	246	440	1.8×10^6	1.3×10^4
P-AGTGA /Cu	412	457	0.24×10^6	2.1×10^2

Using the k^0 values, which are scaled to the same reaction Gibbs energy, one can estimate β directly from

$$\ln\left(\frac{k^0(\mathbf{P-AG})}{k^0(\mathbf{P-AGTGA}}\right) = \beta\ (\mathrm{D_{DA}}(\mathbf{P-AG}) - \mathrm{D_{DA}}(\mathbf{P-AGTGA})) \qquad \textbf{Equation 5.17}$$

Using the results in Table 5.3 and the distances 1.4 nm and 2.4 nm from the MD simulations, one finds that $\beta = 0.41$ $Å^{-1}$.

According to previous electrochemical experiments, charge transfer in duplexes with seven or more bases pairs (duplexes with less than seven base pairs were not measured by electrochemical methods) is in the 'hopping' regime and k^0 is about 1 s^{-1}.[65] Assuming that the β obtained here holds for up to seven base pairs, then the k^0 of a $[Ru(Bpy)_3]^{2+}$ and Q containing PNA with seven base pairs between the donor and acceptor is predicted to be at most about 10 s^{-1}. Given the rough nature of the estimates and the differences in the experiments, this comparison is considered to be acceptable.

5.5.6 Support Plane Analysis and Maximum Error in P-AG-P' system

When two decays have similar lifetimes, it is crucial to determine the fitting errors in the two decays to ascertain whether the difference is outside of the noise limit. In component fitting, the confidence interval can be obtained by using the Support Plane Analysis[60] function of the FAST (Fluorescence Analysis Software Technology) software. The results from this analysis for the **P-AG-P'** system are listed in Table 5.4. The "Probability 60%" columns correspond to $p = 0.4$, and the "Probability 90%" columns correspond to $p = 0.1$. The confidence interval is determined from the standard deviation. The parameters in Table 5.4 show that no overlap of the confidence intervals occurs between the two cases, **P-AGTGA** and **P-AGTGA/Cu**. Also, the differences between the lifetimes of the two PNAs are much larger than the range of either confidence interval. Thus the difference between the lifetimes is significant; it does not arise from noise.

Table 5.4. Support plane analysis of **P-AGTGA** and **P-AGTGA/**Cu

		Probability 60%		Probability 90%	
	τ (ns)	Conf $_{low}$	Conf $_{high}$	Conf $_{low}$	Conf $_{high}$
P-AGTGA	457	457.0	457.9	456.5	458.3
P-AGTGA/Cu	412	411.8	412.5	411.5	412.9

Even if the lifetimes are the same for **P-AG/Cu** and **P-AGTGA/Cu**, we can still assume a detection limit to estimate the maximum charge transfer rate in **P-AGTGA/Cu**. By propagation of errors in Equation 5.9, we have

$$\Delta_k^2 = \frac{1}{\tau^4} \cdot \Delta_\tau^2 + \frac{1}{\tau_0^4} \cdot \Delta_{\tau_0}^2 \qquad \textbf{Equation 5.18}$$

where Δ_k, Δ_τ, and Δ_{τ_0} are the limits of errors for k_{ET}, τ, and τ_0, respectively. Assuming that the experimental error limit of the luminescence lifetime determination is 3%, Equation 5.18 gives a Δ_k of $0.09 \times 10^6\ \mathrm{s}^{-1}$, meaning that the k_{ET} of the 5-basepair separated system is probably not

much larger than $0.3 \times 10^6\ s^{-1}$. Actually, the relative standard deviations of τ and τ_0 are only 1.4% and 1.5% between three experiments (412 ns, 423 ns, 415 ns for τ and 457 ns, 470 ns, 460 ns for τ_0), suggesting that the error estimate given here is a conservative one.

5.5.7 Conformation Distributions by Enantiomer

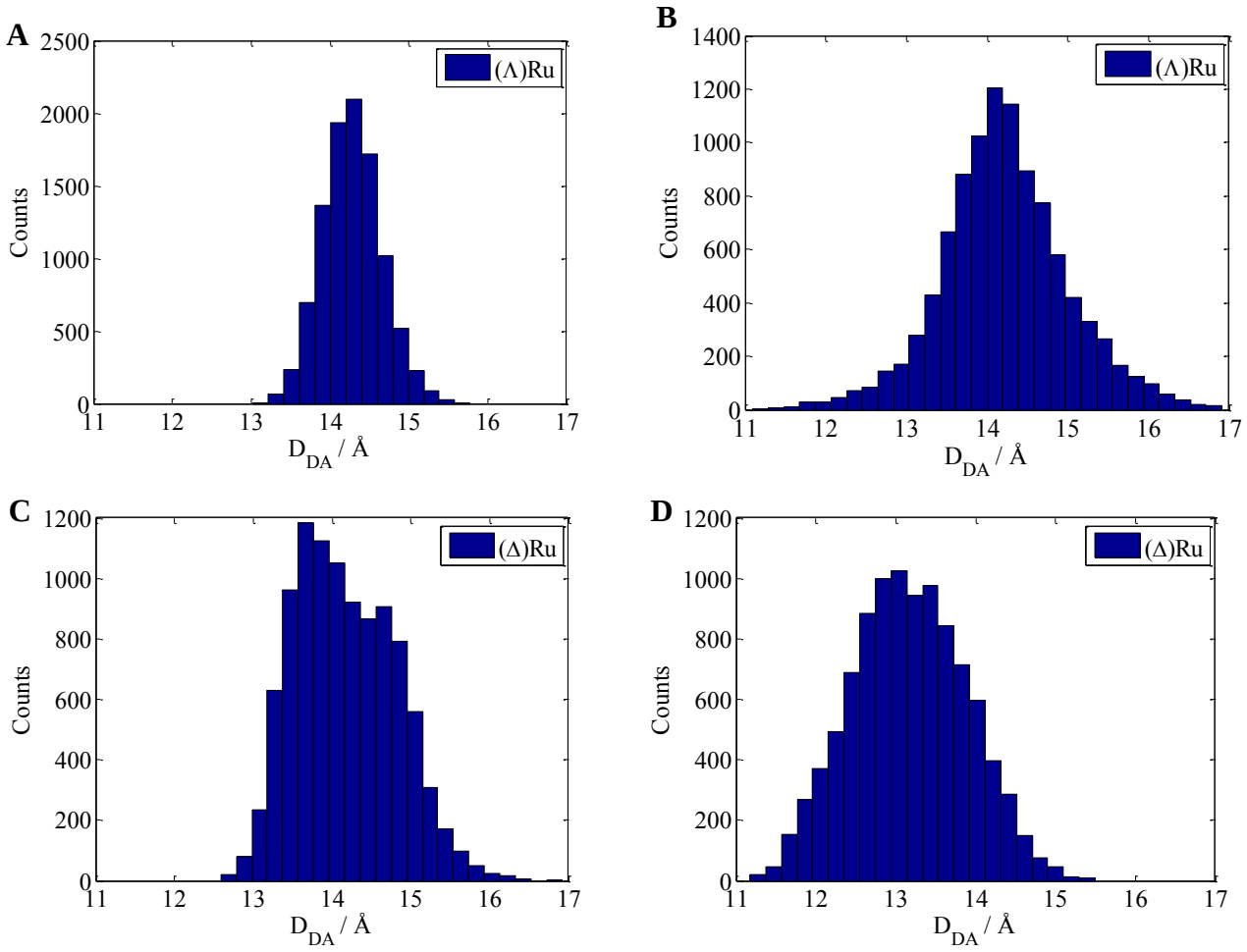

Figure 5.14. The donor-to-acceptor distance distributions are shown for four different trajectories of the **P-AG** duplex. Panels A and B are for the case of the Λ- donor chirality, and panels C and D are for the Δ- donor chirality.

The distribution of donor-acceptor distances D_{DA} are shown in Figure 5.14 for four trajectories of **P-AG** - two for each of the $[Ru(Bpy)_3]^{2+}$ optical isomers. Figure 5.15 shows D_{DA}

distributions for four MD trajectories of tailed **P-AG-P'**, two for each of the $[Ru(Bpy)_3]^{2+}$ optical isomers.

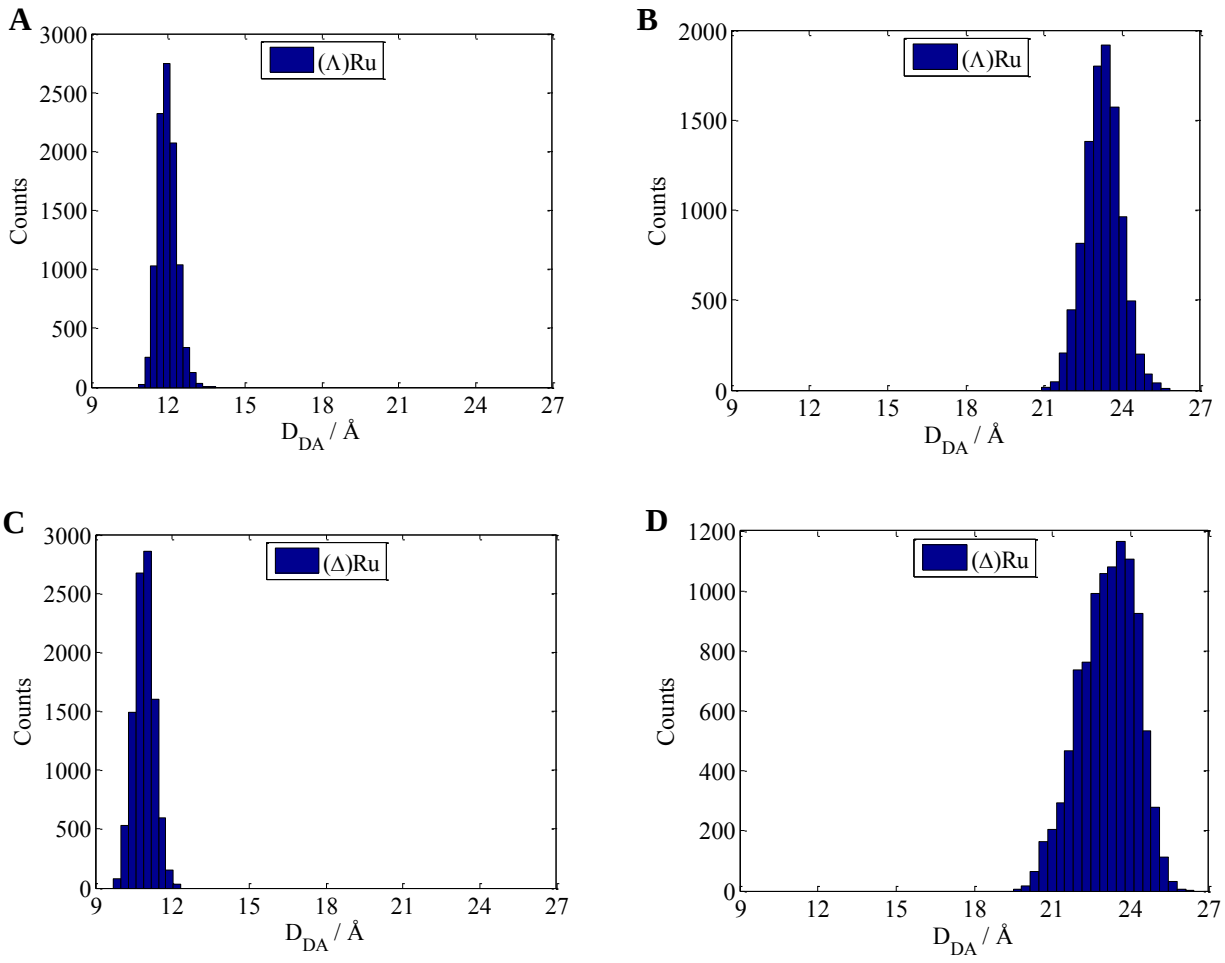

Figure 5.15. Donor-to-acceptor distance distributions are shown for four different trajectories of the **P-AG-P'**duplex**.** Panels A and B are for the case of the Λ- donor chirality, and panels C and D are for the Δ- donor chirality. For illustration purposes, trajectories are shown for the two dominant conformations that were observed.

5.5.8 Alternative Definition of D_{DA}

In the main text, D_{DA} is defined as the distance between Ru atom and the centroid of the AT base pair. D_{DA} can also be defined as the distance between the Ru atom and the center of the two N atoms in the A-T base pair, as shown in Figure 5.16:

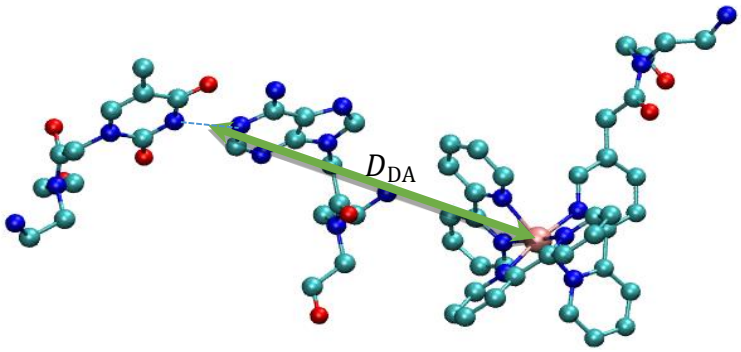

Figure 5.16. The alternative definition of $\boldsymbol{D_{\mathrm{DA}}}$.

This change of definition does not cause a significant change in the distribution of of D_{DA} values; see Figure 5.17.

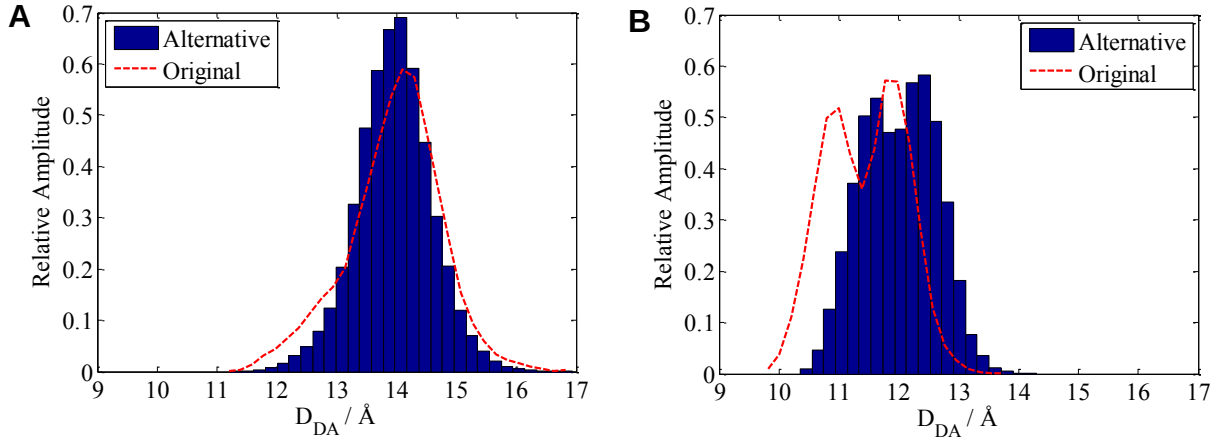

Figure 5.17. Distance distribution are shown for **P-AG** in panel A and for **P-AG-P'** in panel B. Not that only the short distance (quenched condition) peak is shown for **P-AG-P'**.

5.5.9 Cyclic Voltammogram of Cysteine-Ru(Bpy)$_3^{2+}$

The oxidation potential of Ru monomer in a Cysteine-Ru(Bpy)$_3^{2+}$ self-assembled monolayer (SAM) was measured by cyclic voltammetry and is found to be +1.15 V (versus NHE). The SAM modified electrode was prepared as previously reported.[23]

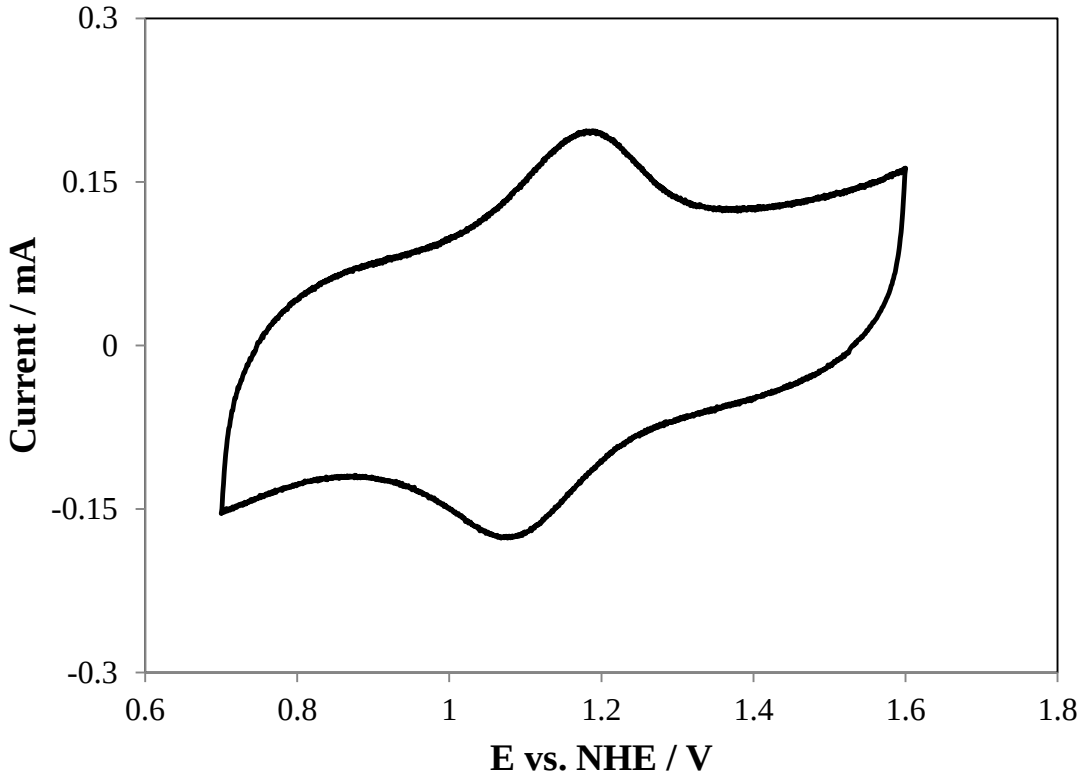

Figure 5.18. Cyclic voltammogram of Cys-Ru(bpy)$_3^{2+}$ SAM on a gold electrode. Measured in 0.1 M tetrabutylammonium tetrafluoroborate/MeCN with Ag/$AgNO_3$ reference electrode at a scan rate of 100 V/s.

5.6 REFERENCES

(1) Rothemund, P. W. K. *Nature* **2006**, *440*, 297.

(2) Dietz, H.; Douglas, S. M.; Shih, W. M. *Science (80-.).* **2009**, *325*, 725.

(3) Yan, H. *Science* **2004**, *306*, 2048.

(4) Bhatia, D.; Sharma, S.; Krishnan, Y. *Curr. Opin. Biotechnol.* **2011**, *22*, 475.

(5) Krishnan, Y.; Simmel, F. C. *Angew. Chemie, Int. Ed.* **2011**, *50*, 3124.

(6) Seeman, N. C. *Annu. Rev. Biochem.* **2010**, *79*, 65.

(7) Nielsen, P.; Egholm, M.; Berg, R.; Buchardt, O. *Science (80-.).* **1991**, *254*, 1497.

(8) Egholm, M.; Nielsen, P. E.; Buchardt, O.; Berg, R. H. *J. Am. Chem. Soc.* **1992**, *114*, 9677.

(9) Uhlmann, E.; Peyman, A.; Breipohl, G.; Will, D. W. *Angew. Chemie Int. Ed.* **1998**, *37*, 2796.

(10) Nielsen, P. E. *Peptide Nucleic Acids: Protocols and Applications*; Peter Nielson, Ed.; 2nd ed.; Horizon Bioscience, 2004.

(11) Achim, C.; Armitage, B. A.; Ly, D. H.; Schneider, J. W. In *Wiley Encyclopedia of Chemical Biology*; Begley, T., Ed.; John Wiley & Sons, Inc.: Hoboken, NJ, USA, 2009; Vol. 3, pp. 588–597.

(12) Rozners, E. *J. Nucleic Acids* **2012**, *2012*, 518162.

(13) Nielsen, P. E. *Chem. Biodivers.* **2010**, *7*, 786.

(14) De Leon, A.; Kong, J.; Achim, C. In *Metallofoldamers: Supramolecular Architectures from Helicates to Biomimetics*; Maayan, G.; Albrecht, M., Eds.; John Wiley & Sons, Ltd, 2013; pp. 333–378.

(15) Watson, R. M.; Skorik, Y. a; Patra, G. K.; Achim, C. *J. Am. Chem. Soc.* **2005**, *127*, 14628.

(16) Ma, Z.; Olechnowicz, F.; Skorik, Y. a; Achim, C. *Inorg. Chem.* **2011**, *50*, 6083.

(17) Nickita, N.; Gasser, G.; Bond, A. M.; Spiccia, L. *Eur. J. Inorg. Chem.* **2009**, *2009*, 2179.

(18) Joshi, T.; Barbante, G. J.; Francis, P. S.; Hogan, C. F.; Bond, A. M.; Gasser, G.; Spiccia, L. *Inorg. Chem.* **2012**, *51*, 3302.

(19) Metzler-Nolte, N. In *Bioorganometallics: Biomolecules, Labeling, Medicine*; Jaouen, G., Ed.; Wiley-VCH Verlag GmbH & Co. KGaA: Weinheim, FRG, 2005; pp. 125–179.

(20) Hüsken, N.; Gębala, M.; Battistel, A.; La Mantia, F.; Schuhmann, W.; Metzler-Nolte, N. *Chemphyschem* **2012**, *13*, 131.

(21) Baldoli, C.; Rigamonti, C.; Maiorana, S.; Licandro, E.; Falciola, L.; Mussini, P. R. *Chem. - A Eur. J.* **2006**, *12*, 4091.

(22) Wierzbinski, E.; de Leon, A.; Davis, K. L.; Bezer, S.; Wolak, M. A.; Kofke, M. J.; Schlaf, R.; Achim, C.; Waldeck, D. H. *Langmuir* **2012**, *28*, 1971.

(23) Paul, A.; Watson, R. M. R. M.; Lund, P.; Xing, Y.; Burke, K.; He, Y.; Borguet, E.; Achim, C.; Waldeck, D. H. D. H. *J. Phys. Chem. C* **2008**, *112*, 7233.

(24) Wierzbinski, E.; Venkatramani, R.; Davis, K. L.; Bezer, S.; Kong, J.; Xing, Y.; Borguet, E.; Achim, C.; Beratan, D. N.; Waldeck, D. H. *ACS Nano* **2013**, *7*, 5391.

(25) Schuster, G. B. *Acc. Chem. Res.* **2000**, *33*, 253.

(26) Kanvah, S.; Joseph, J.; Schuster, G. B.; Barnett, R. N.; Cleveland, C. L.; Landman, U. *Acc. Chem. Res.* **2010**, *43*, 280.

(27) Shao, F.; O'Neill, M. a; Barton, J. K. *Proc. Natl. Acad. Sci. U. S. A.* **2004**, *101*, 17914.

(28) Stemp, E. D. A.; Arkin, M. R.; Barton, J. K. *J. Am. Chem. Soc.* **1997**, *119*, 2921.

(29) Wagenknecht, H.-A. *Angew. Chem. Int. Ed. Engl.* **2003**, *42*, 2454.

(30) Giese, B.; Amaudrut, J.; Köhler, A. K.; Spormann, M.; Wessely, S. *Nature* **2001**, *412*, 318.

(31) Meggers, E.; Michel-Beyerle, M. E.; Giese, B. *J. Am. Chem. Soc.* **1998**, *120*, 12950.

(32) Senthilkumar, K.; Grozema, F. C.; Guerra, C. F.; Bickelhaupt, F. M.; Lewis, F. D.; Berlin, Y. A.; Ratner, M. A.; Siebbeles, L. D. A. *J. Am. Chem. Soc.* **2005**, *127*, 14894.

(33) Fukui, K.; Tanaka, K. *Angew. Chemie Int. Ed.* **1998**, *37*, 158.

(34) Genereux, J. C.; Barton, J. K. *Chem. Rev.* **2010**, *110*, 1642.

(35) Holmlin, R. E.; Stemp, E. D. A.; Barton, J. K. *J. Am. Chem. Soc.* **1996**, *118*, 5236.

(36) Murphy, C.; Arkin, M.; Jenkins, Y.; Ghatlia, N.; Bossmann, S.; Turro, N.; Barton, J. *Science (80-.).* **1993**, *262*, 1025.

(37) Kumar, C. V; Barton, J. K.; Turro, N. J. *J. Am. Chem. Soc.* **1985**, *107*, 5518.

(38) Brun, A.; Harriman, A. *J. Am. Chem. Soc.* **1992**, *114*, 3656.

(39) Lewis, F. D.; Letsinger, R. L.; Wasielewski, M. R. *Acc. Chem. Res.* **2001**, *34*, 159.

(40) Lewis, F. D.; Wu, T.; Zhang, Y.; Letsinger, R. L.; Greenfield, S. R.; Wasielewski, M. R. *Science* **1997**, *277*, 673.

(41) Franzini, R. M.; Watson, R. M.; Patra, G. K.; Breece, R. M.; Tierney, D. L.; Hendrich, M. P.; Achim, C. *Inorg. Chem.* **2006**, *45*, 9798.

(42) Kise, K. J.; Bowler, B. E. *Inorg. Chem.* **2002**, *41*, 379.

(43) Livesey, a. K.; Brochon, J. C. *Biophys. J.* **1987**, *52*, 693.

(44) Alcala, J. R.; Gratton, E.; Prendergast, F. G. *Biophys. J.* **1987**, *51*, 925.

(45) Alcala, J. R.; Gratton, E.; Prendergast, F. G. *Biophys. J.* **1987**, *51*, 587.

(46) Lakowicz, J. R.; Cherek, H.; Gryczynski, I.; Joshi, N.; Johnson, M. L. *Biophys. Chem.* **1987**, *28*, 35.

(47) Gakamsky, D. M.; Goldin, A. a.; Petrov, E. P.; Rubinov, A. N. *Biophys. Chem.* **1992**, *44*, 47.

(48) Epstein, C. L.; Schotland, J. *SIAM Rev.* **2008**, *50*, 504.

(49) Fogarty, A. C.; Jones, A. C.; Camp, P. J. *Phys. Chem. Chem. Phys.* **2011**, *13*, 3819.

(50) Wierzbinski, E.; de Leon, A.; Yin, X.; Balaeff, A.; Davis, K. L.; Rapireddy, S.; Reppireddy, S.; Venkatramani, R.; Keinan, S.; Ly, D. H.; Madrid, M.; Beratan, D. N.; Achim, C.; Waldeck, D. H.; Rappireddy, S. *J. Am. Chem. Soc.* **2012**, *134*, 9335.

(51) Venkatramani, R.; Davis, K. L.; Wierzbinski, E.; Bezer, S.; Balaeff, A.; Keinan, S.; Paul, A.; Kocsis, L.; Beratan, D. N.; Achim, C.; Waldeck, D. H. *J. Am. Chem. Soc.* **2011**, *133*, 62.

(52) He, W.; Hatcher, E.; Balaeff, A.; Beratan, D. N.; Gil, R. R.; Madrid, M.; Achim, C. *J. Am. Chem. Soc.* **2008**, *130*, 13264.

(53) Hornak, V.; Abel, R.; Okur, A.; Strockbine, B.; Roitberg, A.; Simmerling, C. *Proteins* **2006**, *65*, 712.

(54) Moret, M.-E.; Tavernelli, I.; Rothlisberger, U. *J. Phys. Chem. B* **2009**, *113*, 7737.

(55) Case, D. A.; Darden, T. A.; Cheatham, T. E. I.; Simmerling, C. L.; Wang, J.; Duke, R. E.; Luo, R.; Walker, R. C.; Zhang, W.; Merz, K. M.; Roberts, B.; Hayik, S.; Roitberg, A.; Seabra, G.; Swails, J.; Goetz, A. W.; Kolossváry, I.; Wong, K. F.; Paesani, F.; Vanicek, J.; Wolf, R. M.; Liu, J.; Wu, X.; Brozell, S. R.; Steinbrecher, T.; Gohlke, H.; Cai, Q.; Ye, X.; Hsieh, M.-J.; Cui, G.; Roe, D. R.; Mathews, D. H.; Seetin, M. G.; Salomon-Ferrer, R.;

Sagui, C.; Babin, V.; Luchko, T.; Gusarov, S.; Kovalenko, A.; Kollman, P. A. AMBER 12 **2012**.

(56) Mergny, J.; Lacroix, L. *Oligonucleotides* **2003**, *13*, 515.

(57) Rehm, D.; Weller, A. *Isr. J. Chem.* **1970**, *8*, 259.

(58) Tachiya, M. *Chem. Phys. Lett.* **1994**, *230*, 491.

(59) Gray, H. B.; Winkler, J. R. *Annu. Rev. Biochem.* **1996**, *65*, 537.

(60) Straume, M.; Frasier-Cadoret, S. G.; Johnson, M. L. *Top. Fluoresc. Spectrosc.* **1991**, *2*, 177.

(61) Monzon, L. M. A.; Burke, F.; Coey, J. M. D. *J. Phys. Chem. C* **2011**, *115*, 9182.

(62) Kalyanasundaram, K. *Coord. Chem. Rev.* **1982**, *46*, 159.

(63) Zimmt, M. B.; Waldeck, D. H. *J. Phys. Chem. A* **2003**, *107*, 3580.

(64) Tachiya, M. *J. Phys. Chem.* **1993**, *97*, 5911.

(65) Paul, A.; Watson, R. M.; Wierzbinski, E.; Davis, K. L.; Sha, A.; Achim, C.; Waldeck, D. H. *J. Phys. Chem. B* **2010**, *114*, 14140.

(66) Daublain, P.; Thazhathveetil, A. K.; Wang, Q.; Trifonov, A.; Fiebig, T.; Lewis, F. D. *J. Am. Chem. Soc.* **2009**, *131*, 16790.

(67) Daublain, P.; Thazhathveetil, A. K.; Shafirovich, V.; Wang, Q.; Trifonov, A.; Fiebig, T.; Lewis, F. D. *J. Phys. Chem. B* **2010**, *114*, 14265.

(68) Shafirovich, V.; Dourandin, A.; Huang, W.; Luneva, N. P.; Geacintov, Q. E. *Phys. Chem. Chem. Phys.* **2000**, *2*, 4399.

(69) Wagenknecht, H.-A. *Nat. Prod. Rep.* **2006**, *23*, 973.

(70) Lewis, F. D.; Liu, X.; Liu, J.; Miller, S. E.; Hayes, R. T.; Wasielewski, M. R. *Nature* **2000**, *406*, 51.

(71) Kawai, K.; Takada, T.; Tojo, S.; Majima, T. *J. Am. Chem. Soc.* **2003**, *125*, 6842.

(72) Lewis, F. D.; Wu, Y.; Zhang, L.; Zuo, X.; Hayes, R. T.; Wasielewski, M. R. *J. Am. Chem. Soc.* **2004**, *126*, 8206.

(73) Behrens, C.; Burgdorf, L. T.; Schwögler, A.; Carell, T. *Angew. Chemie Int. Ed.* **2002**, *41*, 1763.

(74) Elias, B.; Shao, F.; Barton, J. K. *J. Am. Chem. Soc.* **2008**, *130*, 1152.

(75) Park, M. J.; Fujitsuka, M.; Kawai, K.; Majima, T. *J. Am. Chem. Soc.* **2011**, *133*, 15320.

(76) Breeger, S.; Hennecke, U.; Carell, T. *J. Am. Chem. Soc.* **2004**, *126*, 1302.

(77) Zeng, Y.; Zimmt, M. B. *J. Phys. Chem.* **1992**, *96*, 8395.

6.0 CONCLUDING REMARKS

In this dissertation, experimental methods as well as theoretical/computational methods have been employed to study the fundamental charge transfer properties of peptide nucleic acids and small organic molecules. Chapter 2 is dedicated to electrochemical measurement of charge transfer in the "hopping" regime. A new three-step phenomenological model was developed to simulate the multiple-step charge transfer process. As a first test, both the three-step model and a traditional single-step non-adiabatic tunneling model have been applied to the electrochemical measurement of a 10-base pair PNA duplex SAM. It is shown that the fitting results of the single-step model can be explained in terms of the apparent charge transfer rate constant k_{tot}^{0} within the three-step framework; however, the three-step model predicts the importance of the energy barriers between the molecular bridge and the electrochemical reporter (injection barrier) in multi-step charge hopping process, which is not explicitly included in the single-step model. A temperature dependence study of a 10-base pair PNA duplex was performed. An injection barrier of 0.24 eV was extracted by comparing the three-step model simulation with the experimental data. This value is in reasonable agreement with the results obtained using photoelectron spectroscopy. Further experiments have been done to vary the charge transfer rate in each major step of the electron transfer in the 10-base pair PNA system. All experimental results are consistent with the predictions of the three-step model. Although designed for electrochemical measurements, the model may be used in a broader context such as for comparing electrochemical data with spectroscopic results.

In Chapters 3-5, experimental measurements are combined with theoretical computations. The effect of oxygen heteroatoms on the single molecule conductance of saturated organic chains

is the focus of Chapter 3. STM-controlled break junction measurements showed that the molecular conductance of ether chains is smaller than that of alkane chains. NEGF methods were used to show that the contribution of the molecular orbitals to the molecular conductance depends strongly on their delocalization, with higher contributions for more delocalized orbitals. Delocalization of the orbitals was found to be higher in the alkyl chains than in the oligoethers, a trend that is in agreement with that of the conductances determined experimentally. In addition, an NBO pathway analysis was performed for the alkane and ether chains such that the results can also be interpreted in the language of Marcus theory of non-adiabatic electron transfer. For the shortest chains, 5-C and 5-O, the effect of the self-energy[a] shift from C to O is compensated by an increased coupling. For the longer chains, the non-nearest neighbor contributions to the overall electronic coupling decreases this compensation and the difference in couplings through the two chains is more strongly manifested.

Optimized structures have been used in the theoretical analysis in Chapter 3 to obtain a single, static picture of charge transfer. In Chapter 4 and 5, more flexible and complicated systems are studied, which required a more dynamic picture and the analysis of an ensemble of conformations. The study in Chapter 4 explored the influence of structural flexibility on the charge transfer rate constant through PNA. Both the experimental and theoretical components of this study indicate that charge transport in PNA can be suppressed by limiting the conformational flexibility of the PNA duplex, e.g., by changing the backbone chemistry. While the charge transfer occurs through the nucleobases, the fluctuations of the PNA backbone broaden the nucleobase energy levels and thus increase the charge transfer rate. The fluctuating nature of the higher

[a] The diagonal elements of corresponding Fock matrix, not the self-energy matrix or self-energy operator in NEGF methods.

molecular conductance might not be the most desirable property if one wants to simply replicate the mechanism of the solid-state electronics to molecular electronics. As findings of fundamental science, the intrinsic fluctuations may lead to the development of molecular devices with novel mechanisms that are very different from the ones found in solid-state devices.

Finally, Chapter 5 explores a new scaffold for intramolecular photoinduced electron transfer studies. It is experimentally shown that $[Ru(Bpy)_3]^{2+}$* can transfer an electron to a $[CuQ_2]$ complex incorporated into the nucleobase stack of a PNA duplex. If the $[Ru(Bpy)_3]^{2+}$ complex can access the terminus of the duplex and interact with the nucleobase π-stack system. The electron transfer occurs through the nucleobase stack and is affected by mismatches and the number of nucleobase pairs between the donor and acceptor. If the $[Ru(Bpy)_3]^{2+}$ cannot access the PNA terminus, charge transfer can still proceed directly through space from the $[Ru(Bpy)_3]^{2+}$* to the $[CuQ_2]$ if they are close enough, however the charge transfer rate does not depend on the mismatches or the intervening nucleobase pairs. Comparing with the electrochemical method used in Chapter 4, the photophysical method in Chapter 5 allows one to reveal more details of charge transfer dynamics (and therefore possible conformational distributions) by using a lifetime distribution analysis. The conformational distribution has been corroborated by molecular dynamics simulations. Different from long-range hole hopping, the excess electron transfer in nucleic acids demonstrated in this chapter is still not well understood in the charge transfer community. This work shows again that the combined experimental and theoretical/computational study may be the best way to solve such complicated problems.

In summary, a new electrochemical model is proposed and verified, and different experimental methods together with appropriate computational approaches have been employed to explore the effects of different electronic structure (Chapter 3) as well as different geometries

and dynamics (Chapter 4 and 5) on the molecular conductance and electron transfer rate. If the explored system is rigid and not conformationally gated, one may focus on the optimized structure and analyze the conductance by the NEGF formulism or electronic coupling calculations, otherwise the dynamic effects must be taken into account, e.g., generating an ensemble of conformations by molecular dynamics. In a bigger picture, the non-adiabatic electron transfer within the framework of Marcus theory explored in this dissertation is a special case of a broader area of non-adiabatic dynamics. Because of the complexity, numerical simulations are preferred for quantitative estimation of transition probabilities for non-adiabatic dynamics other than electron transfer. However, clear physical pictures and simple lessons are usually lost in the huge amount of data, which is just the opposite of Marcus' paradigm. As more complex non-adiabatic electron transfer systems are being explored, the evolution of electron transfer theory and models may eventually lead to or inspire novel general theories that bridge the current gap between the electron transfer and other non-adiabatic dynamics without obscuring the usefulness for guidance to experiments and understanding mechanisms by adding too many parameters.

APPENDIX

MATLAB SCRIPTS FOR CHAPTER 1

The main MATLAB script for the three-step model (Words after "%" are comments):

```
close all; % delete all windows.

%%----Part I: In this part, variables, functions and parameters for the simulation and data output are defined.----%%
xaxis='sr'; %The xaxis could be 'lam' or  'sr'. 'sr' means "scan rate".
yaxis='shift'; %The yaxis could be 'shift' or 'width'
method='mmm'; %The method could be 'mcc', 'mcm' or 'mmm'. Note: Now only 'mmm' method is supported.
ifplotshift=true; %true if you need to plot peak shifts.
plotextra=false; %plot extra parameters. 'False' by default.
plotK=false;
%upperlimit=1e-4;
tstart=tic;
global dos Estep ifplotk0; %Make the three variables "global" so other scripts can use them.

%% ----------------------Definations related to k0--------------------------%
%Electrode-Bridge interface
dos=true; %use the 'DOS' model described in chapter 1. Always true.
deEB=0.235; % define the barrier height or ε_h.

%The followings are the kBE (electrode-bridge), kBB(bridge hopping) and kBF(bridge-reporter) rates at
equilibrium.
kBE_fp=37.5e3;
%On the Bridge
kBB_fp=2e3; %kBBarray=(1:0.1:2)*1e3;
%Bridge-Reporter Interface
kBF_fp=3.3e3;

scalingfactor=kBE_fp/kBF_fp; %scaling factor is used to control the asymmetry.

%% ----------------------Definitions about dynamic changes----------------%
%-------Lambdas------%
larray=0.1:0.1:1.0; %Defines the reorganization energy array to calculate. Used only when λ is to be plotted.
lambdaEB=0.2;
lambdaBB=0.1;
lambdaBF=0.6;
%-------Electric Potential Drop Percentages---%
ptgEB=0.2; %Percentage of the potential drop occurring at the Electrode-Bridge interface or "EB%" in the paper.
ptgBB=0.05; % This is "BB%", the potential drop across the bridge.

%% ------Simulation Setups-----%
T=298; %temperature
```

```
E0=0.0; %formal potential set to 0.
Einit=-0.4; %Initial voltage set to -0.4 V.
Eend=0.4; %Final voltage set to 0.4 V.
Estep=2e-4; % Voltage step. The interval between to calculated voltages.
varray=[1 3 5 8 12 18 30]*1e-3; %Scan rate (scan speed) array, in mV/sec.

ifplotk0=false;
xarray=[]; %to be plotted on the x-axis.

%% ----------------------Part II: Start Simulation----------%
if strcmp(method,'mcc')
   cvode=@pebf_mcc; %not implemented yet.
   ptgEB=1;
elseif strcmp(method,'mcm')
   cvode=@pebf_mcm; %not implemented yet.
   %ptgEB=0.5;
elseif strcmp(method,'mmm')
   cvode=@pebf_mmm; %call pebf_mmm for actual simulation.
end

%close all;

%Initializing the array to store rate data.
if strcmp(xaxis,'lam'); %if the x-axis is λ.
   Ecell=cell(1,length(larray));
   pparray=zeros(1,length(larray));
   %warray=pparray;
   k0array=pparray;
   kEBcell=Ecell;
   kBEcell=Ecell;
   akBFcell=Ecell;
   akFBcell=Ecell;
   Icell=Ecell;
   Solcell=Ecell;
   Timecell=Ecell;
   Ycell=Ecell;
   kBFcell=Ecell;
   kFBcell=Ecell;
   kBBoxcell=Ecell;
   kBBredcell=Ecell;
   pcell=Ecell;
   wcell=Ecell;
   lestr=cell(length(larray),1);
   i=1;
   for lambdaEB=larray

%The cvode used later is actually pebf_mmm.
%Only Ecell, pcell, and Icell would be used. kEBcell, kBEcell.. and other variables stores the calculated rate
constants and are for debug use only.

[k0array(i),Solcell{i},Ecell{i},Icell{i},kEBcell{i},kBEcell{i},kBBoxcell{i},kBBredcell{i},kBFcell{i},kFBcell{i},p
cell{i},wcell{i}]=cvode(T,v,E0,Einit,Eend,deEB,kBE_fp,scalingfactor,lambdaEB,ptgEB,kBB_fp,lambdaBB,ptgBB,
lambdaBF,ptgTUN);
      Timecell{i}=Solcell{i}.x;
      Ycell{i}=Solcell{i}.y;
      lestr{i}=[num2str(larray(i)),' eV'];
```

```
        i=i+1;
    end
    xarray=larray;
    xxlabel='\lambda_{EB} / eV';
    xtitle='vs. \lambda_{EB}';

%Make call for simulation as a function of scan speed (scan rate).
elseif strcmp(xaxis,'sr'); %scan rate is chosen by default.
%The cvode used later is actually pebf_mmm.
%Only Ecell, pcell, and Icell would be used. kEBcell, kBEcell.. and other variables stores the calculated rate
constants and are for debug use only.

    pparray=zeros(1,length(varray));
    %warray=pparray;
    k0array=pparray;
    Ecell=cell(1,length(varray));
    kEBcell=Ecell;
    kBEcell=Ecell;
    akBFcell=Ecell;
    akFBcell=Ecell;
    Icell=Ecell;
    Solcell=Ecell;
    Timecell=Ecell;
    Ycell=Ecell;
    kBFcell=Ecell;
    kFBcell=Ecell;
    kBBoxcell=Ecell;
    kBBredcell=Ecell;
    pcell=Ecell;
    wcell=Ecell;
    lestr=cell(length(varray),1);
    i=1;
    for v=varray

[k0array(i),Solcell{i},Ecell{i},Icell{i},kEBcell{i},kBEcell{i},kBBoxcell{i},kBBredcell{i},kBFcell{i},kFBcell{i},p
cell{i},wcell{i}]=cvode(T,v,E0,Einit,Eend,deEB,kBE_fp,scalingfactor,lambdaEB,ptgEB,kBB_fp,lambdaBB,ptgBB,
lambdaBF,ptgTUN);
        Timecell{i}=Solcell{i}.x;
        Ycell{i}=Solcell{i}.y;
        lestr{i}=[num2str(varray(i)*1e3),' mV/s'];
        i=i+1;
    end
    xarray=log10(varray);
    xxlabel='log_{10}(v)';
    xtitle='vs. Scan Rate';

else %If none of the above (lambda or scan rate) is selected.
    disp('Nothing to do...')
end
warray=zeros(2,length(wcell)); %the array to store peak widths.
pparray=zeros(2,length(pcell)); %the array to store peak positions.
for i=1:length(wcell);
    warray(:,i)=wcell{i};
    pparray(:,i)=pcell{i};
end
%--------------------------------------------------------------------------%
```

```
%Plotting the "production" curve, or working curve, or the trumpet plot.
if ifplotshift
   if strcmp(yaxis,'width') %Plot width on y-axis. Disabled by default.
      yarray=warray;
      yylabel='FWHM / mV';
      fulltitle=['Width ',xtitle];
   elseif strcmp(yaxis,'shift') %Plot shift on y-axis. Chosen by default.
      yarray=pparray*1000;
      yylabel='E-E_0 / mV';
      fulltitle=['Shift ',xtitle];
   else
      disp('I am confused, but what to plot?')
   end
   h=figure;hold all;plot(xarray,yarray,'--rs','LineWidth',2,...
      'MarkerEdgeColor','k',...
      'MarkerFaceColor','g',...
      'MarkerSize',10);
   %title(fulltitle);%,'FontSize',20);
   xlabel(xxlabel);%,'FontSize',20);
   ylabel(yylabel);%,'FontSize',20);
   grid off;
   set(findall(h,'-property','FontSize'),'FontSize',16,'FontName','Times');
   print(h,'-dpng','-r75',[fulltitle,'.png']);
   %print(h,'-depsc',fulltitle,'.eps']);
   %End of Plotting Production Curve.
   %--------------------------------------------------------------------------%
   box on;
   set(gca,'YTick',-100:25:100);
end

%% Plotting CVs for all lambdas/scan rates,...
ni=0;
h=figure;hold all;
%The length of Ecell is the number of CVs to be plotted. Ecell stores the potential data and Icell stores the current
data.
for i=1:length(Ecell)
   plot(Ecell{i},Icell{i},'LineWidth',2);
   temparr=Ecell{i};
   save(['run_pebf_Ecell_to_symm',num2str(i),'.dat'],'temparr','-ascii')
   temparr=Icell{i};
   save(['run_pebf_Icell_to_symm',num2str(i),'.dat'],'temparr','-ascii')
end
xlim([Einit,Eend]);
ylim([-0.4 0.3]);
set(gca,'YTick',-0.3:0.1:0.3);
grid off;
box on;
legend(lestr,'Location','Best');%title('CVs');
set(findall(h,'-property','FontSize'),'FontSize',16,'FontName','Times');
print(h,'-dpng','-r75','CVs.png');

%End of Plotting CVs

%save the data.
save -ascii run_pebf_parray_to_symm.dat pparray
```

%end of the main script.

The definition of function *pebf_mmm* (where the kinetic equations are solved) in the above script:

```
function [k0,Sol,Earray,Iarray,kEBarray,kBEarray,kBBoxarray,kBBredarray,kBFarray,kFBarray,Vp,width] =
pebf_mmm(T,v,E0,Einit,Eend,deEB,kBE_fp,scalingfactor,lambdaEB,frctEB,kBB_fp,lambdaBB,frctBB,lambdaBF,
~)
%Electrode-Bridge-Fc System.
%E-->B: Marcus (m)
%B-->B: Constant (c)
%C-->C: Marcus (m)
%version 0.5
%choose whether DOS model is used
global dos Estep;


%% --------------------Parameter Defination Area--------------------------%
kB=8.617343e-5; %Boltzmann Constant in eV/K
%T=298;
kT=kB*T;
%Estep=1e-4; %1e-4 is the step used in eif_marc.m.

%kBBox=kBB_fp*2; %I use kBBox and kBBred b/c it's easier to extend.
%kBBred=kBB_fp/2;%kBB_fp;
if dos==true;
   cEB=kBE_fp/(T^0.5*intkred(lambdaEB,-deEB));
   kEB_fp=cEB*T^0.5*intkox(lambdaEB,-deEB);
   kBF_fp=kBE_fp/scalingfactor; %to get cBF;
   disp(['kEB_fp= ',num2str(kEB_fp,'%0.4g')]);
   disp(['kBE_fp= ',num2str(kBE_fp,'%0.4g')]);
   disp(['kBB_fp= ',num2str(kBB_fp,'%0.4g')]);
   disp(['kBF_fp= ',num2str(kBF_fp,'%0.4g')]);
   disp(['kFB_fp= ',num2str(kBF_fp*kEB_fp/kBE_fp,'%0.4g')]);
else
   cEB=kBE_fp/(T^(-0.5)*exp(-(lambdaEB-deEB).^2/4/lambdaEB/kT));
   kEB_fp=cEB*T^(-0.5)*exp(-(lambdaEB+deEB).^2/4/lambdaEB/kT);
   kBF_fp=kBE_fp/scalingfactor; %to get cBF;
   disp(['kEB_fp= ',num2str(kEB_fp,'%0.4g')]);
   disp(['kBE_fp= ',num2str(kBE_fp,'%0.4g')]);
   disp(['kBB_fp= ',num2str(kBB_fp,'%0.4g')]);
   disp(['kBF_fp= ',num2str(kBF_fp,'%0.4g')]);
   disp(['kFB_fp= ',num2str(kBF_fp*kEB_fp/kBE_fp,'%0.4g')]);
end
%lambdaBF=0.8;
cBF=kBF_fp*T^(0.5)*exp((lambdaBF-deEB)^2/4/lambdaBF/kT); %The constant to replace actual dos.
cBB=kBB_fp*T^(0.5)*exp(lambdaBB/4/kT); %The constant to replace actual dos.
frctBF=1-frctEB-frctBB; % BF%. Note I used frctBF and frctEB, frctBB in this script.

%% Calculate k0
k0=pebf_fk0(kEB_fp,kBE_fp,kBB_fp,kBF_fp); %Find k0 at eqiulibuim.
display(['k0= ',num2str(k0)]);
%k0=1;%when no need to find this value now, set to 1.
```

```
%% -------------------Starting the oxidation process----------------------%
tic; %Solving the ode using Solver provided by MATLAB
display('ODE Timer Started...');
opts=odeset('MaxStep',Estep/v,'Vectorized','off');
%display('ODE Started');

Sol=ode15s(@pdba21_ode,[0 (Eend-Einit)/v],[0, 0, 0],opts); %was ode15s

pTime=Sol.x(1):1e-3/abs(v):Sol.x(end);
pY=interpa(Sol.x,Sol.y,pTime);
pY(pY>1)=1;

pEarray=Einit+v*pTime;

%If taking the last hopping site into account...
%pIarray=[0,diff(pY(3,:))./diff(pTime)]+[0,diff(pY(2,:))./diff(pTime)];
pIarray=[0,diff(pY(3,:))./diff(pTime)];

pkBF=kBF(pTime);
pkFB=kFB(pTime);
pkBBox=kBBox(pTime);
pkBBred=kBBred(pTime);
pkEB=pkBF; %Initialize pkEB & pkBE.
pkBE=pkBF;

i=1;
for E=pEarray
%    if dos==true
       pkEB(i)=kEB_marcus(pTime(i));
       pkBE(i)=kBE_marcus(pTime(i));
   i=i+1;
end


try
   pwidth=fwhm(pEarray,pIarray);
catch ME
   disp(ME);
   pwidth=0;
end
%% -------------------Starting the reduction process----------------------%
v=-v;
Eori=Einit;
Einit=Eend;
Eend=Eori;
nSol=ode15s(@pdba21_ode,[0 (Eend-Einit)/v],pY(:,end)',opts); %was ode15s

nTime=nSol.x(1):1e-3/abs(v):nSol.x(end);
nY=interpa(nSol.x,nSol.y,nTime);

nEarray=Einit+v*nTime;

%if taking the last hopping site into account...
%nIarray=[0,diff(nY(3,:))./diff(nTime)]+[0,diff(nY(2,:))./diff(nTime)];
nIarray=[0,diff(nY(3,:))./diff(nTime)];
```

```
Sol.x=[pTime nTime+pTime(end)];
Sol.y=[pY nY];
% Time=Sol.x;
% Y=Sol.y;
Earray=[pEarray nEarray];
Iarray=[pIarray nIarray];



try
   nwidth=fwhm(nEarray,nIarray);
catch ME
   disp(ME);
   nwidth=0;
end

tempt=toc;%Finishing Solving the two ODEs...
disp(['ODE Done. Time used: ',num2str(tempt),' seconds']);
%% ----------------End of Reduction Process-----------------------------%

%Iarray(Iarray<0)=0;
%Iarray(1:round(length(Iarray)/50))=0;
%Iarray=smooth(Earray,Iarray)';
%Iarray(Iarray<0)=0;
%figure;
%plot(Earray,Y);grid;
%figure;
%plot(Earray,Iarray);grid;

pVp=pEarray(pIarray==max(pIarray))-E0;
nVp=nEarray(nIarray==min(nIarray))-E0;
%cEBlc kox and kred. Just for output, won't be used in Solving ODEs.
%kEBarray=zeros(1,length(Earray));
%kBEarray=zeros(1,length(Earray));
v=-v;
%Eend=Einit;
Einit=Eori;
% akBF=[pakBF,nakBF]; %Apparent kBF
% akFB=[pakFB,nakFB]; %Apparent kFB
kBFarray=[pkBF fliplr(pkBF)]; %the array of kBF
kFBarray=[pkFB fliplr(pkFB)]; %the array of kFB
kBBoxarray=[pkBBox pkBBox];
kBBredarray=[pkBBred pkBBred];
kEBarray=[pkEB fliplr(pkEB)];
kBEarray=[pkBE fliplr(pkBE)];

pVp=mean(pVp); %in case the CVs are "stepwise" (esp. using crude step).
nVp=mean(nVp); %in case the CVs are "stepwise" (esp. using crude step).

Vp=[pVp,nVp];
Vp=Vp(1:2); %just for debugging; usually there is only 1 pVp and 1 nVp.
width=[pwidth,nwidth];
%k0=1;
%Earray((Iarray-0.5*max(Iarray)<0.1)
%% ----------Definition of subfunctions-----------------------------------%
```

```
    function dy=pdba21_ode(t,y)
        dy     = zeros(3,1);
        %The kinetic equations. Note the rate constants are changing.

        dy(1) = kEB_marcus(t)*1-kBE_marcus(t)*y(1)-kBBox(t)*y(1)+kBBred(t)*y(2); % including the reverse
reaction
        dy(2) = kBBox(t)*y(1)-kBBred(t)*y(2)-kBF(t)*y(2)*(1-y(3))+kFB(t)*y(3); % including the reverse reaction
        dy(3) = kBF(t)*y(2)*(1-y(3))-kFB(t)*y(3);
    end

    function Pot=Bias(t) %Total Potential Drop (bias) between the Electrode and Fc. Positive and Negtive.
        Pot=Einit-E0+v*t;
    end
%% The following three functions calculate the potential difference at Bridge/Ferrocene, Bridge/Bridge and
Electrode/Bridge interface.
    function Pot=etaBF(t) %Positive at f.p.
        Pot=deEB+Bias(t)*frctBF;
    end
    function Pot=etaBB(t) %Zero at f.p.
        Pot=Bias(t)*frctBB;
    end
    function Pot=etaEB(t) %Note it is negtive at f.p.
        Pot=frctEB*Bias(t)-deEB;
    end

    %%The following functions calculate the potential dependence of the rate constants using Marcus theory.
    function k=kBBox(t)
        k=cBB*T^(-0.5)*exp(-(lambdaBB-etaBB(t)).^2/4/lambdaBB/kT);
    end

    function k=kBBred(t)
        k=cBB*T^(-0.5)*exp(-(lambdaBB+etaBB(t)).^2/4/lambdaBB/kT);
    end

    function k=kEB_marcus(t)
        if dos==true
            k=cEB*T^0.5*intkox(lambdaEB,etaEB(t));
        else
            k=cEB*T^(-0.5)*exp(-(lambdaEB-etaEB(t)).^2/4/lambdaEB/kT); %to check the origin of asymmetry.
        end
    end

    function k=kBE_marcus(t)
        if dos==true
            k=cEB*T^0.5*intkred(lambdaEB,etaEB(t));
        else
            k=cEB*T^(-0.5)*exp(-(lambdaEB+etaEB(t)).^2/4/lambdaEB/kT); %to check the origin of asymmetry.
        end
    end

    function k=kBF(t)
        k=cBF*T^(-0.5)*exp(-(lambdaBF-etaBF(t)).^2/4/lambdaBF/kT);
        %k=kBF_fp;
    end

    function k=kFB(t)
```

```
      k=cBF*T^(-0.5)*exp(-(lambdaBF+etaBF(t)).^2/4/lambdaBF/kT);
      %k=kBF(t)*kFB_fp/kBF_fp; %This is idneticEBl to the fixt kBF and kFB!
      %k=kFB_fp;
   end

%The following functions calculate the integral over potentials.
   function y=intkox(lambda,eta) %The integral part of k_eg
      y=quadgk(@k_eta,(lambda-eta)/kT-100,(lambda-eta)/kT+100);
      %y=quadgk(@k_eta,-Inf,Inf);
      function y=k_eta(x)
         NsExp=(x-(lambda-eta)/kT).^2*(kT/4/lambda); %The exponent part (no sign)
         pA=exp(NsExp);
         pB=exp(x+NsExp);
         y=1./(pA+pB);
      end
   end
   function y=intkred(lambda,eta) %The integral part of k_eg
      y=quadgk(@k_eta,(lambda-eta)/kT-100,(lambda-eta)/kT+100);
      %y=quadgk(@k_eta,-Inf,Inf);
      function y=k_eta(x)
         NsExp=(x-(lambda+eta)/kT).^2*(kT/4/lambda); %Thune exponent part (no sign)
         pA=exp(NsExp);
         pB=exp(x+NsExp);
         y=1./(pA+pB);
      end
   end

end
```

The main script for the single-step model

```
%all definitions are similar as in the scripts for the three-step model.
close all; %close all windows
xaxis='sr'; %Calc Working curve for an assigned k0.
tstart=tic;
k0=0.275;%k0=0.125 for lower limit, 0.275 for upper limit.
tim=100;
T=298;%Temperature is 298K.
E0=0; %Formal potential set to 0.
Einit=-0.4;
Eend=0.4;
global Estep;
Estep=2e-4; %Use 1e-4 for production CV
%v_k0=[0.001 0.00316 0.01 0.0316 0.1 0.316 1];% 10 100];% 3.16 10 31.6 100]% 316 1000]; %v/k0
%lambdaarray=v_k0*k0; %Real v, in V/s
%varray=[1 5 30]*1e-3;
varray=[30]*1e-3;% 80 100]*1e-3;
varray=[1 3 5 8 12 18 30]*1e-3;
larray=0.1:0.1:1;

ifsave=false; %Do not save if only need a test!
if strcmp(xaxis,'sr');
   lambda=0.8;
   SepArray=varray;
   Ecell=cell(1,length(varray));
   Solcell=Ecell;
   Icell=Ecell;
   koxcell=Ecell;
   kredcell=Ecell;
   pcell=Ecell;
   wcell=Ecell;
   lestr=cell(length(varray),1);
   i=1;
   for v=varray
      %Get peak position by solving ode.

[Solcell{i},Ecell{i},Icell{i},koxcell{i},kredcell{i},pcell{i},wcell{i}]=peif_marc(k0,T,lambda,E0,Einit,Eend,v);
      SepArray(i)=max(pcell{i})-min(pcell{i});
      %[Sol,Earray,Iarray,kayox,kayred,Vp,width]=peif_marc(k0,T,lambda,E0,Einit,Eend,v);
      lestr{i}=[num2str(varray(i)*1e3),' mV/s'];
      i=i+1;
   end
   %eval(['parray_',num2str(k0*tim),'_div_',num2str(tim),'=parray;']); %Save parray at different k0 to different
arrays
   %Start plotting the working curve
   warray=zeros(2,length(pcell));
   parray=zeros(2,length(pcell));
   for i=1:length(wcell);
      warray(:,i)=wcell{i};
      parray(:,i)=pcell{i};
   end
   h=figure;
   plot(log10(varray),parray*1000,'--rs','LineWidth',2,...
      'MarkerEdgeColor','k',...
```

```
        'MarkerFaceColor','g',...
        'MarkerSize',10);
    set(gca,'FontSize',16);
    xlabel('log_{10}(v)','FontSize',16);ylabel('E-E_0/mV','FontSize',16);
    %title('Shift vs. Scan Rate','FontSize',16);
    print(h,'-dpng',['peif_workingcurve_k0_',num2str(k0),'.png']);
    grid off;
    box on;
    ylim([-100,100]);
    set(gca,'YTick',-100:25:100);
set(findall(h,'-property','FontSize'),'FontSize',16,'FontName','Times');
elseif strcmp(xaxis,'lam') %Try to get the relationship between the peak width and lambda.
    v=varray(10);
    Ecell=cell(1,length(larray));
    Solcell=Ecell;
    Icell=Ecell;
    koxcell=Ecell;
    kredcell=Ecell;
    lestr=cell(length(larray),1);
    i=1;
    for lambda=larray
        %Get peak position by solving ode.

[Solcell{i},Ecell{i},Icell{i},koxcell{i},kredcell{i},pcell{i},wcell{i}]=peif_marc(k0,T,lambda,E0,Einit,Eend,v);
        lestr{i}=[num2str(larray(i)),' eV'];
        i=i+1;
    end

    %Start plotting the FWHM vs. E curve
    h=figure;
    plot(larray,warray,'--rs','LineWidth',2,...
        'MarkerEdgeColor','k',...
        'MarkerFaceColor','g',...
        'MarkerSize',10);
    set(gca,'FontSize',16);
    xlabel('\lambda /eV','FontSize',16);ylabel('FWHM/V','FontSize',16);
    title('FWHM vs. \lambda: Elec-Fc System','FontSize',16);
    print(h,'-dpng',['peif_fwhm_k0_',num2str(k0),'.png']);
    %Finish plotting
else
    disp('Nothing to do...')
end

%Plotting CVs
h=figure;hold all;
for i=1:length(Ecell(1:end))
    plot(Ecell{i},Icell{i},'LineWidth',2);
    temparr=Ecell{i};
    if ifsave==true
        save(['run_peif_Ecell_',num2str(i),'.dat'],'temparr','-ascii')
    end
    temparr=Icell{i};
    if ifsave==true
        save(['run_peif_Icell_',num2str(i),'.dat'],'temparr','-ascii')
    end
end
```

```
legend(lestr(1:end));%title('CVs');
grid off;
box on;
set(findall(h,'-property','FontSize'),'FontSize',16,'FontName','Times');
set(gca,'YTick',-0.3:0.1:0.3);

return;

%Plotting rate constants
figure;plot(Ecell{1},[koxcell{1};-kredcell{1}]);title('k_{ox} and k_{red}');

%Plotting populations
PFc=Solcell{1}.y;
corrarray=ones(1,length(PFc)/2);
corrarray=[corrarray,-corrarray]; %to make reverse scan negtive

figure;plot(Ecell{1},PFc.*corrarray,'k.');title('P_{Fc}');

disp('----------------------------------------');
disp(['k0: ',num2str(k0)]);
disp(['SepArray: ',num2str(SepArray)]);
disp('----------------------------------------');

return;

%Plotting k_ox and k_red vs. E
figure;hold all;%Plotting kox
for i=1:length(Ecell)
   plot(Ecell{i},log10(koxcell{i}));
end
legend(lestr);title('log_{10}k^{ox}');xlabel('Bias/V');

figure;hold all;%Plotting kred
for i=1:length(Ecell)
   plot(Ecell{i},log10(kredcell{i}));
end
legend(lestr);title('log_{10}k^{red}');xlabel('Bias/V');

disp(warray);
toc(tstart);
```

The definition of *peif_marc* (where the kinetic equations are solved) in the main script for the single-step model:

```
function [Sol,Earray,Iarray,kayox,kayred,Vp,width]=peif_marc(k0,T,lambda,E0,Einit,Eend,v)
%Electrode-Insulator-Fc system, simulated using full Marcus formulism
kB=8.617343e-5; %Boltzmann Constant in eV/K
%T=298;
kT=kB*T;
global Estep
%Estep=1e-3; %step of voltage (in volt)
cA=k0/intkox(0)/T;
%mod='ode';
%Eend=E0+0.2;
```

```
%Calc k at different voltages
%pEarray=Einit:Estep:Eend-E0;

%if mod=='ode'
tic; %pSolving the ode using pSolver provided by MATLAB
%matlabpool(maxNumCompThreads); %Set the pool, so parfor can be used.
opts=odeset('MaxStep',Estep/v);
%----------------Start Solving the Oxidation Process----------------------%
pSol=ode15s(@eif_ode,[0 (Eend-Einit)/v],0,opts);
% 12/29/2012: Looks like @eif_ode is what I need to modify for the p-presentation.
pTime=pSol.x(1):Estep/abs(v):pSol.x(end);
pY=interpa(pSol.x,pSol.y,pTime);
% while pY(end)<0.995
%     Eend=Eend+0.1;
%     pSol=odextend(pSol,[],(Eend-Einit)/v);
%     pTime=pSol.x;
%     pY=pSol.y;
% end
pEarray=Einit+v*pTime;
pIarray=[0,diff(pY)./diff(pTime)];
%figure;plot(pEarray,pY);grid;
try
   pwidth=fwhm(pEarray,pIarray);
catch ME
   disp(ME);
   pwidth=0;
end
%----------------Finish Solving the Oxidation Process----------------------%
%----------------Start Solving the Reduction Process----------------------%
v=-v;
Eori=Einit;
Einit=Eend;
Eend=Eori;
nSol=ode15s(@eif_ode,[0 (Eend-Einit)/v],pY(end),opts);
% 12/29/2012: eif_ode again.
nTime=nSol.x(1):Estep/abs(v):nSol.x(end);
nY=interpa(nSol.x,nSol.y,nTime);
% while pY(end)<0.995
%     Eend=Eend+0.1;
%     pSol=odextend(pSol,[],(Eend-Einit)/v);
%     pTime=pSol.x;
%     pY=pSol.y;
% end
nEarray=Einit+v*nTime;
nIarray=[0,diff(nY)./diff(nTime)];
%figure;plot(pEarray,pY);grid;

try
   nwidth=fwhm(nEarray,nIarray);
catch ME
   disp(ME);
   nwidth=0;
end
%----------------Finish Solving the Reduction Process----------------------%
toc;%Finishing Solving the ODE...
```

```
Sol=pSol;
Sol.x=[pTime nTime+pTime(end)];
Sol.y=[pY nY];
Earray=[pEarray,nEarray];
Iarray=[pIarray,nIarray];
kayox=zeros(1,length(Earray));
kayred=zeros(1,length(Earray));

%Calc kox and kred. Just for output, won't be used in pSolving ODEs.
i=1;
for E=Earray
   kayox(i)=cA*T*intkox(E);
   kayred(i)=cA*T*intkred(E);
   i=i+1;
end
pVp=pEarray(pIarray==max(pIarray))-E0;
nVp=nEarray(nIarray==min(nIarray))-E0;
Vp=[pVp,nVp];
width=[pwidth,nwidth];
%--------------defination of subfunctions----------------------%

%kinetic equations.
   function dy=eif_ode(t,y)
      %% The following is the orignal expression.
      dy=(1-y)*cA*T*intkox(Einit+v*t-E0)-y*cA*T*intkred(Einit+v*t-E0);
      %% The followin is used to explore the asymmetry of the TSM.
      %dy=(1-y)*cA*T*intkox(Einit+v*t-E0)-y*cA*T*intkred(Einit+v*t-E0);
   end

   function y=intkox(eta) %The integral part of k_eg
      y=quadgk(@k_eta,(lambda-eta)/kT-100,(lambda-eta)/kT+100);
      %y=quad(@k_eta,-1000,1000);
      function y=k_eta(x)
         NsExp=(x-(lambda-eta)/kT).^2*(kT/4/lambda); %The exponent part (no sign)
         pA=exp(NsExp);
         pB=exp(x+NsExp);
         y=1./(pA+pB);
      end
   end

   function y=intkred(eta) %The integral part of k_eg
      y=quadgk(@k_eta,(lambda-eta)/kT-100,(lambda-eta)/kT+100);
      %y=quad(@k_eta,-1000,1000);
      function y=k_eta(x)
         NsExp=(x-(lambda+eta)/kT).^2*(kT/4/lambda); %The exponent part (no sign)
         pA=exp(NsExp);
         pB=exp(x+NsExp);
         y=1./(pA+pB);
      end
   end

end
```